

**Direct fault dating trials at the  
Äspö Hard Rock Laboratory**

R H Maddock<sup>1</sup>, E A Hailwood<sup>2</sup>, E J Rhodes<sup>3</sup>, R Muir Wood<sup>4</sup>

- 1 GeoScience Ltd, Ascot, UK
- 2 Department of Oceanography, Southampton University, UK
- 3 Royal Holloway College, University of London, UK
- 4 BEQE, Warrington, UK

October 1993

DIRECT FAULT DATING TRIALS AT THE ÄSPÖ HARD ROCK  
LABORATORY

R H Maddock<sup>1</sup>, E A Hailwood<sup>2</sup>, E J Rhodes<sup>3</sup>, R Muir Wood<sup>4</sup>

1 GeoScience Ltd, Ascot, UK

2 Department of Oceanography, Southampton  
University, UK

3 Royal Holloway College, University of London, UK

4 BEQE, Warrington, UK

October 1993

This report concerns a study which was conducted for SKB. The conclusions and viewpoints presented in the report are those of the author(s) and do not necessarily coincide with those of the client.

Information on SKB technical reports from 1977-1978 (TR 121), 1979 (TR 79-28), 1980 (TR 80-26), 1981 (TR 81-17), 1982 (TR 82-28), 1983 (TR 83-77), 1984 (TR 85-01), 1985 (TR 85-20), 1986 (TR 86-31), 1987 (TR 87-33), 1988 (TR 88-32), 1989 (TR 89-40), 1990 (TR 90-46), 1991 (TR 91-64) and 1992 (TR 92-46) is available through SKB.

DIRECT FAULT DATING TRIALS  
AT THE ÄSPÖ HARD ROCK LABORATORY

R.H. Maddock<sup>1</sup>, E.A. Hailwood<sup>2</sup>, E.J. Rhodes<sup>3</sup> &  
R. Muir Wood<sup>4</sup>

October 1993

- 1 GeoScience Ltd, Silwood Park, Ascot, SL5 7QW, UK
- 2 Department of Oceanography, Southampton University, UK
- 3 Royal Holloway College, University of London, UK
- 4 BEQE, Warrington, UK

Keywords: Äspö, fault, faultrock, fracture zone, isotopic dating, ESR dating, mineralogy, palaeomagnetic dating

**ABSTRACT**

Over seventy rock samples were collected from fault and fracture zones in the Äspö Hard Rock Laboratory tunnel for a study of direct fault dating techniques. Following microstructural and mineralogical analysis, isotopic, palaeomagnetic and electron spin resonance (ESR) methods were employed in an attempt to determine the age of the most recent movements on the sampled faults.

The larger fracture zones contain faultrock assemblages and microstructures which are consistent with a prolonged and polyphase movement history, although the cumulative displacement is difficult to quantify. For the important fracture zones NE-4 and NE-3, the most recent shear displacements involved formation of fault gouge cemented by authigenic 'illite'. Dating studies were targeted particularly at the gouge but also at older faultrock and vein phases.

ESR dating of quartz grains, separated from gouge from fracture zones NE-4 and NE-3, strongly indicates that the ESR signals have not been reset by fault movements for a minimum time period of several hundred thousand to one million years. These minimum ages are inherently limited by the dating technique.

Palaeomagnetic dating of gouge from Fracture Zone NE-4 shows that a stable component of magnetisation overlaps both Precambrian (c.1350Ma) and Permo-Triassic (c.270-190Ma) parts of the apparent polar wander curve. The younger age of magnetisation is preferred on geological grounds and by comparison with the isotopic dating results. The magnetisation may correspond to a diagenetic event following fault movement. Palaeomagnetic ages determined on countryrock and epidote vein samples are largely consistent with independent age constraints.

K-Ar dating of clay fractions (<2 to <0.05 $\mu$ m) separated from gouge from four faults, including fracture zones NE-4 and NE-3, gave model ages in the range 706-301Ma. Accounting for the effects of contamination by potassium-bearing porphyroclasts, it is likely that authigenic 'illite' was formed at least 250 million years ago, after the most recent significant fault movements. Oxygen and hydrogen isotope analyses of the dated clay fractions show that they are not in equilibrium with present-day groundwaters at Äspö. It is possible that the clays were precipitated from an isotopically-heavier brine.

This multi-disciplinary trial of fault dating techniques has been successful in showing the potential for fault dating studies to become a standard component of investigations on the long-term stability of bedrock.

**ABSTRACT (SWEDISH)**

Mer än 70 prover från förkastningar och sprickzoner i Äspö-tunneln har insamlats. I syfte att bestämma åldrarna på de senaste förkastningsrörelserna i berget har proverna analyserats med avseende på paleomagnetiska egenskaper, isotopförhållanden (K/Ar, Rb/Sr, stabila syre- och väteisotoper) samt elektronspinresonans (ESR). Mineralogi och mikrostrukturer har också studerats.

De större sprickzonerna har en komplex historia och uppvisar tydliga tecken på upprepade aktivering. Det totala förkastningsbeloppet är svårt att bestämma. I sprickzonerna NE-3 och NE-4 har den senaste reaktivering resulterat i en uppkrossning som delvis cementerats med autogen illit/smektit. Dateringsarbetet har koncentrerats på just denna sena lermineralbildning men även prover från äldre mineraliseringar i sprickzonerna samt sidoberget har analyserats.

ESR-datering av kvartskorn från sprickzonerna NE-3 och NE-4 visar att ingen resetting av ESR-signalen orsakad av förkastningsrörelser har ägt rum under det daterbara tidsintervallet (0.7 till 1 miljoner år).

Paleomagnetisk datering av uppkrossat och senare lercementerat material från sprickzon NE-4 visar att en stabilkomponent av magnetisering överlappar APW (Apparent Polar Wander)-kurvan för två olika tidsintervaller (ca 1350 Ma och ca 270-190 Ma). Den yngre åldern för magnetisering bedöms som mer trovärdig baserat på geologisk information såväl som K-Ar dateringar på illit/smektit (>250 Ma). Magnetisering kan vara ett resultat av diagenetisk omvandling som postdaterar förkastningsrörelserna. Paleomagnetiska åldrar på Smålandsgraniten (ca 1750 Ma) och epidotläkta sprickor (ca 1350 Ma) visar åldrar i överensstämmelse med radiometriska resultat.

K-Ar-dateringar av lermineraldominerade extremt finkorniga fraktioner (<2 till <0.05 m) av material från fyra olika krosszoner inkluderande zonerna NE-3 och NE-4 gav modellåldrar i intervallet 705 till 301 Ma. Kontaminering av kaliumförande porfyroklaster kan förklara den stora spridningen i resultatet. Det är dock troligt att illiten/smektiten bildades för åtminstone 250 miljoner år sedan och att mineralbildningen postdaterar den sista stora reaktiveringen. Analyser av stabila syre- och väteisotopförhållanden i de daterade lermineralen visar att de inte är i jämvikt med det grundvatten som provtagits i området. Snarare är lermineralen bildade i jämvikt med ett mer salint vatten eventuellt vid högre temperaturer.

## SUMMARY

This report documents a programme of "Direct Fault Dating Trials at the Äspö Hard Rock Laboratory" undertaken by GeoScience Limited, UK, for Svensk Kärnbränslehantering AB (SKB, Swedish Nuclear Fuel and Waste Management Co). The programme was coordinated and part of the analytical work performed by GeoScience staff. State-of-the-art dating analyses were made by the authors, and others, at the Universities of Southampton and London and at the Scottish Universities Research and Reactor Centre.

The objectives of the project were to collect faultrock and vein materials from the Äspö Hard Rock Laboratory and to undertake 'direct fault dating' trials of selected samples, targeted towards constraining the minimum age of the most recent movements on the sampled faults.

Some seventy rock samples were collected and examined to provide information on the history of fault movements and to assess the suitability of the samples for dating. The characterization included XRD and electron microprobe analysis together with microstructural analysis by optical and electron microscopy. These analyses demonstrated that many fracture zones, including EW-7, NE-4 and NE-3, contain sequentially-developed faultrocks, recording the localization of strain over geological time. The oldest, mylonitic faultrocks were deformed semi-plastically at elevated temperature and pressure. Subsequent episodes of faulting involved repeated cataclastic deformation and vein formation. The faultrocks identified on textural and mineralogical grounds as being related to the most recent fault movements are poorly-lithified gouges cemented by authigenic 'illite'.

Palaeomagnetic, electron spin resonance (ESR) and isotopic dating techniques were employed in attempts to date the most recent movements on the faults. Thus dating concentrated on the fault gouges. Each dating technique requires that certain criteria are met, and these were largely satisfied for the Äspö samples.

Palaeomagnetic dating involves comparison with a pre-established chronology. Palaeomagnetic ages were therefore determined for countryrock, cataclasite and vein samples, as well as, the younger gouges. The country rock samples yielded a Proterozoic palaeomagnetic age (c.1800Ma), consistent with independent age data. Stable components of magnetisation in epidote-rich cataclasites and veins overlapped late Proterozoic and Palaeozoic parts of the apparent polar wander curve. Geological data support the late-Proterozoic age for acquisition of magnetisation.

A stable component of magnetisation in gouge from Fracture Zone NE-4 is not significantly different in orientation from the epidote veins. However, a Permo-Triassic (c.270-190Ma) age of magnetisation is preferred on geological grounds and from comparison with the isotopic dating results. The magnetisation may correspond to a diagenetic event following fault movement.

Isotopic dating employed the K-Ar technique. K-Ar analyses of five 'wallrock' samples gave model ages in the range 1280-437Ma. Fine grainsize fractions ( $<2\mu\text{m}$  to  $<0.05\mu\text{m}$ ) were separated from eight gouge samples from fracture zones NE-4, NE-3 and two minor faults, to try to isolate the authigenic 'illite'. The separates were examined by scanning and transmission electron microscopy and XRD. K-Ar model ages measured on the separates ranged from 706 to 302Ma (Precambrian to Upper Carboniferous). The finest grainsize fractions generally gave younger model ages than the coarser fractions due to contamination by potassium-bearing porphyroclasts. Taking into account such contamination, it is likely that the authigenic 'illite' was formed at about 300Ma, after the most recent, significant fault movements. Trial Rb-Sr dating of gouge separates from NE-4 was also undertaken.

The oxygen and hydrogen isotopic compositions of the dated clay fractions are not in equilibrium with present-day groundwaters at Äspö. It is possible that the clays were precipitated from an isotopically-heavier brine and have partially equilibrated with present-day waters.

Quartz grains were separated from seven gouge samples, from NE-4, NE-3 and a minor fault, for ESR dating. ESR spectra were measured for various paramagnetic centres (E', OHC, Ge and Al) in the quartz. The measurements indicated that saturation had been achieved prior to artificial irradiation, and therefore resetting of the ESR signals by fault movement had not occurred in the recent geological past. Assuming normal signal growth characteristics, the minimum age of resetting - which is inherently limited by the technique - is of the order of several hundred thousand years to one million years.

The ages given by the various dating methods reflect both inherent differences in the techniques and differences in the phase or phenomenon being dated. Nevertheless, the results of the palaeomagnetic and K-Ar analyses of gouges strongly suggest that authigenic mineral growth in fracture zones NE-4, NE-3 and two other minor faults took place at least 250 million years ago. The most recent fault movements are interpreted to precede this mineral growth. It is possible that the fault movements and mineral growth were related to elevated heatflow associated with burial beneath two to three kilometres of Palaeozoic sedimentary cover.

**ACKNOWLEDGEMENTS**

This project was initiated following discussions between L. Ericsson and R. Stanfors (SKB) and R. Muir Wood and R.H. Maddock in November 1990. The work subsequently developed into two phases and the continuing support of L. Ericsson and R. Stanfors is gratefully acknowledged.

None of the work would have been possible without the logistical, intellectual and practical assistance of the SKB and contractor's staff at the Äspö Hard Rock Laboratory. In particular we thank R. Christiansen, A. Stråhle, R. Stanfors, L. Stenberg, E. Thorsen & O. Zellman.

We are grateful to C. Hughes & S. Barlow (Manchester University), for mineral separations, A. Beard & S. Hirons (Birkbeck College) for assistance with SEM and XRD analyses, A. Fallick & B. Davidson (SURRC) for mineral separations and isotopic analyses, F. Ting (Southampton University) for assistance with the palaeomagnetic analyses, J. Hugget (Petroclays Ltd) for STEM and XRD analyses, W. Howliston & M. Walters (GeoScience Ltd) for computing, and M. Gillespie (British Geological Survey), A. Fallick & M. Turner (GeoScience Ltd) for discussions on isotopic analyses of fault gouge.

E-L. Tullborg kindly provided an essential critique of an earlier draft of this Report and corrected some of our misconceptions concerning Swedish geology. Any remaining errors are, however, the responsibility of the authors alone.



## TABLE OF CONTENTS

	Page
<b>ABSTRACT</b>	ii
<b>ABSTRACT (SWEDISH)</b>	iii
<b>SUMMARY</b>	iv
<b>ACKNOWLEDGEMENTS</b>	v
<b>TABLE OF CONTENTS</b>	vii
<b>1 INTRODUCTION</b>	<b>1</b>
1.1 PREAMBLE	1
1.2 OBJECTIVES	1
1.3 METHODOLOGY	1
1.4 REPORT STRUCTURE	3
<b>2 TECTONIC AND STRUCTURAL SETTING OF THE ÄSPÖ HRL</b>	<b>4</b>
2.1 INTRODUCTION	4
2.2 TECTONIC EVOLUTION OF SOUTHERN SWEDEN	4
2.2.1 Precambrian structural framework	4
2.2.2 Late Precambrian rifting	7
2.2.3 Palaeozoic	7
2.2.4 Mesozoic	9
2.2.5 Tertiary and Quaternary	10
2.3 STRUCTURAL EVOLUTION OF THE ÄSPÖ HRL	10
2.3.1 General geology	10
2.3.2 Evolution of mylonitic fabrics	10
2.3.3 Evolution of brittle deformation	11
2.3.4 Relationship between fractures and fluid flow	17
2.3.5 Summary	17
<b>3 SAMPLE LOCALITIES</b>	<b>19</b>
3.1 INTRODUCTION	19
3.1.1 Sampling strategy	19
3.1.2 Terminology	19
3.1.3 Sample localities	20
3.2 INFORMATION GALLERY AREA	20
3.2.1 NNE-trending epidote vein	20
3.2.2 Gouge seam, chainage 118m	20
3.2.3 Aplite dyke, chainage 140m	25
3.3 GEOCHEMISTRY LABORATORY FAULT	25
3.4 FRACTURE ZONE EW-7	25
3.5 FRACTURE ZONE NE-4	31
3.6 FRACTURE ZONE NE-3	35
3.7 NW-STRIKING FAULT, CHAINAGE 1103m	35
3.8 NNE-STRIKING FAULT, CHAINAGE 1130m	37
3.9 PUMP STATION	37
3.10 FRACTURE ZONE EW-3	38
3.11 OTHER LOCALITIES	40
<b>4 MINERALOGY AND MICROSTRUCTURES</b>	<b>41</b>
4.1 INTRODUCTION	41
4.2 INFORMATION GALLERY	42
4.2.1 Epidote vein, chainage 112m	42
4.2.2 Fault, chainage 118m	42
4.3 GEOCHEMISTRY LABORATORY FAULT	44

4.4	FRACTURE ZONE EW-7	46
4.4.1	Fault 1	46
4.4.2	Fault 2	47
4.5	FRACTURE ZONE NE-4	53
4.5.1	Preamble	53
4.5.2	Mylonite sample A91/29	53
4.5.3	Cataclasite sample A91/36	55
4.5.4	Gouge samples A91/30 and A91/33	57
4.5.5	Gouge sample AS14.10	59
4.6	NNE-TRENDING FAULT, 1130m CHAINAGE	63
4.7	OTHER LOCALITIES	65
4.8	XRD AND GRAIN SIZE ANALYSES	67
4.8.1	XRD analyses	67
4.8.2	Grainsize analyses	67
4.9	SYNTHESIS	67
5	<b>PALAEOMAGNETIC ANALYSES</b>	72
5.1	INTRODUCTION	72
5.2	SAMPLING	73
5.3	MAGNETIC INTENSITY	75
5.4	DEMAGNETISATION ANALYSES AND MAGNETIC STABILITY	77
5.4.1	Epidote veins/breccia, carbonate vein and aplite dyke	77
5.4.2	Fault gouge	78
5.4.3	Hostrock	83
5.5	COMPONENTS OF MAGNETISATION IN EACH ROCK TYPE	83
5.5.1	Epidote veins/breccia, carbonate vein and aplite dyke	83
5.5.2	Fault gouge	90
5.5.3	Hostrock	90
5.6	DISAGGREGATION EXPERIMENTS	94
5.7	MAGNETOMINERALOGICAL INVESTIGATIONS USING IRM-ACQUISITION ANALYSES	98
5.8	MAGNETIC FABRIC	98
5.8.1	Protomylonitic granite	102
5.8.2	Fault gouge	102
5.9	INTERPRETATION OF RESULTS AND DATING OF FAULTROCKS	104
5.9.1	Magnetisation directions	104
5.9.2	Acquisition of magnetisation	107
5.9.3	Comparison with apparent polar wander curves for Baltica	108
5.10	CONCLUSIONS	113
6	<b>ISOTOPIC ANALYSES</b>	115
6.1	INTRODUCTION	115
6.2	REVIEW OF EXISTING STUDIES	115
6.2.1	Radiometric dating of fault gouge	115
6.2.2	Stable isotope chemistry of fault gouge	116
6.2.3	Comment	116
6.2.4	Note on illite terminology	117
6.3	APPLICATION OF K-Ar METHOD TO DIRECT DATING FAULT GOUGE	117
6.3.1	Systematics	117
6.3.2	General assumptions	119
6.3.3	Dating authigenic illite in fault gouge	120

6.4	ANALYTICAL METHODS	122
6.4.1	Mineral separation	122
6.4.2	Mineral characterization	122
6.4.3	K-Ar analysis	123
6.4.4	Rb-Sr analysis	123
6.4.5	Stable isotope analysis	124
6.5	CHARACTERIZATION RESULTS	124
6.5.1	Sample details	124
6.5.2	XRD analysis	125
6.5.3	STEM analysis	130
6.5.4	Mineral chemistry of illitic gouge	136
6.6	K-Ar RESULTS	139
6.6.1	Countryrocks	139
6.6.2	Gouge materials	140
6.6.3	Isotopic disturbance and mixing	144
6.6.4	Porphyroclast contamination modelling	145
6.7	Rb-Sr ANALYSES	151
6.8	STABLE ISOTOPE ANALYSES	152
6.8.1	Results	152
6.8.2	Discussion	155
6.9	SYNTHESIS OF RESULTS	158
7	<b>ESR ANALYSES</b>	160
7.1	INTRODUCTION	160
7.1.1	Background	160
7.1.2	ESR dating of quartz from fault gouge	162
7.2	SAMPLE COLLECTION AND FIELD MEASUREMENTS	163
7.3	MINERAL SEPARATION PROCEDURES	164
7.4	MEASUREMENTS AND RESULTS	168
7.4.1	Environmental radiation dosimetry	168
7.4.2	ESR spectrometry	170
7.5	INTERPRETATION AND DATING	179
7.6	CONCLUSIONS	180
8	<b>CONCLUSIONS AND RECOMMENDATIONS</b>	181
8.1	SUMMARY OF RESULTS	181
8.2	RECOMMENDATIONS	183
9	<b>REFERENCES</b>	184
<b>APPENDIX 1</b>	Preliminary mineral separations of fault gouge and grain size analysis	
<b>APPENDIX 2</b>	SEM microprobe and STEM mineral analyses	
<b>APPENDIX 3</b>	Orientation data for palaeomagnetic samples	
<b>APPENDIX 4</b>	Portable gamma-ray spectroscopy measurements for ESR dating	

**TABLES**

2-1	Tectonic evolution of southern Sweden	5
2-2	Mineralization events at Äspö	14
2-3	Summary of deformation and fracture filling	18
3-1	Faultrock nomenclature	20
3-2	List of samples	22

3-3	Gouge seams in fracture zone NE-4	34
4-1	Summarized results of XRD mineral analyses	68
5-1	Rock types and number of sites sampled	74
5-2	Palaeomagnetic data	84
5-3	Disaggregation analysis for fault gouge samples	96
5-4	Characteristic magnetisation and pole positions	105
5-5	Summary of palaeomagnetic dating results	113
6-1	Materials selected for isotopic analysis	125
6-2	Sample fraction characterisation	126
6-3	Summary XRD, mineralogy and grainsizes	129
6-4	SEM microprobe analyses of illitic materials	137
6-5	STEM analyses of illitic material	138
6-6	K-Ar isotope analyses of wallrocks	141
6-7	K-Ar isotope analyses of gouge separates	142
6-8	Rb-Sr isotopic data	152
6-9	Stable isotope analyses of gouge separates	154
7-1	Gouges sampled for ESR dating	164
7-2	Summary of mineral separation procedures	166
7-3	Environmental radiation dosimetry	168
7-4	Neutron activation analysis results	169
7-5	Summary of ESR signal growth	173

## FIGURES

2-1	Large-scale structure of the Baltic Shield	6
2-2	Geological setting and structure of Äspö HRL	12
2-3	Structure of Äspö HRL	13
2-4	Stereoplots of fractures recorded in Äspö HRL tunnel	16
3-1	Schematic map of sample localities	21
3-2	Information Gallery and Geochemistry Laboratory faults	26
3-3	Fracture Zone EW-7, schematic log of side tunnel	27
3-4	Fracture Zone EW-7, faults 1 and 2	30
3-5	Fracture Zone NE-4	32
3-6	Schematic log of NE-4	33
3-7	Minor NW- and NNE-trending faults	36
3-8	Fracture Zone EW-3	39
4-1	Photomicrographs of Information Gallery faultrocks	43
4-2	Photomicrographs of Geochemistry Laboratory faultrocks	45
4-3	Photomicrographs of Fracture Zone EW-7 faultrocks	48
4-4	Photomicrographs of Fracture Zone EW-7 faultrocks	50
4-5	Photomicrographs of Fracture Zone EW-7 faultrocks	52
4-6	Photomicrographs of Fracture Zone NE-4 faultrocks	54
4-7	Photomicrographs of Fracture Zone NE-4 faultrocks	56
4-8	Photomicrographs of Fracture Zone NE-4 faultrocks	58
4-9	Photomicrographs of Fracture Zone NE-4 faultrocks	60
4-10	Photomicrographs of Fracture Zone NE-4 faultrocks	62
4-11	Photomicrographs of Fracture Zone NE-4 faultrocks	64
4-12	Photomicrographs of faultrocks, chainage 1130m	66
4-13	Grain size analyses of fault gouge samples	69
5-1	NRM intensity histograms	76
5-2	Demagnetisation behaviour of epidote/cataclasite veins	79
5-3	Demagnetisation behaviour of gouge and breccia	81
5-4	Demagnetisation behaviour of country rock	82
5-5	Stereoplots of vein/cataclasite and aplite NRM vectors	91
5-6	Stereoplots of gouge and breccia NRM vectors	92

5-7	Stereoplots of country rock NRM vectors	93
5-8	Susceptibility and ARM of gouge granule and 'clay' components	97
5-9	IRM acquisition curves for epidote vein and breccia	99
5-10	IRM acquisition curves for gouge granule and 'clay' components	100
5-11	IRM acquisition curves for country rock samples	101
5-12	Stereoplots of faultrock magnetic fabrics	103
5-13	Stereoplot showing 'Group A' NRM vectors	106
5-14	Apparent polar wander path, Scandinavia, 1900-900Ma	109
5-15	Apparent polar wander path, Baltica, 500Ma-present	110
6-1	Illite terminology	118
6-2	XRD traces of gouge separates	127
6-3	TEM micrographs of gouge separates	132
6-4	Length vs width scatter plots of gouge separates	134
6-5	Histograms of K-Ar calculated ages	143
6-6	$^{40}\text{K}$ vs $^{40}\text{Ar}$ diagrams	146
6-7	$^{40}\text{Ar}/^{36}\text{Ar}$ vs $^{40}\text{K}/^{36}\text{Ar}$ diagrams	147
6-8	$^{40}\text{Ar}/^{36}\text{Ar}$ vs $1/^{36}\text{Ar}$ diagrams	148
6-9	Information Gallery samples	149
6-10	Effects of K-feldspar contamination	150
6-11	Histograms of $\text{H}_2\text{O}^+$ , $\delta^{18}\text{O}$ and $\delta\text{D}$ values	153
6-12	$\delta^{18}\text{O}_{\text{H}_2\text{O}}$ in equilibrium with illite	156
6-13	Crossplot of $\delta^{18}\text{O}$ vs $\delta\text{D}$	156
7-1	Background to ESR dating technique	161
7-2	Optical photomicrographs of quartz separates	167
7-3	RT ESR spectra of samples A91/6, 8, 23, 32	174
7-4	RT ESR spectra of samples A91/38, 39	175
7-5	Cryogenic ESR spectra of samples A91/6 & A91/8	176
7-6	$\text{LN}_2$ ESR spectra of samples A91/23, 32, 38, 39	177
7-7	$\text{LN}_2$ ESR spectra of samples A91/23, 6, 8, 32, 39	178

## 1 INTRODUCTION

### 1.1 PREAMBLE

The containment afforded by an underground, high-level nuclear waste repository is dependent not only on the engineered barriers of the facility but also on the inherent geological characteristics of the rock mass within which it is constructed. Of these characteristics, faults and large fractures are among the most important since such features have the potential to act as pathways or barriers to groundwater flow, and to exert an influence on bedrock stability.

Careful analysis and dating of faultrocks and fracture fillings can contribute directly to understanding the tectonic and hydrogeologic evolution of the rock mass, and also provide constraints on the timing of the latest movements on faults.

### 1.2 OBJECTIVES

Bearing in mind the above statement, the objectives of this project were threefold:

- 1) To sample fault and fracture materials from the Äspö Underground Hard Rock Laboratory (HRL).
- 2) To determine the suitability of the samples for various dating techniques, and to undertake dating trials of selected samples.
- 3) To review the results of the dating trials, and provide recommendations on how uncertainties in the interpretation of calculated ages may be reduced.

### 1.3 METHODOLOGY

In the past few years, new dating techniques and new methods of investigating faultrocks have inspired research into 'direct fault dating'. Direct fault dating aims to constrain the age of fault movements by dating intrafault material (faultrock) itself. Faultrock dating becomes important when it is necessary to constrain the age of the most recent movement on a fault, and there are no undisturbed materials cross-cutting or overlying the fault which are amenable to meaningful dating.

In the field of direct fault dating, many of the dating techniques whose application is comparatively routine for undeformed rock and fossil, archaeological or speleological materials, are still evolving in their application. A proper understanding of the microstructure

and mineralogy of faultrocks and related materials, and their wallrocks, is a pre-requisite to any direct dating attempts. For this reason, very careful attention must be paid to sample collection in the field, and the preparation and microstructural and mineralogical characterization of specimens for dating.

The choice of suitable dating techniques depends upon the nature of the materials being dated. In this study, the faultrocks formed during the most recent fault movements were found to be amenable to dating by palaeomagnetic, electron spin resonance (ESR) and isotopic methods. Each technique involves a different 'clock' by which dating is achieved and each technique requires certain criteria to be met by the samples.

The palaeomagnetic dating technique relies upon a comparison between the direction of characteristic magnetisation in the faultrock with the predicted geomagnetic field vector for the locality for different geological periods. For meaningful application of this technique it is necessary to demonstrate: (i) that the faultrocks acquired a component of magnetization at the time of faulting, or through some subsequent hydrothermal event; (ii) that this magnetization is parallel to the Earth's contemporary magnetic field; (iii) that subsequent local tectonic re-orientation can be corrected for; and, (iv) that it is possible to predict the Earth's magnetic field for the region through geological time.

Electron spin resonance (ESR) spectrometry measures the concentration of electrons trapped in crystal defects as a result of natural irradiation (largely through the decay of K, U and Th within the crystal and its local environment). For fault dating, the successful application of the technique is dependent upon the annihilation, during fault displacement, of the accumulated defects in quartz grains within fault gouge. Thus the ESR 'clock' may be reset to zero at a time corresponding to the last movement on the fault. However, the physical processes of resetting during fault movement are not fully understood. Optimally, samples for ESR dating should be collected from a depth of 100m or more - a condition which was met by most samples from the Äspö tunnel.

In essence, isotopic dating of faultrocks relies upon being able to identify, separate and date mineral phases within the faultrock, which formed either during or after fault movement. Irrespective of which isotope system is utilized for dating it is necessary to demonstrate an understanding of the relationship between fault movements and growth of the separated and dated mineral phase(s). In practice this is a non-trivial task, and considerable space is devoted in this report to describing the microstructures and characterizing the mineralogy of the

isotopically dated fault gouge materials. Due consideration is also paid to various potential sources of error in the resultant model ages.

#### 1.4 REPORT STRUCTURE

This document reports the results of two phases of study following fieldwork undertaken in November 1991 and in November 1992 respectively. The results of the first phase of work were reported to SKB in July 1992 (GeoScience Report CB91/R1/086). The present Report includes the consolidated results of both phases of study, and thus supersedes the previous Report.

Following an introductory summary of the tectonic setting of Äspö in Section 2, descriptions of the fault and fracture zone localities and of the mineralogy and microstructure of the faultrocks are given in Sections 3 and 4 respectively. The results of the dating trials, together with a brief outline of the techniques used, are presented separately for palaeomagnetic, isotopic and electron spin resonance analyses in Sections 5, 6 and 7. The conclusions and recommendations of the study are synthesized in Section 8.



## 2 TECTONIC AND STRUCTURAL SETTING OF THE ÄSPÖ HRL

### 2.1 INTRODUCTION

The purpose of this section is to provide a tectonic and chronological framework to the geology of the Äspö HRL, with a level of detail appropriate to consideration of the results of the direct fault dating trials.

From a tectonic viewpoint, it is necessary to draw upon a wide geographical area whereas the description of the structural evolution of Äspö itself is drawn essentially from local observations.

### 2.2 TECTONIC EVOLUTION OF SOUTHERN SWEDEN

The tectonic evolution of southern Sweden is summarized in Table 2-1 and discussed in more detail below.

#### 2.2.1 Precambrian structural framework

The Baltic Shield in southern Sweden is made up of two Precambrian orogenic terranes: the Svecofennian and the Southwest Scandinavian Domain which were consolidated at about 1800Ma and 1550Ma respectively (Fig 2-1). These were the last major episodes of orogenesis in southern Sweden in which considerable crustal thickening and magmatism accompanied widespread crustal deformation. Along its western margin, the Svecofennian is intruded by the post-orogenic cordilleran-style Transscandinavian Igneous Belt (TIB) of 1780-1600Ma age (Lundqvist 1979; Gorbatshev 1980). Äspö itself is situated within this igneous belt. Formation of the TIB was more-or-less contemporaneous with orogenesis in the gneiss of the Southwest Scandinavian Domain.

Southwest Scandinavia was subject to further reworking and intrusion around 1400Ma and during the (Grenvillian) Sveconorwegian episode of reworking from c. 1250-900Ma (Gorbatshev 1980). This had the effect of resetting K-Ar model ages to around 1000Ma (Lundqvist 1979; Gorbatshev et al 1987), and also overprinting palaeomagnetic signatures in dykes of various primary ages of intrusion (Bylund 1992), across a wide zone within and to the east of the Protogine Zone (Fig 2-1).

In the Svecofennian/TIB of southeast Sweden, significant granite intrusion occurred at c. 1550Ma and 1400-1350Ma and basic dyke intrusion at 1750-1400Ma and 1000-800Ma (Lundqvist 1979; Gorbatshev et al 1987).

Table 2-1 Summary of the tectonic evolution of southern Sweden

Period	Age (Ma)	Event
Late Cretaceous/Early Tertiary	100-60	compressional inversion*
Mid-Cretaceous	120	volcanism*
Late Jurassic/Early Cretaceous	150-120	rifting*
Mid-Jurassic	165	volcanism*
Late Triassic/early Jurassic	200-160	rifting*
Carboniferous/Permian	290	rifting & volcanism
Variscan	300	compressional inversion*
Late Precambrian	1000-600	rifting & dyke intrusion
Precambrian	1250-900	Sveconorwegian reworking (SW Sweden)
	1550-1350	anorogenic granite intrusion
	1780-1600	Transscandinavian Igneous Belt
	1800	Svecofennian consolidation

Note: \* denotes known only from within the Fennoscandian Border Zone

The Protogine Zone, a fundamental lineament apparently tracing a pre-1700Ma suture (Gorbatshev 1980), delimits the boundary between the penetratively deformed and reworked gneiss of the Southwest Scandinavian Domain and the significantly less-deformed TIB (Fig 2-1). This lithological mismatch suggests substantial crustal shortening or strike-slip displacement (Gorbatshev et al 1987), and the zone has been the locus of repeated subsequent deformation. The Mylonite Zone (Fig 2-1) appears to have been active from c. 1500Ma to about 900Ma, although it too probably originated in Svecofennian times (Lundqvist 1979).

The southern edge of the shield is demarcated by the Tornquist Line (Fennoscandian Border Zone), also a major continental suture, which has localised many kilometres of displacement during the last few hundred million years.

Following the accretion and consolidation of the shield, the region has maintained a cratonic character for hundred's of millions of years. A number of episodes of comparatively minor rifting can however be identified within the shield, each of which led to the deposition of an unmetamorphosed sedimentary succession.

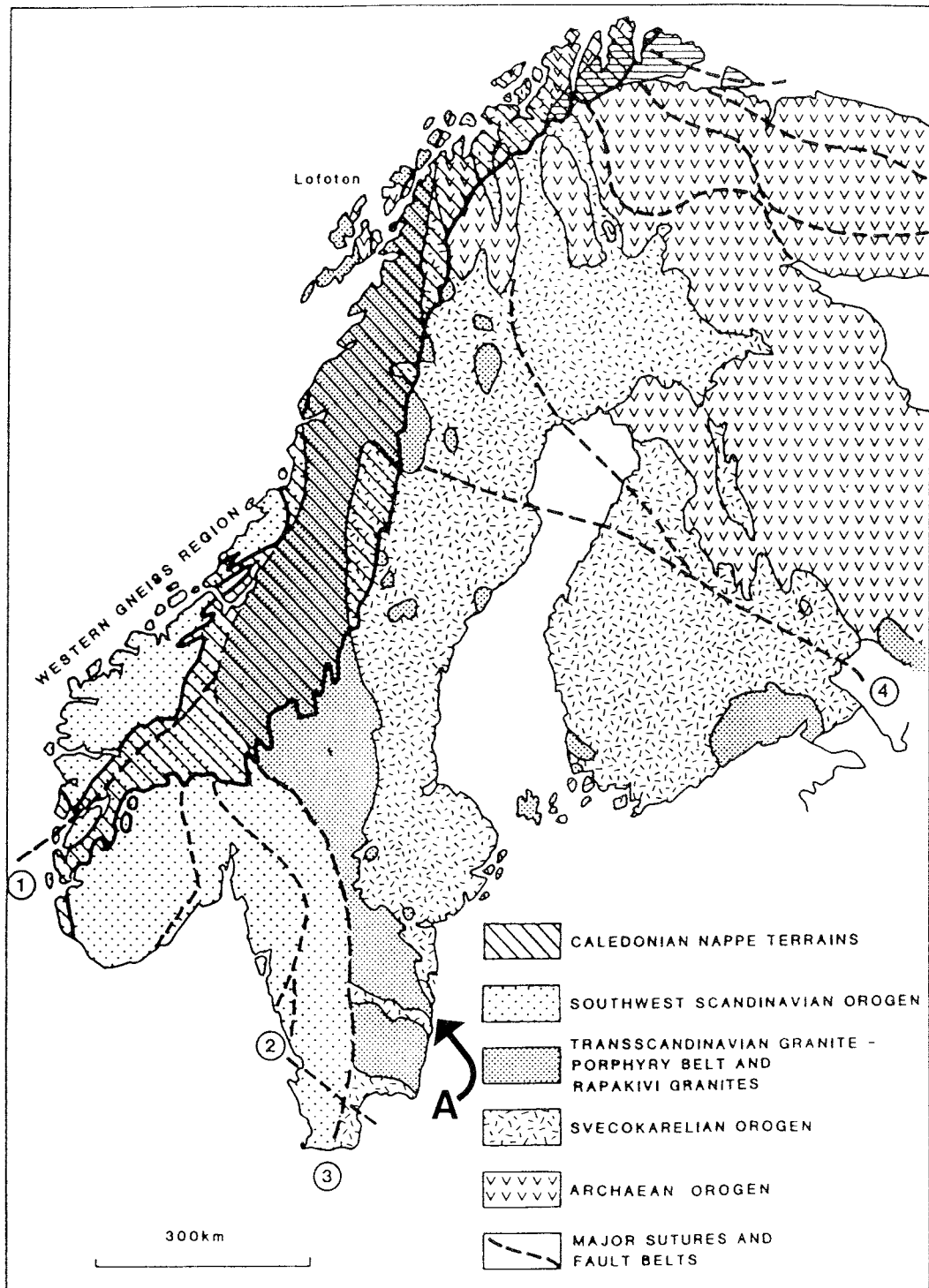


Fig. 2.1 Orogens of the Baltic Shield. The horizontally ruled area in northernmost Scandinavia is the Timanide Aulacogen resting on Archaean crust covered by Svecokarelian sediments. The sutures and fault belts indicated by digits are: 1. 'Faltungsgaben' delimiting the Western Gneiss Region in Norway; 2. 'Mylonite Zone' suture; 3. 'Protogine Zone' suture; 4. Ladoga-Lofoten belt of faulting.

**Figure 2-1** Map showing the large-scale structure of the Baltic Shield. The location of the Äspö HRL is marked by 'A'. (after Gorbatshev 1985)

### 2.2.2 Late Precambrian rifting

The most important phases of rifting occurred in the late Precambrian (c. 1000-600Ma). Up to 1km of Middle and Upper Rhiphaean age sediments are found around the Gulf of Bothnia and Baltic and some of the bounding faults have displacements of up to 1000m (including the Landsort-Kappelshamn line to the north of Gotland; Floden 1980). A series of narrow NNE-SSW trending graben structures with vertical displacements in excess of 500m developed in the central Baltic are of possible Upper Rhiphaean or Vendian age (Ulmishek 1991). Up to 1km of late Rhiphaean - early Vendian (c. 600Ma) rift subsidence occurred in the Lake Vattern area (Vidal 1984), again controlled by a narrow NNE trending rift.

Penetration of much of the Baltioscandian platform occurred in the latest Precambrian (Bergstrom and Gee 1985).

### 2.2.3 Palaeozoic

#### (a) **Clastic dykes**

Scattered fissure-fillings including clastic dykes puncture the exhumed sub-Cambrian peneplain (Martinsson 1968; Samuelsson 1975); most are regarded as Cambrian in age but few are reliably dated (Bergstrom and Gee 1985). Clastic dykes in the Äspö region have a NE strike (Talbot et al 1988) whereas in the Göteborg area of southwest Sweden similar dykes have a predominant WNW-ESE strike (Samuelsson 1975). This suggests that either the dykes are of different ages or that they did not reflect *regional* extension vectors. As well as sandstone, the dykes contain other infills including calcite and fluorite in the Äspö region (Talbot et al 1988) and shale, limestone, calcite, asphaltite and clay in the Göteborg area (Samuelsson 1975).

#### (a) **Basin subsidence**

The Lower Palaeozoic succession in the Baltic Basin probably developed as a result of post-rift thermal sag; to the east of Gotland, sedimentation was unaffected by the late Precambrian rift structures (Ulmishek 1991). In the Baltic Basin the sedimentary sequence is complete from the late Vendian through to the Lower Devonian, attaining maximum thicknesses of 4km in the south; elsewhere, a few hundred metres of early Palaeozoic sediments survive across much of the Baltic.

Onshore, platform sequences of a few hundred metres thickness of Cambrian and/or Ordovician strata (clastics, black shales and limestones) remain scattered across

southern Sweden, Bornholm, Öland and Gotland (Bergstrom and Gee 1985; Bruton et al 1985). The Cambrian and Ordovician strata of Öland and the adjacent mainland (Cambrian only) lie just a few kilometres to the southeast and south of Äspö. In southeastern Scandinavia, remnants of the autochthonous Silurian cover are preserved in Scania, Vastergotland, Ostergotland, Bornholm and Gotland.

By end-Silurian times, a cover of Old Red Sandstone across all of Scandinavia (Basset 1985) may have been as thick as two to three kilometres (Tullborg et al 1994).

#### **(b) Mid-Palaeozoic 'Caledonian' inversion**

Tectonothermal deformation in the Scandinavian Caledonides began in the Early Ordovician (c. 510Ma), reached its culmination during collision of Laurentia and Baltica during the Silurian (c. 440-410Ma), and had largely waned by the time of Devonian orogenic collapse (c. 410-365) (Roberts and Gee 1985; McClay et al 1986). The Caledonian front lies some 350km northeast of Äspö (Fig 2-1), although the autochthonous Lower Palaeozoic platform sequences can, in places, be traced into the parautochthonous and allochthonous Caledonides.

In the Baltic Basin the Lower Devonian and locally the entire Upper Silurian section have been eroded from the crests of a series of E-W and NE-SW trending arches controlled by high angle reverse faults passing in a chain from Latvia to northern Poland. The maximum vertical offset seen on these faults is 300-350m, although most faults and associated monoclines have amplitudes between 100-150m (Ulmishek 1991).

Displacement of a complex of faults trending between NNE-SSW and E-W which affect the sub-Cambrian peneplain and remnant cover of Lower Palaeozoic sediments in south central Sweden (Ahlin 1982, 1987) and the Gulf of Bothnia, may chiefly be of Caledonian (mid-Devonian, c. 380Ma) age. The throw on these faults is typically 40-60m rising to 200-300m on the West Botnian coastal boundary fault north of Gavle. This is the last significant tectonic episode recorded from the Baltic basin. 'Hercynian' (Late Devonian to Carboniferous) sediments distributed across the truncated Caledonian sedimentary sequence in the southern and eastern Baltic are almost entirely undeformed.

#### **(c) End-Palaeozoic rifting and intrusion**

Towards the end of the Palaeozoic the Oslo Graben formed as a result of rifting associated with extensive magmatic activity dated at 305 to 245Ma (quoted in Gorbatshev et

al 1987). The major graben boundary faults have displacements of 2-3km, and formed in response to E-W extension, probably on the site of a pre-existing continental fracture zone (Ramberg and Spjeldnaes 1978). Dykes which follow the NW Tornquist Line trend in Scania, and sills in Vastergotland are also of this age (Klingspor 1976; Gorbatshev 1987) and suggest more widespread elevated heat flow and uplift. Some confirmation of this is given by palaeomagnetic overprints recorded in Ordovician age 'Orthoceras Limestones' from these areas (Perroud et al 1992).

It is possible that some of the faulting seen in and around the Lake Vanern area was active at this time, and also likely that Variscan age NW-SE dextral wrench faulting occurred along the Fennoscandian Border Zone (Liboriussen et al 1987).

#### 2.2.4 Mesozoic

##### (a) Rifting

Knowledge of Mesozoic tectonics in Sweden is entirely restricted to the Fennoscandian Border Zone, where deformation was concentrated along the southern edge of the Baltic shield. Rifting began in the Late Triassic and accelerated into the Jurassic, with rifts forming along NNW-SSE trends with intervening horsts (Liboriussen et al 1987; Norling and Bergstrom 1987). Transverse troughs with an ENE-WSW trend also developed in a transtensional (sinistral) regime along the Fennoscandian Border Zone. Horizontal and vertical displacements on faults within the zone can be measured in kilometres (eg. Sivhed 1991).

In the Mid-Jurassic (c. 165Ma), a phase of regional uplift and alkali-basaltic volcanism in the central Scania area of the Fennoscandian Border Zone has parallels with mid North Sea activity (Klingspor 1976).

Rifting along the Fennoscandian Border Zone was renewed in the late Jurassic and early Cretaceous (Norling and Bergstrom 1987) and further volcanism has been dated from the Santonian (120Ma; Printzlau and Larsen 1972).

##### (b) Late Cretaceous inversion

Late Cretaceous dextral wrench movement, along the Tornquist Line led to inversion of the Mesozoic basins in the Fennoscandian Border Zone, uplift and also some related transtensional basin subsidence in the Danish Basin (Liboriussen et al 1987). This phase of dextral transpression was most significant during Santonian-Campanian times, but appears to have been renewed in the late Palaeocene (Liboriussen et al 1987).

### 2.2.5 Tertiary and Quaternary

There are no Tertiary sediments known from anywhere in Sweden. By Neogene times the Fennoscandian Border Zone appears to have stabilized although narrow NE-SW elongated Quaternary-filled basins occur in the Kattegat.

A recent review of the seismotectonics of Sweden found the documented evidence for (Quaternary or Recent) neotectonics in southern Sweden to be very weak (BEQE 1992).

## 2.3 STRUCTURAL EVOLUTION OF THE ÄSPÖ HRL

### 2.3.1 General geology

The geological evolution of the Äspö region mirrors on a smaller scale that of southern Sweden.

The Äspö region is made up of Småland Granite together with minor enclaves of older metavolcanics and gneiss and more abundant younger intrusives (Fig 2-2). Svecokarelian (broadly equivalent to Svecofennian) deformation in the enclaves predates intrusion of the post-orogenic Transscandinavian Igneous Belt Småland Granite at around 1840-1760Ma (Kornfalt and Wikman 1987).

The most significant of the younger intrusives are the anorogenic Göttemar and Uthammar granites dated at 1400-1350Ma (Fig 2-2). A NNW-striking swarm of basic dykes which fed sills that dip c. 20° to the SW was intruded during the latest Grenvillian (c. 1000Ma). Still younger, narrow, N-S striking dolerite dykes are also present (Wikberg et al 1991).

From about 900Ma to the beginning of the Phanerozoic, a period of erosion and peneplanation occurred. Presumed Cambrian age clastic dykes and faulted Cambrian strata are found close to Äspö (Section 2.2.3 and below) Little is known about the post-Cambrian development of the Äspö area except that which can be inferred from the regional picture (Section 2.2) and from the relative ages of younger fractures and their fillings.

### 2.3.2 Evolution of mylonitic fabrics

The gross structure of the Äspö region is imparted by the broad E-W alignment of intrusions and enclaves within the Småland Granite and by geophysical lineaments which strike N-S, E-W, NE and NW (Fig 2-2; Wikberg et al 1991). The dominant fabric within the HRL site area is a steep NE-ENE penetrative foliation. This structural trend also corresponds to the orientation of basic sheets back-veined by two or more generations of aplite and pegmatite

(Talbot and Munier 1989), and has localized subsequent plastic and brittle reactivation (Fig 2-3).

The NE-ENE foliation is defined by early gneissic zones deformed at amphibolite facies, and reactivated by (?)greenschist facies mylonitic shear zones during uplift between 1700-1400Ma (Talbot 1990). The most prominent example is the Äspö Shear Zone (EW-1 in Fig 2-3) containing steep N-dipping, E-W striking mylonites, ten metres or more in length. (The Äspö Shear Zone is also coincident with a regional scale geophysical lineament). Small mylonitic shears, a few metres long and a about a centimetre in width have widely dispersed orientations.

Some uncertainty remains concerning the age and number of penetrative mylonitic foliations (see Talbot 1990), although regional considerations suggest that the E-W mylonites predate those with NE strikes (Talbot and Munier 1989). Most significantly, however, no mylonites have been found in the 1400-1350Ma Uthammar or Göttemar granites although a weak biotite alignment is developed in the country rocks immediately surrounding these intrusions (Talbot 1990).

Kinematic interpretations of the mylonites are given by Talbot (1990; 1991) but will not be discussed further here.

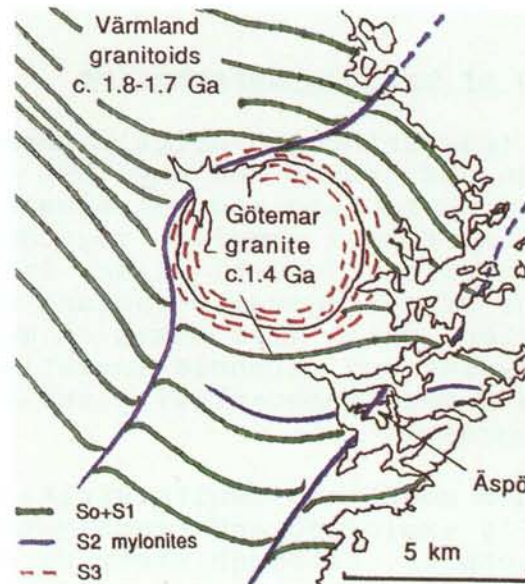
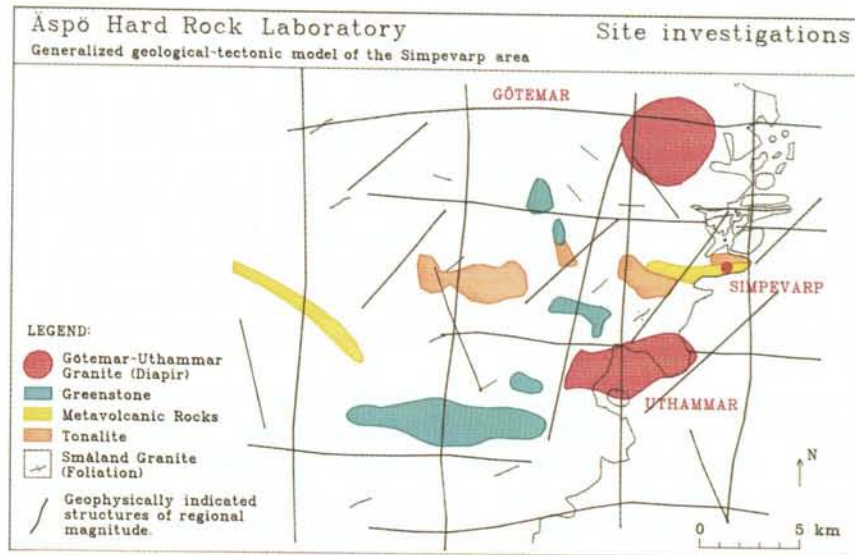
### 2.3.3 Evolution of brittle deformation

The nature of fracturing and brittle (non-mylonitic) faulting within and around the Äspö HRL site area has been determined by mapping and petrological study of outcrop, core and tunnel samples, together with a large program of geophysical investigation. Initial interpretations of geological structure made prior to tunnel excavation, which were based on mapping, remote sensing, geophysics and borehole investigation, (Wikberg et al 1991) have been substantially verified during the tunnelling programme.

Brittle fracture zones and faults striking NE, E-W and N-S have generally exploited and reactivated the existing mylonitic structures, although steep NW and near-horizontal fractures, largely independent of existing structures, also developed (Wikberg et al 1991).

Epidote veins, commonly associated with quartz, follow the mylonitic zones and are believed to have formed as a consequence of intrusion of the Göttemar and Uthammar granites (c. 1400-1350Ma). Two generations of epidote have been identified by microscopy (eg. Tullborg et al 1991) but generally have not been discriminated during surface and tunnel mapping studies (eg. Munier 1992).





**Figure 2-2** (a) Map showing the geological setting of the Äspö region (after Wikberg et al 1991); (b) map showing the main fabric elements of the Äspö region (after Talbot 1990).

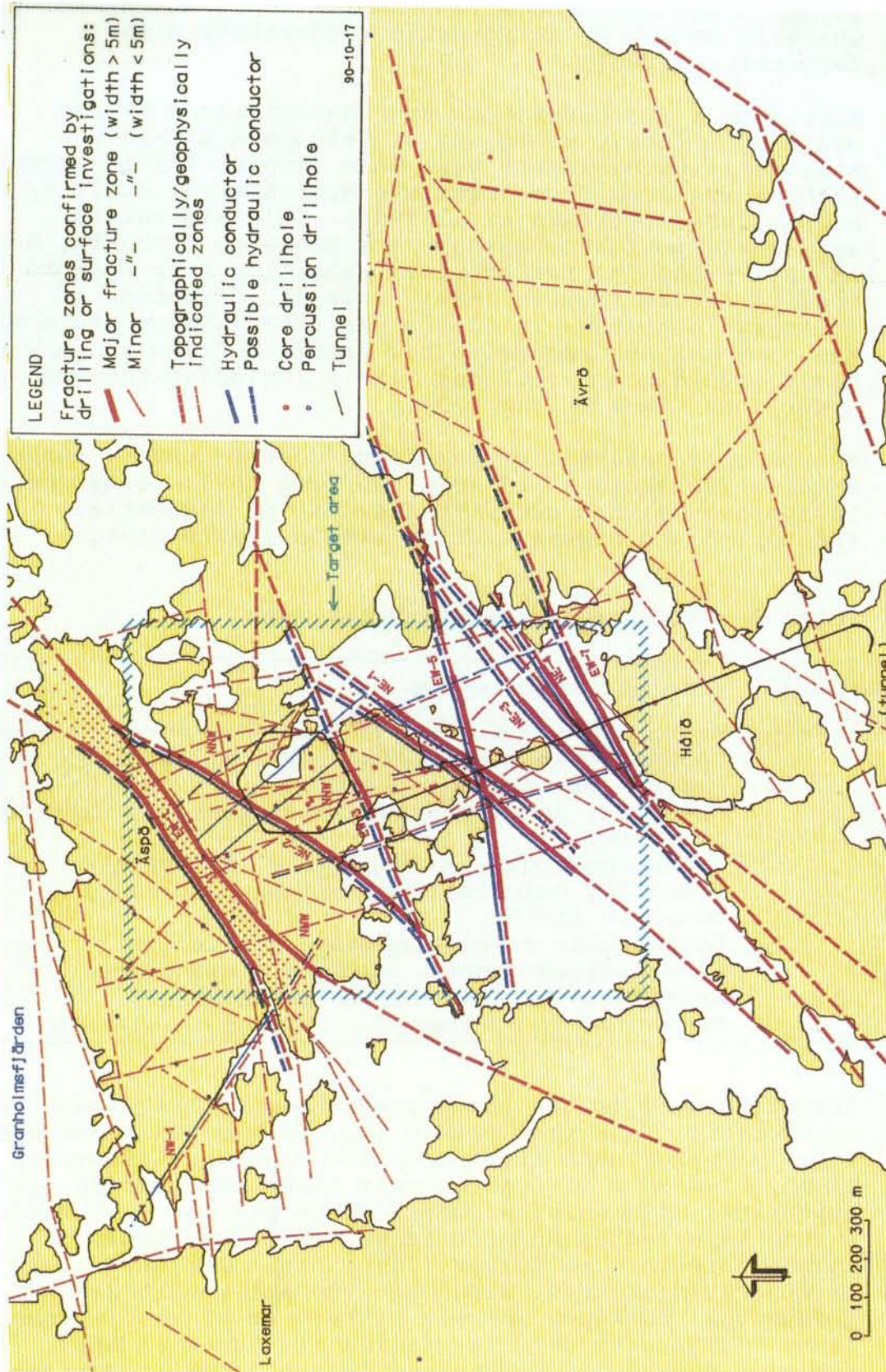


Figure 2-3 Pre-investigation fracture zone interpretation map of Äspö (after Wikberg et al 1991).

Somewhat surprisingly, Talbot (1990) describes an amygdaloidal dolerite sill (shallow depth of intrusion) which is offset by an epidotic (moderately high temperature) fault.

Extensional fractures that are characterized by red staining of their walls and of feldspars within a millimetre to decimetre wide halo (Munier 1992), appear to have resulted from oxidative hydrothermal activity at about 1100Ma (Wikberg et al 1991). This alteration apparently postdates epidote but predates prehnite, and is interpreted to reflect the transition from epidote to zeolite facies (Munier 1989). However, oxidation of 'primary' magnetite is also a characteristic feature of the fine-grained and mylonitic granites found in many of the fracture zones (Eliasson 1993) including the Äspö Shear Zone (EW-1 in Fig 2-3).

Microscopic analysis of core and, more recently, tunnel samples (Tullborg et al 1991; Wikberg 1991; Landstrom and Tullborg 1993) has added to the list of sequential fracturing and mineralization events (Table 2-2).

Table 2-2 Mineralization events at Äspö

Relative age	Mineralization event
6	Gypsum, chlorite, illite, pyrite, adularia, quartz probably kaolinite.
5	Prehnite, hematite-stained laumontite, calcite & fluorite.
4	Idiomorphic quartz, muscovite, hematite, fluorite, calcite, spherulitic chlorite & possible Fe-OOH.
3	Idiomorphic Fe-rich epidote & fluorite.
2	Fine-grained quartz, epidote & muscovite associated with mylonitic deformation.
1	Formation of 'primary' foliation in granite.

Assigning ages to the younger episodes of fracturing and mineralization is problematic (eg. Munier 1992) and has largely relied upon inference. The Cambrian limestones of Öland, 20km east of Äspö contain minor NE-striking faults associated with calcite veins. These are the only faults in the Äspö region whose movement is demonstrably Phanerozoic in age. Talbot (1990) has correlated these, on kinematic grounds, with 'zeolite and synglacial kinematics' on Äspö, whereas Wikberg et al (1991) compare these faults with chlorite-filled fractures on Äspö. Although synglacial fracturing is mentioned in various publications, disruption of the bedrock at Äspö associated with Quaternary glaciation appears to be

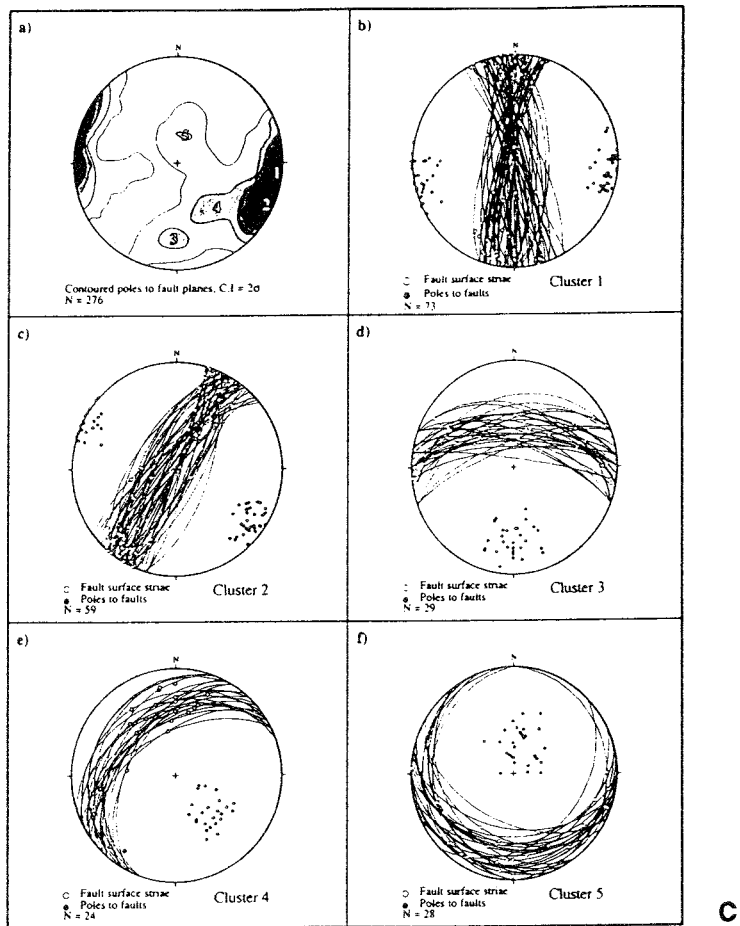
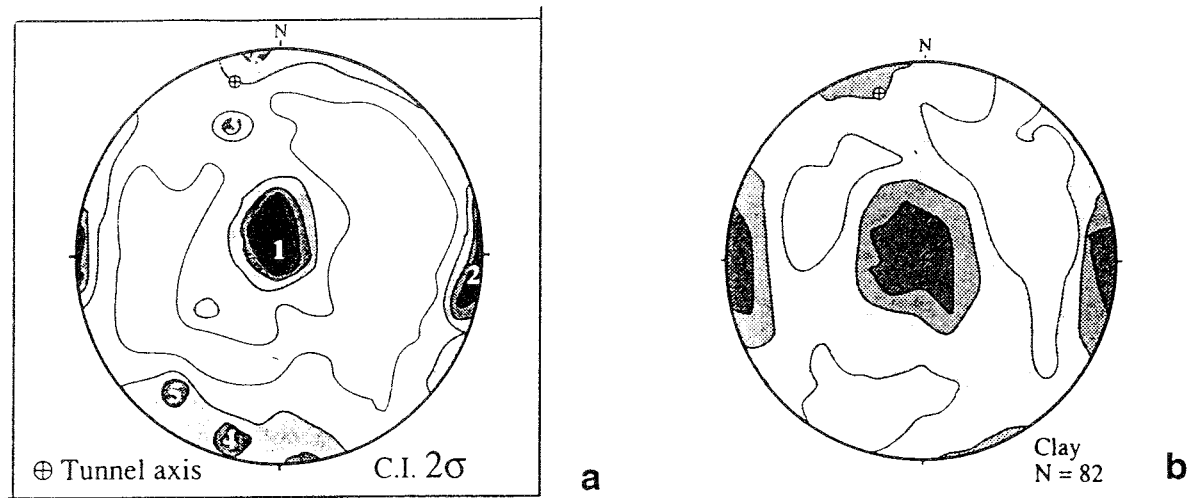
superficial, being restricted to a depth of a few metres at most (Morner 1989; Talbot 1990).

**(a) Äspö HRL tunnel study**

The geometric, mineralogical and kinematic attributes of fractures (>1.5m in trace length) mapped in the first 750m of the Äspö tunnel have been reported by Munier (1992; 1993). This substantial study confirmed the sequence of mineralization identified above and also found:

- (i) Six sets of fractures were recognized (Fig 2-4a), most of which have been repeatedly mineralized.
- (ii) Epidote and quartz-healed fractures together with flowing and 'fault gouge (clay)' filled fractures were found to be significantly longer than other fractures.
- (iii) Chlorite-healed fractures were found to be the most abundant and most homogeneously distributed.
- (iv) Although several generations of calcite were recognized, veins containing only calcite were never seen to be crosscut by later fractures and were interpreted as the youngest fracture-filling event. Nevertheless, clay-filled and flowing fractures were interpreted to postdate the calcite veins.
- (v) Two percent (82 in number) of all recorded fractures were found to contain 'fault gouge' or 'clay' ( $\pm$  other minerals), with an orthorhombic arrangement of N-S and ENE-striking steep sets and a sub-horizontal set (Fig 2-4b). The number of clay/gouge filled fractures mapped as faults was not specified.
- (vi) For 276 slickensided, mainly chlorite-healed, faults five sets were recognized (Fig 2-4c): three of which are steep and strike N-S, NE and E-W, and two dip moderately to the NE and S. The slip directions are variable, and the finite slip which could be determined for only twelve faults varies between 1 and 30cm.

Although comprehensive in most respects the study was, as noted by Munier (1992), necessarily biased owing to the practical difficulties of mapping the major fracture zones (Fig 2-3) encountered in the tunnel. Munier also noted the mineralogical and kinematic complexity of many of the fractures which have been multiply reactivated.



**Figure 2-4** Orientation data for fractures (>1.5m trace length) recorded in the first 750m of the Äspö HRL tunnel (after Munier 1993). (a) Contoured stereoplot of poles to all fractures; (b) contoured stereoplot of poles to clay filled fractures; (c) stereographic projections of faults and slickenline lineations for all faults measured.

#### 2.3.4 Relationship between fractures and fluid flow

The principal hydraulic paths in the site area are the major fracture zones (Fig 2-3), with the NE and NW striking zones more transmissive than the E-W zones. Some zones appear to have been partly sealed through the effects of cementation mineralization. In addition, specific individual open fractures have been found to be transmissive (Wikberg et al 1991).

In borehole/core studies (eg. Munier et al 1988), transmissivity appeared to vary according to fracture filling, decreasing from hematite/Fe-oxide- to chlorite- to calcite-healed fractures. Nevertheless, fractures within conductive zones are often coated with chlorite, calcite and epidote; chlorite and calcite being the most common fracture coatings in all open fractures.

Whereas dissolution of fracture-filling calcite by CO<sub>2</sub>-rich surface waters is restricted to the uppermost few ten's of metres in core, calcite samples lining flowing fractures show stable isotope signatures that are consistent with equilibration with meteoric water at ambient underground temperatures (Tullborg et al 1991). This includes calcite presumed, by association with other minerals, to be originally of hydrothermal origin.

The presence of pyrite on grain boundaries in fault gouge from Fracture Zone NE-1 suggests that reducing conditions prevail today at sampled depths of 180 and 400m (Landstrom and Tullborg 1993). In the tunnel, however, flowing fractures are commonly associated with active staining by a brown (organic-rich?) Fe-OOH 'slime'.

#### 2.3.5 Summary

The history of deformation and fracture-related mineralization at Äspö, determined from a combination of studies, is summarized in Table 2-3. This provides an indication of the current state of knowledge and a framework for the present study. It is apparent that the deformation and mineralization relating to early orogenic activity is fairly well understood but that for the post-1200Ma period it is much less well constrained. Thus in both the Äspö region and in the Hard Rock Laboratory itself, the youngest fault movements are known only to have occurred sometime during the last 600Ma up to glacial times.

Table 2-3 Summary of deformation and fracture-filling events in the Äspö area (modified from Wikberg et al 1991).

Age (Ma)	Rock Type or Structure	Deformation Events	Fracture Fillings
Synglacial-present day	Fractures	Reactivation of existing structures  Fracturing?	Present groundwater; relatively reducing; isotopic re-equilibration of calcite with meteoric water?  Calcite, Fe-OOH, pyrite & clay minerals like kaolinite?
380-2 (End-Caledonian to Quaternary)	?	Reactivation of existing structures	Gypsum, chlorite, illite, probable adularia calcite & possible Fe-OOH?
600-380	Post-chlorite veins  Deposition of Lower Palaeozoic platform sediments  Clastic dykes	Late 'Caledonian' reactivation of older structures?  Burial 'metamorphism'  Local extension	?  Calcite & fluorite cements
c.900-600	?	Uplift & peneplanation	?
1000-800	Basic dyke intrusion	Local extension	?
c.1100	Proterozoic platform sediments?	Burial 'metamorphism'	Prehnite, hematite-stained laumontite, calcite & fluorite
1400-1350	Intrusion of Götemar and Uthammar granites & dolerite  Chlorite veins	Late hydrothermal circulation in anorogenic granite Extension	Fe-rich idiomorphic epidote. 1st generation of fluorite. Idiomorphic quartz, muscovite, hematite, fluorite, calcite & spherulitic chlorite
1700-1400	Regional uplift	Mylonitic shear zones	Mylonites & shear bands with fine-grained epidote, muscovite & recrystallized quartz
1800-1700	Intrusion of Småland granitoids, mafic dykes & fine-grained granites	Magma mingling & mixing with complex back-veining; imposition of steep NE to ENE penetrative foliation, locally enhanced in amphibolite facies gneissic zones	Igneous 'veins'
c. 1800Ma	Consolidation & deformation of Svecofennian rocks		

### 3 FAULTROCK AND FRACTURE SAMPLES

#### 3.1 INTRODUCTION

##### 3.1.1 Sampling strategy

The sampling strategy was directed towards obtaining suites of samples of faultrocks, concentrating on those formed during the most recent phases of movement. Because of the limitations of time and of access for sampling (mostly undertaken during ongoing tunnelling operations), systematic coverage of all faultrock and fracture-fill types and orientations has not been achieved. However, comprehensive sampling of the important fracture zone system NE-4/EW-7 (Wikberg et al 1991) was possible, together with selective sampling of other significant fractures zones and a number of minor fault and vein systems. In addition, a number of minor intrusions, fine-grained red granites and mylonitic granites were sampled for palaeomagnetic dating because of the general uncertainty over their ages.

Sampling of faultrock and fracture-filling materials was undertaken during visits to the Äspö HRL in September and November 1991, and in November 1992 during the second phase of work. The second visit in 1991 was required due to problems of access to the important Fracture Zone NE-4, which had been largely obscured by shotcrete. To facilitate access to NE-4 a shallow trench was excavated in the floor of the tunnel. The trenching approach was repeated for sampling of fracture zones NE-3, NE-1 and EW-3 in November 1992, but with less success.

Specialized sampling techniques were adopted for specific analytical techniques. In particular, this included oriented sampling of poorly-lithified fault gouge and fault breccia in perspex cubes for palaeomagnetic analysis and in liquid fibreglass resin for petrographic study.

##### 3.1.2 Terminology

The term 'Fracture Zone' is adopted from its general use in SKB reports. It refers to zones of significant thickness (metres or tens of metres) of fracturing, defined from a combination of geophysical, geological and hydrogeological data (eg. Wikberg et al 1991). Anticipating the results of this study, it is clear that all of the named fracture zones are faults in the sense that they show evidence of shear displacement and contain faultrocks. Most have suffered both plastic and brittle deformation, leading to characteristically different types of faultrocks. The descriptive faultrock classification used here is shown in Table 3-1.



Table 3-1 Faultrock nomenclature (Sibson 1977 &amp; Fry 1984)

Description	Random Fabric	Foliated	<u>Proportion of visible fragments</u>
Incohesive (ie. not lithified)	Fault gouge	Foliated fault gouge	<30%
	Fault breccia	Foliated fault breccia	>30%
Cohesive (ie. lithified)	Crush breccia	Mylonitic crush breccia	90-100%
	Protocataclasite	Protomylonite	50-90%
	Cataclasite	Mylonite	10-50%
	Ultracataclasite	Ultramylonite	<10%
	Vein breccia	Mylonitic schist or gneiss	New mineral vein matrix

### 3.1.3 Sample localities

The sample localities are shown schematically in Fig 3-1, and a comprehensive list of samples is given in Table 3-2. Core and cube samples collected for palaeomagnetic analyses are identified by the code AS#, other samples by the codes A91/# or A92/#. A brief description of each of the principal sample localities follows.

## 3.2 INFORMATION GALLERY AREA

### 3.2.1 NNE-trending epidote vein

A prominent pale green epidote vein exposed by excavation of the south wall of the information gallery is oriented 017/80°W (strike and dip) (Fig 3-2a). The vein has a dip extent of about 1.5m and is traceable along-strike for about 30cm. Its surface is locally polished and scarred by at least three generations of slickenline lineations, which pitch 70°, 90° and 120° in a clockwise sense. The epidote itself is up to 5mm thick and forms a vein breccia over a further depth of about 1cm into the rock behind the vein. The displacement across the fault is unknown.

### 3.2.2 Gouge seam, chainage 118m

A 1-4cm thick clay seam trending 164/36°W is exposed on the west wall of the main tunnel immediately to the N of the Information Gallery at chainage 118-122m (Fig 3-2b). The clay seam is traceable for about 4m along-strike cutting through reddened granite and appears to pass into a chlorite-epidote vein. It was not possible to determine whether or not any shear displacement had occurred across this feature. The clay seam is cut by a prominent E-W trending/S-dipping joint set containing discontinuous (?) calcite mineralization.

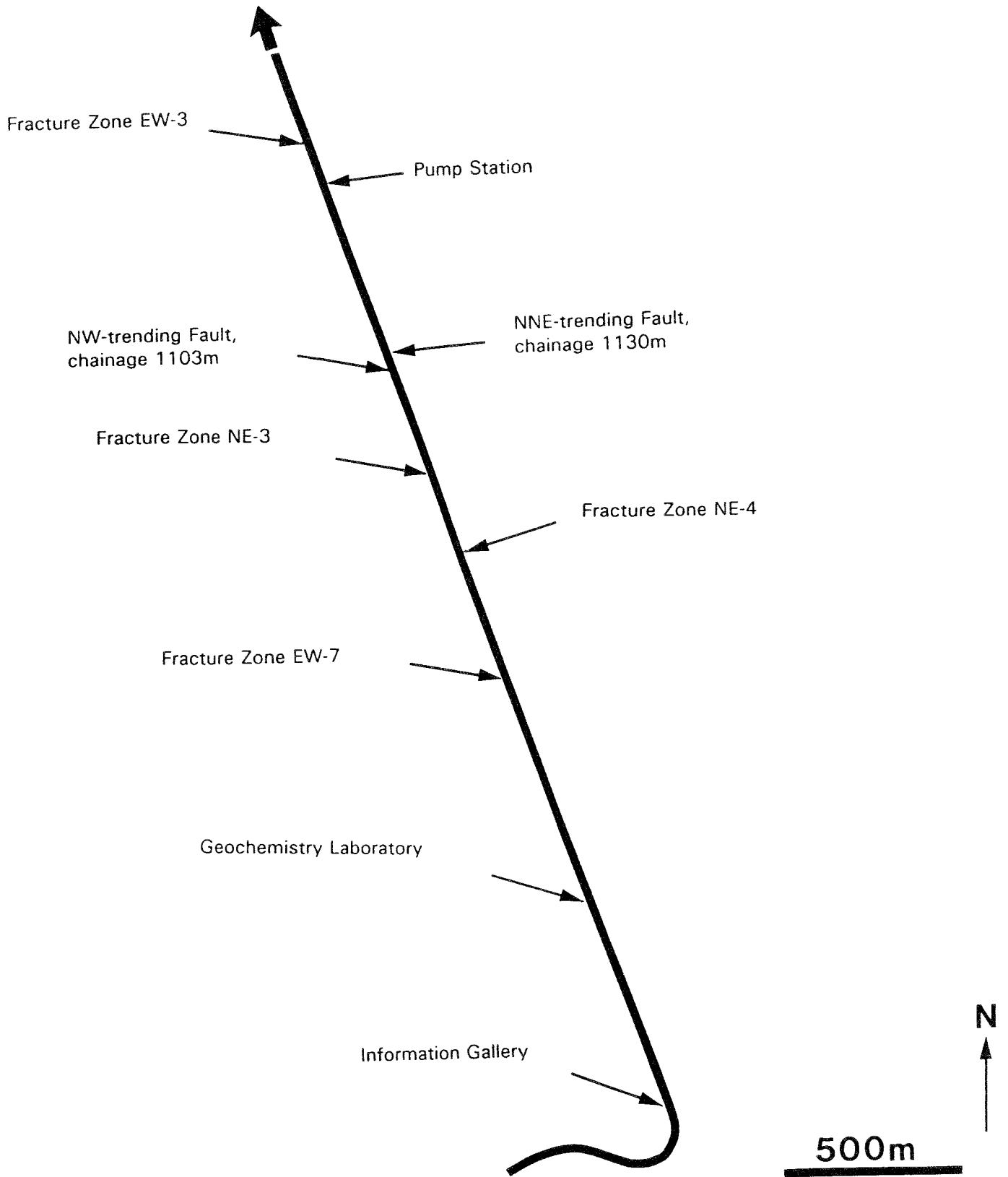


Figure 3-1 Sketch map of sample localities in Äspö HRL tunnel.

Table 3-2 List of samples

Locality	Feature orientation	Sample/ Site No	Chainage/Depth (m)	Description
<b>Tunnel Mouth</b>	-	AS12	c.-85/-	grey granite hostrock palmag bulk sample
		AS13	c.-20/-	" " " "
<b>Information Gallery</b>				
fault		A91/3	c.100/14	epidote cataclasite/vein-breccia
epidote vein on S wall	017/80W	A91/4	112/16	slickensided epidote vein/cataclasite
"	"	AS1	"	6 palmag core samples of A91/4
fault/alteration on N wall	164/36W	A91/23	115/16	gouge/alteration seam
"	"	A91/24	"	zeolitic(?) infill to S-dipping joint
"	"	A91/25	"	granite enclosed by A91/23
"	"	A92/7	"	gouge/alteration seam (repeat sampling of A91/23)
dyke at N end of wide section	085/75N	A91/5	140/19	aplite dyke
"	"	AS2	"	5 palmag core samples of A91/5
<b>Geochemistry Laboratory</b>	013/V	A92/9		gouge (bulk sample)
"	"	A92/10		granitic wallrock
"	"	ASV1		bulk palmag sample of epidote-chlorite-calcite vein
"	"	AS29		3 palmag bulk samples of epidote-chlorite-calcite vein
<b>Fracture Zone EW-7</b>				
fault 1 on W wall of side tunnel	060/70E	A91/13	c.670/93	mylonite with epidote
"	"	A91/14	"	quartz-chlorite vein breccia
"	"	A91/15	"	chlorite vein breccia
"	"	A91/16	"	mylonite
"	"	A91/17	"	fault breccia
"	-	A91/18	"	red granite (dry), 75cm N of A91/17
"	-	A91/19	"	red granite (wet), adjacent to A91/17
"	060/70E	AS9	"	4 palmag core samples
fault 1 on E wall of side tunnel	c.060	A91/22	"	mylonite
fault 2 on E wall of side tunnel	178/85W	A91/20	"	cataclasite with epidote
"	"	A91/21	"	calcite-epidote-fluorite vein
"	"	A91/2	"	epidote vein
"	"	AS6	"	3 palmag cores
"	"	AS7	"	5 palmag cores
"	"	AS8	"	3 palmag cores
wallrock 10m S of fault 1	-	AS10	"	6 palmag cores, basic hostrock
"	-	AS11	"	6 palmag cores, granitic hostrock
			"	"

Locality	Feature orientation	Sample/ Site No	Chainage/Depth (m)	Description
<b>Fracture Zone NE-4</b>				
E wall of tunnel, below shotcrete	040/58E	A91/6	851.70/117	gouge seam 1 (bulk sample)
"	070/60S	A91/7	852.20/117	gouge seam 2 (bulk sample)
"	065/70S	A91/8	852.40/117	gouge seam 3 (bulk sample)
"	-	A91/9	852.30/117	float beneath/derived from gouge (bulk sample)
"	-	A91/10	852.30/117	wallrock between gouge seams 2 & 3
"	-	A91/11	849.80/117	granitic wallrock
"	065/70S	A91/12	852.40/117	gouge seam 3 (bulk sample, contaminated?)
"	065/70S	AS5	852.40/117	2 palmag cubes gouge seam 3
trench in tunnel floor	c.050/70S	A91/26	850.90/117	gouge next palmag cubes AS14.1,2,3 (bulk sample)
"	"	A91/27	850.90/117	gouge next palmag cubes AS14.4,5,6 (bulk sample)
"	"	A91/28	850.90/117	gouge next palmag samples AS14.7,8,9 (bulk sample)
"	C.042/54	A91/29	c.852.70/117	mylonite derived from granite
"	047/60S	A91/30	850.70/117	crush-breccia/cataclasite contact (impregnated)
"	-	A91/31	850.80/117	crush breccia (impregnated)
"	c.050/70S	A91/32	c.850.90/117	gouge
"	047/60S	A91/33	850.40/117	red cataclasite
"	164/V	A91/34	852.10/117	grout
"	054/77S	A91/35	857.50/117	quartz vein cutting epidote cataclasite
"	c.047/56S	A91/36	851.30/117	protocataclasite/cataclasite partly cemented by calcite
"	c.039/73S	AS14	850.90/117	10 palmag cubes of gouge
<b>Tunnel face, 19-06-91</b>	-	A91/1	c.750/105	protocataclasite cut by epidote vein, cataclasite & calcite
<b>Tunnel face, 05-10-91</b>	014/88	AS3	c.909/125	palmag bulk epidote vein
"	016/49	AS4		palmag bulk epidote vein
<b>Fracture zone NE-3</b>				
contemporary tunnel face, 03-11-91	c.038/V	A91/37	c.950/130	grey gouge (bulk sample) (038/vert)
"	c.090/10N	A91/38	"	gouge (bulk sample) E-W/N-dip)
"	c.020/54E	A91/39	"	gouge (bulk sample) 020/54E)
"	-	A91/40	"	granite wallrock beneath A91/39
"	-	A91/41	"	granite wallrock beneath A91/38
trench in tunnel floor		AS20	956/130	6 palmag cores of red fine-grained granite
<b>Minor NW-striking fault</b>	137/75E	A92/6	1103	calcite + epidote vein
"	"	AS27	"	2 bulk palmag samples

Locality	Feature orientation	Sample/ Site No	Chainage/Depth (m)	Description
<b>Minor NNE-striking fault</b>	022/80W	A92/1	1130	calcite vein cutting epidotic cataclasite
"	"	A92/2	"	calcite + fl + py + FeOOH vein cutting epidote cataclasite
"	"	A92/3	"	epidote fault breccia (bulk sample)
"	"	A92/4	"	mylonite with epidote cut by cataclasite & calcite veins
"	"	A92/5	"	epidote cataclasite with slickenside
"	"	AS24	"	bulk palmag sample epidote cataclasite
"	"	AS25	"	bulk palmag sample epidote cataclasite
"	"	AS26	"	3 bulk palmag samples epidote cataclasite
<b>Pump Station</b>	c.068/30N	AS28	1360	6 palmag cores of gently NNW-dipping microgranite
<b>Fracture zone EW-3</b>	078/79S	A92/8	1419	red protomylonitic granite cut by veins
"	082/85N	AS21	1417	6 palmag cores of red protomylonitic granite
"	065/85S	AS22	1418	6 palmag cores of red protomylonitic granite
"	078/79S	AS23	1419	6 palmag cores of red protomylonitic granite
<b>Borehole Core</b>				
Fracture zone EW-5?		KAS05/01	328.17-328.27	protomylonite cut by cataclasite & gouge
"		KAS05/02	326.74-326.96	protomylonite cut by cataclasite
Fracture zone EW-X?		KAS05/03	400.02-400.11	altered granite
Fracture zone NE-2		KAS08/01	44.66-44.76	epidote cataclasite
"		KAS08/02	51.00-51.10	epidote cataclasite/altered rock
Fracture zone NE-1		KAS08/03	547.27-547.37	cataclasite with calcite
<p>Note: 1) identification of fracture zones from Wikberg et al (1991) and pers. comm. R Stanfors and Äspö site staff; ? indicates uncertain identification  2) depths only are given for borehole samples  3) orientations of features are given as strike &amp; dip except in core where dips only are recorded</p>				

### 3.2.3 Aplite dyke

Further into the tunnel at chainage 140m, a 5cm thick steeply-dipping E-W trending aplite dyke (085/75°N) was sampled for palaeomagnetic analysis (Fig 3-2c). The aplite dyke offsets an earlier NNE-trending (020/50°E) pegmatite vein but is itself seen to be offset in the tunnel roof by a vertical, N-trending epidote-bearing fracture. Both the aplite dyke and its country rocks are affected by shallow-dipping zones of reddening.

### 3.3 GEOCHEMISTRY LABORATORY FAULT

At the Geochemistry Laboratory on the W wall of the tunnel close to chainage 450m, a c. 20cm thick NNE-striking, near vertical fault is exposed (Fig 3-2d). The fault zone includes epidote-rich vein breccia and cataclasite and calcite veins but locally comprises a soft gouge-like material. A number of faultrock samples were collected for palaeomagnetic, isotopic and petrographic analysis.

### 3.4 FRACTURE ZONE EW-7

Fracture Zone EW-7 is part of the NNE to NE-trending anastomosing fracture zone system which also includes NE-3 and NE-4, (Fig 2-3). From the W wall of the main HRL tunnel a side tunnel has been excavated near chainage 670m for hydrogeological testing of EW-7. This side tunnel provides clear exposure of two well-developed fault and vein systems, related reddening of the wallrocks, and cross-cutting intrusive relationships in the hostrocks (Fig 3-3).

The bulk of the hostrocks comprises massive 'granite' which is coarsely banded on a decimeter scale by discontinuous layers of more basic and more acid pegmatitic rock. The layering strikes nearly E-W and dips gently (c.35°) to the south. In the southern part of the tunnel, a larger basic body (≥5m thick and 10m+ lateral extent) within the granite is similarly oriented and itself contains centimetric granitic stringers also of the same trend. The contact between the granite and the basic body is generally sharp but nevertheless irregular, suggesting a back-veining relationship.

**Figure 3-2** [overleaf] Information Gallery and Geochemistry Laboratory. (a) NNE-striking epidote vein on S wall of Information Gallery; (b) clay-filled fracture on N wall of Information Gallery; (c) palaeomagnetic core sampling of E-W trending aplite dyke at chainage 140m, W wall of tunnel, near Information Gallery; (d) NNE-striking Geochemistry Laboratory fault, W wall of tunnel.



**a**



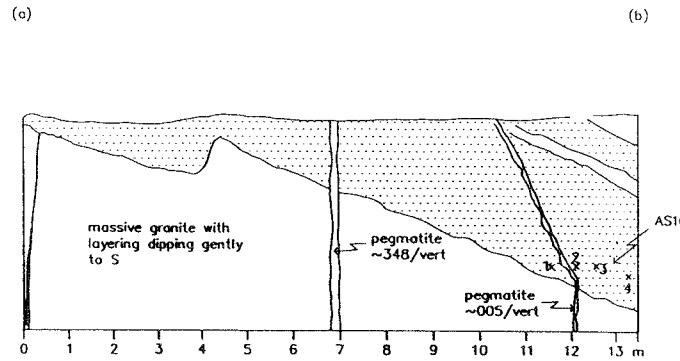
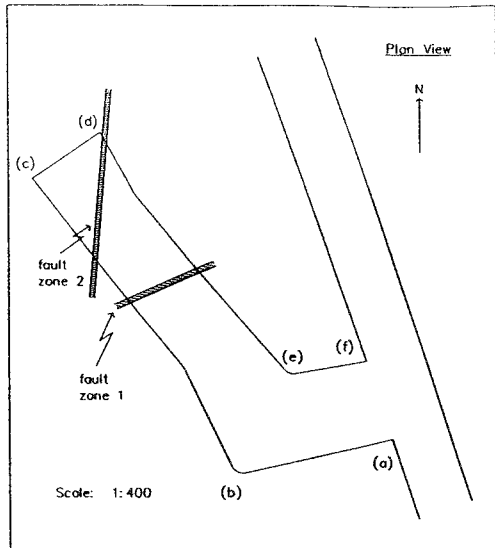
**b**



**c**

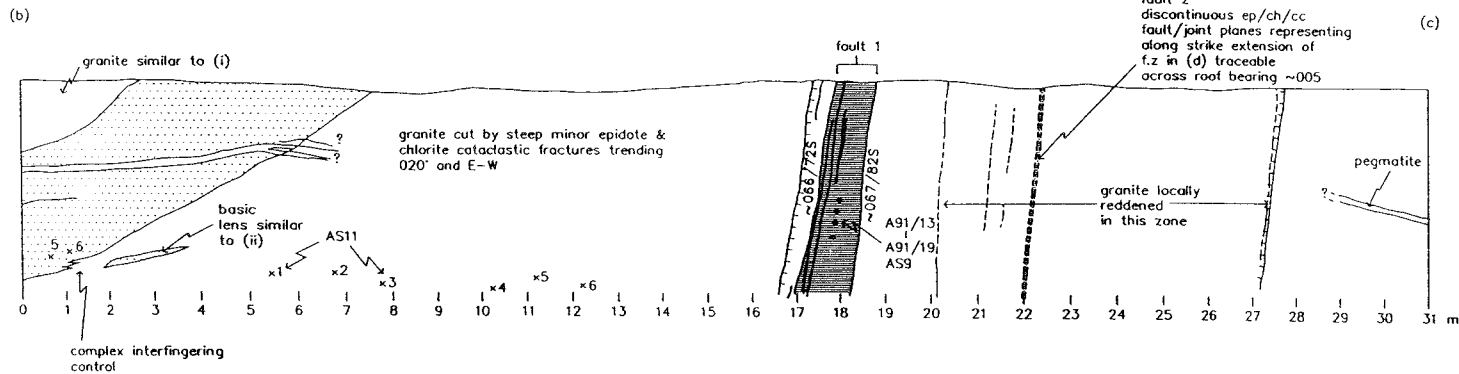


**d**



- KEY
- GRANITE
  - BASIC GNEISS
  - PEGMATITE
  - LIMITS OF INTENSE REDDENING OF GRANITE ENCLOSED BY HACHURES
  - FAULT ZONE
  - \*5 PALAEOMAGNETIC SAMPLE LOCATION OR SITE
  - \*AS10 OTHER SAMPLE LOCATION
  - \*A91/7 OTHER SAMPLE LOCATION

HORIZONTAL = VERTICAL SCALE = 1 cm = 1 m  
(Except for plan view)



DRAWN BY  
R. H. MADDOCK

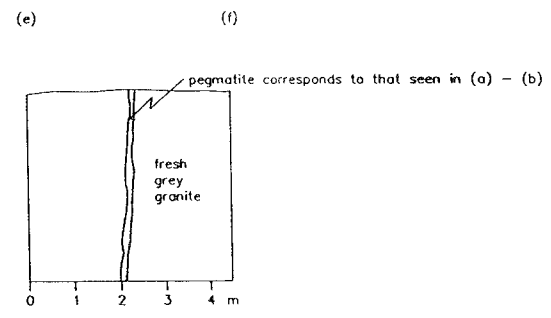
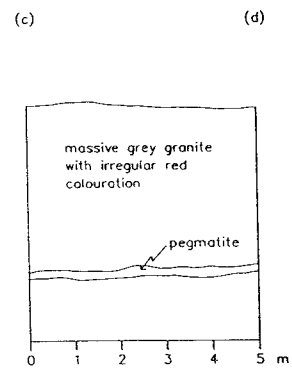
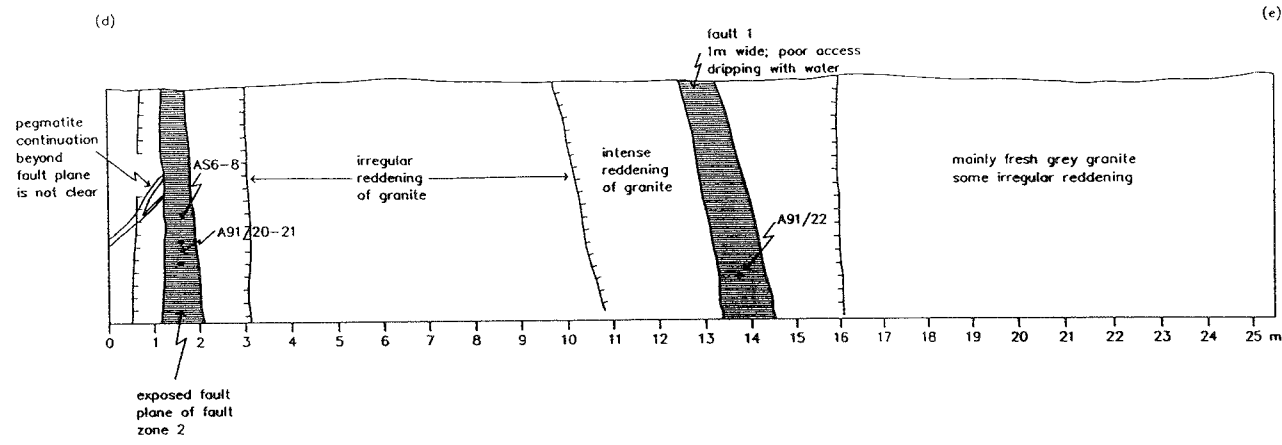
CLIENT  
SKB

TITLE  
SCHEMATIC LOG OF SIDE TUNNEL AT 670m CHAINAGE (FRACTURE ZONE EW-7)


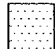
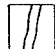
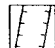

DATE  
APR 92

FIG  
3.3






KEY

-  GRANITE
-  BASIC GNEISS
-  PEGMATITE
-  LIMITS OF INTENSE REDDENING OF GRANITE ENCLOSED BY HAGHURES
-  FAULT ZONE
- ×5 PALAEOMAGNETIC SAMPLE LOCATION OR SITE
- ×AS10
- A91/7 OTHER SAMPLE LOCATION

HORIZONTAL = VERTICAL SCALE = 1 cm = 1 m  
(Except for plan view)

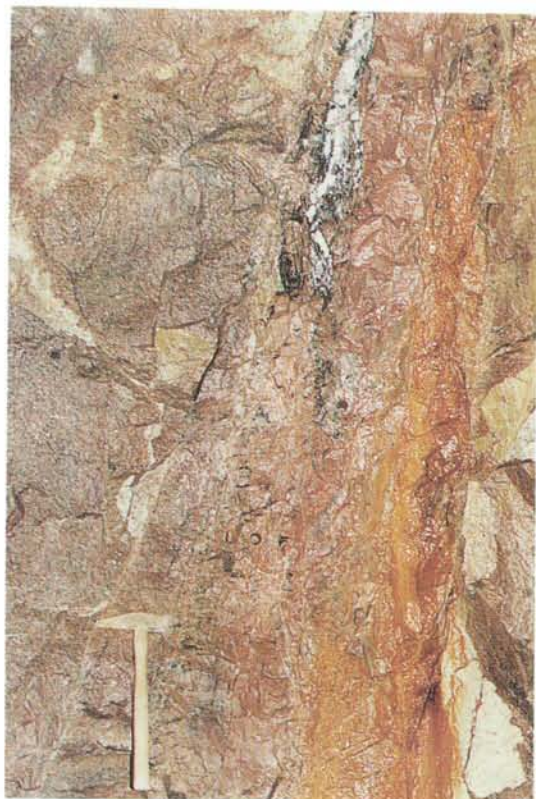
 GEOSCIENCE Copyright GeoScience Limited	DRAWN BY R. H. MADDOCK	CLIENT SKB	TITLE	DATE APR 92	FIG 3.3 (cont)

Samples of each of these rock units were collected for palaeomagnetic analysis. Both lithologies are cut by two steeply-dipping acid pegmatites which strike  $348^{\circ}$  and  $005^{\circ}$ .

Two prominent, steeply-dipping fault zones are developed which trend ENE and nearly N-S, here named 'Fault 1' and 'Fault 2' respectively (Fig 3-3).

Fault 1 is up to 1m thick, tapering upwards and enveloped by planar to rough, millimetric epidote veins which strike ENE and dip steeply S (Fig 3-4a). No markers were seen to allow an estimation of the displacement across the fault. The oldest tectonic fabric visible in the fault is a mylonitic foliation which affects lenses of rock up to 5cm thick and traceable for about 20cm vertically (Fig 3-4b). En-masse, these lenses define anastomosing zones of variable mylonitic strain. The mylonitic foliation, which is visibly defined by elongate quartz and alkali-feldspar, is oriented sub-parallel to the fault zone margins (measured at  $060/70^{\circ}$ E). Closely-spaced, narrow dark-green epidote veins appear to have 'invaded' the mylonitic foliation locally although it is difficult to determine macroscopically the relative ages of these veins and the mylonitic foliation. Both the mylonitic foliation and epidote veins are cut by dark, chlorite veins, also containing fluorite. The chlorite veins have a steep dip but, in general, a more northerly-trending strike. The chlorite veining also brecciates massive milky-white quartz veining which postdates the mylonite and epidote fabrics. The northern part of the fault zone adjacent to its enveloping fracture is intensely fractured, locally comprising a friable fault breccia, with local water flow and a coating of iron-stained sludge (Fig 3-4a). Pervasive reddening of the country rocks extends for several metres either side of the fault zone to which it is clearly related (Fig 3-3) (Elsewhere in the side tunnel tufa is precipitating from the flowing waters).

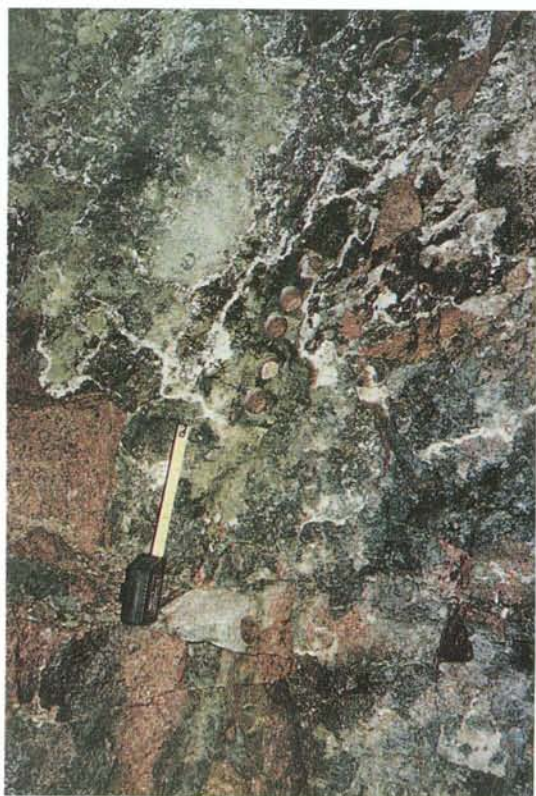
**Figure 3-4** [overleaf] Fracture Zone EW-7, chainage 670-680m. **(a)** Fault 1 exposed in W wall of side tunnel (see Fig 3-3), showing mylonitic granitic cut by sub-parallel epidote, quartz and black chlorite veins; note the reddened nature of the granite and the iron-staining associated with active water flow; palaeomagnetic site AS9; **(b)** detail of (a) showing mylonitic foliation dipping steeply to SSE with foliation-parallel epidote and quartz veins; **(c)** fault 2 exposed in E wall of side tunnel (see Fig 3-3), showing reddened granite partly brecciated by epidote-cataclasite and cut by carbonate + epidote + quartz vein which has a northerly strike; palaeomagnetic sites AS6 (topmost 2 cores), AS7 (middle 5 cores) and AS8 (lowermost 3 cores); **(d)** detail of (c) showing epidote vein breccia of palaeomagnetic site AS8.



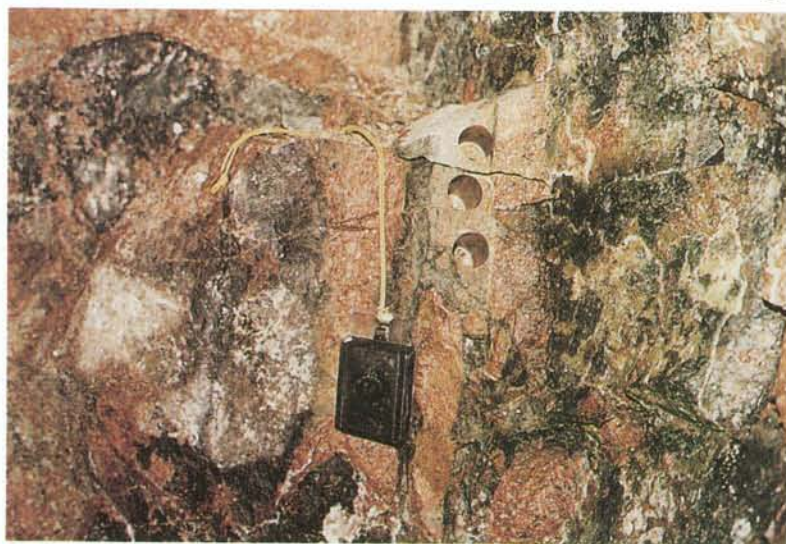
**a**



**b**



**c**



**d**

The youngest deformation associated with this fault appears to be the intense fracturing and the local formation of fault breccia. This material was sampled with a view to ESR dating but unfortunately found to be unsuitable because of its coarse grain size.

Fault 2 comprises a narrow (<20cm), irregular zone of chlorite vein breccia, cataclasite and epidote+quartz+calcite veins, which strikes a few degrees either side of N and dips very steeply westwards. The fault is discontinuous in the W wall of the side tunnel but continuous and well-exposed on the E wall. A gently NW-dipping pegmatite dyke exposed to the W of the fault zone cannot be traced across it suggesting a minimum offset of several metres is possible (Fig 3-3). The bulk of the zone is made up of chlorite-cemented cataclasite and vein breccia separating irregular screens of reddened granite and enveloped by epidote+quartz+calcite+chlorite veins (Figs 3-4c & d). Intensive reddening of the granite wallrocks extends up to 1m either side of the fault. In contrast to the E-W Fault 1, however, Fault 2 shows no evidence of present-day water flow.

### 3.5 FRACTURE ZONE NE-4

Fracture Zone NE-4 was identified during the pre-investigation phase and predicted to be "certain" in geological status (associated with alteration, fracturing and mylonite) and "probable" hydraulically (Wikberg et al 1991).

In the HRL tunnel, the fracture zone was intersected at about chainage 850m. During the first site visit access to the fracture zone was restricted to discontinuous exposure along the gap between the base of the shotcrete and the tunnel floor. A zone of altered and highly-fractured granite with quartz, epidote and carbonate veins, together with three prominent gouge seams was observed (Fig 3-5a & b). Considerable amounts of water flowed from the area of the gouge seams. Details of the gouge seams are given in Table 3-3.

**Figure 3-5** [overleaf] Fracture Zone NE-4, chainage 850-860m .  
**(a)** Exposure at base of shotcrete, E wall of tunnel, chainage 850m; within the highly-fractured, reddened granite three SE-dipping gouge seams are visible (labelled 1, 2 & 3; Table 3-3); a portable  $\gamma$ -ray spectrometer is being used to measure environmental dose rate for ESR dating; **(b)** orienting a perspex cube sample of gouge seam 1 for palaeomagnetic analysis; **(c)** excavation of trench in tunnel floor to expose fracture zone; **(d)** trench floor showing crush breccia and cataclasite cut by gouge seams (zones 3, 4 & 5, Fig 3-6); **(e)** detail of (d) showing gouge seams cutting crush breccia and cataclasite (see Fig 3-6). [N is to base of photos (d) & (e)]

a



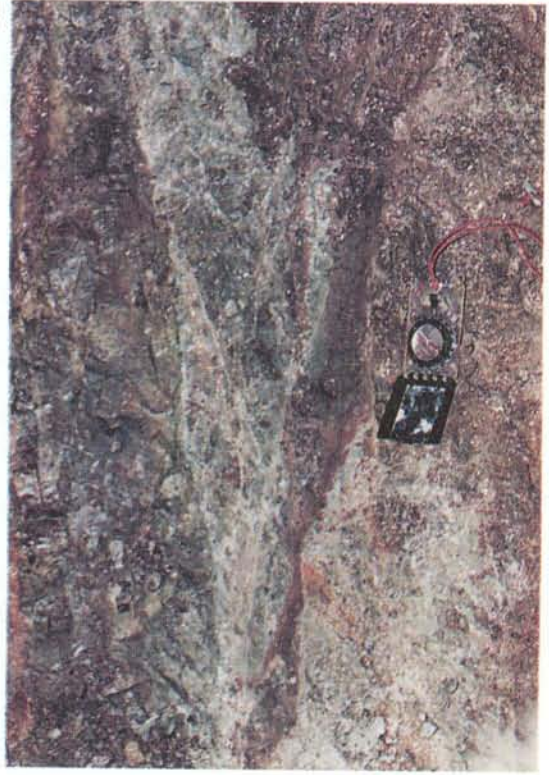
b



c

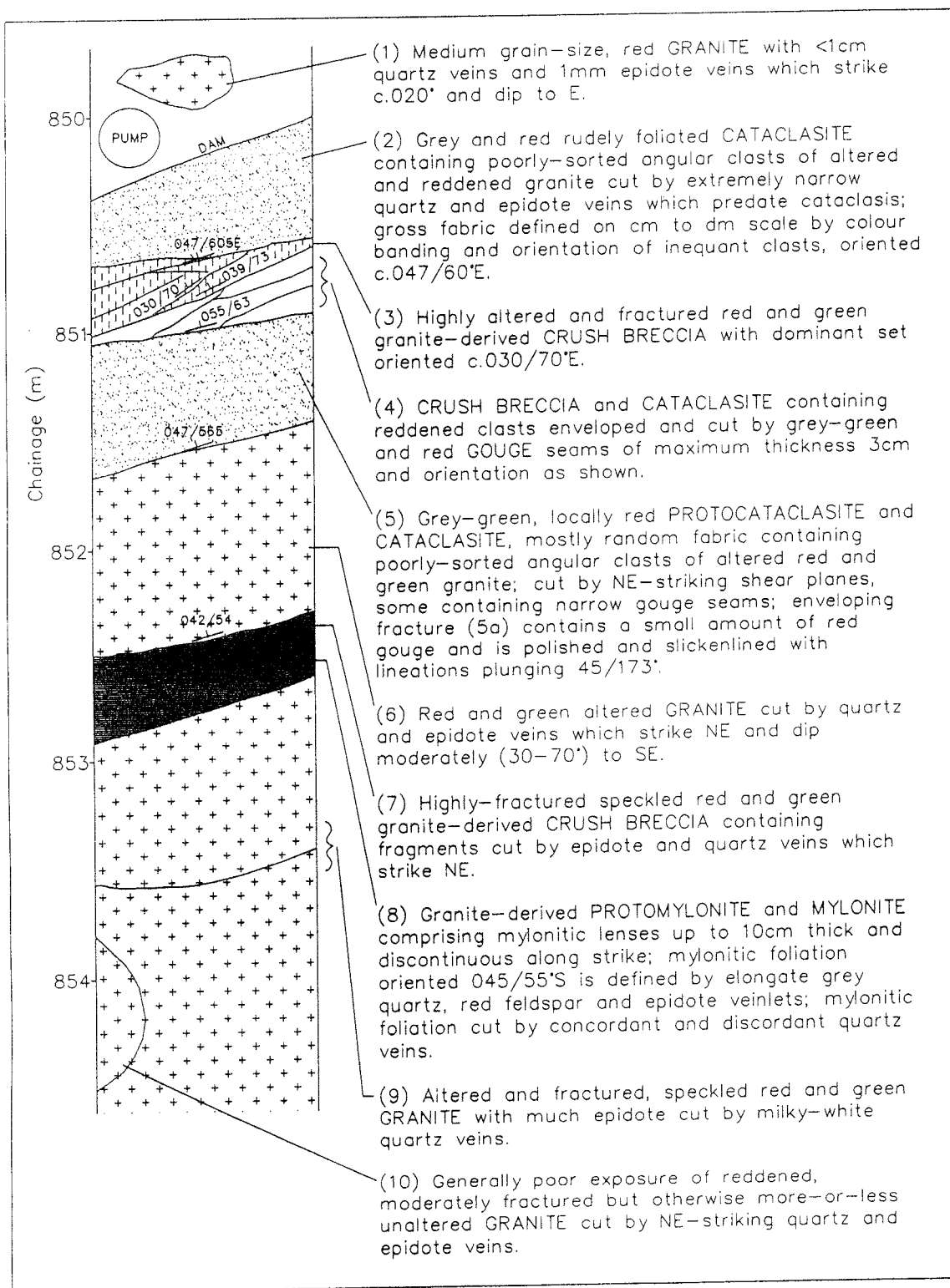


d



e





DRAWN BY

RHM

CLIENT

SKB

TITLE

SCHEMATIC LOG OF TRENCH AT 850M CHAINAGE  
(FRACTURE ZONE NE-4)

DATE

JUN 92

FIG

3.6

Table 3-3 Details of gouge seams in fracture zone NE-4 exposed beneath shotcrete

Gouge Seam	Sample No	Chainage (m)	Orientation	Comment
1	A91/6	851.70	040/58°E	Up to 1cm thick; light buff coloured
2	A91/7	852.20	070/60°S	0.5cm thick; grey-green coloured
3	A91/8	852.40	065/70°S	0.5cm thick; grey-green coloured

Note: compass-determined orientations may be inaccurate due to effects of magnetic materials in the shotcrete

In November 1991 an approximately 1m deep by 1m wide trench was excavated, by back-acting hoe, extending from chainage 849m to about 861m to better-expose Fracture Zone NE-4 (Fig 3-5c). The trench was cleaned by high-pressure water hose, and required constant pumping to evacuate inflowing water. The trench extended past the northern limit of NE-4 but not to the southern limit. Logging of the trench revealed that the fracture zone is made up of centimetric to metric scale slivers of fractured and veined granite and more-or-less deformed faultrocks which vary from mylonite through cataclasite to gouge (Figs 3-5 & 3-6). The overall fabric of these elements, and thus the fracture zone as a whole, strikes broadly NE and dips moderately (50-70°) to the SE. The faultrock and vein materials show relative age relationships comparable to those observed in EW-7 (Section 3.3) but with the additional development of significant amounts of cataclasite and gouge. The greater quantity these faultrocks suggests that Fracture Zone NE-4 has accommodated significantly more (post-mylonitic) brittle shear displacement than EW-7. The wallrocks around Fracture Zone NE-4 are again characteristically reddened.

It is clear from outcrop that the grey-green gouge seams crosscut the other faultrocks, and were themselves the product of fault movement rather than simply the result of in-situ alteration of the pre-existing cataclastic faultrocks (Figs 3-5d & e). Sampling for dating fault movement therefore concentrated on the gouge materials.

Although the trench extended across the same chainage interval, and was excavated <2m away from the exposure at the of the base tunnel wall, individual gouge seams could not be correlated between the two. This is consistent with the gouge seams having an anastomosing habit, with individual seams extending perhaps only a metre or so. A corollary of this is that the gouge seams are unlikely to have accommodated very large displacements (probably much less than a few tens of metres).

A systematic interpretation of the kinematics of the brittle and gouge-related faulting is impossible due to

sparse and conflicting observations. Slickenside lineations on an enveloping fracture ([5a] in Fig 3-6) plunge  $45^\circ$  southwards indicating dominant dip slip on that shear plane. This displacement direction is supported by tectonic and magnetic fabrics found in the gouge (Sections 4 and 5). The orientation of the majority of the gouge seams and the offset of clasts along these, however, suggests a significant component of strike-slip displacement.

### 3.6 FRACTURE ZONE NE-3

Rapid sampling was undertaken at the tunnel face, on 03-11-91, where it had intersected Fracture Zone NE-3 (Fig 2-3). In the E-W oriented end-face of the tunnel three prominent gouge bearing faults were sampled. A polished fault surface oriented c.  $020/54^\circ\text{E}$ , and locally containing gouge, truncated two other gouge-bearing faults, one striking c.  $038^\circ$  with a vertical dip and the other E-W with a gentle northerly dip. A considerable amount of water was flowing through the fracture zone as a whole which hampered detailed logging. Bulk samples of the gouges and countryrocks were, however, collected for isotope and ESR analysis.

A further attempt to sample this fracture zone was made in November 1992, when a trench was excavated in the tunnel floor at chainage 945-955m. Six cores of red fine-grained granite were taken for palaeomagnetic analysis but no gouge was found. (Proper exposure of the fracture zone was greatly hampered by water-assisted sloughing of spoil from the trench walls.)

### 3.7 NW-STRIKING FAULT, 1103m CHAINAGE

A narrow (<2cm), nearly planar carbonate vein was traced from the W wall of the tunnel at chainage 1103m (Fig 3-7a), across the tunnel roof to the E wall at chainage 1097m. The fault has an average strike of  $317^\circ$  dipping steeply ( $75^\circ$ ) to the NE. The surface of the carbonate is coated with ?clay and Fe-OOH but this appeared to be surficial, dripped down from above.

**Figure 3-7** [overleaf] Minor faults and microgranite intrusion. (a) NW-trending calcite-epidote mineralized fault at chainage 1103m, W wall of tunnel; (b) NNE-trending calcite-epidote mineralized fault at chainage 1130m, E wall of tunnel; (c) same fault as (b) at chainage 1119m on W wall of tunnel; note curvilinear nature of fault and orientation marks on faultrock infill for palaeomagnetic sampling; (d) NNW-dipping microgranite intrusion on W wall of tunnel at Pump Station, chainage 1360m.



a



b



c



d



### 3.8 NNE-TRENDING FAULT, 1130m CHAINAGE

This fault is exposed in the W wall of the tunnel at chainage 1119m, traceable across the roof until it meets the E wall of a widened tunnel section at 1130m. The fault zone, which is up to a metre wide, has an average strike of  $022^\circ$  with a vertical or very steep westward dip. The fault zone is generally damp on both sides of the tunnel but did not flow freely.

On the W wall of the tunnel, the fault zone consists of up to 1m thickness protocataclasite, cataclasite and epidote vein breccia containing red granite clasts, with dark porphyritic granite to either side. The faultrock is cut by several prominent polished and slickensided surfaces which trend sub-parallel to the fault zone envelope (Fig 3-7b). In three-dimensions these are curviplanar defining a large-scale 'rodding' of amplitude 1-10cm and wavelength about 1m elongated along-strike of the fault zone. This form together with local horizontal or gently pitching slickenline lineations suggests that the most recent movement, and possibly the bulk of the brittle displacement, was strike-slip. The sense of shear could not be determined.

The fault zone has a similar though rather more complicated aspect on the E wall of the tunnel. The dark porphyritic granite passes into finer-grained red granite with a weak to strongly-developed mylonitic foliation which trends parallel to the fault zone envelope (Fig 3-7c). The mylonitic foliation is also associated with narrow 'dirty' green epidote veins of the same orientation. An epidote-rich cataclasite zone up to 10cm thick, follows and cuts the mylonitic foliation and appears to contain clasts of the mylonitic granite. The cataclasite has a similar form to that in the W wall of the tunnel. The cataclasite is again cut by curviplanar, rodded slickensided surfaces with near-horizontal lineations. One of these passes along-strike into an extensional veinlet containing quartz and hematite or Fe-OOH. The cataclasite is also cut by concordant and discordant milky-white calcite veins and blebs to several centimetres across.

Samples of the faultrock and vein materials were collected for palaeomagnetic and petrographic analysis.

### 3.9 PUMP STATION

A shallow-dipping red microgranite dyke was sampled from the W wall of the tunnel close to a pump station at chainage 1360m (Fig 3-7d). The granite dyke is about 30cm thick with a sheet dip of about  $30^\circ$  to the NNW. Six cores were taken for palaeomagnetic analysis.

### 3.10 FRACTURE ZONE EW-3

In November 1992 a trench was excavated in the tunnel floor between chainage 1410 and 1420m to expose Fracture Zone EW-3. The trench exposed dark to red feldspar porphyritic granite with sparse basic schlieren, with abundant mylonitic zones and stringers to 10cm width and 1m or more along-strike extent (Fig 3-8a). At the northern limit of the trench (c. 1421m) the red mylonitic granite passes into dark porphyritic granite.

The mylonitic foliation, best developed between chainage 1416 and 1420m, trends ENE (065-085°) and dips steeply (80+°) to the N or very locally to the S (Fig 3-8a). The mylonitic foliation is defined by elongate grains of quartz and feldspar. It could not be confirmed whether the mylonite developed from the dark porphyritic granite or from a finer-grained(?), red(?) granite intrusion.

Both the mylonitic and the non-mylonitic granite are cut by quartz and 'dirty' green epidote veins, locally forming protocataclasite and epidote vein breccia (eg. at chainage 1413-1415m).

Three gouge seams, each <1mm thick, were found trending parallel to the gross foliation but clearly postdating the other faultrocks and veins (Fig 3-8b).

Most of the exposed granite is fractured by joints and veins with a 5-20cm spacing. Three systematic joint sets were recorded: (i) N-S trending with a steep easterly dip, some coated with chlorite(?) and quartz; (ii) WNW (300°) trending with a steep northerly dip; and (iii) ENE (080°) trending with a moderate to steep southerly dip.

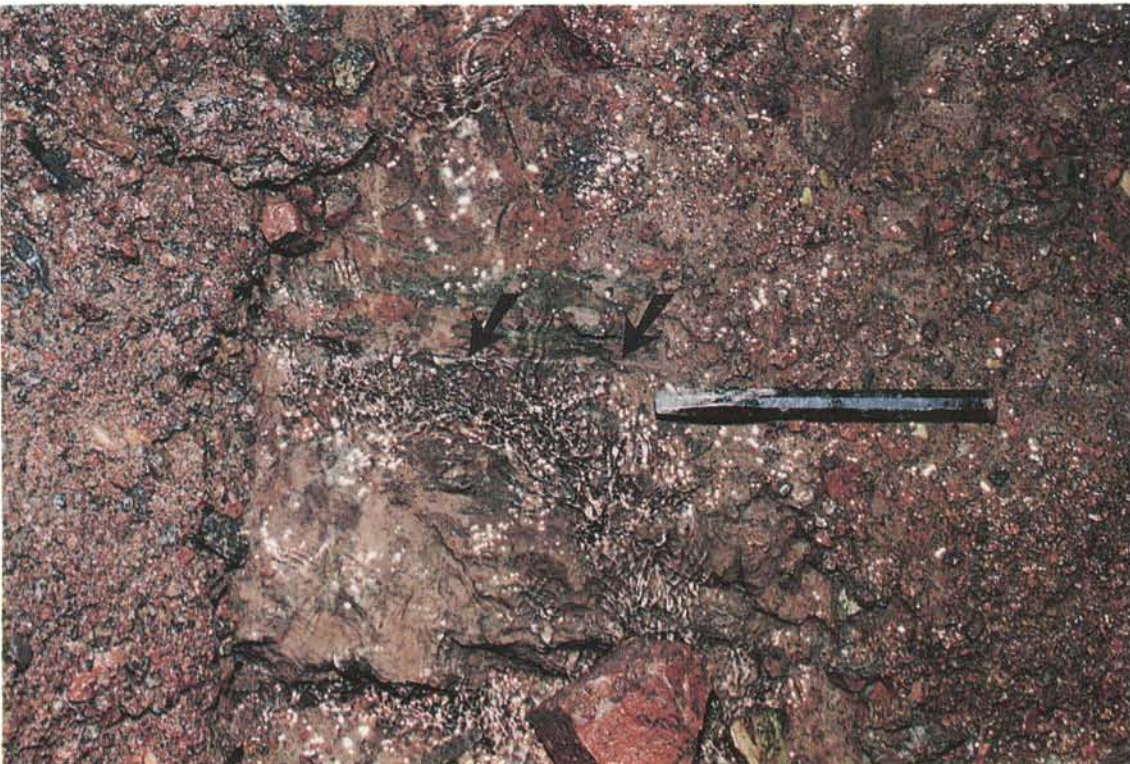
A suite of cores were taken from the mylonitic granite, between chainage 1417-1420m, for palaeomagnetic analysis (Fig 3-8a). The gouge material proved impossible to sample due to water flow and sloughing.

**Figure 3-8** [overleaf] Fracture Zone EW-3, chainage 1410-1420m. **(a)** Trench floor showing contact between dark porphyritic granite and red mylonitic granite which has been drilled for palaeomagnetic samples, chainage 1417m; **(b)** millimetric gouge seam (arrowed) cutting and trending sub-parallel to protomylonitic foliation of reddened and epidotized granite, chainage 1414m. [N is to the base of both photos.]

**a**



**b**



### 3.11 OTHER LOCALITIES

A number of other samples, principally of countryrock and epidote-quartz vein systems for palaeomagnetic analysis, were collected from miscellaneous sites in and around the tunnel. These are documented in Table 3-1.

In November 1992, a trench was excavated in the tunnel floor between chainage 1295 and 1310m in an attempt to expose Fracture Zone NE-1 (Fig 2-3). Satisfactory exposure of faultrock was not possible due to water-assisted sloughing of spoil from the trench walls, and very little gouge material was seen. No samples were collected.

## 4 MINERALOGY AND MICROSTRUCTURES

### 4.1 INTRODUCTION

A proper understanding of the microstructure and mineralogy of faultrocks, fracture infills and their wallrocks is a prerequisite to any direct dating attempts. Microstructural analysis can in addition provide information concerning:

- (i) the style of faulting, ie. seismic or aseismic, and the palaeostress history of the faultrock;
- (ii) the evidence for fault reactivation, ie. displacement on the same fault at different periods in geological time;
- (iii) the senses and directions of fault movements;
- (iv) the relative ages of fault movements.

In the present study, greatest effort was put into examining faultrock and vein materials from fracture zones EW-7 and NE-4. This was due in large part to the fact that these fracture zones were most easily sampled. Large format (3x5 inch) covered thin-sections and polished thin-sections (2x1 inch) were prepared for microscopy. Owing to the poorly-consolidated nature of many of the faultrocks, repeated low-vacuum oven resin impregnation was required for some thin-section preparation. As well as optical microscopy, the polished thin-sections were examined by backscattered scanning electron (BSE) microscopy providing atomic number contrast images. A JEOL 733 SEM was used, fitted with a 'LINK Systems' solid state analyzer for quantitative X-ray microanalysis. Mineral chemical analyses are given in Appendix 1. A fracture surface of one gouge sample was examined by secondary electron imaging (SEI) in the same instrument.

Selected samples were also analyzed by XRD to determine the mineralogical composition of the whole-rock and  $<2\mu\text{m}$  ('clay fraction') components. Finally, the grainsize distributions of selected gouge and cataclasite samples were determined during mineral separation of clay and quartz fractions for isotopic and ESR dating respectively.

The petrographic descriptions which follow are arranged in the same order of the 'outcrop' descriptions of Section 3, to which cross-reference should be made as appropriate.

## 4.2 INFORMATION GALLERY

### 4.2.1 Epidote vein, chainage 112m

A thin-section cut normal to the dip and strike of the vein reveals a fourfold sequence of deformation and vein formation.

The wallrock granite consists largely of recrystallized quartz and reddened and sericitized feldspars with accessory epidote. Mylonite, locally ultramylonite, which cuts the wallrock with a sharp margin but appears to have been derived from the wallrock (Fig 4-1a). The matrix of the mylonite is largely made up of fine-grained ( $<20\mu\text{m}$ ) albite and quartz with lesser K-spar, and accessory epidote, sphene and chlorite (Fig 4-1a & b). The mylonite is cut by bright yellow-green, Fe-rich epidote forming the vein visible at outcrop. The epidote vein has exploited the planar discontinuity formed by the mylonite (Fig 4-1a). Epidote of this type, and presumed to be of the same age, is also more pervasively though sparsely distributed through the mylonite and wallrock.

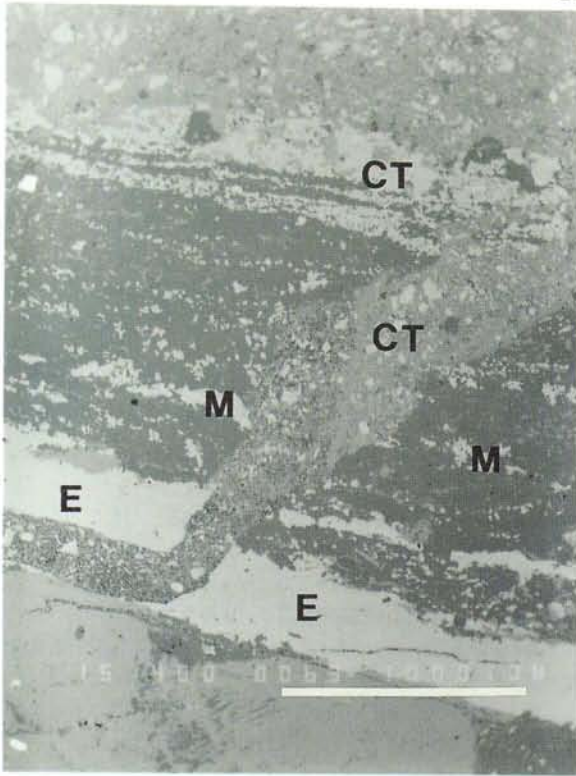
Cataclasite, mainly developed parallel to the mylonite and epidote vein but also cutting discordantly across them contains poorly-sorted, generally angular clasts derived from the mylonite and epidote vein (Fig 4-1a). The cataclasite matrix, which locally forms cross-cutting veins (Fig 4-1b), consists of prehnite and K-spar (Fig 4-1c & d). The matrix prehnite consists of small ( $<20\mu\text{m}$ ) xenoblastic grains which are zoned with respect to  $\text{Fe}^{\text{III}}$  and Al. The matrix K-spar, also xenoblastic, appears to have infilled a porosity created by fracturing of the prehnite, with some void space remaining (Fig 4-1c & d). The K-spar contains no detectable albite or anorthite components.

### 4.2.2 Fault, chainage 118m

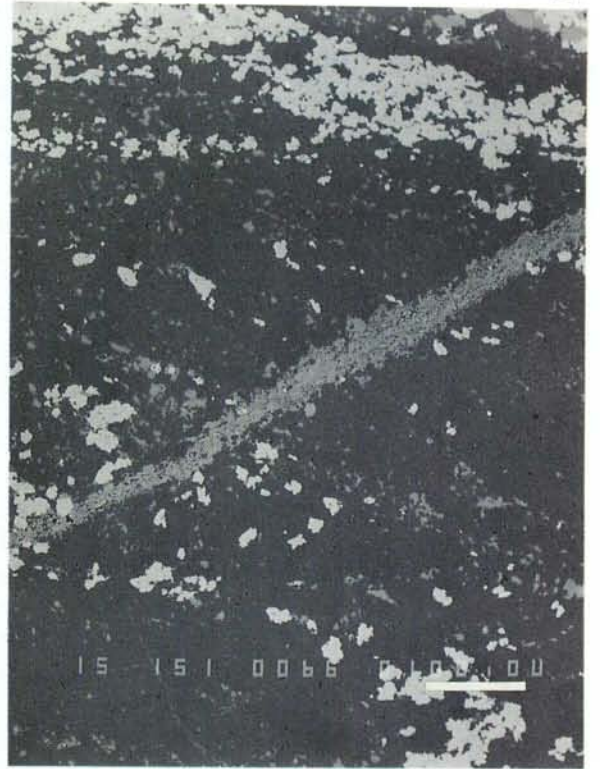
It was not possible to make a thin-section of the gouge material from this fault. The composition of the illite separated from the gouge is discussed further in Section 6.5.

**Figure 4-1** [overleaf] SEM BSE micrographs of mylonite, epidote vein and cataclasite (A91/4), from Information Gallery. **(a)** Elbow-shaped cataclasite (CT) vein cutting epidote vein (E) and mylonite (M); scale bar = 1mm, [FOTO BSE/63]; **(b)** prehnite + K-spar vein, cutting mylonite; scale bar =  $100\mu\text{m}$ , [FOTO BSE/66]; **(c)** detail of (b) showing fractures in prehnite filled by K-spar; scale bar =  $10\mu\text{m}$ , [FOTO BSE/67]; **(d)** cataclasite continuous with, and showing same texture and mineralogy as vein in (b); scale bar =  $10\mu\text{m}$ , [FOTO BSE/68].

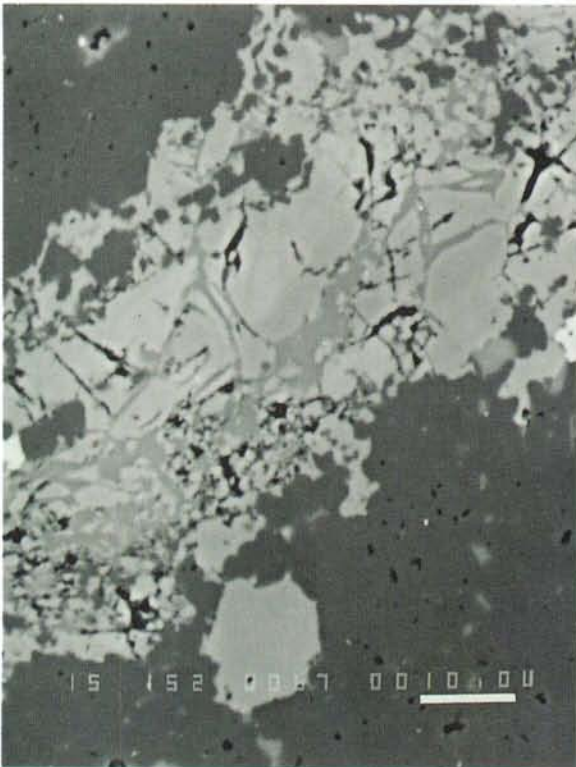
**a**



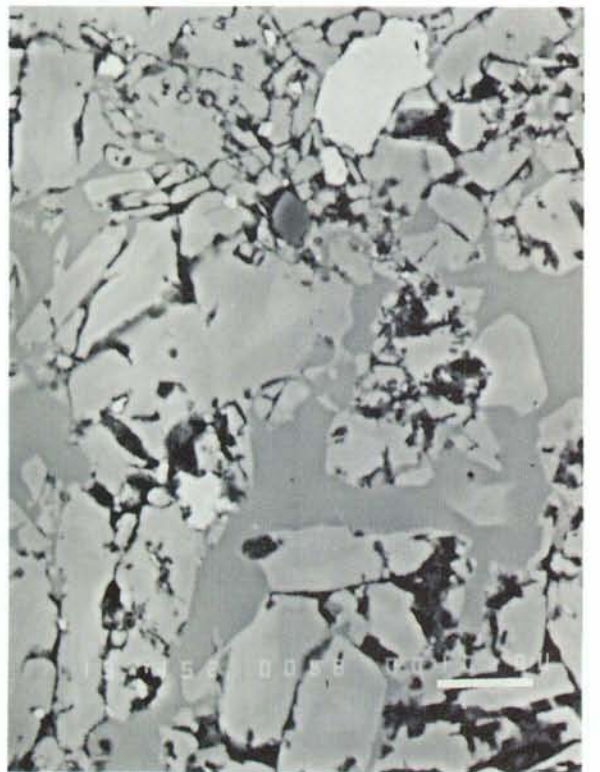
**b**



**c**



**d**





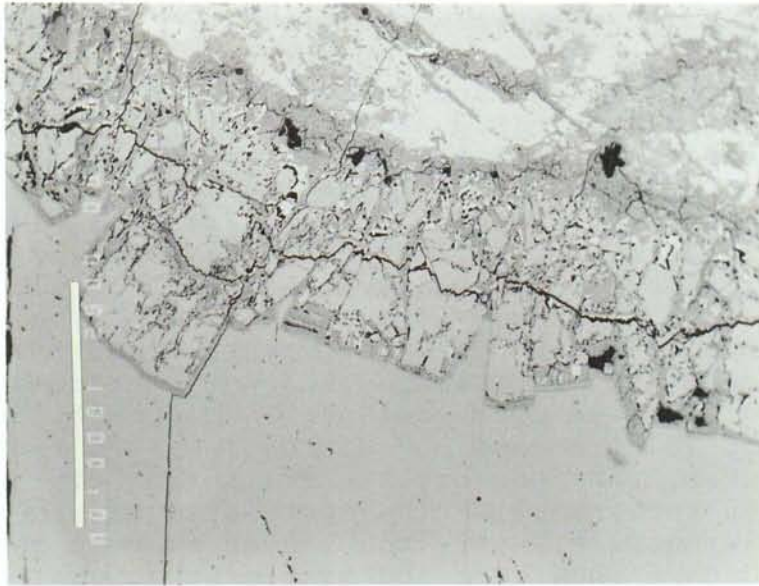
### 4.3 GEOCHEMISTRY LABORATORY FAULT

This fault is largely made up of altered cataclasite cut by extensional prehnite + calcite veins. The primary nature of the cataclasite is difficult to discern in detail. It contains poorly-sorted and angular clasts of sericitized plagioclase, K-spar, quartz and vein epidote up to 5mm in diameter, with accessory sphene (Fig 4-2a). These phases are altered and replaced by 'dirty' green epidote, green chlorite, prehnite, 'illite' and sparse calcite, in order of crystallization. The 'dirty green' epidote locally forms the matrix to the calcite, whereas the other phases appear to overprint and replace porphyroclast and matrix material. The prehnite, illite and calcite appear also to locally infill void space. The illitic alteration is the most pervasive.

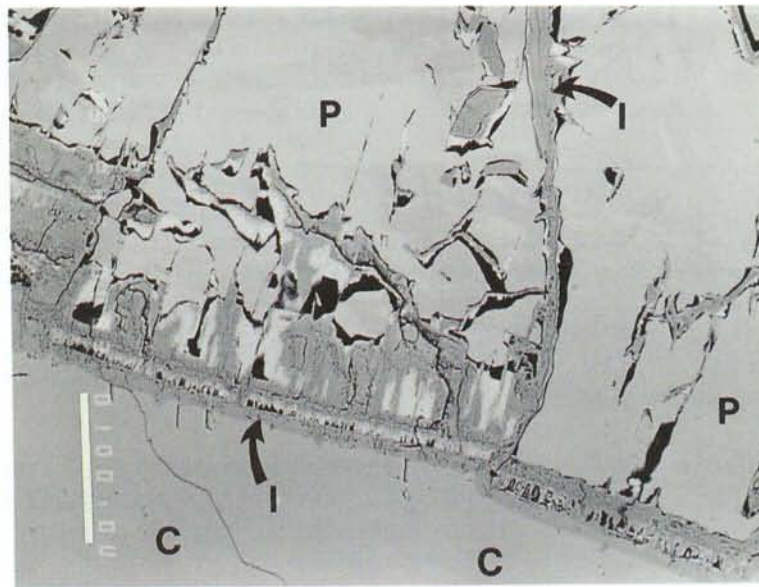
The cataclasite is cut by several extension veins of similar mineralogy and up to 100 $\mu$ m in width. The most prominent example, however, is up to 8mm in width and strikes parallel to the overall fault trend. The mineralogy and texture of this vein is illustrated in Fig 4-2. The margins of the vein consist of stubby euhedral prehnite crystals up to 1mm in length, and faceted toward the vein centre indicating that they grew into void space. The prehnite is weakly zoned with respect to Fe<sup>III</sup> and Al (Fig 4-2b). The grain boundaries of the prehnite together with a fracture 'porosity' within the grains, possibly associated with corrosion, are coated and infilled by 'illite' (Fig 4-2b & c). This 'illite' is locally continuous with the pervasively distributed 'illite' within the vein wallrock cataclasite. The centre of the vein, up to 8mm across, is infilled by twinned xenoblastic calcite, which demonstrably grew after the 'illite'. Microprobe analyses indicate that the calcite contains little or no Fe, Mn or Mg (Appendix 1).

The composition of the 'illite' is discussed further in Section 6.5.

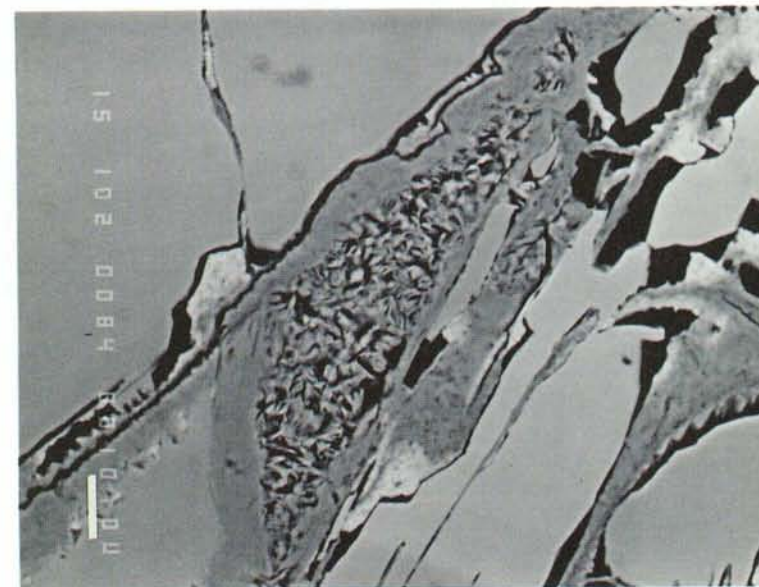
**Figure 4-2** [overleaf] SEM BSE micrographs of Geochemistry Laboratory faultrocks (A92/9). **(a)** Epidote-rich cataclasite (top) cut by extensional vein containing prehnite, 'illite' and calcite; scale bar = 1mm, [FOTO BSE/82]; **(b)** detail of (a) showing weakly-zoned, stubby euhedral prehnite (P) with fractures infilled by 'illite' (I) at the vein margin, and later calcite (C) in the vein centre; scale bar = 100 $\mu$ m, [FOTO BSE/83]; **(c)** detail of (a) showing platy habit of 'illite' occupying fractures within and coating grain boundaries of prehnite; scale bar = 10 $\mu$ m, [FOTO BSE/84]



**a**



**b**



**c**

#### 4.4 FRACTURE ZONE EW-7

##### 4.4.1 Fault 1

The oldest fault-related deformation in Fault 1 of Fracture Zone EW-7 (Fig 3-3 and 3-4), is shown by the mylonites (Fig 4-3a & b). The mylonites exhibit a well-developed planar fabric defined by modal mineralogical variation and by dynamic recrystallization microstructures. Layers, 1-2mm thick, dominated by quartz and feldspar alternate with layers largely composed of epidote with accessory sphene and zircon (Fig 4-3a & b). The quartz is substantially recrystallized to equant 50-100 $\mu$ m grains and subgrains, although some longer ribbon quartz grains are also present. In contrast, the feldspars (plagioclase and microcline) are larger, <0.5cm in diameter, and show brittle fracturing with weakly-developed recrystallization restricted to microfractures and grain margins. Where the latter is best developed, the feldspars show core and mantle structures. The epidote also shows core and mantle structures indicative of dynamic recrystallization but is more commonly substantially recrystallized to <100 $\mu$ m diameter grains. These grains tend to be drawn out into strings along the foliation (Fig 4-3a & b), which correspond to the 'veins' of epidote macroscopically visible at outcrop (Fig 3-4).

A further distinctive feature of the feldspars in the mylonite is their red colouration, which appears to have resulted from oxidative alteration with the formation of finely-dispersed hematite, perhaps by exsolution of lattice-bound iron. This feature appears to be a principal cause of the reddening of the granite wallrocks around all of the fault and fracture zones (eg. Fig 3-3 & 3-4; Eliasson, 1993).

The mylonites contain abundant microscopic kinematic indicators, which with statistically representative samples could be used to determine shear sense across the mylonite zones (cf. Talbot 1991).

The mylonite is cut by narrow quartz veins and occasional cataclasite veins. The most significant post-mylonite deformation, however, consists of massive quartz and chlorite veins associated with brecciation of the quartz- and cataclasite-veined mylonites. The quartz veins are up to 10cm across whereas the chlorite vein breccias are generally narrower (Fig 3-4). Vein breccias with a matrix of dark green chlorite enclose porphyroclasts of mylonite identical to that described above (Fig 4-3c & d). The mylonite clasts vary in size to several millimetres across but are moderately well-sorted and rounded. The chlorite also appears to brecciate some of the quartz veins (Fig 4-4a) and commonly has a spherulitic habit,

with spherulites to 100 $\mu$ m diameter (Fig 4-4b). No mineral-chemical differences were detected between the spherulitic and non-spherulitic chlorites (Appendix 1).

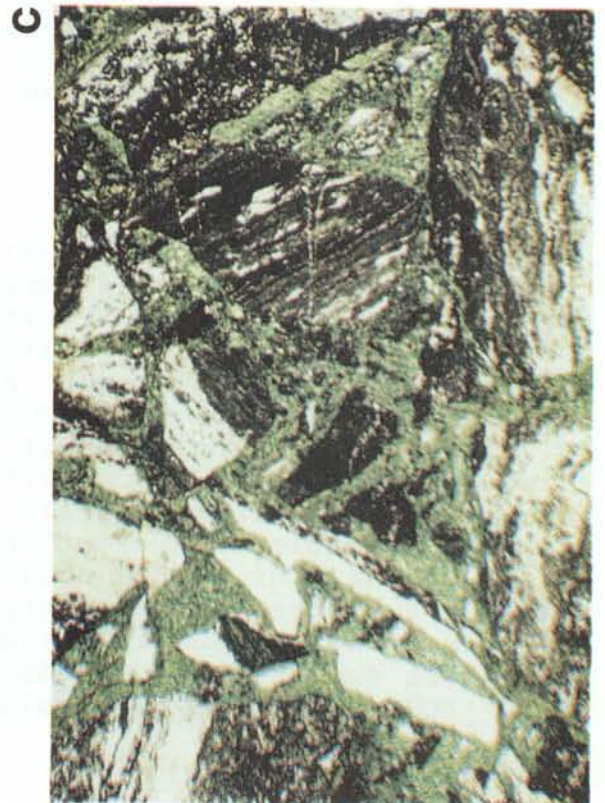
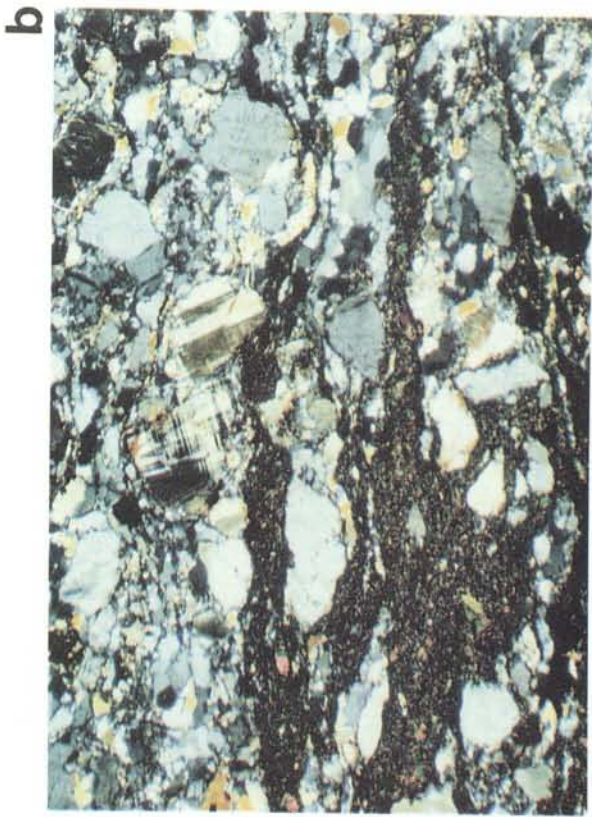
#### 4.4.2 Fault 2

Fault 2 is characterized by a suite of veins, vein-breccia, crush-breccia and cataclasite which cut altered granite which shows locally and weakly-developed mylonitic textures. A fairly complex mineral paragenesis is apparent with many contemporaneous phases as well as clear cross-cutting relationships.

The hostrock consists of sericitized plagioclase, K-spar and quartz with clots of chlorite, sphene and bright yellow epidote. The felsic phases show proto-cataclastic textures with strongly undulose extinction as well as weak mylonitic textures.

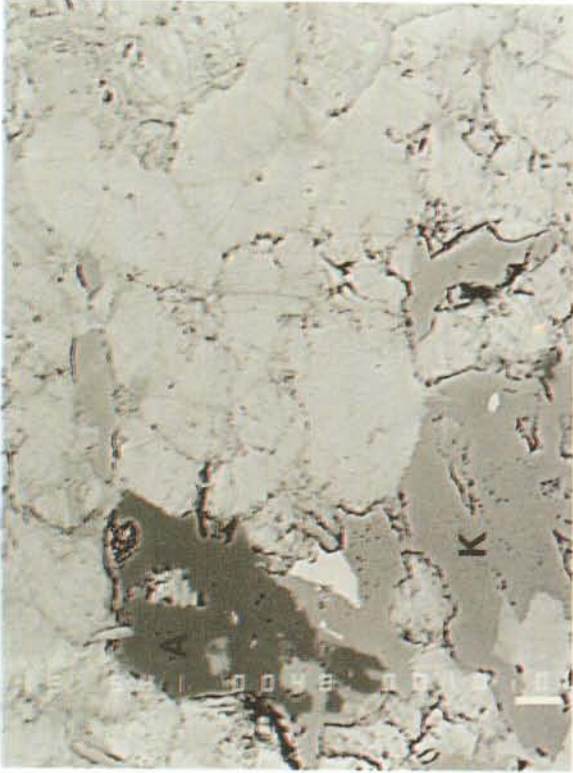
The earliest cataclastic deformation appears to precede the formation of extensional veins of bright yellow epidote and calcite (Fig 4-5a & b). The early cataclasite consists of veins 1mm to 1cm wide with a matrix dominated by dark green epidote and/or fine-grained quartz (Fig 4-4c & d). The bright yellow epidote veins, up to 1mm wide, trend parallel to the fault as a whole and the epidote is similar to that seen in the hostrock. Calcite veins of similar orientation and dimensions appear to have formed pencontemporaneously or later than the epidote. The epidote (and to a lesser extent the calcite) veins are themselves locally brecciated and sheared parallel to the fault zone envelope (Fig 4-4c). The youngest fractures and veins consist of narrow (<250 $\mu$ m) extensional veins, discordant to the fabric of the fault zone, and which are infilled with intergrown xenoblastic calcite and K-spar.

**Figure 4-3** [overleaf] Optical photomicrographs of mylonite (A91/22) and chlorite vein breccia (A91/15) from Fault 1, side tunnel, Fracture Zone EW-7. **(a)** mylonite (A91/22) showing well-developed mylonitic foliation defined by layering of epidote and felsic minerals, and dynamic recrystallization microstructures; note red iron staining of feldspar and discordant extensional quartz vein in the bottom lhs; PPL, field of view = 4mm, [FOTO 2/9]; **(b)** X-nicols view of (a); quartz and epidote show grain size refinement due to dynamic recrystallization whereas plagioclase and microcline show more brittle behaviour (large sheared microcline grain provides an excellent kinematic indicator; [FOTO 2/10]; **(c)** chlorite vein breccia (A91/15), showing bright green chlorite enclosing clasts of quartz-veined epidote mylonite. PPL, field of view = 8mm, [FOTO 2/19]; **(d)** X-nicols view of (c); [FOTO 2/20].



**Figure 4-4** [overleaf] Photomicrographs of chlorite vein breccia (A91/14) and epidote vein breccia (A91/20), from faults 1 and 2 respectively, side tunnel, Fracture Zone EW-7. **(a)** Optical micrograph of chlorite vein breccia (A91/14) showing bright green chlorite-healed fractures in massive quartz vein; note both the quartz and chlorite are cut by a carbonate-healed fracture, visible on the rhs; PPL, field of view = 8mm, [FOTO 2/21]; **(b)** BSE micrograph of A91/14 showing spherulitic habit of chlorite which encloses clasts of albite (A), K-spar (K) and quartz; scale bar = 10 $\mu$ m, [FOTO BSE/48]; **(c)** optical micrograph (PPL) of epidote cataclasite (A91/20). PPL, field of view = 8mm, [FOTO 2/17]; **(d)** X-nicols view of (c); [FOTO 2/18].

**b**



**d**



**a**

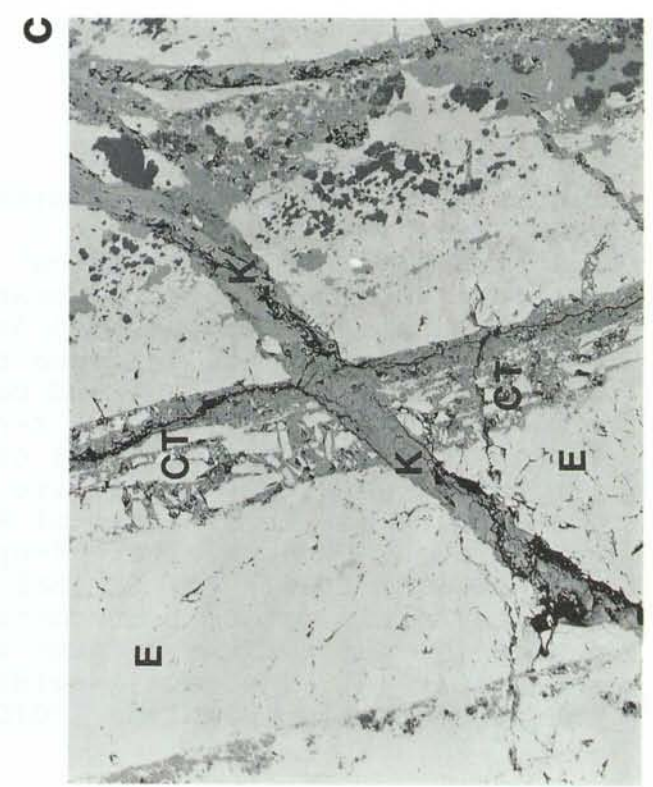
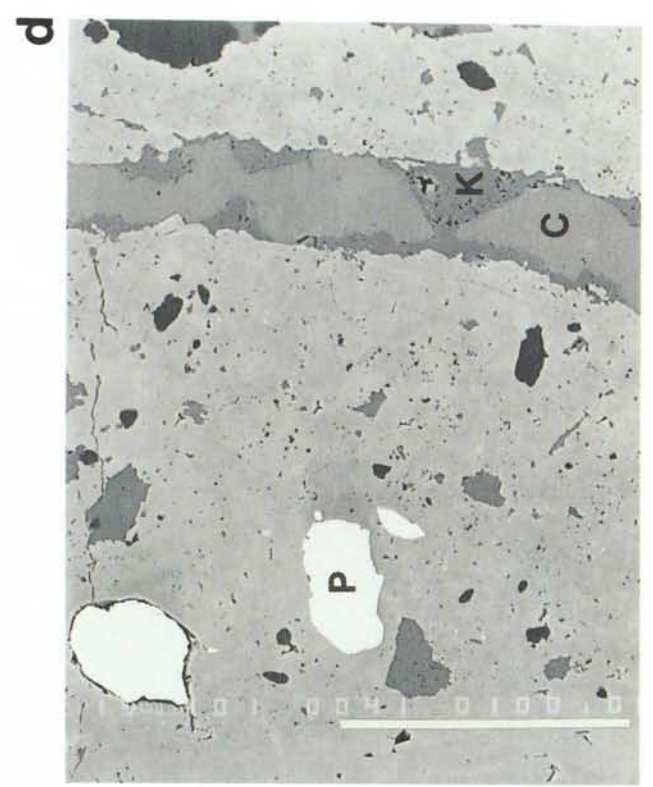


**c**



**Figure 4-5** [overleaf] Photomicrographs of epidote-calcite vein (A91/21 & A91/2), Fault 2, E wall of side tunnel, Fracture Zone EW-7. **(a)** Optical micrograph of A91/21 showing multiple veining of altered granite visible on the rhs. Older quartz-matrix (1) and sheared dark epidote-matrix (2) cataclasite veins are intruded by later extensional veins of bright yellow epidote (3) and carbonate (4); PPL, field of view = 8mm, [FOTO 2/13]; **(b)** X-nicols view of (a); [FOTO 2/14]; **(c)** SEM BSE micrograph of A91/2 showing epidote vein (E) cut by parallel cataclasite vein (CT) containing clasts of the epidote set in a matrix of K-spar + chlorite + epidote; Both are cut by a calcite + K-spar vein (K); field of view = 2mm, [FOTO BSE/20]; **(d)** SEM BSE micrograph of A91/21 showing epidote-matrix cataclasite containing clasts of K-spar (K), quartz (Q) and pyrite (P), cut by vein healed by carbonate (C) and K-spar (K); The matrix epidote has itself been brecciated and subsequently annealed; [FOTO BSE/41]





## 4.5 FRACTURE ZONE NE-4

### 4.5.1 Preamble

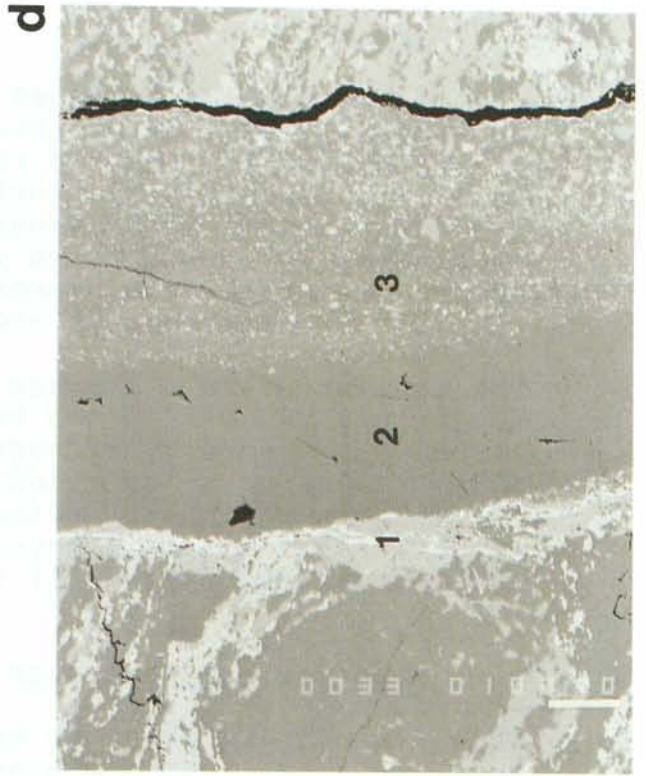
All of the samples examined from this fracture zone were collected in the trench (Fig 3-6) and, with the exception of the mylonite, required resin impregnation during sampling as well as sectioning. With the aid of impregnation and by sectioning one of the palaeomagnetic cube samples, it was found possible to preserve to a reasonable degree the microstructures of the poorly-lithified fault breccias and fault gouges.

The consistent relative age relationship of the faultrocks visible in the trench (Section 3.5) was largely confirmed by microstructural examination. The oldest faultrocks are mylonites, successively deformed by several generations of veins, cataclasites, crush breccias and, lastly, clay-rich fault gouges. Each of the major faultrock types will be described separately.

### 4.5.2 Mylonite sample A91/29

This mylonite (similar to that described from Fracture Zone EW-7) has a strong planar fabric defined by mineralogical layering and the elongation of inequant felsic porphyroclasts. Millimetre or narrower layers are dominated by quartz and/or feldspars, and epidote respectively (Fig 4-6). The quartz shows substantial grainsize refinement due to dynamic recrystallization, with occasional relict cores up to 500 $\mu$ m in diameter mantled by much smaller grains; ribbon quartz also occurs. As in EW-7, the often coarser-grained feldspars show brittle cold-working microstructures including microfractures, undulose extinction and deformation twinning. The largest porphyroclasts are granitic lithic fragments.

**Figure 4-6** [overleaf] Photomicrographs of mylonite (A91/29) from Fracture Zone NE-4. **(a)** Optical micrograph showing mylonite cut by cataclasite vein; mylonitic foliation is defined by mineralogical layering and dynamic recrystallization textures; cataclasite vein shows no shear offset and has a central seam of quartz-cemented cataclasite flanked by quartz; PPL, field of view = 8mm, [FOTO 1/1]; **(b)** X-nicols view of (a); quartz shows dynamically-recrystallized grains whereas the feldspars are larger and fractured; [FOTO 1/2]; **(c)** SEM BSE micrograph of cataclasite seen in (a); scale bar = 1mm, [FOTO BSE/30]; **(d)** SEM BSE micrograph showing compound chlorite (1) + quartz (2) + cataclasite (3) vein cutting mylonitic foliation; hematite (bright phase) has exsolved from the chlorite; the open fracture (black) is probably a preparation artefact; scale bar = 100 $\mu$ m [FOTO BSE/33].



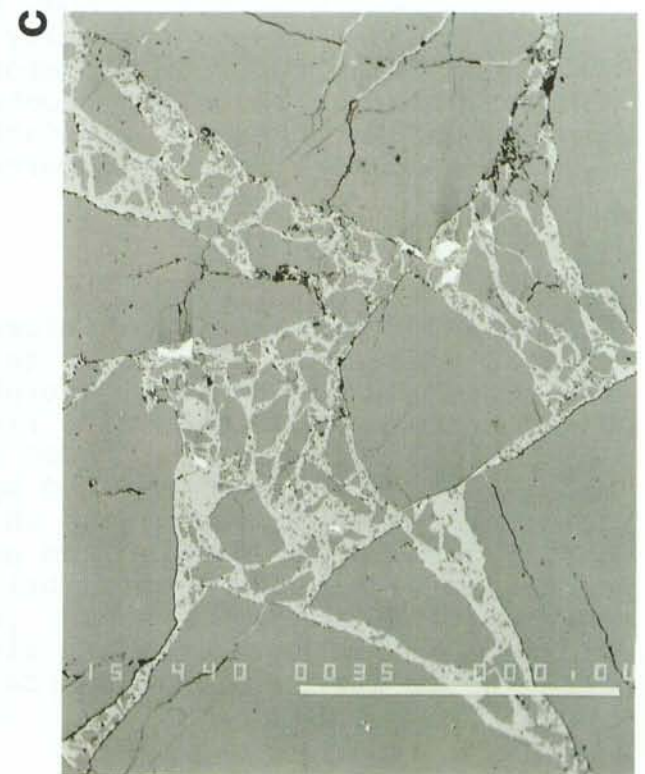
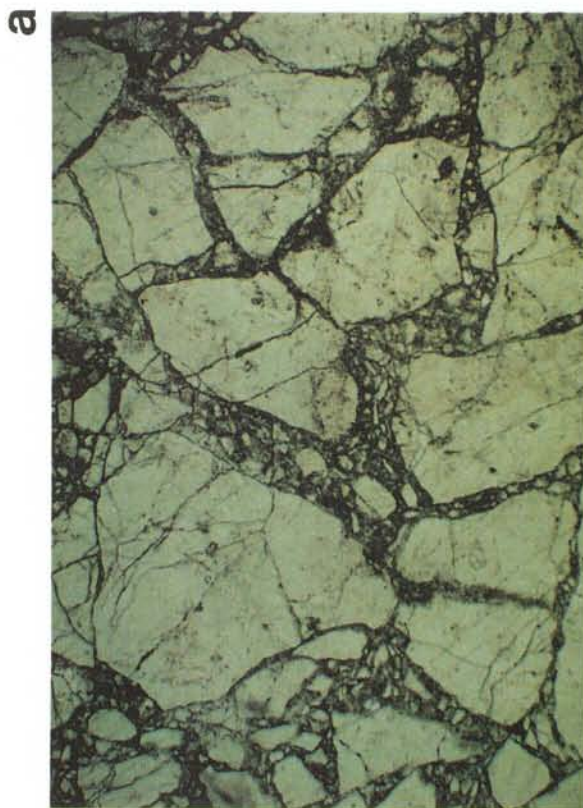
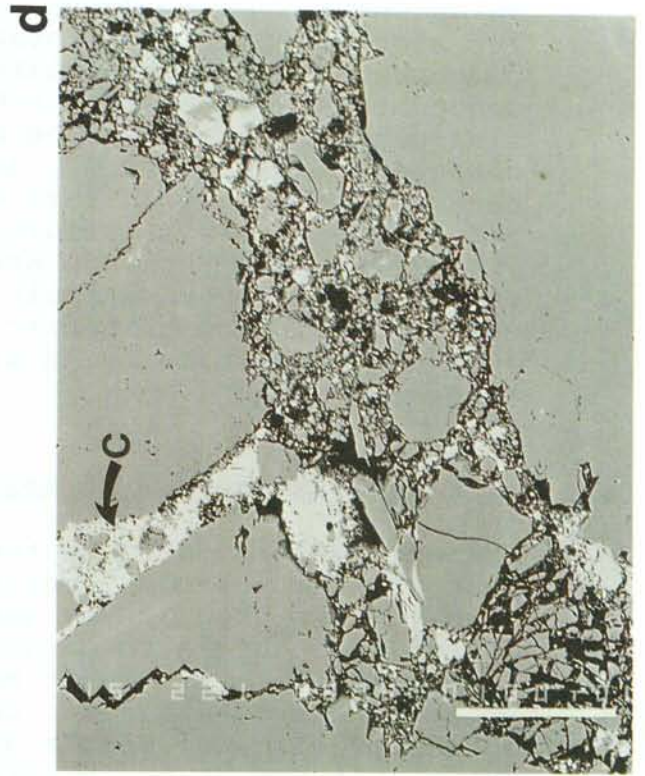
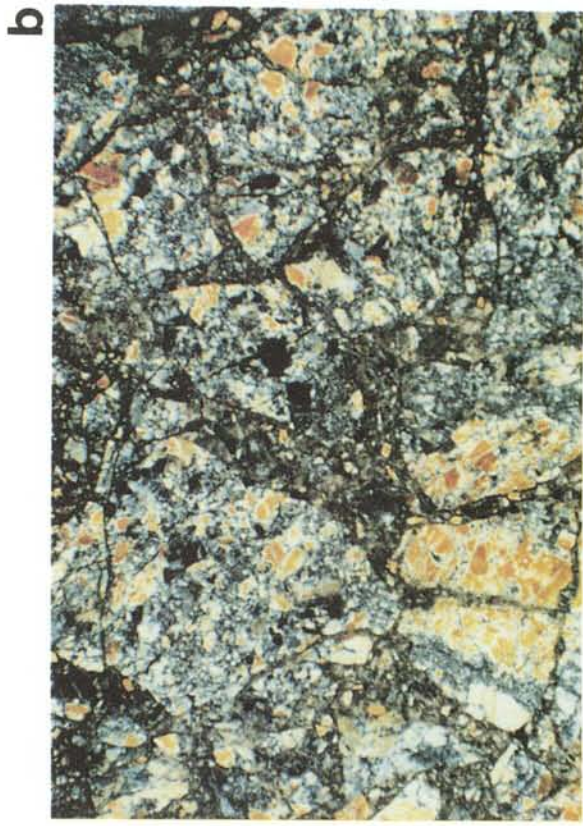
The mylonite is cut by discordant veins and fractures which contain cataclasite, quartz and chlorite (Fig 4-6). The microstructures of these veins are quite complex, but suggest that the cataclasite, quartz and chlorite are penecontemporaneous (Fig 4-6). Microprobe analyses of the same mineral phases in the mylonite and in the cataclasite (Appendix 1), are comparable indicating that cataclasite porphyroclasts were derived directly from the mylonite with minimal fluid-assisted alteration. However, oxidative alteration has affected the mylonite in two ways. The feldspar minerals are stained red, presumably due to exsolution of ferric iron and hematite has exsolved from chlorite in a vein (Figs 4-6a & d respectively).

#### 4.5.3 Cataclasite sample A91/36

The more-consolidated of the brittle faultrocks (which postdate the mylonite, related veins and early cataclasite described above) are transitional in grain size, from crush breccia to cataclasite, and degree of lithification, from fault breccia to cataclasite and vein breccia. Where lithified, cementation is by cataclastic matrix or calcite. Sample A91/36 is typical in that it shows this variation in lithification, grain size and matrix mineralogy over a small scale (Fig 4-7). The sample will be referred to as a cataclasite although its transitional nature should be noted.

The matrix of A91/36 is dominated by quartz fragment-rich cataclasite but elsewhere consists of calcite, becoming transitional to a calcite vein breccia. The quartz-rich cataclasite matrix is made up of poorly-sorted, angular to rounded clasts typically  $<50\mu\text{m}$ , with illitic material comprising the finest components (Fig 4-7). The vein breccia matrix calcite contains variable small amounts of Fe and Mn (Appendix 1). Cathodoluminescence might reveal more complex microstructures within the calcite.

**Figure 4-7** [overleaf] Photomicrographs of cataclasite (A91/36), Fracture Zone NE-4. **(a)** Optical micrograph of fractured quartz and lithic porphyroclasts in matrix of cataclasite and calcite; PPL, field of view = 8mm; [FOTO 2/7]; **(b)** X-nicols view of (a); [FOTO 2/8]; **(c)** SEM BSE micrograph showing quartz clasts cemented by a matrix of cataclasite and calcite; larger quartz clasts show intragranular fractures partly cemented by calcite and partly open, and some of which terminate within the clasts; bright phase in the calcite is chalcopyrite; scale bar = 1mm, [FOTO BSE/35]; **(d)** SEM BSE micrograph showing quartz and lithic clasts in fine-grained cataclasite matrix with minor calcite (arrowed); scale bar =  $100\mu\text{m}$ , [FOTO BSE/36].



It is difficult to determine the relative ages of the calcite and cataclasite matrices, but the latter appears to contain clasts of the former (Fig 4-7d), suggesting that the cataclasite may postdate the calcite. In thin-section, the quartz-rich cataclasite matrix has a markedly higher porosity than the calcite (Fig 4-7c & d) although this may, in part, be a preparation artefact.

Porphyroclasts in A91/36 are dominated by quartz, granite and earlier generations of cataclasite. Although the cataclasite clearly formed as a result of brittle (probably seismic) faulting, on a small scale there is evidence for more ductile, slower strain rate deformation. Many of the clasts contain intra-granular fractures, partly healed by calcite, but which often terminate within the grains (Fig 4-7c). This is suggestive of low-temperature ductile fracture with significant plasticity preceding fracture.

#### 4.5.4 Gouge samples A91/30 and A91/33

Macroscopically, these gouge samples consist of irregular red-brown porphyroclasts set in a more porous, light grey-green matrix (Fig 4-8).

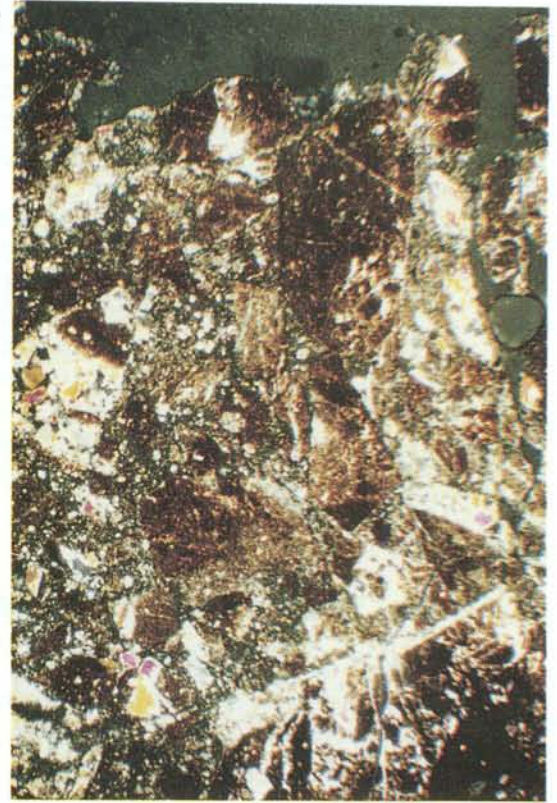
The generally angular porphyroclasts in the gouge range in size from several centimetres to  $10\mu\text{m}$  or less. The larger clasts are themselves mainly cataclasite; many show evidence of still earlier brittle and plastic (mylonitic) deformation. For example, the large angular red/brown porphyroclast in Fig 4-8a & b is a cataclasite which contains clasts of mylonite, epidote vein, and early cataclasite similar to that seen cutting mylonite sample A91/29 (Section 4.5.2). The entire clast is cut by narrow ( $<100\mu\text{m}$ ) quartz veins, terminating at the clast edge and therefore predating incorporation of the clast into the surrounding gouge. The red/brown colour of the clasts is due to finely-dispersed hematite and/or Fe-OOH phases which are absent from the later, grey-green gouge. This relationship between older 'oxidised' clasts and 'reduced' young gouge matrix seems to be typical of all of the gouge samples from NE-4 (Fig 4-8).

**Figure 4-8** [overleaf] Optical photomicrographs of gouge (A91/30) and crush breccia (A91/33), Fracture Zone NE-4. **(a)** Gouge (A91/30) showing dark brown (red in reflected light) clasts in buff coloured matrix; the angular clasts show evidence for at least three episodes of deformation predating their incorporation as clasts in the gouge (see text); PPL, field of view = 8mm, [FOTO 1/7]; **(b)** X-nicols view of (a), [FOTO 1/8]; **(c)** Crush breccia (A91/33) showing red-brown clasts of early cataclasite set in a matrix of buff-coloured cataclasite (compare (a)); PPL, field of view = 8mm, [FOTO 1/27]; **(d)** X-nicols view of (c); [FOTO 1/28].

b



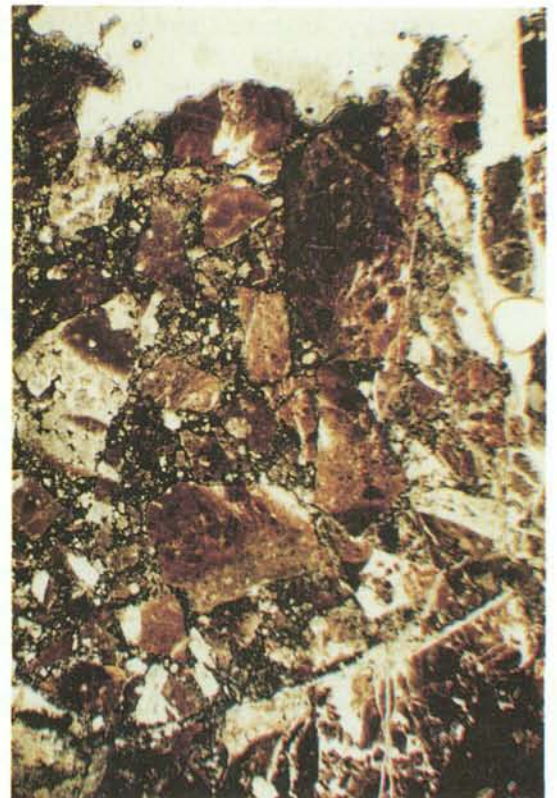
d



a



c



The gouge also contains, however, minor shears of darker colour and finer grain size, which appear to have localized high strains (Fig 4-9a & b). The trace of these features is generally sub-parallel to the trace of the fractures and colour-banding seen in the gouge in the trench (Fig 3-7).

The youngest deformation features in the gouge are partly-mineralized open fractures (Fig 4-9). The fractures and related voids contain blue impregnation resin and their openness may have been enhanced by sample preparation. However, the fractures are also (naturally) healed by wispy illitic material and smaller quantities of euhedral K-spar (Fig 4-9). The grainsize of the 'illite' varies from  $<10\mu\text{m}$  to sub-micron, beyond the resolution of the SEM; the grain shape appears to be 'wispy laths' but this may be influenced by the air-drying. The K-spar is similar in habit to euhedral adularia but it contains small components of albite and anorthite. It is possible that some of the grains are cleavage fragments; others show possible corrosion effects. This illite + K-spar microstructure was also seen in other gouge samples from NE-4.

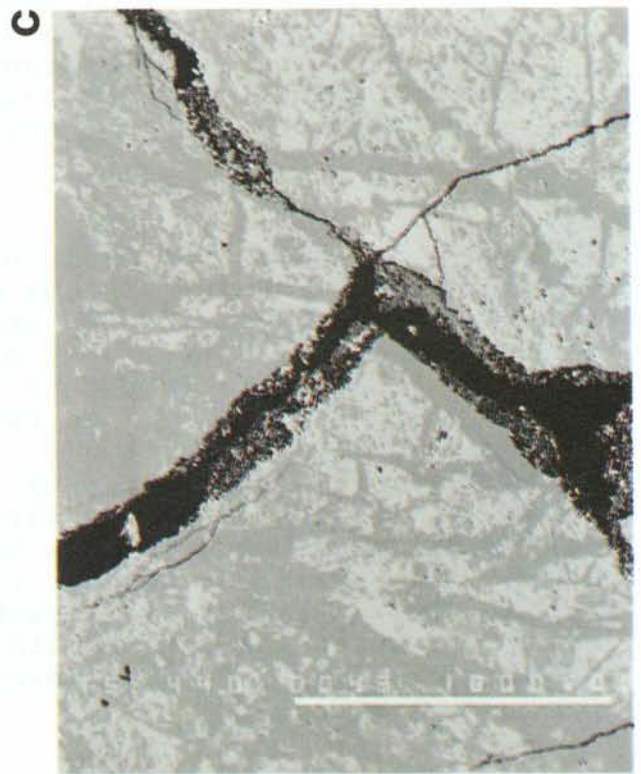
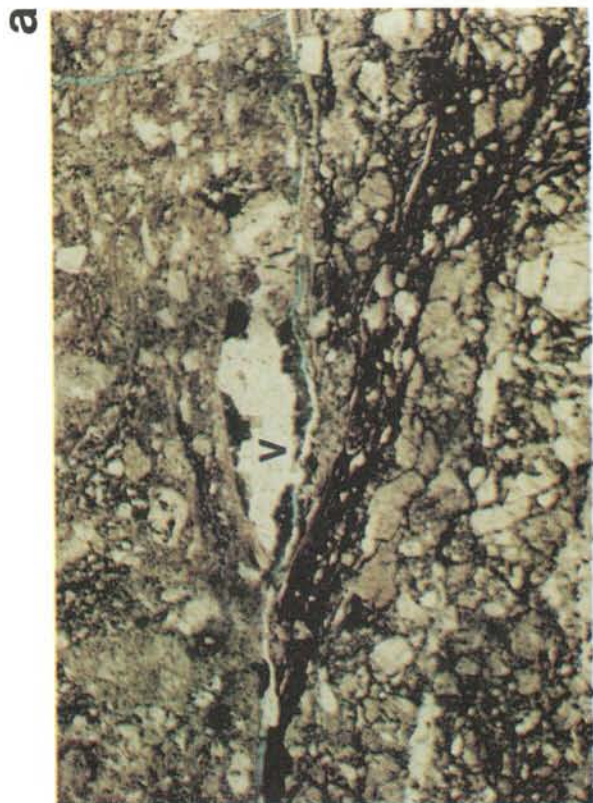
#### 4.5.5 Gouge sample AS14.10

Following (non-thermal) palaeomagnetic analysis, a polished thin-section was prepared from an oriented cube of gouge (AS14.10), collected from the same part of the trench as the gouges described above. The section was cut normal to the dip and strike of the magnetic fabric.

Macroscopically, the section comprises a centimetre-thick layer of grey-green gouge sandwiched between red-brown gouge; ie. the sample straddles a colour banding contact. The grey-green gouge contains clasts of red-brown gouge, confirming the relative age relationships seen in samples A91/30 and A91/33.

**Figure 4-9** [overleaf] Photomicrographs of gouge sample A91/30, Fracture Zone NE-4. **(a)** Optical micrograph showing cataclasite composed of poorly sorted and rounded felsic and lithic clasts; the cataclasite is cut by a dark Fe-stained and clay-rich shear dipping from left to right; an open fracture (V), partially impregnated by blue resin, contains illitic material and K-spar. PPL, field of view = 2mm, [FOTO 1/15]; **(b)** X-nicols view of (a); [FOTO 1/16]; **(c)** SEM BSE micrograph showing clasts of K-spar and albite veined by quartz, which are cut by open fractures; the latter contain mineral phases with a texture similar to that in (a); scale bar = 1mm, [FOTO BSE/43]; **(d)** detail of (c) showing randomly-oriented 'wispy' illitic material intergrown with euhedral K-spar; the illitic material has 'beards' of sub-micron whiskers; scale bar =  $10\mu\text{m}$ , [FOTO BSE/45].



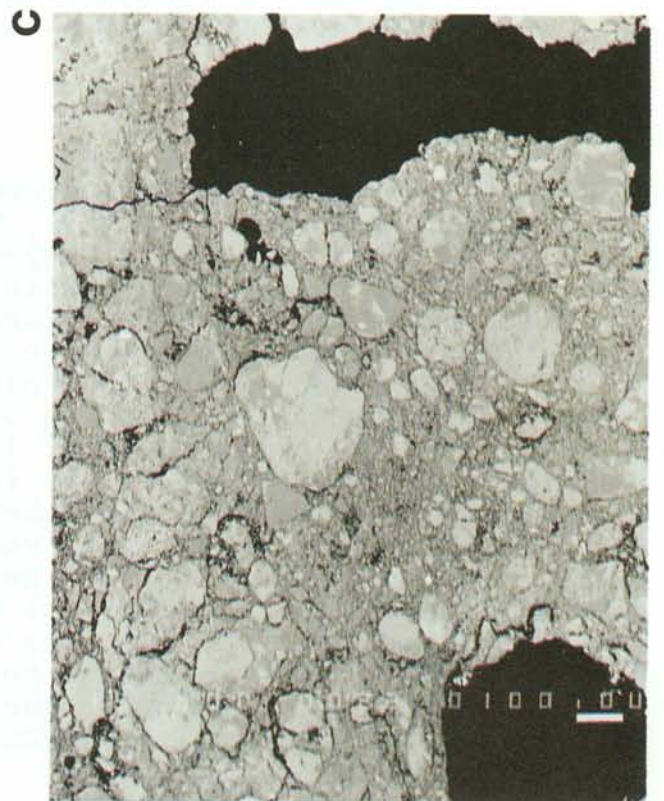
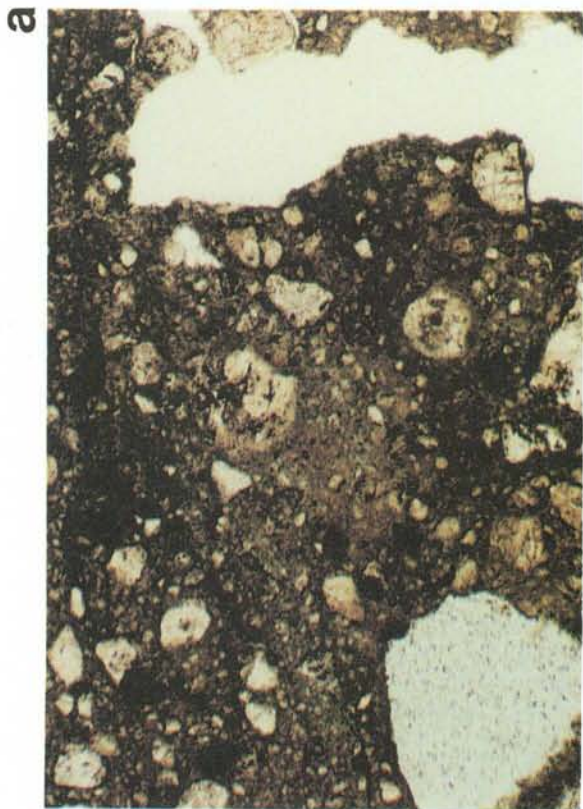
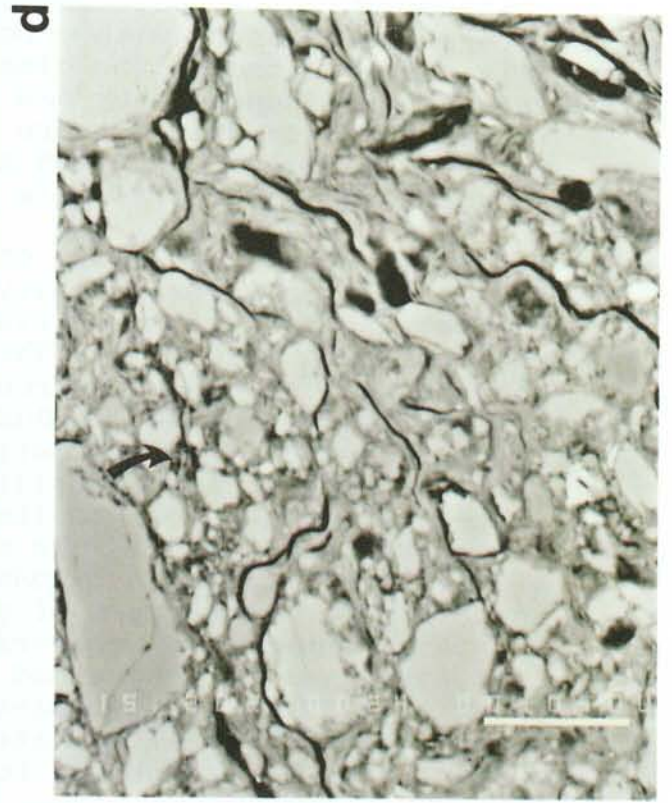
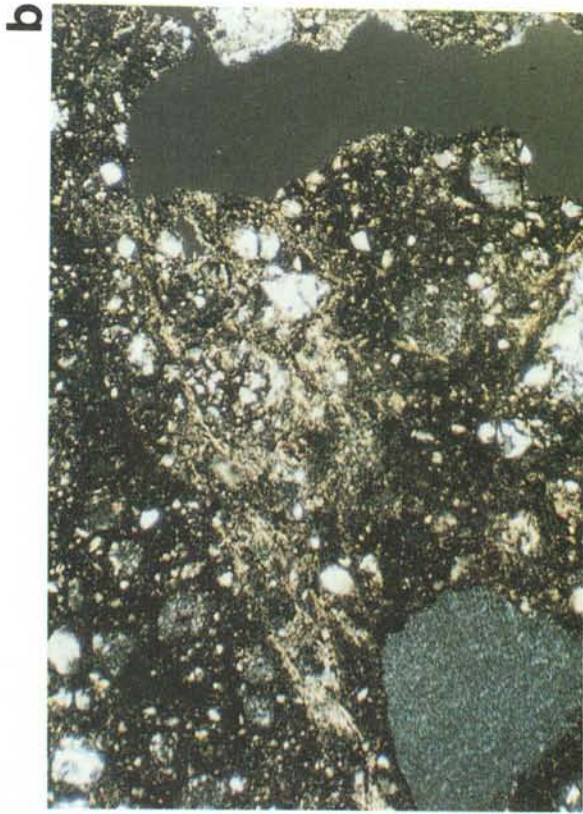


Both the colour types of gouge contain porphyroclasts of granite, mylonite, cataclasite, epidote and quartz vein materials, together with constituent monomineralic clasts (Fig 4-10). Although the clasts remain poorly-sorted and irregularly-shaped, they are within this small area (25x25mm) comparatively more sorted and more rounded than in gouge samples A91/30 and A91/33. This may reflect a greater degree of cataclasis or higher strain.

The small-scale complexity of the mineralogy and microstructure is graphically revealed by comparing optical and backscattered electron photomicrographs of the same area (Fig 4-10). The fine-grained matrix interstitial to the porphyroclasts is dominated by phyllosilicate phases, including 'illite' and chlorite. Locally a strong fabric, defined by the preferred orientation of the phyllosilicates, is developed in the grey-green gouge close to its contact with the red-brown gouge (Fig 4-10b & d). This suggests that relatively higher strains were accommodated in this area. Elsewhere in both the colour types of gouge, the matrix consists of micron to sub-micron, more-randomly arranged phyllosilicates. Very fine-grained calcite is also present in the matrix. This is most clearly seen in the grey-green gouge, where the illitic material appears to coat the porphyroclastic grains and to infill void space (Fig 4-11a). This material is clearly of authigenic origin and appears to have grown in void space following the last movement within this gouge seam.

Similar authigenic phyllosilicates are present in the matrix of the red brown gouge, but the matrix is also distinguished by abundant, fine-grained (<2 $\mu$ m) Ti- and Fe-oxy/(?)hydroxides (Fig 4-11b).

**Figure 4-10** [overleaf] Photomicrographs of fault gouge palaeomagnetic sample (AS14.10), Fracture Zone NE-4. **(a)** Optical micrograph showing 'grey-green' gouge composed of poorly-sorted, sub-rounded clasts of quartz, feldspar and granitic mylonite in a brown, largely optically irresolvable, matrix; white areas are holes in the section; PPL, field of view = 2mm, [FOTO 1/21]; **(b)** X-nicols view of (a) showing trace of planar fabric, dipping 30° from right to left, defined by the preferred orientation of illitic material in the gouge matrix; in geographic space the fabric strikes NE and dips SE, sub-parallel to the magnetic fabric; [FOTO 1/22]; **(c)** SEM BSE micrograph of same area as (a) revealing complexity of grain size, shape and mineralogy of the clasts; scale bar = 100 $\mu$ m, [FOTO BSE/22]; **(d)** detail of (c) showing oriented inequant porphyroclasts of K-spar, quartz and albite in an illitic matrix; the fabric corresponds to the optical fabric in (b); the finest phyllosilicates appear to be more randomly oriented (arrowed); scale bar = 10 $\mu$ m, [FOTO BSE/24].



A gold-coated fracture surface, created by breaking in half a portion of the grey-green gouge was examined by secondary electron imaging (SEI) in the SEM. The sample showed obviously porphyroclastic grains of quartz and feldspar, with a corroded appearance, partially coated by illite (Fig 4-11c & d). The coating relationship together with the euhedral to sub-euhedral habit of the illite clearly confirm its authigenic origin. Apart from its euhedral habit, however, the specific texture of the illite is almost certainly strongly influenced by the air-dried nature of the sample.

The composition of the 'illite' in gouge samples from NE-4 is discussed further in Section 6.5.

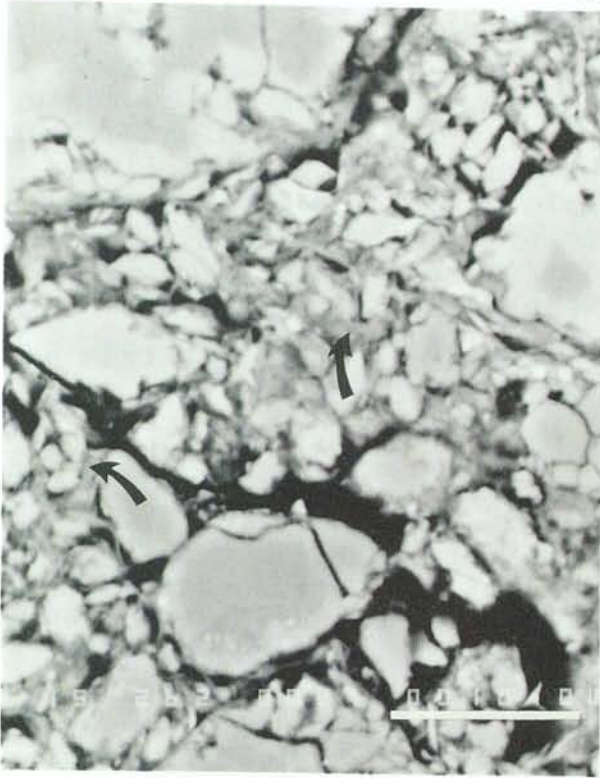
#### 4.6 NNE-TRENDING FAULT, 1130m CHAINAGE

The faultrocks within this fault include, in order of formation, mylonitic granite, epidote cataclasite/vein breccia, chlorite veins, calcite vein breccia, and late extensional veins with a complex mineral paragenesis including fluorite, sulphides and calcite.

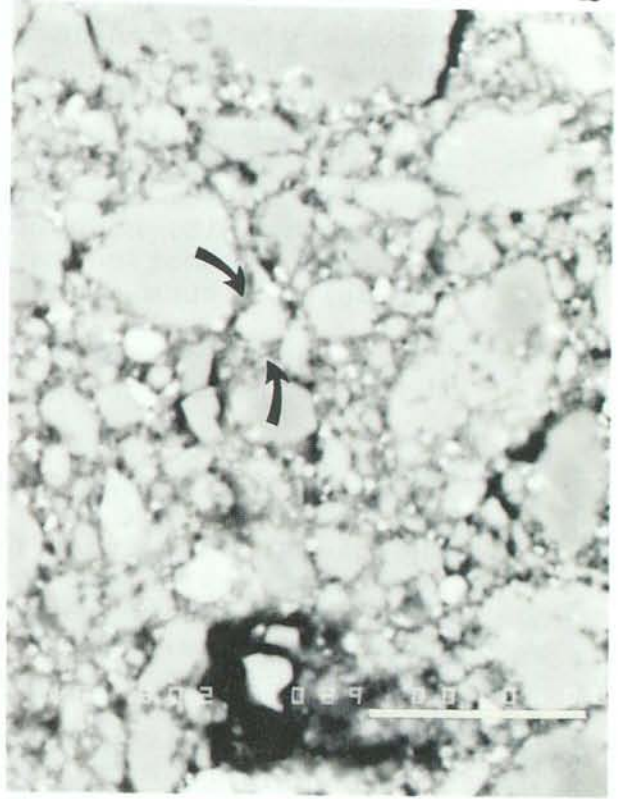
A protomylonitic granite (A92/4) shows a similar mineralogy and microstructures to those described from fracture zones EW-7 and NE-4, and is cut by epidote-rich matrix cataclasite and calcite veins (Fig 4-12a). Again, the mineralogy and microstructure of the epidote-rich cataclasite is comparable to that of samples from EW-7 and NE-4.

**Figure 4-11** [overleaf] Photomicrographs of fault gouge palaeomagnetic sample (AS14.10), Fracture Zone NE-4. **(a)** SEM BSE micrograph of grey-green gouge with clasts of cataclasite, granite, K-spar, albite, quartz, epidote and pyrite in matrix of sub-micron wispy illite (arrowed); scale bar = 10 $\mu$ m, [FOTO BSE/27]; **(b)** SEM BSE micrograph of red-brown gouge with clasts of cataclasite, granite, K-spar, albite, quartz and epidote in ultra-fine grained illitic matrix (arrowed); bright phases include titanium and Fe-oxy/hydroxide minerals; scale bar = 10 $\mu$ m, [FOTO BSE/29]; **(c)** SEM SEI micrograph of fracture surface showing authigenic platy illite overgrowing (?) corroded quartz grain; scale bar = 1 $\mu$ m, [FOTO BSE/85]; **(d)** SEM SEI micrograph of fracture surface showing euhedral lath-shaped and pseudohexagonal illitic material (arrowed); scale bar = 1 $\mu$ m, [FOTO BSE/86].

**a**



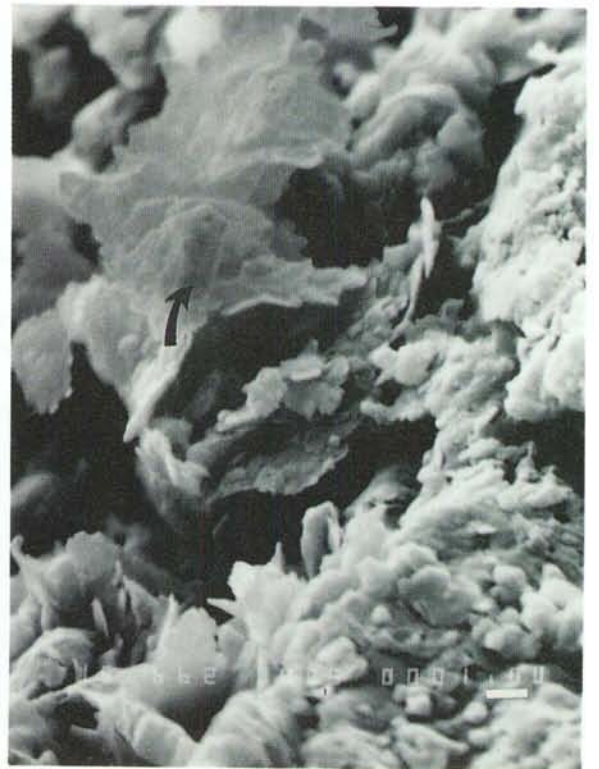
**b**



**c**



**d**



The cataclasite and protomylonite are cut by calcite veins and calcite-matrix cataclasite (Fig 4-12b), the calcite contains small amounts of Mn and Mg (Appendix 1). Still younger compound extensional veins contain euhedral fluorite (showing characteristic cathodoluminescence) with a discontinuous coating of later sulphide (pyrite and chalcopyrite), finally infilled by xenoblastic calcite which is weakly zoned with respect to Mn and Mg (Fig 4-12b, c & d; Appendix 1).

#### 4.7 OTHER LOCALITIES

Due to access difficulties it was possible to collect only bulk samples of the fault gouges from Fracture Zone NE-3, and consequently no petrographic work has been undertaken. A sample of granite wallrock (A91/41) from NE-3 has a mineralogy comparable to that seen in other countryrock samples but no strong mylonitic fabric was seen. The composition of 'illite' separated from the gouge samples from NE-3 is discussed in Section 6.5.

Sample A92/8, a granite from Fracture Zone EW-3, sampled for palaeomagnetic analysis, shows a weak mylonitic foliation, reddened feldspars and is cut by cataclasite and prehnite + calcite veins. This sample has not been examined in detail.

The calcite vein from the NW-striking fault at chainage 1103m, sampled for palaeomagnetic analysis, has not been examined petrographically.

The petrography of the microgranite from the Pump station locality, chainage 1360m, and of the aplite dyke, chainage 140m, has not been examined in detail.

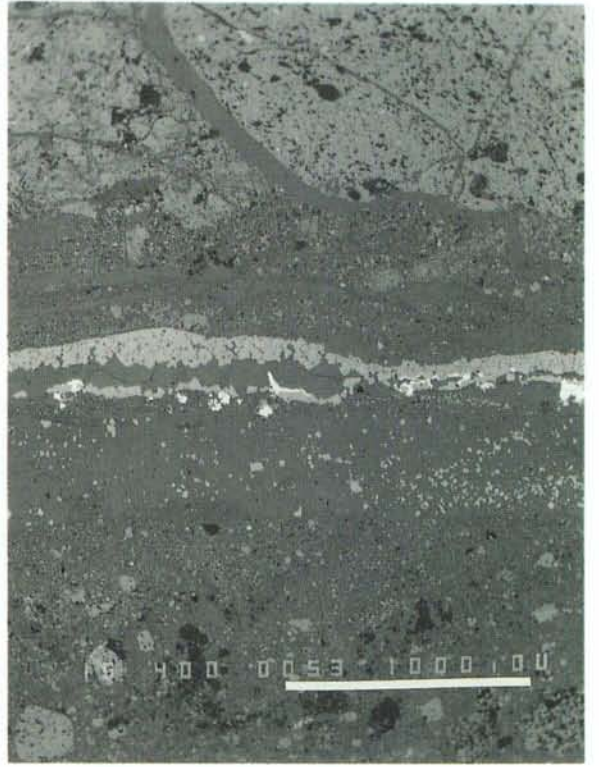
A number of core samples, from pre-investigation boreholes, which have been correlated with various fracture zones (Table 3-1) were examined but are not considered here. Microprobe analyses of mineral phases in some of these samples are given in Appendix 1.

**Figure 4-12** [overleaf] SEM BSE & CL photomicrographs of epidote cataclasite (A92/1) and veins (A92/2), NNE-trending fault, 1130m chainage. **(a)** Epidote-rich cataclasite crosscut by calcite vein; scale bar = 1mm, [FOTO BSE/51]; **(b)** compound extensional vein cutting two generations of cataclasite; scale bar = 1mm; **(c)** detail of (b) showing extensional vein containing euhedral fluorite (F), partly coated by pyrite (P) and infilled by calcite (C); scale bar = 100 $\mu$ m, [FOTO BSE/55]; **(d)** CL image of (c) revealing zoned drusy habit of fluorite; scale bar = 100 $\mu$ m, [FOTO BSE/54].

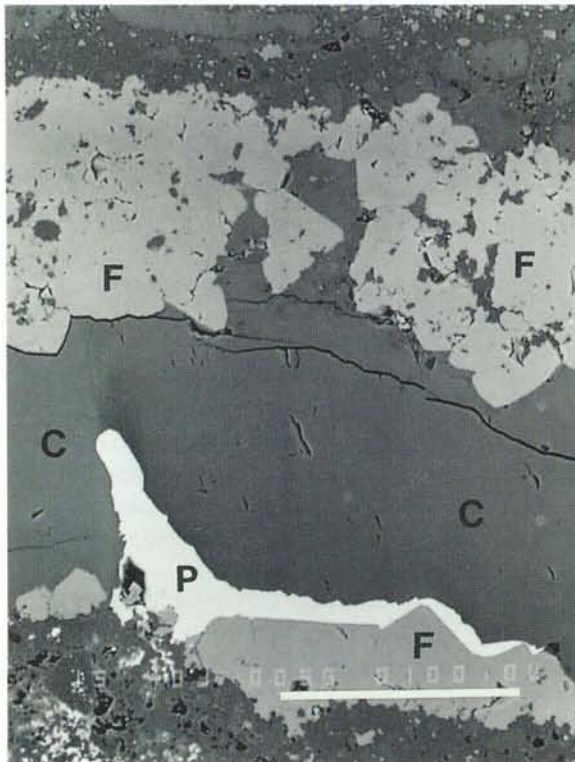
**a**



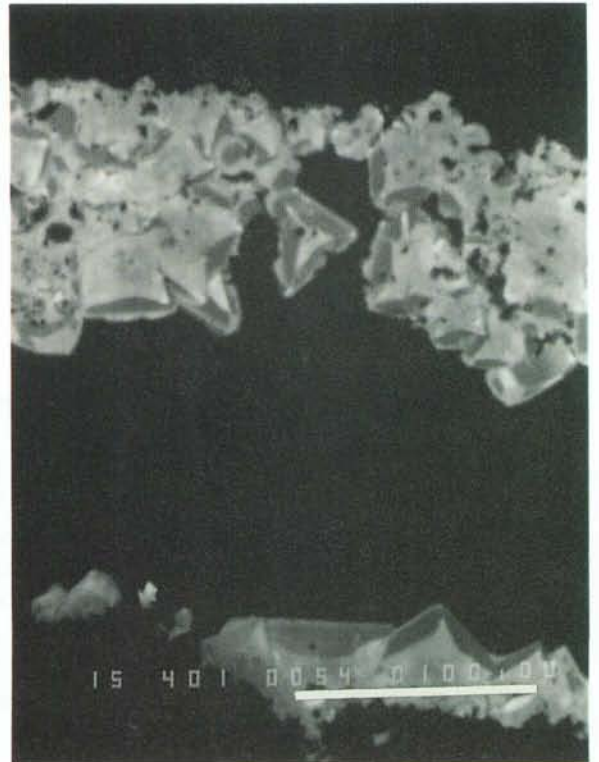
**b**



**c**



**d**



## 4.8 GOUGE GRAIN SIZE AND XRD ANALYSES

### 4.8.1 XRD analyses

XRD analyses of the whole-rock and  $<2\mu\text{m}$  fraction of eight gouge samples are given in Table 4-1. The analyses show that the majority of the gouges have a rather similar mineralogy dominated by quartz, K-spar, chlorite, illite and mixed-layer phases, together with hematite. In detail however, the mineralogy of the  $<2\mu\text{m}$  fraction shows significant variation, with some samples dominated by chlorite and illite and others dominated by mixed-layer phases. The mineralogy of the finer fractions separated from the gouge for isotopic dating is considered in Section 6.5.

### 4.8.2 Grain size analyses

During the initial stages of mineral separation to isolate the clay and quartz fractions from the gouge for isotopic and ESR dating respectively (Appendix 2), quantitative measurements of the equivalent spherical diameter (ESD) grainsize distribution in the range  $>2\text{mm}$  to  $<2\mu\text{m}$  were made (Fig 4-13). Obviously, the distributions may be biased by sampling artefacts (nature of exposure, different mass of gouge, etc); nevertheless, some interesting patterns are apparent. The  $>2\text{mm}$  fraction is typically 20-50% of the total mass, with the remaining fractions each  $<15\%$ . The majority of samples show a continuous though gentle decrease in mass-fraction with decreasing grainsize. Samples A91/23 (Information Gallery), A91/32 (NE-4) and A91/39 (NE-3), however, contain a relatively larger  $<2\mu\text{m}$  mass-fraction consistent with their field characteristics as well-developed gouges. The cataclasite A91/36 shows an expected large mass-fraction of the  $>2\text{mm}$  grainsize. It is evident from these measurements that the gouges offer an enormous area of potentially reactive surfaces, which may have significance for the migration and retardation of radionuclides through the gouge materials.

## 4.9 SYNTHESIS

The mineralogical and microstructural study of faultrocks from selected faults and fracture zones has shown:

- (i) close confirmation of the previously-identified mineral paragenesis for faults and fractures at Äspö (Table 2-2), although differences in detail are apparent, such as the repeated occurrence of K-feldspar mineralization and the relationship between deformation and authigenic mineral growth;



Table 4-1 XRD analyses of gouge 'whole-rock' samples

SAMPLE	A91/23	A91/6	A91/7	A91/8	A91/32	A91/36	A91/38	A91/39
WHOLE-ROCK ANALYSIS								
quartz	-	D	D	D	D	D	D	D
K-feldspar	D	S	S	S	S	S	S	S
albite	S	M	-	-	-	-	-	-
calcite	S	-	-	-	-	-	-	-
white mica	-	-	-	-	S	M	S	S
chlorite	S	M	-	-	S	M	S	-
illite	S	-	-	-	-	-	-	-
illite-smectite	S	-	-	-	-	-	-	-
chlorite-smectite	S	-	-	-	-	-	-	-
mica-smectite	-	-	-	-	-	-	-	M
kaolinite	S	M	S	M	?	?	-	-
LESS THAN 2 MICRON FRACTION								
quartz	-	D	S	D	S	S	S	S
K-feldspar	-	S	S	D	S	S	S	S
albite	-	S	-	-	?	-	S	S
white mica	-	-	-	-	D	S	S	S
chlorite	-	S	S	S	D	D	D	D
illite	D	-	S	S	-	-	-	-
illite-smectite	D (R1, <5%)	S (R2, <7%)	D (RO, <10%)	S (R2, <13%)	S (RO, <8%)	S (RO, <9%)	M(RO)	S (R2, <7%)
chlorite-smectite	D	M	S	M	-	-	-	-
kaolinite	?	?	?	S	-	-	-	-
haematite	-	-	M	-	M	M	M	-
pyrophyllite	-	-	-	-	-	-	M	-

Note: 1) D = dominant phase, S = subordinate phase; M = minor phase, ? = possibly present, - = not detected  
 2) RO = random ordering, R1 & R2 = regular ordering mixed layers; % figure = % of expandable layers

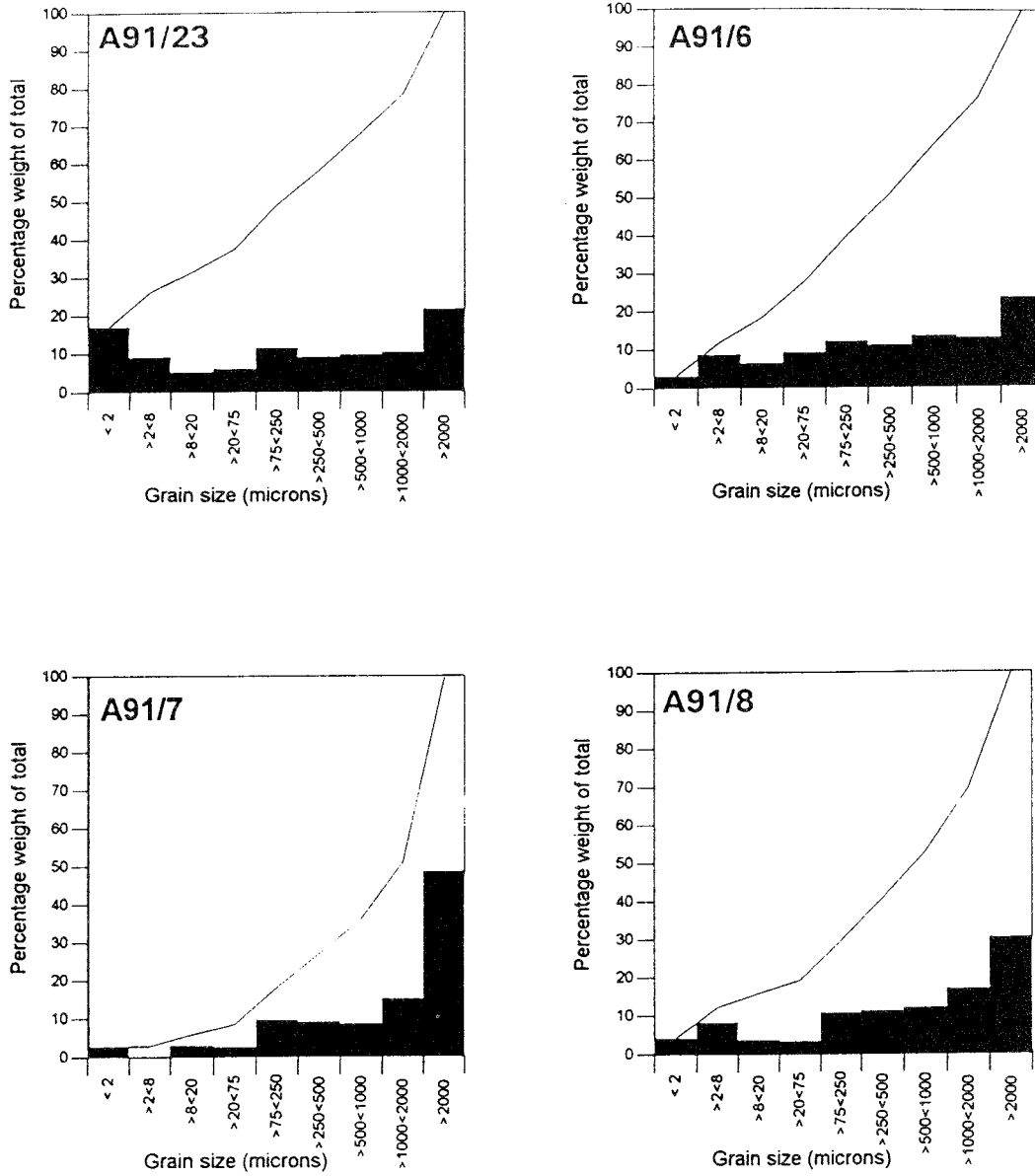


Figure 4-13 Frequency distribution of >2mm to <2 $\mu$ m grain sizes in selected fault gouge samples.

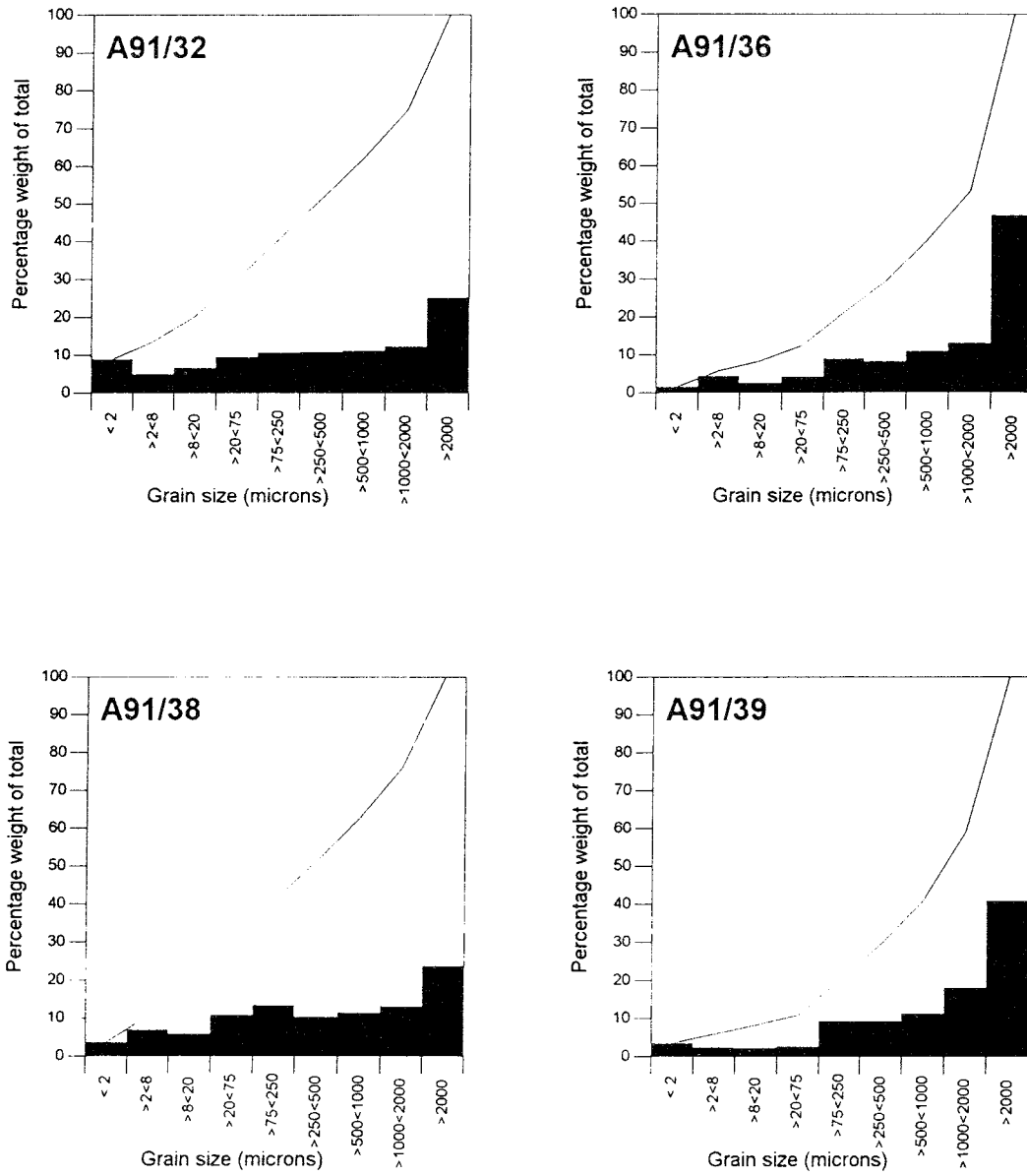


Figure 4-13 (cont) Frequency distribution of >2mm to <2 $\mu$ m grain sizes in selected fault gouge samples.

- (ii) most faults and fracture zones show evidence for multiple reactivation including: early mylonitic deformation (more than one episode?); repeated high-temperature cataclasis involving epidote, calcite and chlorite mineralization; extensional vein formation, infilled with prehnite, illite, fluorite sulphide and calcite; the youngest fault movements which formed cataclasites, fault breccias and fault gouge cemented by authigenic 'illite' and minor K-spar; late calcite veins may postdate or be of the same age as the 'illite';
- (iii) the changing style of deformation (plastic to brittle) and mineral paragenesis is consistent with the prolonged uplift of the Äspö rocks from amphibolite facies through greenschist and zeolite facies to 'diagenetic' conditions;
- (iv) it is difficult to gauge with any accuracy the amounts of shear strain, the magnitudes of displacements, and the senses of shear associated with the different episodes of faulting;
- (v) the faults and fracture zones were the locus of major palaeo-fluid fluxes due to temporal increases in fracture-controlled porosity and permeability; the greatest present-day porosity is shown by the youngest faultrocks, ie. gouge in NE-4 and fault breccia in Fault 1 of EW-7; these features are also seen in the tunnel to be permeable (anisotropic?);
- (vi) with the possible exception of Fault 1 of EW-7, no evidence was found in the tunnel exposures and faultrock samples examined for late, thoroughgoing shear fractures which might be associated with earthquake activity postdating gouge formation;
- (vii) the complex microstructure and mineralogy, including ferromagnetic phases, in the faultrocks confirms the need for care in the interpretation of palaeo-magnetic, ESR and isotopic dates for these rocks;
- (viii) the late authigenic 'illite' occurs as a cataclasite matrix cement and vein-infill in gouge from NE-4, as a pre-calcite cement and alteration phase in the Geochemistry Laboratory fault, and in veins (of unknown microstructure) in the Information Gallery, NE-3 and EW-3 faults; these offer a clear target for K-Ar dating.
- (ix) the source of the 'illite' is presumed to be feldspar and mica breakdown.

## 5 PALAEOMAGNETIC ANALYSES

### 5.1 INTRODUCTION

The principle of the palaeomagnetic method of faultrock dating is to compare the direction of characteristic remanent magnetisation in the faultrock with the predicted direction of the geomagnetic field vector at the sampling site for different geological periods (eg. Gutmanis et al 1991, Hailwood et al 1992).

The direction of the local geomagnetic field vector at a given site on the Earth's surface varies with time, principally in response to large scale plate motions and smaller-scale local tectonic movements of the site relative to the geomagnetic poles. Because of the random nature of such motions, the mean direction of the geomagnetic field vector at a specific locality (when averaged over a period of a few tens of thousands of years to remove the effects of short-term geomagnetic secular variation), is seldom repeated over geological time. Thus, under appropriate conditions, the method is capable of giving unambiguous dating results. The method provides information on the *age of magnetisation* of the rock. If the magnetisation is *primary* then this age refers to the true age of the rock. However, many rocks carry two or more components of magnetisation, each acquired at different times in the history of the rock and each relating to a specific magnetisation event. Such events may include, for example, episodes of heating, due to deep burial or emplacement of nearby igneous bodies, or episodes of movement of groundwater or other geothermal fluids along the conduits provided by the fault zones. In such cases, the age obtained from palaeomagnetic dating will refer to the magnetisation event, rather than the original time of formation of the faultrock. However, it will still provide a potentially important constraint on the minimum possible age of the faultrock, and hence the history of movement on the fault.

In order to apply the method successfully, the following conditions must be satisfied:

- (i) the rock must carry a stable remanent magnetisation, dating from a specific geological event, which can be related in some way to the geological history of the fault zone;
- (ii) the mean characteristic magnetisation of the rock samples must have been acquired over a time interval in the order of  $10^3$  years, so that short-term geomagnetic secular variations are effectively averaged out;

- (iii) the direction of the mean magnetisation vector must be defined with sufficient precision to enable it to be compared meaningfully with predicted geomagnetic field vectors for different geological periods;
- (iv) the magnetic vector of the faultrock must provide a reliable record of the local geomagnetic field vector at the time of magnetisation and must not be deflected from the latter (for example as a result of the magnetic anisotropy which many fault rocks exhibit);
- (v) it must be possible to predict the direction of the local geomagnetic field vector at the sampling site for the appropriate interval of geological time, with an adequate level of confidence.

Evaluation of palaeomagnetic data from faultrocks in the context of these conditions requires that the nature and origin of the remanent magnetisation be analyzed in detail and that progressive demagnetisation analyses are used, to identify and separate the different components of magnetisation in each sample. In the present study, both thermal and alternating field (AF) demagnetisation was used to isolate the different components of magnetisation. The magnetomineralogy was investigated by isothermal remanent magnetisation (IRM) acquisition analyses and disaggregation/remagnetisation experiments.

## 5.2 SAMPLING

The rock types sampled for this palaeomagnetic study include fault gouge, epidotic veins, breccia and related cataclastic materials together with a variety of hostrock types (Table 5-1). Included in the latter group are undeformed granite, metabasite, microgranite and aplite, as well as red fine-grained granite and red proto-mylonitic granite from within major fracture zones. The locations of the palaeomagnetic sampling sites are given in Table 3-1 and shown in Figs 3-1 to 3-8. Orientation data for the majority of samples collected are given in Appendix 2.

Many of the consolidated (well-lithified) rocks investigated in this study (including epidote veins and breccia, aplite dyke and various host rocks) were sampled using a portable coring drill. This provided 25mm diameter drill core specimens. Each core sample was oriented *in situ* using an orientation table which incorporated a magnetic compass and clinometer. The compass bearing was checked at certain localities by comparison with the orientation of a precisely-targeted laser beam, used for guiding the tunnel excavation. No significant deviation of the magnetic compass bearing (due, for example, to the magnetisation of the

surrounding rocks or tunnel services and reinforcement structures) was observed. After orientation, the core samples were removed from the exposure. Subsequently, in the laboratory, a cylindrical specimen, approximately 25mm in length, was cut from each core, for palaeomagnetic analysis. Where possible, at least six independently-oriented core samples were taken at each sampling site.

Table 5-1 Rock types and numbers of sites sampled

Rock Type	Site Numbers	Fracture Zone/ Locality	Fault, vein or dyke orientation	No of Specimens
Fault gouge	AS5	NE-4	065/70S	2
	AS14	NE-4	c.039/73S	10
<b>'Veins' &amp; cataclasite</b>				
Thin (c.5mm) epidote	Vein 1 (AS1)	Info Gallery	017/80W	11
"	Vein 2 (AS3)	950m fault	014/88	2
"	Vein 3 (AS4)	950m fault	016/49	2
"	Vein 4 (AS7)	EW-7, Fault 2	178/85W	4
Thick (c.10cm) epidote	Vein 5 (AS24)	1130m fault	022/80W	6
"	(AS25)	1130m fault	022/80W	8
"	(AS26)	1130m fault	022/80W	6
"	Vein 6 (ASV)	Geochem Lab	013/vert	17
"	(AS29)	Geochem Lab	013/vert	10
Epidote vein breccia	AS8	EW-7, Fault 2	178/85W	3
Chlorite vein breccia	AS9	EW-7, Fault 1	060/70E	4
Carbonate vein	AS27	1103m fault	137/75E	8
<b>Hostrocks</b>				
Grey granite	AS12	Tunnel mouth	-	9
"	AS13	Tunnel mouth	-	9
Granite	AS11	EW-7	-	6
Metabasite	AS10	EW-7	-	6
Microgranite	AS28	Pump station	c.068/30N	6
Aplite dyke	AS2	Info Gallery	085/75N	6
Red fine-grained granite	AS20	NE-3	-	6
Red protomylonitic granite	AS21	EW-3	-	6
	AS22	EW-3	-	6
	AS23	EW-3	-	5

One of the important rock units sampled is the set of epidote veins, breccia and cataclasites, located along steep, mainly NNE-striking faults (Sections 3 and 4). These veins have been numbered 1 to 5, for ease of reference in the palaeomagnetic study (Table 5-1). Four of the veins are thin, typically about 5mm, while the other two are thicker, about 10-20 cm. Veins 1 and 4 were sampled by drilling a set of closely-parallel drill cores perpendicular to the plane of the vein. In the laboratory, the cores were sliced to provide thin oriented disks of vein material and all traces of country rock were removed from the disks, by careful grinding, using a lapping wheel. Sets of four or more individual disks were then combined to form composite cylindrical palaeomagnetic samples, approximately 25mm in diameter and 20mm in length.

For epidote Veins 2 and 3 and the carbonate vein at Site AS27, the vein material was removed from tunnel-wall outcrop as a thin 'sheet', typical dimensions of individual pieces being about 10cm x 10cm x 5mm. The strike and dip of the sheet sample was measured using a conventional compass-clinometer. In the laboratory, each sheet was cut into 20mm x 20mm square pieces, with the orientation of each piece being carefully preserved. The pieces were then combined together, typically four at a time, to form one or more approximately cube-shaped samples per sheet.

The thicker epidote-rich Veins 5 and 6 were sampled by taking several separately-oriented 'hand samples', each with typical dimensions of 10-20cm. Several separate palaeomagnetic specimens were then cut from each of these in the laboratory.

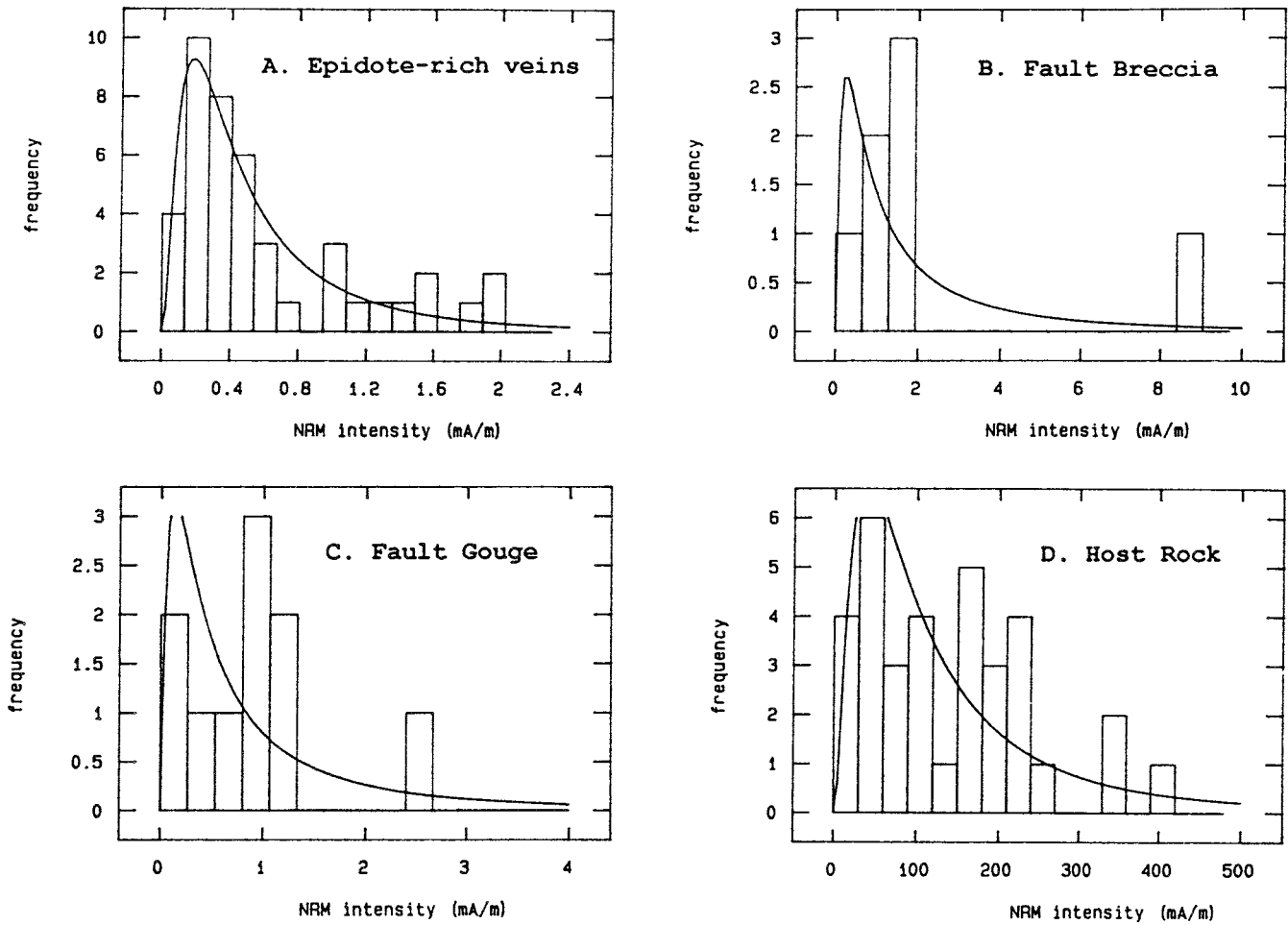
For the soft clay-rich fault gouge from Fracture Zone NE-4 (Sites AS5 & 14; see Section 3.5 and 4.5), cube-shaped samples were carefully trimmed from the *in situ* gouge veins, using a sharp knife. An open-ended non-magnetic plastic sample box, of dimension 20mm x 20mm x 20mm was then fitted over the gouge sample (Fig 3-5b). The orientation of the upper surface of the box was carefully measured using a clinometer and magnetic compass. The palaeomagnetic sample, enclosed within the box, was then removed from the exposure and the lid was placed on the box and sealed, to prevent the sample from drying out.

It is important to be able to compare the direction of characteristic magnetisation of the faultrocks with that of the surrounding 'hostrocks', in order to investigate the presence of any regional magnetic overprint. To facilitate this in the present study, the 'hostrocks' (including protomylonite) were sampled at several sites within the tunnel and a further two sites at the surface, near the tunnel entrance.

### 5.3 MAGNETIC INTENSITY

The distributions of magnetic intensity values for the different rock types sampled are illustrated in Fig. 5-1. Weakest values, mostly in the range 0.1 to 0.5 milliAmperes per metre (mA/m), were observed in the epidote vein samples. The values for the vein-breccia and gouge samples were somewhat higher, typically about 1.0mA/m, while the highest values, typically 1-200mA/m were observed in the country rocks. These differences in magnetic intensity reflect differences in the composition and/or concentration of magnetic mineral particles in the different rock types.





**Figure 5-1** Histograms showing distributions of natural remanent magnetisation (NRM) intensity values for each of the principal rock types studied.

#### 5.4 DEMAGNETISATION ANALYSES AND MAGNETIC STABILITY

All palaeomagnetic measurements in this study were carried out on a high-sensitivity 3-axis cryogenic magnetometer system, manufactured by 2-G Enterprises Inc. Each palaeomagnetic specimen was subjected to incremental demagnetisation, in order to explore its magnetic stability and to isolate the different components of magnetisation carried. Both alternating field (AF) and thermal demagnetisation were used. The AF demagnetisation was carried out in a 3-axis stationary-sample demagnetiser coupled to the 2-G magnetometer system. The thermal demagnetisation was performed with a Schonstedt TSD-1 demagnetiser.

A set of representative samples from each principal lithology was first analyzed by the AF method and a second set by the thermal method. The method selected for the remaining samples of each lithology depended upon the responses of the pilot samples to the two methods and also on the physical state of the specimens (the soft, clay-rich gouge samples were generally unsuitable for thermal treatment). Of the 156 specimens available for the study, 63 were analyzed by alternating field (AF) treatment and the other 93 by thermal treatment.

Examples of the results of these analyses are shown in Figs 5-2 to 5-4. For each sample illustrated, the change in direction of remanent magnetisation after each demagnetisation step is shown on a stereographic projection (the initial direction is shown by a circle with a slash) and the corresponding changes in the normalised magnetic intensity are shown on the graph beneath. The results are also shown in the form of vector end point (VEP) diagrams at the right hand side of each figure. In the latter diagrams the vectors are projected onto a horizontal and a vertical plane. Vectors removed during sets of successive demagnetising steps are identified from linear segments on the VEP diagrams.

##### 5.4.1 Epidote veins/breccia, carbonate vein and aplite dyke

In most cases, the responses of vein samples to AF and thermal demagnetisation were very similar. Figure 5-2A shows an example of a typical response to AF treatment (specimen AS1.1 from Vein 1). After removal of a very soft component during the first one or two demagnetising steps, the points on the VEP diagram fall on two successive approximately linear segments, defining two significant components of magnetisation. The first is removed during treatment up to about 7.5 milliTesla (mT), leaving a second, more stable component, which is progressively removed during further treatment up to 35mT. The linear segments defining the latter component

on the VEP diagrams are directed approximately through the origin, confirming that no further component exists in this sample.

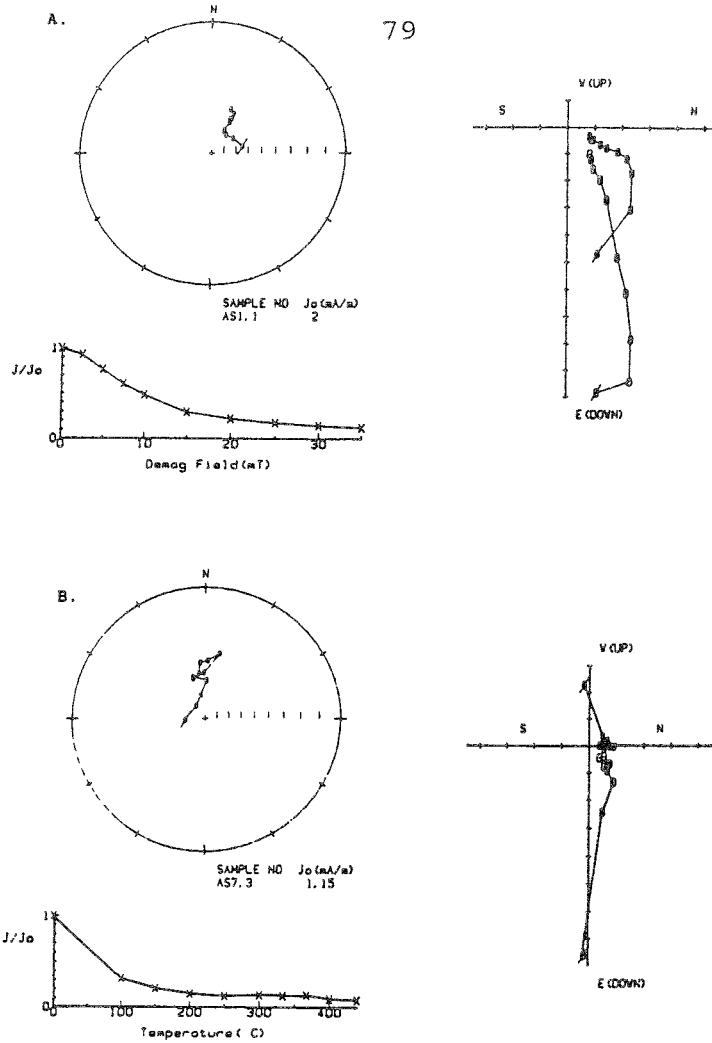
Figures 5-2B and C illustrate the response to thermal demagnetisation of samples from the thin epidote-rich veins. The directional changes shown on the stereographic projection are broadly similar to those accompanying AF treatment of sample AS1.1 (Fig 5-2A). In both cases the vectors move towards an end point with a north to north-easterly declination and positive inclination, which is moderately steep in specimen AS7.3 and shallower in AS1.9. The magnetic intensity drops off rapidly during thermal treatment up to 150°C, as the lower stability component is removed. During treatment at higher temperatures, small random directional changes occur for AS7.3, but the vector retains a northerly, moderately-steep positive inclination. Thus, the stronger, but lower-stability component is carried by grains with blocking temperature up to about 150°C and the weaker, but higher-stability component by grains with blocking temperatures above about 200°C.

Of the two thicker epidote-rich veins, Vein 5 showed similar palaeomagnetic properties to those of the thin veins, while Vein 6 showed a totally different behaviour. In this vein, and also in the aplite dyke, thermal demagnetisation isolated a stable magnetisation with a north to northwesterly declination and moderately-steep negative inclination (Fig 5-2D).

The epidotic breccias showed similar characteristics to those of the thin epidote-rich veins (Figs 5-2E & F).

#### 5.4.2 Fault gouge

The responses of samples of fault gouge, to AF and thermal demagnetisation respectively, are illustrated in Figs 5-3A & B. In most cases, AF treatment above about 20mT isolated a high stability component with a northeasterly declination and moderate to steep positive inclination. Because of the nature of the soft clay-rich gouge, it was difficult to apply the thermal demagnetisation method to these samples (which were enclosed in 8cm<sup>3</sup> plastic boxes). However, five samples were successfully treated by this method, the sample being removed from its holder during heating, and then replaced in it for magnetic measurement. The behaviour of these samples generally became erratic at temperatures above about 300°C, but the stable component defined before this erratic behaviour set in (Fig 5-3B) had a broadly similar direction to that defined by AF treatment.



**Figure 5-2** Examples of response to alternating field and thermal demagnetisation of typical epidote-rich vein (A-D) and breccia specimens (E-F). For each specimen, the response is shown on two different types of plots. On the left side, the change in direction of magnetisation after each demagnetisation step is shown on a stereographic projection. The initial (NRM) direction is indicated by a slash through the corresponding point. Solid circles represent points in the lower hemisphere (ie vectors with positive inclinations) and open circles points in the upper hemisphere (ie vectors with negative inclinations). Beneath the stereographic projection is shown a plot of the intensity of magnetisation,  $J$ , after each treatment step, normalised by the initial value,  $J_0$ . The value of  $J_0$  is given in units of mA/m. The diagram at the right hand side displays the demagnetisation data on a Vector End Point (VEP) diagram. On this diagram, the tip of the vector after each demagnetisation step is projected on to a horizontal plane (solid symbols) and also on to a vertical plane (open symbols) which is oriented either N-S or E-W. These two planes have a common horizontal axis (either N-S or E-W). Lines are drawn through consecutive points and the initial (NRM) vectors are indicated by slashes through the symbols.

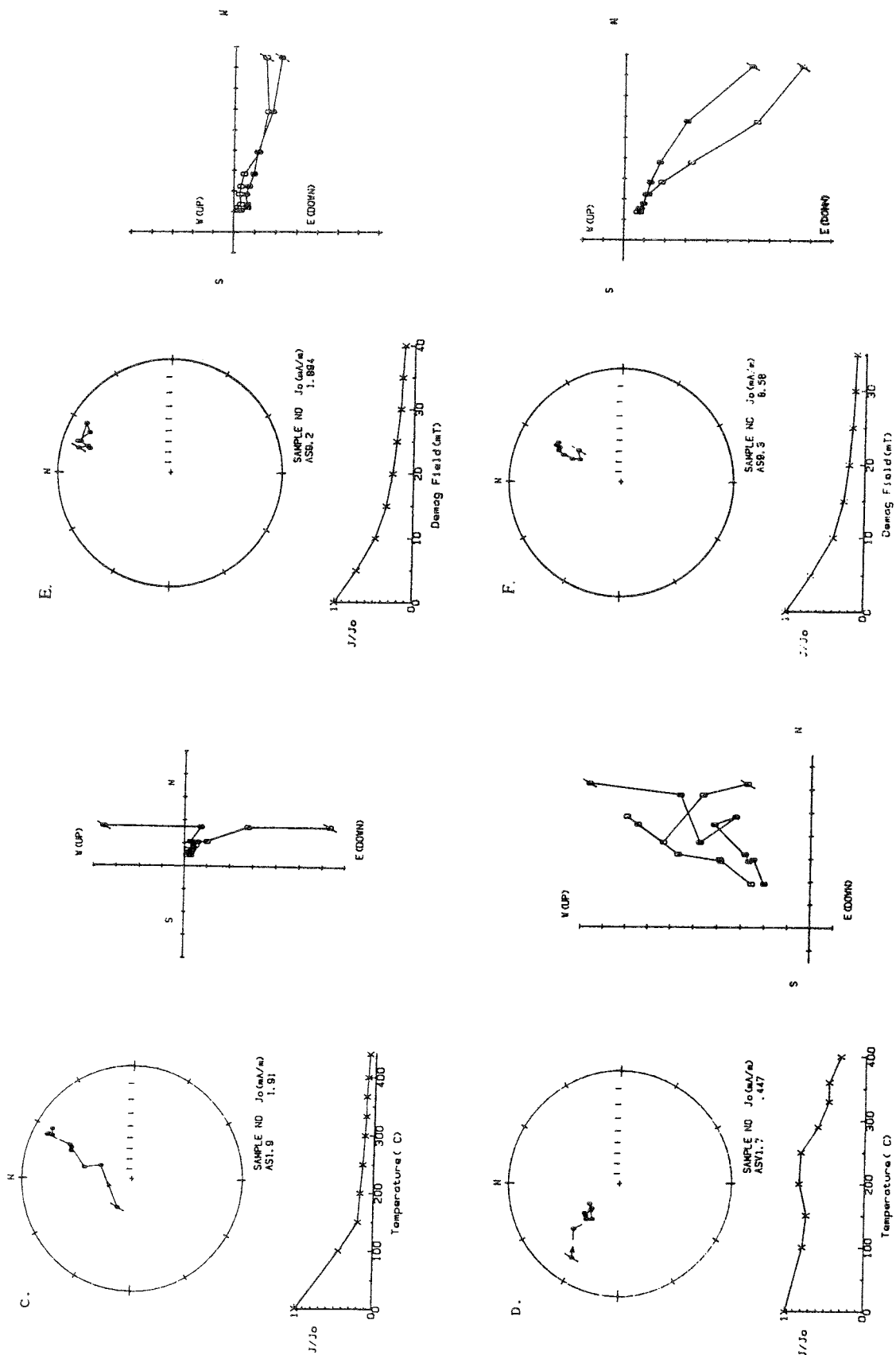
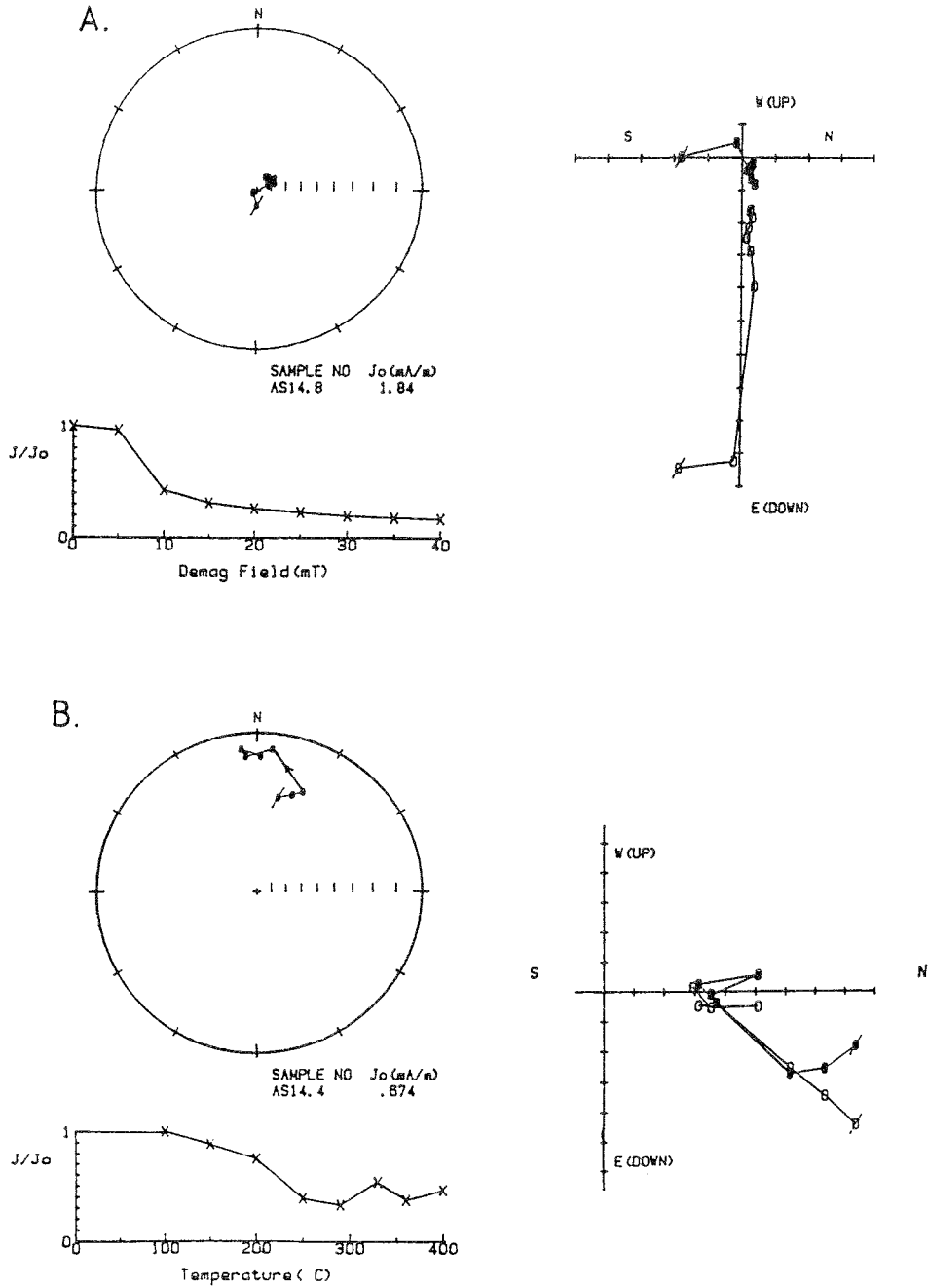


Figure 5-2 (cont)



**Figure 5-3** Examples of response to alternating field and thermal demagnetisation of typical specimens of fault gouge. Symbols and conventions as in Fig 5-2.

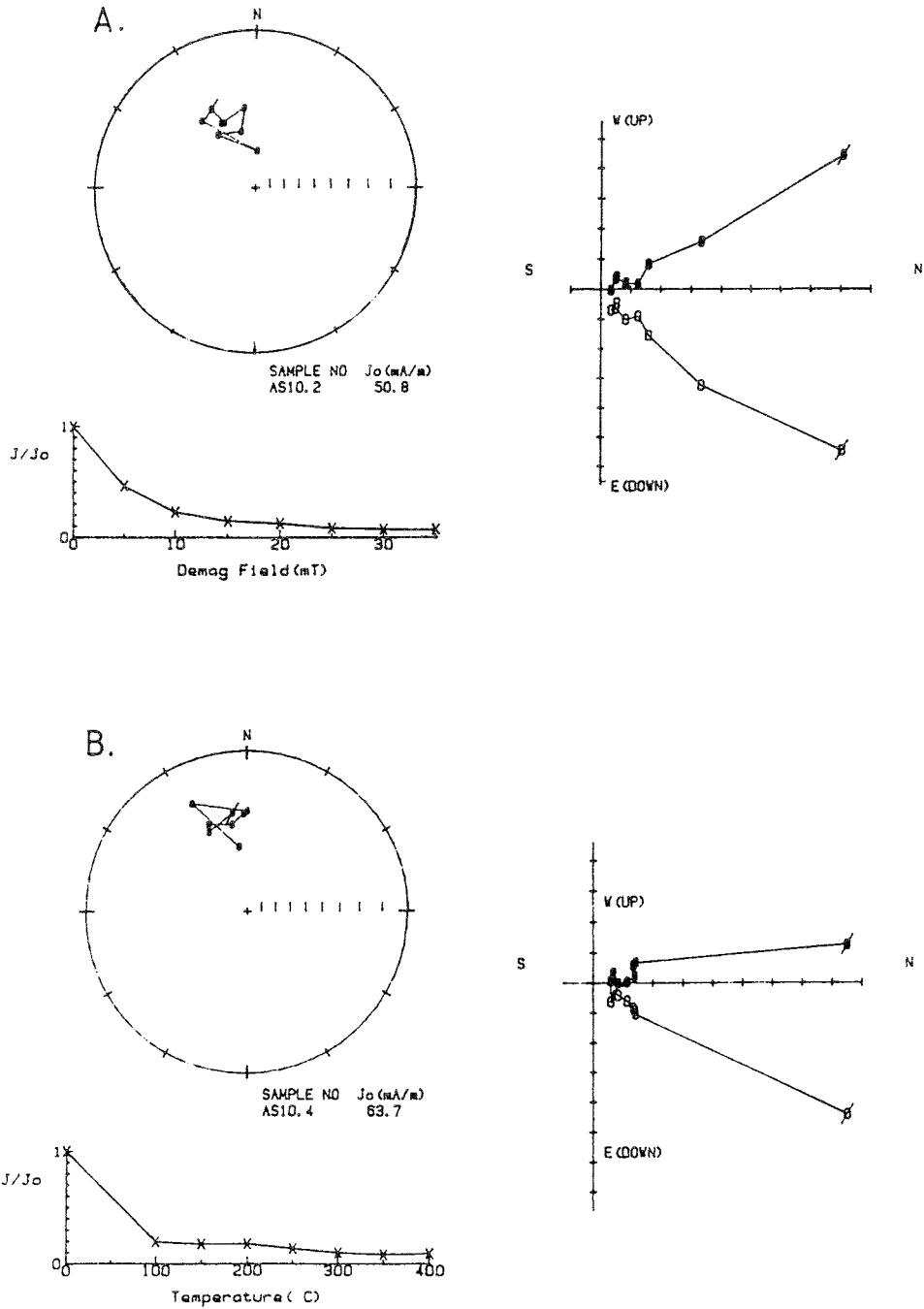


Figure 5-4 Examples of response to alternating field and thermal demagnetisation of typical specimens of hostrock. Symbols and conventions as in Fig 5-2.

### 5.4.3 Hostrock

Most hostrock granite samples carried a strong low-stability component of magnetisation which was removed during the first one or two demagnetising steps (Fig 5-4). At higher treatment levels, both AF and thermal, the vectors tended to retain a northwesterly declination and a moderately steep positive inclination. However, the majority of the hostrock samples, including the red fine-grained and protomylonitic granites (from Sites AS20 and AS21-23, fracture zones NE-3 and EW-3, respectively), are characterised by low magnetic stability and the vectors are imprecisely defined. This is due to their relatively coarse grainsize.

## 5.5 COMPONENTS OF MAGNETISATION IN EACH ROCK TYPE

### 5.5.1 Epidote veins/breccia, carbonate vein and aplite dyke

Approximately equal numbers of specimens from the epidote-rich Veins 1-5 and one sampling site (AS29) in Vein 6 were subjected to demagnetisation analysis by the AF and thermal methods respectively. All 24 specimens from the other site in Vein 6 (ASV) and all 4 from the aplite dyke were subjected to thermal demagnetisation. All 7 specimens from the epidote breccias were analyzed by the AF method. Two principal components of magnetisation were identified in most of the specimens. These components are listed in Table 5-2. The lower stability components were generally removed by AF demagnetisation in applied fields of less than 25mT, or thermal demagnetisation at temperatures less than 250°C. The higher stability components were isolated by AF treatment up to 35 or 40mT or thermal treatment up to 400 or 440°C.

#### (a) Low stability magnetic component

The directions of the lower stability vectors defined from all vein and breccia samples are shown plotted on a stereographic projection in Fig 5-5A. These vectors show significant dispersion, but the main cluster encompasses the recent geomagnetic field vector at the sampling site (calculated on the basis of an axial geocentric dipole field model and indicated by the asterisk in Fig 5-5A). The overall mean magnetic vector for the vein samples (square in Fig 5-5A) is not distinguishable statistically from the recent geomagnetic field vector at the 95% confidence level. Consequently, the low-stability component of remanent magnetization is believed to represent a viscous magnetic overprint in the direction of the recent geomagnetic field.



Table 5-2. Palaeomagnetic data

1	2	3	4	5	6	8	9	10	11
Site/Sample No	Type of sample	Demag Range mT/°C	Low Stab. Component (LSC)			Demag.range mT/°C	Charact.Mag.Dirc. (CMD)		
			Dec	Inc	Rc/ $\alpha_{95}$		Dec	Inc	Rc/ $\alpha_{95}$
Site 1	"Thin" Epidote Vein 1 (-0.5-1cm thick, exposed in visitor's gallery)								
AS1.1	Composite cylinder	2.5-8mT	27.9	75.6	.98/.99	20-35	23.0	55.5	.99/.99
1.2		15-25	352.4	53.8	.92/.99	30-40	12.8	46.9	2.8
1.3	"	7.5-20	28.6	-17.2*	.99/.99	25-35	26.9	-30.3*	.97/.99
1.4	"	10-25	41.6	68.5	.97/.98	25-40	43.7	41.0	.98/.95
1.5	"	100-200°C	29.6	57.2	.95/1.0	250-400	55.2	16.3	13.4
1.6	"	100-200	32.2	64.8	.98/.94	300-400	45.4	10.2	15.1
1.7	"	100-250	21.3	72.9	.98/.98	300-440	30.1	12.0	10.9
1.8	"	100-200	331.3	71.5	.93/.93	250-400	25.0	47.0	12.9
1.9	"	100-200	333.0	70.0	.80/.98	333-440	23.1	9.3	2.6
1.10	"	100-200	354.5	69.3	.71/.98	200-400	27.3	17.2	11.9
1.11	"	100-200	349.7	73.5	.83/.98	360-440	25.4	15.8	.97/.94
Site 3	"Thin" Ep Vein 2 (-0.5-1cm thick, exp. tunnel face)								
AS3.1	Composite cube	2.5-7.5	224.4	-18.6 $\sigma$ *	.99/1.0	25-35	232.7	-14.0 $\sigma$	.90/.70
3.2		10-25	228.5	57.4*	.93/.96				
Site 4	"Thin" Epidote Vein 3 (exp. tunnel face)								
AS4.1	Composite cube	10-25	37.3	59.3	.92/.99	25-35	6.9	54.2	6.9
4.2		10-20	350.2	56.4	.71/.95	20-35	323.2	33.7	5.5
Site 7	"Thin" Epidote Vein 4 (E wall of side tunnel)								
AS7.1	Composite samples	2.5-15	328.6	53.6	1.0/.99	15-35	15.8	68.4	.71/.86
7.2		2.5-7.5	256.7	56.6	.94/.69	20-35	310.6	60.4	5.0
7.3	"	150-250	30.4	55.7	.86/.99	333-440	2.2	43.1	9.5
7.4	"	100-250	10.6	77.3	.18/.75	300-440	353.9	46.9	12.0
Site 24	"Thick" Epidote Vein 5 (~20cm thick follows minor NNE fault)								
AS24.1	Cut cube	100-320	4.3	50.9	10.2	360-510	33.8	30.7	21.2
24.2	"	100-180	54.4	56.4	.98/.95	320-460	28.2	39.0	22.9
24.3	"	100-180	34.6	58.0	.93/1.0	320-510	55.1	25.4	21.5
24.4.1	"					15-35	6.6	65.5	9.0
24.4.2	"	15-25	19.4	69.3	.80/.76	20-35	27.0	47.9	9.1
24.2.1	"	10-25	19.2	67.8	.83/.94	20-35	26.1	50.2	9.1
Site 25	"Thick" Epidote Vein 5								
AS25.2.1	Cut cube	5-20	347.7	73.0	.87/.99	25-35	4.1	54.5	.80/.99
25.2.2	"	140-240	321.4	62.8	.96/.73	280-510	61.6	72.9	10.8
25.2.3	"					280-510	28.0	59.0	14.1
25.2.4	"					360-510	66.1	64.9	5.5
AS25.2.5	"	HRM-140	7.4	70.5	.97/.98	460-510	37.5	51.5	.98/.89

Site/Sample No	Type of sample	Demag Range mT/°C	Low Stab. Component (LSC)			Demag. range mT/°C	Charact. Mag. Dir. (CMD)		
			Dec	Inc	Rc/a <sub>95</sub>		Dec	Inc	Rc/a <sub>95</sub>
25.2.6	"					25-35	98.3	70.4	.88/.87
25.2.7	"					20-35	34.8	67.1	.98/.99
25.1.1	"	100-180	303.8	58.7	.99/.98	410-510	3.0	6.7	.80/.62
<b>Site 26</b>	<b>*Thick* Epidote Vein 5</b>								
AS26.1.1	Cut cube	100-240	357.5	51.2	.31/.89	280-460	27.7	25.0	8.3
26.1.2	"	10-20	336.3	54.7	1.0/.99	25-35	1.3	35.2	2.9
26.1.3	"					25-35	1.3	31.8	.84/.99
26.2.1	"					280-410	55.0	36.1	17.6
26.2.2	"	5-15	341.6	54.5	.99/.99	30-35	9.4	43.3	1.0/1.0
26.3	"	100-180	10.8	54.6	1.0/.90	360-460	176.2	-36.4σ	22.2
<b>Site 27</b>	<b>Thin carbonate vein</b>								
AS27.1	composite cube					10-35	178.7	-30.6	15.2
27.2						140-410	195.3	-42.6	9.8
27.3.1	"					20-35	206.6	-43.7	6.6
27.3.2	"					140-320	182.7	-21.4	17.2
27.4.1	"					320-410	207.3	-5.1	.96/.43
27.4.2	"					20-30	208.8	-54.4	24.8
27.5.1	"					410-510	220.9	18.8*	.99/.96
27.5.2	"					25-35	187.5	-3.3	27.6
<b>AS V</b>	<b>*Thick* Epidote Vein 6, (near Geochemistry Lab)</b>								
ASV1.1	Cut cube					200-400	312.5	-34.5	10.6
1.2		100-200	327.2	41.9	.97/.97	290-400	284.5	-51.5*	.88/.96
1.3	"	NRH-150	34.0	35.2	.59/.86	250-400	250.5	-41.8*	15.7
1.4	"	100-250	318.3	59.8	.88/.85	290-400	325.3	-26.4	16.8
1.5	"	100-250	321.0	32.3	.98/.94	360-400	354.1	-4.7	.83/.71
1.6	"					330-400	314.3	-47.0	22.2
1.7	"	NRH-150	304.0	34.7	.76/.93	360-400	319.1	-45.1	.98/1.0
1.8	"					290-400	308.3	-21.4	.97/.77
1.9	"	200-300	314.5	63.6	.98/.50	333-400	220.9	-55.5*	24.9
1.10	"	150-250	17.9	57.5	.96/.98	333-400	340.3	-51.9	9.9
1.11	"					333-400	355.6	-65.3	19.5
1.12	"	100-250	10.7	44.0	.13/.86	300-400	309.5	5.9	13.8
1.13	"	100-250	33.4	20.7*	.70/.26	333-400	7.9	-45.6	7.5
1.14	"					333-400	351.7	-64.5	5.8
2.1	"	100-200	7.1	78.6	.99/.50	250-360	95.2	9.4σ	15.0
2.2	"	150-250	171.9	44.8*	.80/.95	250-360	328.3	-32.9	26.0
2.3	"	150-250	323.0	55.9	.74/.99	290-400	32.1	17.6*	7.9
ASV2.4	"	100-200	14.4	68.3	.41/.98	290-400	111.5	47.3σ	19.2

Site/Sample No	Type of sample	Demag Range mT/°C	Low Stab. Component (LSC)			Demag. range mT/°C	Charact. Mag. Dirc. (CMD)		
			Dec	Inc	Rc/α <sub>95</sub>		Dec	Inc	Rc/α <sub>95</sub>
2.5	"	NRM-150	59.3	55.3	.99/.99	290-400	55.8	-41.2*	7.9
2.6	"	150-250	332.5	60.5	.62/.35	290-400	58.5	-5.3*	9.1
2.7	"	100-200	208.0	63.8*	.99/.69	290-400	25.4	-26.5	12.8
2.8	"					290-400	354.6	-35.4	6.6
2.9	"					300-400	356.6	-62.6	27.9
2.10	"	100-200	312.4	10.5*	.93/.67	300-400	32.8	-52.9	27.3
<b>Site 29</b>	<b>"Thick" Epidote Vein 6</b>								
29.1+3.1	Cut cube	100-180	305.4	57.2	.86/.91	180-360	351.4	-19.5	14.5
29.1+3.2	"					240-460	356.7	-56.7	7.0
29.1+3.3	"					30-35	345.2	-26.2	.94/.98
29.1+3.4	"					20-35	325.9	31.0*	2.2
29.1+3.5	"					20-35	358.7	-3.6	6.8
29.1+3.6	"					30-35	315.8	32.5*	.99/.99
29.1+3.7	"					20-35	357.6	22.3*	10.3
29.2.1	"					240-410	16.3	-42.9	38.8
29.2.2	"					25-35	308.7	22.1*	.99/.99
29.2.3	"					10-35	38.8	49.6*	11.0
<b>Site 2</b>	<b>Aplite Dyke.</b>								
AS2.1	Core	5-15	326.2	61.8	.99/1.0	15-35	0.3	-34.7	32.4
2.2	"	10-20	7.2	21.1*	.50/.99	15-40	332.2	-30.2	20.7
2.3	"	5-15	3.4	59.4	.26/.97	15-30	2.8	-16.0	21.0
2.5	"	5-15	42.1	69.8	.99/.99	35-40	352.1	21.0*	
<b>Site 5</b>	<b>Fault gouge, two collections (AS5 &amp; 14).</b>								
AS5.1	Cut cube	5-15	169.8	-53.3	.47/.86	20-35	220.2	-22.5*	22.0
5.2		5-10	356.4	35.1	1.0/.99	20-30	5.9	45.9	16.7
<b>Site 14</b>									
14.1	"	100-200	132.0	67.5	.99/.91	290-360	337.1	46.6	12.0
14.2	"	150-250	131.0	63.7	.92/.96	250-360	267.8	78.0	13.3
14.3	"					300-360	54.9	42.3	.99/.99
14.4	"	100-200	337.7	37.9	.92/.99	250-360	359.0	7.1	6.5
14.5	"	150-250	190.9	-43.2*	37.2				
14.6	"								
14.7	"	100-250	315.0	61.7	.61/.48	290-360	351.3	14.0	.93/.96
14.8	"	10-20	61.6	71.8	.99/.97	30-40	38.8	77.8	.77/.99
14.9	"					30-35	16.1	46.0	.57/.98
14.10	"	2.5-10	319.8	79.4	.77/.70	30-50	59.0	74.0	6.8
<b>Site 8</b>	<b>Fault breccia.</b>								
AS8.1	Core	5-15	62.7	60.5	.91/.90	20-35	314.3	83.3	19.1

Site/Sample No	Type of sample	Demag Range mT/°C	Low Stab. Component (LSC)			Demag. range mT/°C	Charact. Mag. Dirc. (CMD)		
			Dec	Inc	Rc/ $\alpha_{95}$		Dec	Inc	Rc/ $\alpha_{95}$
8.2	"	0-15	108.3	50.8	.88/.97	20-35	241.7	68.4	19.3
8.3	"					15-30	131.1	86.3	14.2
Site 9	Fault Breccia.								
AS9.1	Core	5-25	14.3	47.9	.98/.99	20-25	315.6	15.4	8.4
9.2	"	5-20	16.2	19.3	.99/.97	20-40	16.9	9.3	5.2
9.3	"	5-20	29.1	52.0	.99/.99	20-35	23.3	24.1	2.8
9.4	"	5-15	37.8†	40.1	1.0/.99	25-35	33.1	46.6	5.3
Site 10	Host rock, Granite.								
AS10.1	Core	NRM-15	22.1	49.2*	.56/.74	25-35	243.2	28.1*	33.4
10.2	"	5-15	329.4	42.8	.94/.99	20-35	330.1	49.4	19.8
10.3	"	5-15	31.5	39.5	1.0/1.0	15-40	2.7	30.7	17.6
10.4	"	150-250	306.7	35.6*	.65/.99	250-400	345.5	29.9	19.3
10.5	"	5-15	76.0	5.7*	.96/.98	20-30	353.3	-6.5*	28.0
10.6	"	200-300	35.5	59.1	.76/.97				
Site 11	Host rock, Granite								
AS11.1	Core					10-30	229.2	3.9*	.61/.10*
11.2	"	5-15	34.0	31.0	.99/.99	20-40	315.7	38.4	14.0
11.3	"								
11.4	"					200-350	356.7	24.9	15.7
11.5	"	15-35	38.8	66.2	14.0				
11.6	"	5-20	17.5	32.7	.99/.91	30-40	294.5	13.5	32.2
Site 12	Host rock, Granite								
AS12.1	Core	150-250	41.5	62.4	7.3	300-350	353.9	26.2	.41/.82
12.2	"	150-300	63.2	35.3	.72/.76	>300	Trend to shallow -Inc.		
12.3	"					200-400	306.1	31.7	7.3
12.4	"	200-350	48.4	50.8*	.63/.98		Trend to shallow -Inc.		
12.5	"	150-200	209.7	59.5*	.95/.89	250-400	351.7	42.1	20.6
12.6	"	100-200	232.9	49.2*	.93/.99	350-400	293.3	35.9	.82/.87
12.7	"	100-200	59.1	52.8	.90/.99	350-400	342.6	44.7	.55/.99
12.8	"	100-200	70.8	56.3	.98/.97	350-400	43.2	15.3*	.63/.79
12.9	"					250-400	304.5	33.1	18.8
Site 13	Host rock, Granite								
AS13.1	Core	100-200	9.8	46.5	.97/.99	250-400	324.0	16.9	12.9
13.2	"	100-200	320.8	42.7*	.44/.95	300-450	306.4	-3.9	18.5
13.3	"	100-200	354.3	25.6	.76/.85	400-450	304.0	-16.8	.99/.99
13.4	"					400-450	352.1	0.7	12.7"
13.5	"					250-400	2.7	7.7	17.6
13.6	"	100-200	358.2	46.0*	.05/.86	200-350	346.7	-3.7	16.9

Site/Sample No	Type of sample	Demag Range mT/°C	Low Stab. Component (LSC)			Demag.range mT/°C	Charact.Mag.Dirc. (CMD)		
			Dec	Inc	Rc/ $\alpha_{95}$		Dec	Inc	Rc/ $\alpha_{95}$
13.7	"	100-200	15.8	42.4	.86/.67	300-400	325.6	5.1	18.2
13.8	"					250-400	4.1	6.7	16.2
13.9	"					250-400	29.9	0.5	6.3"
<b>Site 28</b>	<b>Micro-granite intrusion at 1360m.</b>								
AS28.1	Core								
28.2	"	5-20	338.9	58.0*	.55/.98	20-35	126.0	2.0*	
28.3	"	NRM-10	21.7	77.0	.73/.99	10-20	117.3	-43.8	29.6
28.4	"					360-510	310.5	53.3	12.4
28.5	"	NRM-140	339.5	63.1	.99/1.0	240-460	312.2	25.6	13.9
28.6	"					240-360	9.3	55.2	12.6
<b>Site 20</b>	<b>Reddened Granite, in trench at 956m.</b>								
AS20.1	Core	NRM-10	300.1	67.6	.87/.90	15-30	14.2	65.0	14.6
20.2	"					5-35	327.7	25.8	12.9
20.3	"	100-180	334.5	66.1	.92/.95	250-460	erratic		
20.4	"	erratic					trending to reverse		
20.5	"	140-240	46.8	55.7	1.0/.69	240-320	318.7	-6.1*	31.2
20.6	"	100-180	58.9	60.8	.96/.98		trending to reverse		
<b>Site 21</b>	<b>Fine reddened Granite, in trench, 1417m.</b>								
AS21.1	Core					25-35	316.6	2.9	6.3
21.2	"					10-35	181.0	52.1*	7.1
21.3	"	100-240	303.5	50.9	.95/.91	240-460	19.8	-26.8*	8.8
21.4	"					240-510	292.7	32.8	6.8
21.5	"					280-510	253.3	-51.8	12.5
21.6	"	100-180	342.9	69.0	.74/.99	360-510	52.5	19.3	.96/.89
<b>Site 22</b>	<b>Fine reddened Granite at 1418m.</b>								
AS22.1	Core					20-30	112.2	-9.4	7.9
22.2	"	5-15	185.2	46.8*	.50/.99	15-35	183.5	14.5	9.2
22.3	"	100-180	178.8	60.7*	.08/.96	240-410	170.1	26.7	7.1
22.4	"	140-240	165.4	25.8*	.60/.69	280-360	146.0	31.0	11.6
22.5	"					240-410	278.5	31.0	7.3
22.6	"					360-460	22.5	-8.0	11.3
<b>Site 23</b>	<b>Fine reddened Granite at 1419m.</b>								
AS23.1	Core					10-35	59.2	44.3	8.0
23.2	"	NRM-20	43.7	66.6	.99/.92	25-35	60.2	41.9	8.9
23.3	"	140-240	36.0	60.1	.99/.85	280-460	34.2	17.6	4.8
23.4	"					410-510	7.3	-3.1	.84/.48
23.5	"					180-460	57.1	30.9	12.4

Note on Table 5-2: The sampling locality is at Lat 58N & Long 16E.

CMD is characteristic magnetisation direction.

\*: does not satisfy reliability criteria or does not form part of main group of vectors. Not included in calculation of mean direction.

δ: vector directions which have been inverted before incorporation into the statistical mean vector. Where there is no entry into the low stability component column, this is because only a single (high stability) component could be identified in these samples.

In 'Demag Range' column, figures <100 refer to AF demagnetisation (mT) and figures >100 to thermal demagnetisation (°C).

In  $Rc/\alpha_{95}$  column, pairs of numbers refer to the regression coefficients for the corresponding linear segments in the horizontal and vertical planes respectively, where the vector is determined from principal component analysis. Single numbers represent the 95% confidence angle ( $\alpha_{95}$ ), where the vector is determined by Fischer statistics.

### (b) High stability magnetic components

The directions of the high magnetic stability vectors identified in the thin epidote-rich Veins 1-5 and the epidote breccia show a broad clustering around a mean direction with a NNE declination and moderate positive inclination (Figs 5-5B & C). The characteristic remanence defined in the carbonate vein at Site AS27 shows a similar axis of magnetisation, but with a reverse polarity (Fig 5-5D). When inverted, the carbonate vein vectors are indistinguishable from the epidote vein and breccia vectors (Fig 5-5E). The overall mean is referred to as the 'Group A' direction. Within the 95% confidence limits, this direction is distinct from that of the recent geomagnetic field in the Äspö region.

Although the majority of the epidote vein specimens carry a 'normal' polarity Group A magnetisation, the characteristic remanence of the single specimen from thin Vein 2 (AS3.1) and one specimen from thick Vein 5 (AS26.3) is 'reverse' polarity (Table 5-2). This indicates that emplacement and/or magnetisation of these veins spanned at least one reversal of the geomagnetic field, so that the magnetization interval represented by the mean vector will be in the order of  $10^5$  years or more (eg. Hailwood 1989). Consequently, short-term secular variation of the field is likely to have been averaged out in the overall mean direction for the Group A vectors.

The high stability components of magnetisation identified in the specimens from the thick epidote-rich Vein 6 (Sites ASV & AS29) are characterised by a general NNW declination and a moderate to steep negative inclination (circles and diamonds in Fig 5-5E). The high stability vectors from the aplite dyke (Site AS2) show broadly similar directions (triangles in Fig 5E). The overall mean is called the 'Group B' direction. These results suggest that the ages of epidote Vein 6 and the aplite dyke may be similar, even though their strikes are orthogonal.

The clear difference between the high stability vectors defined for epidote Veins 1-5 (Group A) and Vein 6 (Group B), indicates that these two sets of veins are likely to have significantly different ages, even though their strikes are similar.

### 5.5.2 Fault gouge

#### (a) Low stability magnetic component

As with the epidote veins/breccia, carbonate vein and the aplite dyke discussed above, the magnetic components removed during demagnetisation of the gouge samples in relatively low demagnetising fields or at low temperature levels show a broad cluster in the general vicinity of the recent geomagnetic field direction (Fig 5-6A). The mean low-stability vector does not differ significantly from the recent geomagnetic field vector at the 95% confidence level. It is concluded that the lower stability component of magnetisation carried by the fault gouge represents an overprint in the recent geomagnetic field.

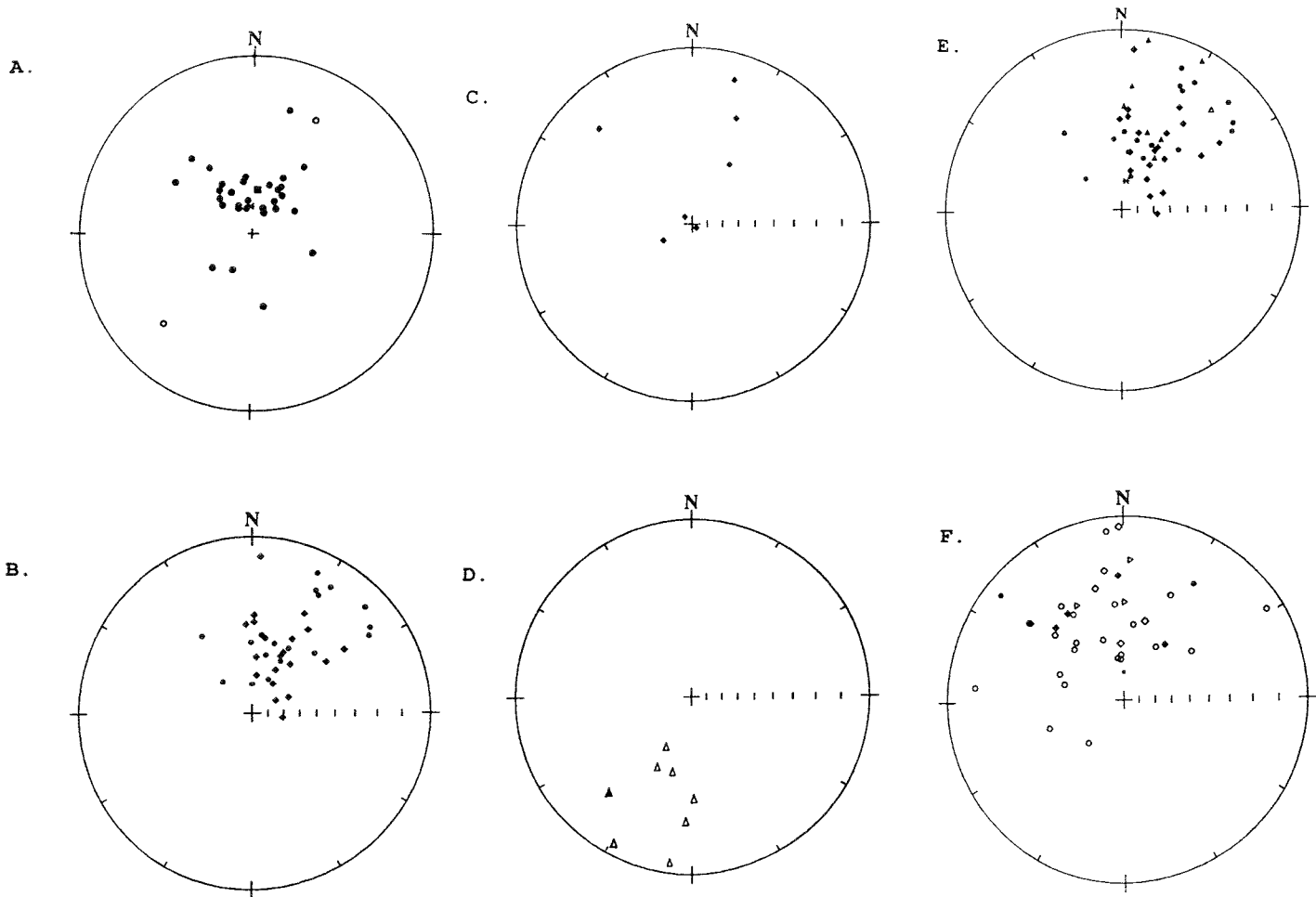
#### (b) High stability magnetic component

The characteristic magnetisation vectors are loosely scattered around a mean direction which is broadly similar to the Group A magnetisation discussed above (Fig 5-6B). The magnetisation of one gouge specimen (AS5.1) is reversed with respect to the other vectors (Table 5-2), indicating that magnetisation of the gouge was probably a prolonged process, spanning at least one reversal of the geomagnetic field. (This specimen was collected from the tunnel wall rather than the trench through fracture zone NE-3).

### 5.5.3 Hostrock

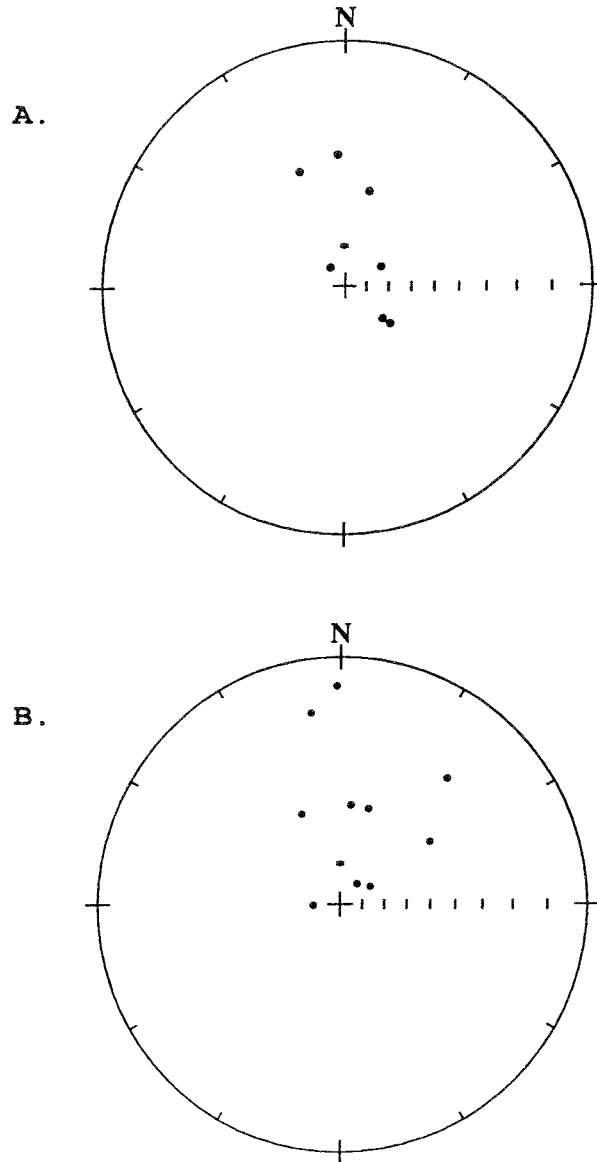
#### (a) Lower stability component

The components of magnetisation identified in the host-rock samples by AF or thermal demagnetisation at relatively low applied fields or temperatures, form a loose cluster of directions, centred in the NE quadrant and with generally shallower inclinations than that of the recent geomagnetic field (Fig 5-7A). The overall mean direction, after exclusion of the two more scattered points, corresponds with the *Group A* direction defined in the epidote veins and breccia and the carbonate vein, and also seen in the gouge.

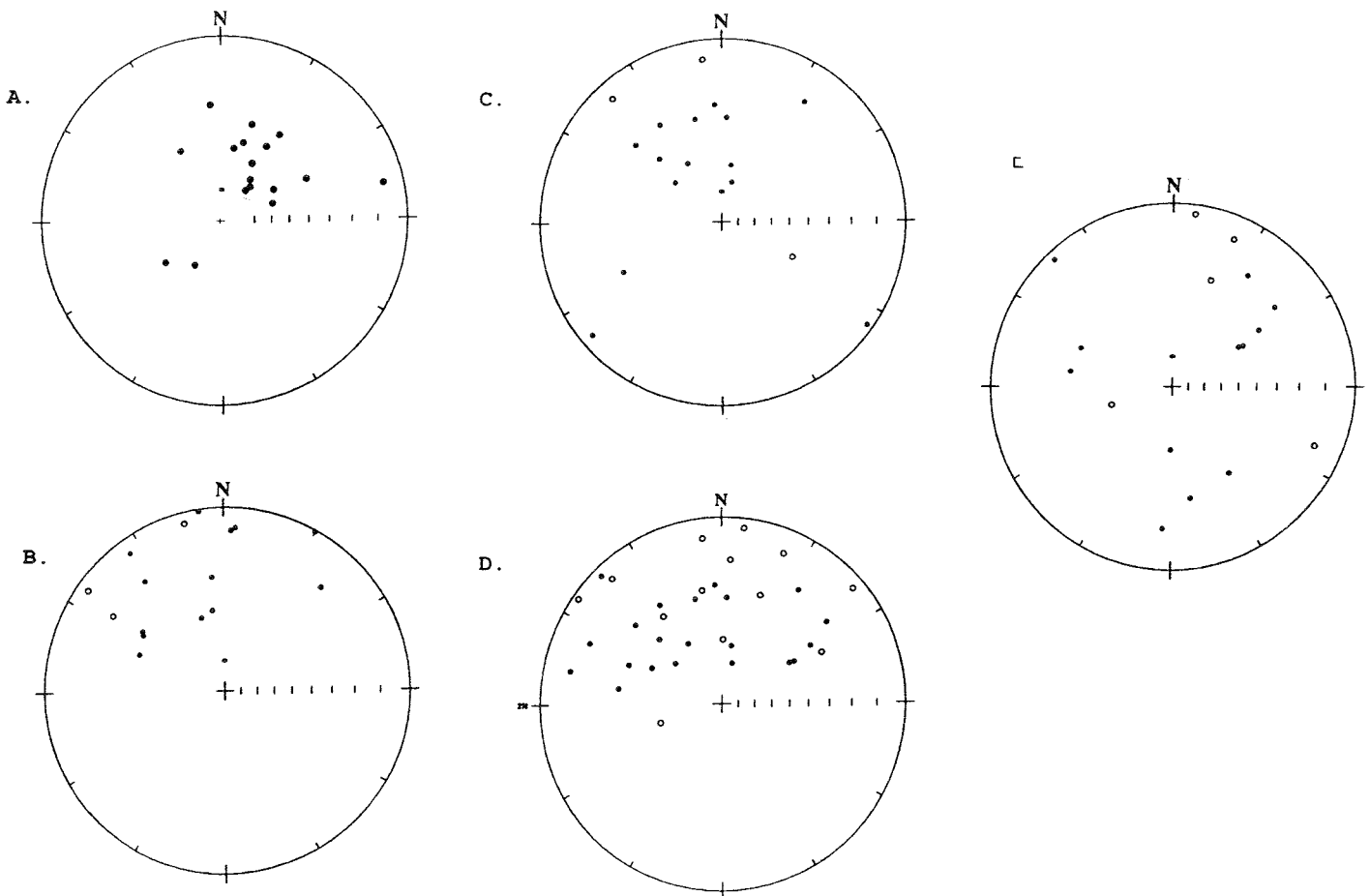


**Figure 5-5** Directions of different components of magnetisation identified in specimens of epidote- and carbonate-rich veins and epidote breccia. Stereographic projection. Solid symbols lower hemisphere, open symbols upper hemisphere. Asterisk is recent geomagnetic field direction. (A) low stability components. Square represents the overall mean direction. (B) high stability components identified in epidote-rich veins (circles, 'thin' Veins 1-4; diamond, 'thick' Vein 5). (C) high stability components in epidote breccia (AS8 & AS9). (D) high stability components in carbonate vein (AS27). (E) epidote-rich veins and breccia and carbonate-rich veins combined, after inversion of carbonate vein vectors. (F) high stability components identified in 'thick' epidote-rich Vein 6 (circles, Site AS-V; diamonds, Site AS29) and aplite dyke (triangles).





**Figure 5-6** Directions of magnetisation identified in specimens of fault gouge. (A) low magnetic stability components, (B) high stability components. Symbols and conventions as in Fig 5-5.



**Figure 5-7** Directions of magnetisation identified in specimens of host rock. **(A)** low magnetic stability components. **(B)** high stability components in fresh grey granite at Sites AS12 & 13. **(C)** high stability components in granite (AS11), metabasite (AS10) and microgranite (AS28). **(D)** high stability components from all host rock specimens combined. In **(D)**, several vectors with southerly declinations, which depart from the main group, have been inverted, on the assumption that their polarity is reverse with respect to that of the other samples. **(E)** Directions of magnetisation identified in specimens of red fine-grained granite (AS20) and red proto-mylonitic granite (AS21-23). Symbols and conventions as in Fig 5-5.

**(b) High stability component**

Because of its coarse grain-size, the magnetic stability of the hostrock is relatively low. Consequently, the high blocking temperature components are often only poorly defined (Table 5-2). Within the relatively wide within-site scatter of vectors, it is not possible to distinguish any clear difference in directions between the 'fresh' grey granite at Sites AS12 & 13 (Fig 5-7B) and the other hostrocks: granite from AS11, metabasite from AS10 or microgranite from AS28 (Fig 5-7C). When magnetic vectors from all hostrock sites are combined together (Fig 5-7D) they form a moderately symmetrical distribution, with a shallow inclination and north to northwesterly declination. The overall mean is termed the 'Group C' direction.

**(c) Protomylonite and fine-grained granite**

Demagnetisation analyses of red fine-grained granite from Fracture Zone NE-3 and red protomylonitic granite from Fracture Zone EW-3 (Sites AS20 and AS21-23 respectively) indicate that the remanent magnetism is generally unstable. Unfortunately, the dispersion of the palaeomagnetic vectors is too great to permit a meaningful interpretation (Fig 5-8). (These vectors are not included in the Group C direction).

**5.6 DISAGGREGATION EXPERIMENTS**

In order to properly interpret palaeomagnetic data from cataclastic faultrocks it is important to establish the nature of the particles carrying the remanent magnetisation (eg. Hailwood et al 1992). For example, the fault gouge comprises a fine-grained clay-rich matrix containing larger clasts (eg. Section 4.5). If the dominant carrier of the remanent magnetism is the fine-grained matrix, then the net magnetisation may well have been acquired at or about the time of faulting by some combination of cataclastic and diagenetic processes. If, however, a significant part of the remanence is carried by the larger clasts whose magnetisation may be inherited from the parent rocks and may not have been reset by the faulting, there is potential for significant error in the dating results. Thus, it is important to establish the relative contributions to the net magnetic properties of the gouge, from the clay matrix and clast components.

In the present study, this was investigated by first disaggregating seven representative specimens into two size fractions. This was done by spreading the gouge material out on a glass microscope plate and manually picking out the 'granules' (clasts) greater than about 0.3mm diameter using a microscope pick. This grainsize

discriminant was chosen for practical reasons and does not necessarily have a direct relationship to fault displacement or authigenic mineral growth. The results are summarised in Table 5-3.

For the seven specimens analyzed, the weight percent of granules was found to vary from 21 to 46%, with a mean value of 31%. The corresponding mean weight percent of the clay matrix is 69%. Thus, the clay matrix typically comprises approximately two thirds by weight of these gouge specimens. These figures correspond reasonably well with independent grainsize measurements, for gouge from Fracture Zone NE-4, made during mineral separation for isotopic dating (see Fig 4-13).

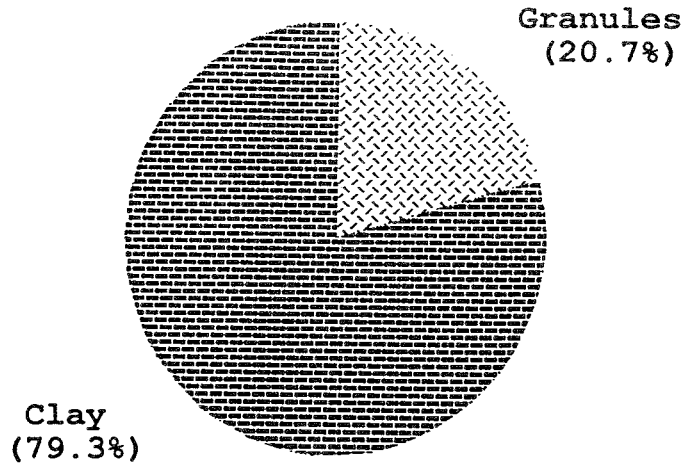
To establish the relative contributions of the clay and granule components to the net magnetic susceptibility of the gouge, synthetic specimens were made up by mixing each of the two fractions separately with non-magnetic resin and allowing this to set. This was done for each of the original seven specimens. The magnetic susceptibility of each synthetic specimen was then measured, using a Highmoor susceptibility bridge. The results were converted to mass-specific values. Using the known proportions of the two components, their relative contributions to the net susceptibility of each specimen could be calculated. The values are listed in Table 5-3. The contribution of the granules to the total susceptibility varies from 12 to 37%, the overall mean value being 21%; the corresponding mean contribution of the clay matrix is 79%. Thus, it is clear that the contribution of the clay matrix to the net magnetic susceptibility of the gouge dominates that of the coarser-grained clasts (Fig 5-8A).

Finally, an experiment was carried out to establish the relative contributions of the two grainsize components to the *remanent* magnetic properties of the gouge. Each of the synthetic specimens was first demagnetised in an applied alternating field of 60mT. It was then given an anhysteretic remanent magnetisation (ARM) by subjecting it to a strong alternating field of intensity 45mT in the presence of the Earth's direct magnetic field in the laboratory. The resultant magnetisation provides a good analogue for the natural remanent magnetisation of the rock. The results show that the contribution of the granules to the net remanent magnetism of the rock varies from 18 to 44%, with an overall mean value of 31%. The corresponding mean contribution of the fine-grained clay matrix is 69% (Fig 5-8B).

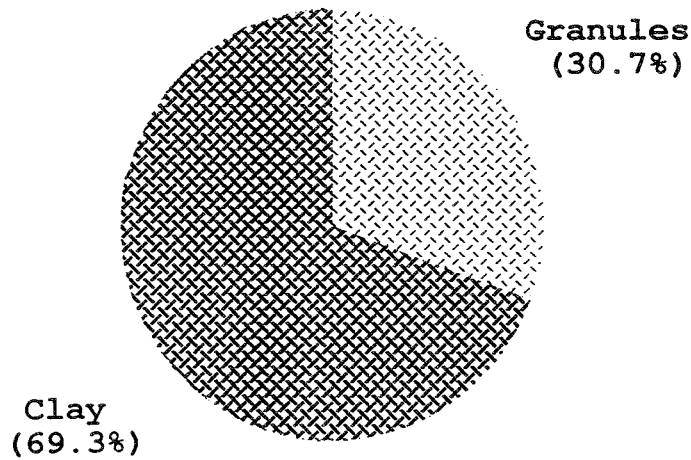
Table 5-3 Disaggregation analysis of fault gouge samples

Sample No	Gross wt (g)	GRANULES				Granule contribution to sus.	Granule contribution to ARM	CLAY				Clay contribution to sus.	Clay contribution to ARM
		Weight (g)	Weight (%)	m.sus (10 <sup>-8</sup> SI)	m.ARM			Weight (g)	Weight (%)	m.sus (10 <sup>-6</sup> SI)	m.ARM		
AS5.1	10.24	3.25	31.7	0.0372	0.516	21.4%	34.0%	6.99	68.3	0.0653	0.465	78.6%	66.0%
AS5.2	12.09	3.03	25.0	0.0133	2.587	16.5%	43.6%	9.06	74.9	0.0233	1.119	83.5%	56.4%
AS14.9	13.90	4.27	30.7	0.0614	2.207	22.8%	35.4%	9.63	69.3	0.0922	1.784	77.2%	64.6%
A91/26*	9.91	2.12	21.3	0.0970	3.886	14.6%	24.6%	7.79	78.7	0.1532	3.216	85.4%	75.4%
A91/27*	8.88	3.27	36.8	0.0755	2.676	20.3%	18.4%	5.61	63.2	0.1724	6.930	79.7%	81.6%
A91/28*	8.72	2.45	28.0	0.2183	6.253	11.8%	23.2%	6.27	72.0	0.2494	8.023	88.2%	76.8%
A91/36*	10.52	4.82	45.8	0.1024	1.442	37.3%	35.8%	5.70	54.2	0.1227	2.180	62.7%	64.2%
MEAN			31.3%			20.7%	30.7%		68.7%			79.3%	69.3%

Note: 1) samples with \* are from unoriented samples taken from same gouge vein as the oriented palaeomagnetic samples.  
 2) sus = magnetic susceptibility; m.sus = susceptibility per unit mass.  
 3) ARM = anhysteretic remanent magnetism acquired by application of peak alternating field of 45mT in the presence of the Earth's field in the laboratory; units are 10<sup>-3</sup> mAm<sup>2</sup>/kg; m.ARM = ARM per unit mass.



A. Relative contribution to susceptibility



B. Relative contribution to remanent magnetism (ARM).

Figure 5-8 Contributions to (A) magnetic susceptibility and (B) remanent magnetism (ARM) of the clay component and granule component respectively of the fault gouge.

## 5.7 MAGNETOMINERALOGICAL INVESTIGATIONS USING IRM-ACQUISITION ANALYSES

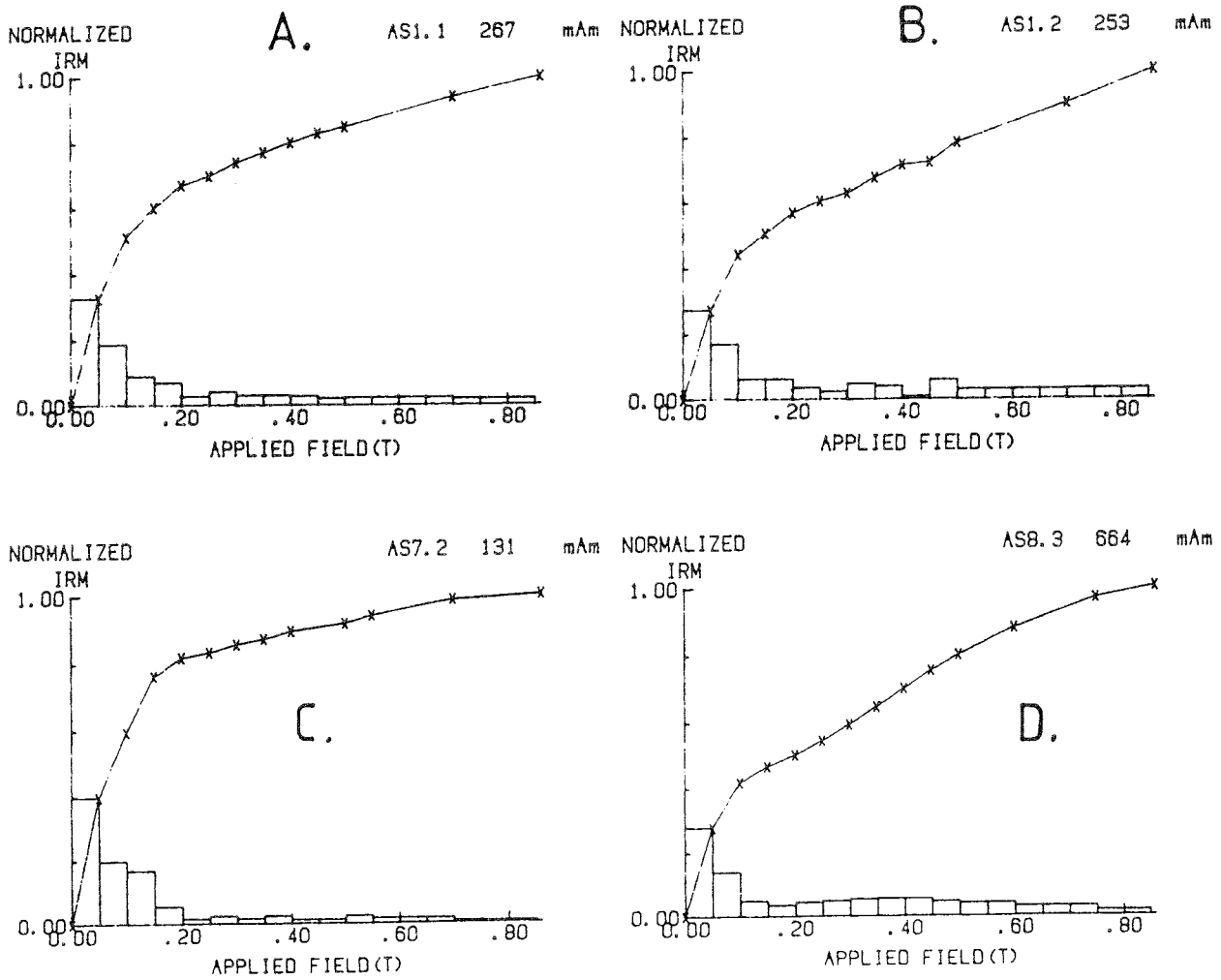
Representative specimens of the epidote vein and breccia material, fault gouge and hostrock were subjected to isothermal remanent magnetisation (IRM) analyses. This procedure involves progressively magnetising the specimen by applying an incrementally increased direct field, the intensity of the resultant magnetisation being measured after each successive increment. The maximum field applied in these experiments was 0.85T (Tesla). The shape of the resulting IRM versus applied field curve provides information on the nature of the magnetic minerals present in the rock.

The epidote vein and breccia specimens show progressive increases in IRM intensity with applied field and the IRM acquisition curves do not saturate in the maximum field used (Fig 5-9). This is the case also for the fault gouge matrix and granule fractions (Fig 5-10). In contrast, the aplite vein and the hostrock specimens (excepting the fine-grained granite and protomylonite) reach magnetic saturation in relatively low applied fields, generally <0.2T (Fig 5-11). This behaviour indicates that the dominant magnetic mineral in the latter material is magnetite, while that in the epidote veins, breccia and gouge is in a higher oxidation state and is probably hematite.

IRM acquisition curves (not shown) for specimens of the protomylonitic granite (Fracture Zone EW-3) and red fine-grained granite (Fracture Zone NE-3) indicate that the magnetomineralogy of the former is almost entirely dominated by hematite while that of the latter includes both hematite and magnetite.

## 5.8 MAGNETIC FABRIC

A pilot study of the anisotropy of magnetic susceptibility (AMS), or magnetic fabric, of selected samples was undertaken. The AMS provides a rapid determination of the (three-dimensional) preferred alignment of magnetic mineral grains within the rock. For magnetic phases which are crystallographically isotropic, such as magnetite, the magnetic susceptibility of slightly elongate grains will have a maximum value ( $K_{\max}$ ) along the grain long axis and a minimum value ( $K_{\min}$ ) along the short axis. Thus, measurements of the variation of magnetic susceptibility with direction can give a precise measure of the bulk grain alignment within the specimen. In the present study, the AMS was measured by means of a high field torque magnetometer operating at an applied field of approximately 0.4T.



**Figure 5-9** Examples of isothermal remanent magnetisation (IRM) acquisition analyses for specimens of epidote-rich vein material (A to C) and epidote breccia (D).



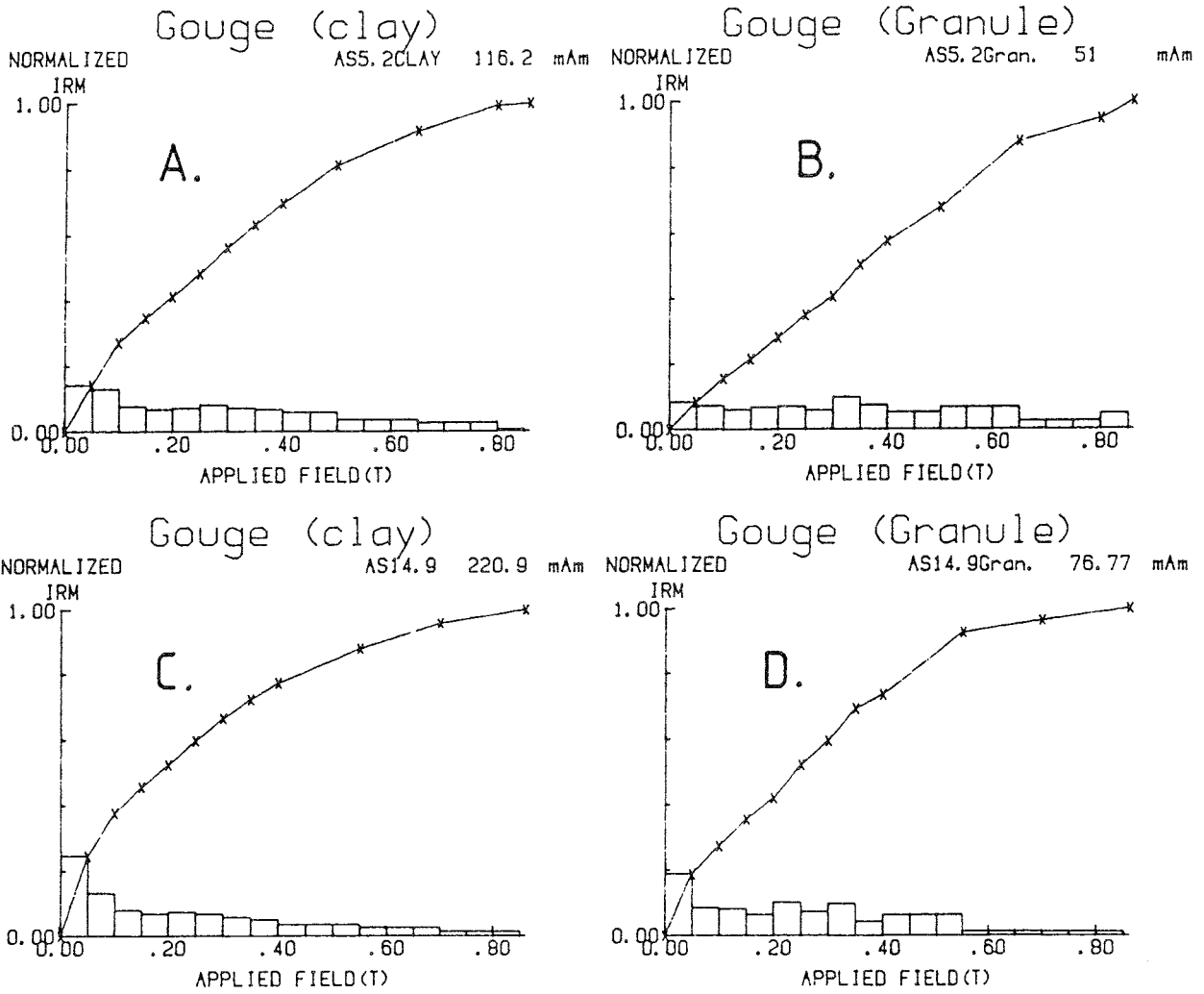


Figure 5-10 Examples of IRM acquisition analyses for specimens of clay component (A & C) and granule component of fault gouge (B & D).

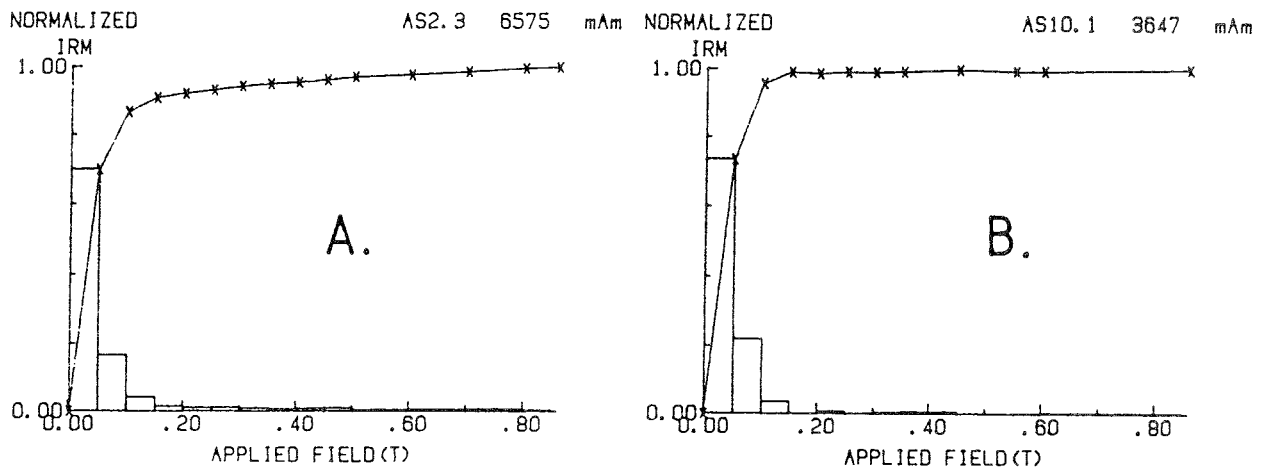


Figure 5-11 Examples of IRM acquisition analyses for specimens of aplite dyke (A) and hostrock (B).

Because of the relatively high spontaneous magnetism of magnetite compared with other magnetic oxides, such as hematite, even a small amount of the former will dominate the magnetic fabric. In the absence of magnetite, the AMS commonly reflects the dimensional and/or crystallographic orientation of paramagnetic minerals, particularly phyllosilicates (eg. Borradaile et al 1987; Richter et al 1993).

Magnetic fabric investigations of protomylonitic granite from Fracture Zone EW-3 and gouge from NE-4 were made to examine the relationship between the magnetic and tectonic fabrics and the measured remanence vectors.

#### 5.8.1 Protomylonitic granite

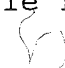
Magnetic fabric measurements for the protomylonitic granite from Fracture Zone EW-3 (Sites AS21-23) are shown in Fig 5-12A. Four of the five  $K_{min}$  axes are (widely) scattered around a mean easterly direction and have very shallow inclinations. The magnetic foliation planes are correspondingly steep and evenly distributed between broadly northeasterly and northwesterly strikes. In two specimens the direction of stable magnetisation lies close to the magnetic fabric plane but for the other three specimens there is no apparent correlation. Furthermore, there is no tendency for specimens with a higher degree of anisotropy to have their remanence located closer to the fabric plane.

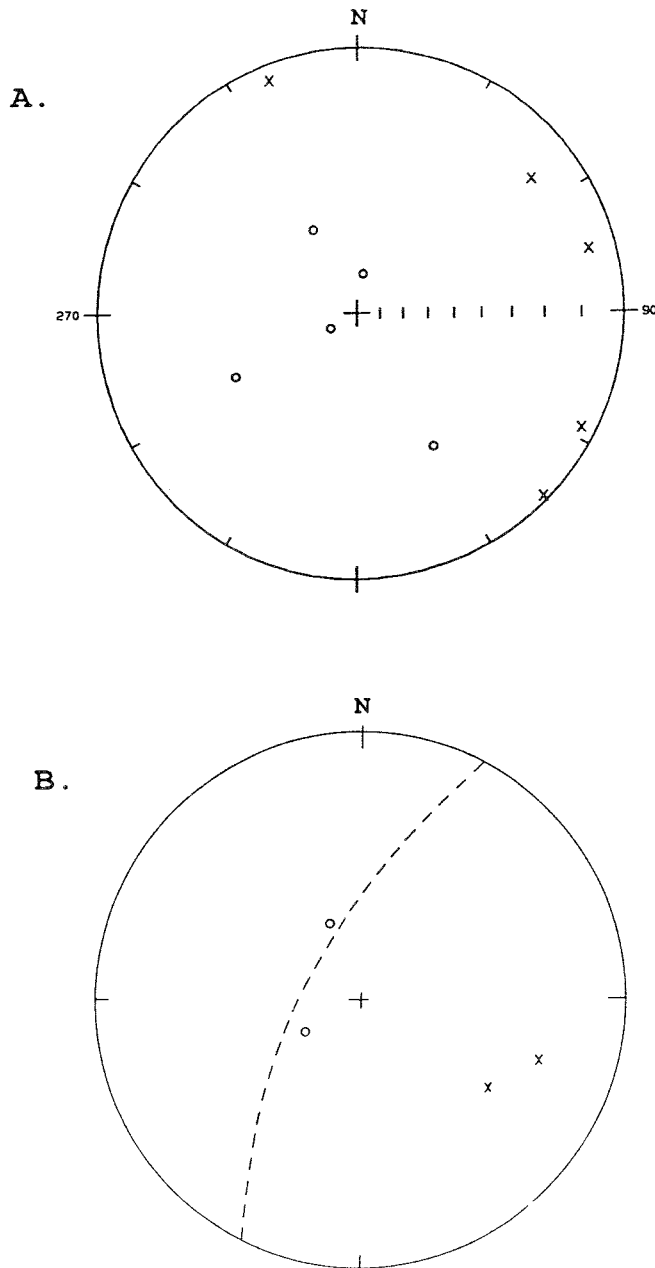
The mylonitic foliation strikes ENE (065-082°) and dips steeply either side of vertical in the vicinity of the sampling sites in Fracture Zone EW-3.

On balance, it seems that there is no clear evidence to suggest that the scatter in remanence directions observed in these specimens (Section 5.5.3) is caused by deflection by the fabric.

#### 5.8.2 Fault gouge

The IRM analyses on the fault gouge material (Fig 5-10) reveal no evidence for the presence of magnetite in these specimens. Thus it is likely that the magnetic fabric reflects the alignment of phyllosilicates. Comparative studies have indicated that the preferred orientation of magnetic minerals is normally closely parallel to that of non-magnetic grains.

Unfortunately, a high proportion of the clay gouge specimens originally available had been destroyed during attempts at thermal demagnetisation. Only two specimens (from site AS14, Fracture Zone NE-4) were available for AMS analysis. The results are shown in Fig 5-12B. 



**Figure 5-12** Upper hemisphere stereographic projections showing maximum susceptibility axes (circles) and minimum susceptibility axes (crosses) defined from high field torque magnetometer measurements. Results are shown for five specimens of red protomylonitic granite (A) from fracture zone EW-3 (Sites AS21-23) and two specimens of fault gouge (B). The minimum susceptibility axes define the pole to the magnetic foliation plane, the mean orientation of which is shown by the dashed great circle in (B).

There is quite good agreement between the results from the two samples. The magnetic foliation plane dips steeply downwards at a mean angle of  $66^\circ$  to the ESE. The mean strike is  $26^\circ$ . A reasonably well-defined magnetic lineation is defined by the maximum susceptibility axes. This lineation lies within the foliation plane and dips steeply upwards towards the WNW.

The orientation of the planar magnetic fabric measured in specimen AS14.10 is closely similar in strike and in dip (within  $10^\circ$ ) to both the macroscopic colour banding and the planar phyllosilicate fabric seen in thin-section of the same gouge sample (Figs 4-8A and B). This fabric appears to correspond to a 'P' foliation (Rutter et al 1986) which would be consistent with a normal dip slip sense of displacement associated with the gouge formation.

## 5.9 INTERPRETATION OF RESULTS AND DATING OF FAULTROCKS

### 5.9.1 Magnetisation directions

In each of the lithologies studied, apart from the granitic hostrock, the low-stability component of magnetisation is aligned close to the recent geomagnetic field vector and is likely to represent a viscous magnetic overprint in the recent field. This overprint must have been acquired during the present normal polarity chron which began about 730,000 years ago (Cande and Kent 1992). However, such overprints may be acquired over rather short intervals of time, of the order of  $10^3$ - $10^5$  years, and consequently provide no dating information of geological significance.

The directions of the higher stability components identified in each of the rock types are summarised in Table 5-4, together with the corresponding palaeomagnetic pole positions. The characteristic magnetisation vectors for the majority of rock types have been shown to fall into three principal groups, labelled A, B and C.

#### (a) Group A direction

This direction is characterised by a general north to northeasterly declination and a moderately steep positive inclination (Table 5-4 and Fig 5-13). It is clearly defined in each of the epidote-rich Veins 1 to 5 and in the carbonate vein (where it has a reverse polarity), but less tightly constrained in the epidote and chlorite vein-breccias. The 95% confidence circles for most of the Vein mean vectors overlap each other and lie within the breccia 95% confidence circle, indicating that, in general, there are no statistically-significant differences between them.

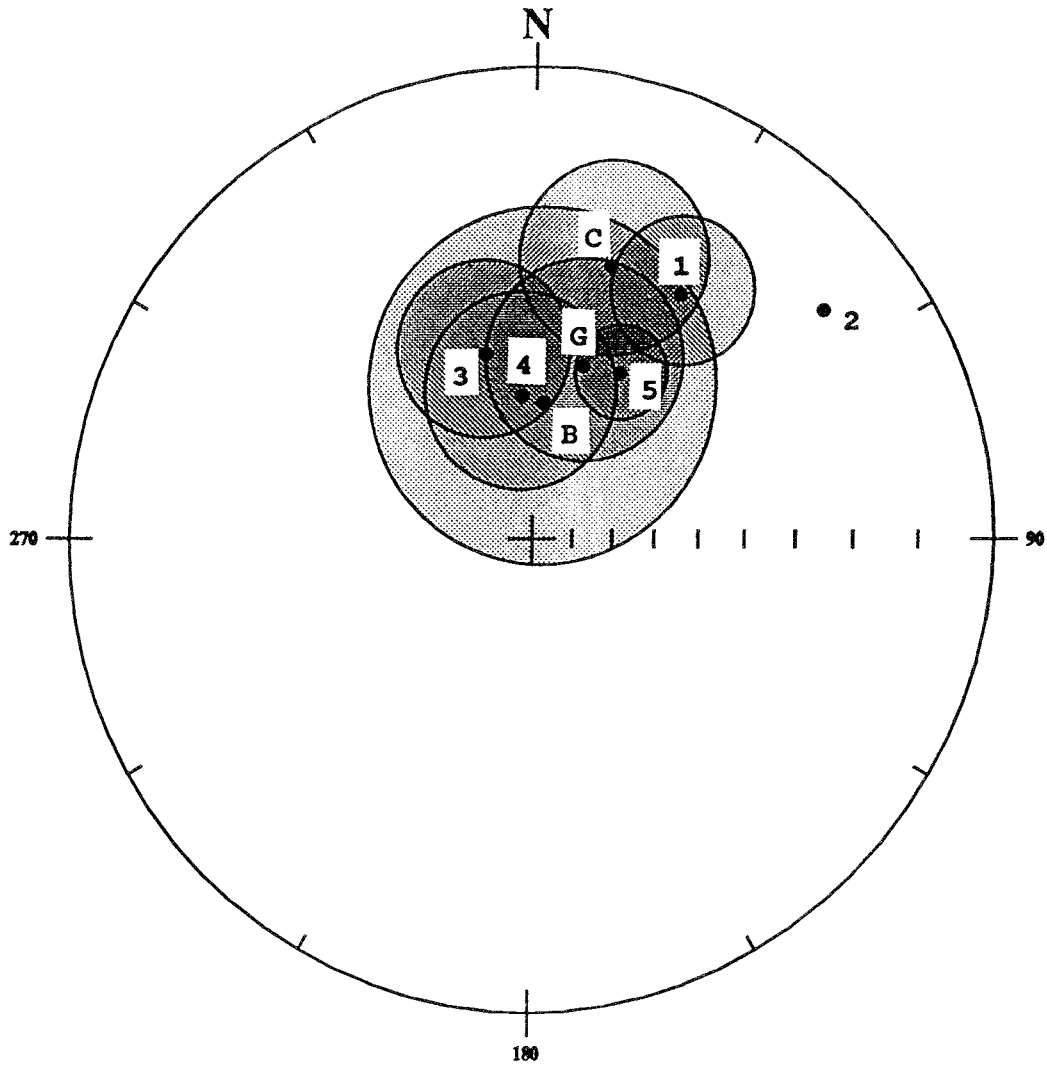
Table 5-4 Characteristic components of magnetisation and pole positions

Rock unit	Mean direction				Overall mean				Pole Pos		Symbol, Fig 5-15 & 5-16
	Dec	Inc	$\alpha_{95}$	N	Dec	Inc	$\alpha_{95}$	N	Lat	Long	
<b>GROUP A DIRECTION</b>											
Epidote Vein 1	32	27	13	10							
Epidote Vein 2	53	14	-	1							
Epidote Vein 3	41	46	18*	2							
Epidote Vein 4	351	57	22	4	26	42	17	7	52N	156E	A
Epidote Vein 5	26	48	10	20							
Carbonate vein	194	-29	17	7							
Epidote breccia	360	58	38	7							
Fault gouge	13	50	21	10	13	50	21	10	61N	172E	
Hostrock low stability component	26	52	11	16	26	52	11	16	59N	150E	
<b>GROUP B DIRECTION</b>											
Epidote Vein 6	339	-40	12	23	343	-40	10	26	8N	211E	B
Aplite dyke	352	-28	28	3							
<b>GROUP C DIRECTION</b>											
Hostrock high stability compt	333	26	12	25	333	26	12	25	41N	231E	C
Note: * angular separation of the two vectors											

Consequently, it is believed that each of these rock units acquired its characteristic magnetisation at more-or-less the same time and it is appropriate to group all mean vectors into one overall mean direction for interpretation and dating purposes. This overall mean Group A direction is listed in Table 5-4.

Statistically, the fault gouge mean vector also falls within the Group A direction (Fig 5-13) but because of its obviously different age of formation - though not necessarily different age of (recorded) magnetisation - it has been grouped separately (Table 5-4).

It may also be significant that the host rock low blocking temperature/low coercivity component is quite similar to the Group A direction (Table 5-4). This suggests that the hostrock may have acquired a partial magnetic overprint at the same time as the emplacement or magnetisation of the epidote and carbonate veins/breccia or, conceivably, the fault gouge.



**Figure 5-13** Mean directions of Group A magnetisations for each individual rock unit. Points "1" to "5" represent epidote-rich Veins 1 to 5 respectively, "C" represents the carbonate-rich vein at Site AS27, and "B" the epidote breccia. "G" is the fault gouge. Lower hemisphere stereographic projection. 95% confidence circles are shown for each rock unit except Vein 2, for which the direction is defined by only a single specimen.

**(b) Group B direction**

The Group B direction is characteristic of the Geochemistry Laboratory Vein 6 and also of the aplite dyke. It is represented by a northwesterly declination and moderately steep negative inclination (Table 5-4). It is clearly distinct from the Group A direction and also from the present geomagnetic field direction.

**(c) Group C direction**

The Group C direction is characteristic of the high temperature/high coercivity components of all of the hostrocks except the aplite dyke, and the red fine-grained granite and protomylonite from within the fracture zones. An important observation is that, although the Group C vectors show significant dispersion, their mean direction is completely distinct from that defined in any of the fault rocks. This indicates that, although *partial* overprinting of the hostrocks may have occurred (represented by their low blocking temperature/low coercivity component), regional magnetic overprinting of all units has not occurred and the magnetisation of the faultrocks almost certainly postdates that of the hostrock.

**5.9.2 Acquisition of magnetisation**

Magnetisation (IRM) acquisition experiments indicate that the principal carrier of magnetisation in the hostrock and the aplite vein is magnetite, whereas in the epidote veins, breccia and gouge it is hematite. The carrier of magnetisation in the protomylonite of Fracture Zone EW-3 is also hematite, but in the fine-grained granite from NE-3 both hematite and magnetite are present.

The IRM data, combined with the demagnetisation characteristics, suggest that in the hostrocks and in the aplite vein, primary components of magnetisation acquired during emplacement of these rocks have been resolved. The situation for the fracture zone protomylonite and fine-grained granite is, however, less clear. The magnetisation may have been primary or, perhaps more likely, have resulted from oxidation of magnetite to hematite during the passage of hydrothermal fluids. Such oxidative fluid movement could have been late-magmatic or related to the mylonitic deformation. In any event, the scatter of the measured vectors does not allow estimation of a meaningful palaeomagnetic date for these fracture zone 'hostrocks'.

A similar question arises concerning the primary (vein formation, fault deformation, or fault cementation) or secondary (later oxidative fluid flow) origin of the



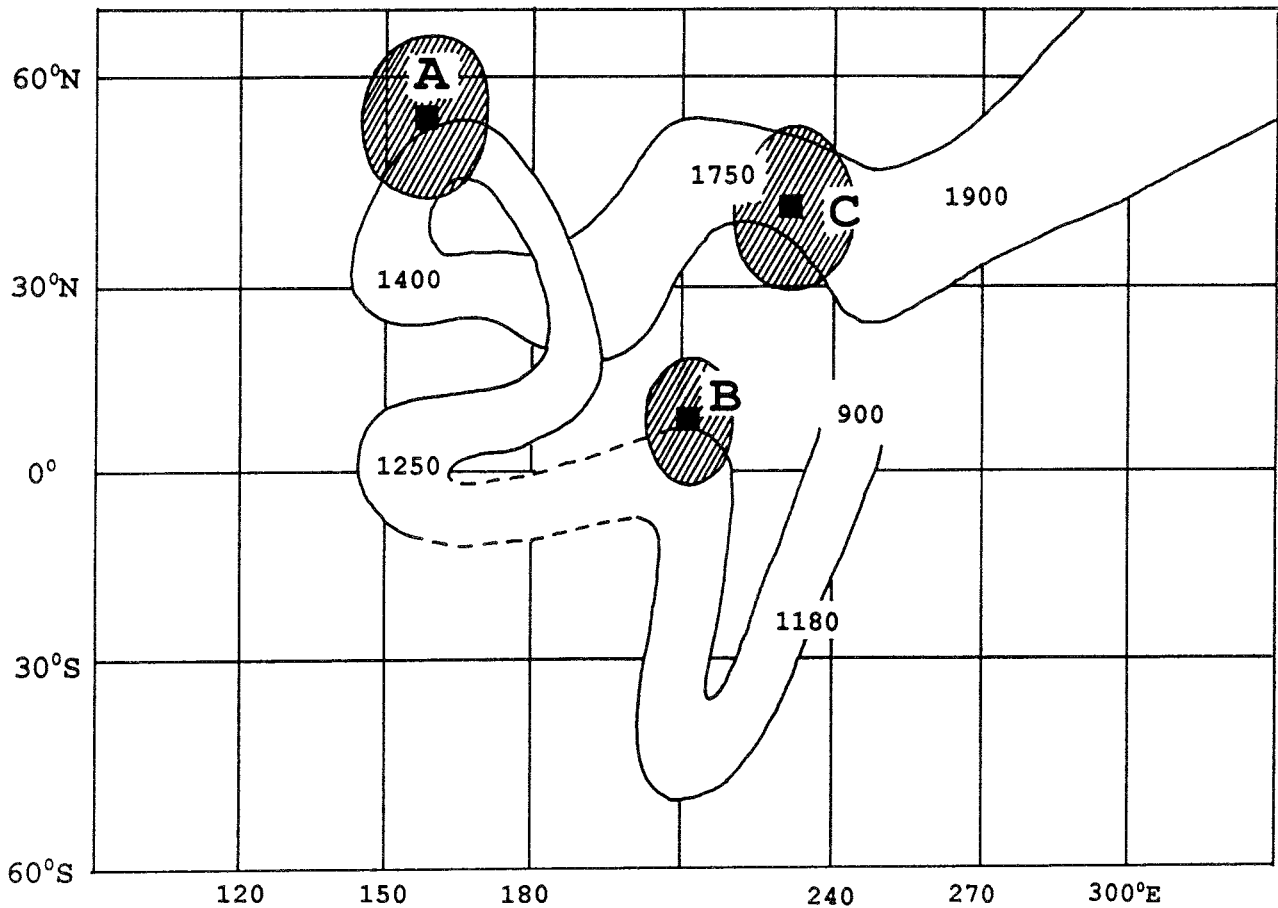
magnetisation of the epidote and chlorite vein/breccia and fault gouge. It is possible that the characteristic magnetisation of these rocks is a chemical remanent magnetism (CRM) acquired during specific episodes of large-scale hydrothermal fluid flow along the fractures. Such CRM's are generally precise recorders of the direction of the ambient geomagnetic field, whereas the fidelity of magnetisations associated with the mechanical processes of brittle faulting is still largely unknown (Hailwood et al 1992). However, it is equally likely that formation of the epidote and chlorite veins/breccia and the gouge (cf. Section 4.5.5) took place under oxidising conditions. In this event, the measured remanence vector would date the age of formation rather than any subsequent hydrothermal circulation. (There are, of course, few independent data which constrain the timescale over which, say, an epidote vein grows).

The sampled epidote veins, chlorite and epidote breccias, and the gouge, show complex microstructures indicating repeated movement and veining (Section 4). For example, epidote Veins 1 and 4 (Sites AS1 & AS7 respectively) are both slickensided. The palaeomagnetic ages of these veins constrains the age of acquisition of magnetisation, which may relate to crystallization or later oxidative fluid flow, but undoubtedly predates the small-scale movements (see Section 2.3.3) causing slickensiding.

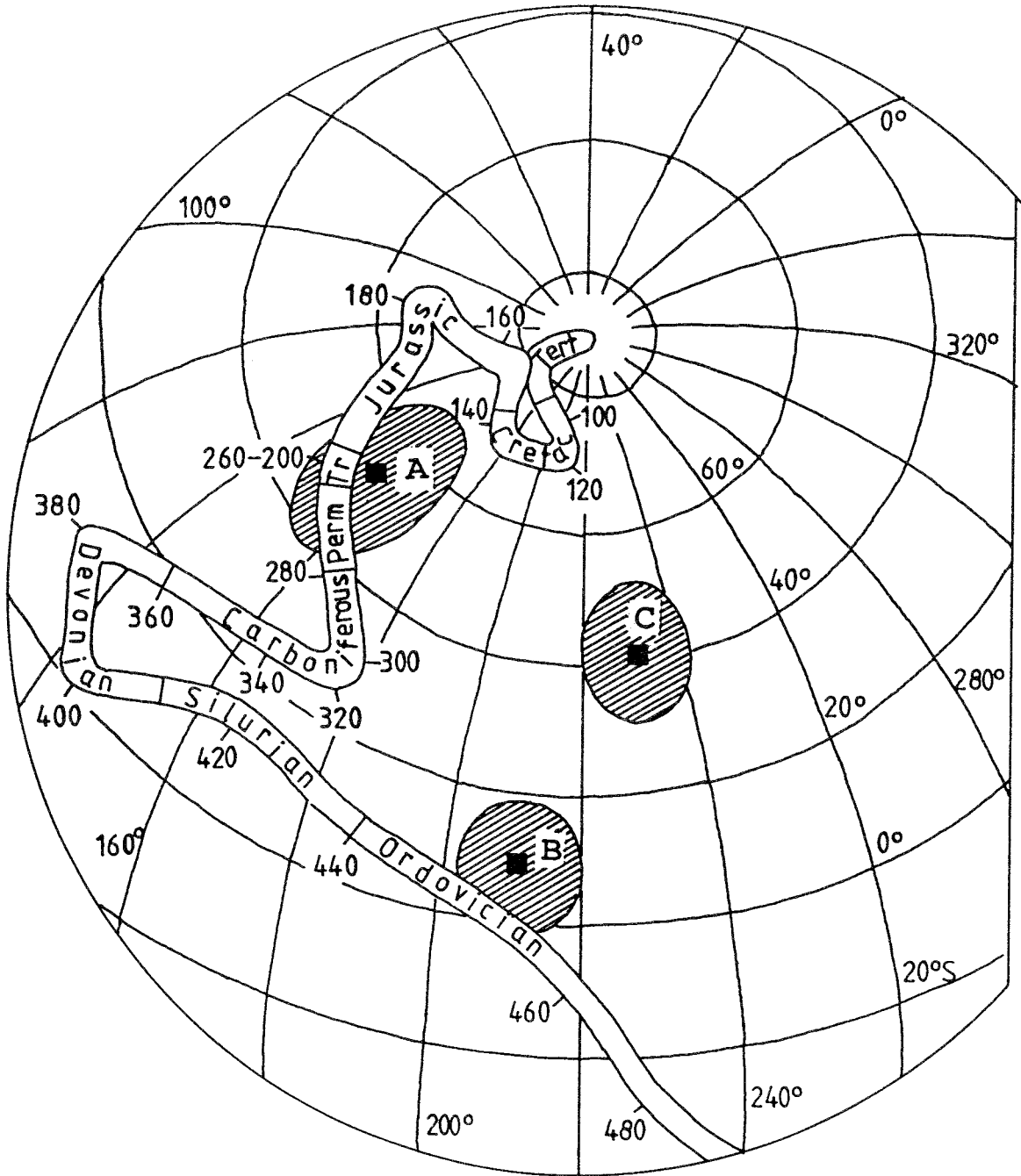
For the gouge, the palaeomagnetic ages are considered more likely to constrain the minimum age of faulting, on the assumption that the magnetisation was acquired during, or after, cementation by authigenic mineral phases (Section 4.5.5). The disaggregation experiments lend some support to this hypothesis.

### 5.9.3 Comparison with apparent polar wander curves for Baltica

The palaeomagnetic pole positions are compared with published 'standard' apparent polar wander (apw) curves for Scandinavia ('Baltica') in Figs 5-14 and 5-15. The comparison of the observed poles with the 'standard' apw curves assumes that geomagnetic secular variation has been properly averaged out in the determination of the mean vectors. The observed records of geomagnetic polarity reversals indicates that this is likely to be the case for the 'Group A' components of the epidote veins/breccia and also the fault gouge, essentially irrespective of the mechanism of acquisition of magnetisation (see Sections 5.5.1, 5.5.2 and 5.9.2).



**Figure 5-14** Palaeomagnetic apparent polar wander curve for Scandinavia for the interval 1900 to 900 Ma, from Piper (1988). Pole positions corresponding to the Group A, B and C mean vectors defined from this study are shown, together with their respective 95% confidence limits.



**Figure 5-15** Apparent polar wander path for Baltica for the interval 500 Ma to present. Numbers next to curve represent ages in Ma. For sources of data see text. Pole positions corresponding to the Group A, B and C mean vectors defined from the present study are shown, together with their respective 95% confidence limits.

Although the country rocks are metamorphosed, there is no systematic evidence of post-consolidation local or regional folding or tilting of these units (Table 2-2). It is therefore not possible to apply a classic palaeomagnetic 'fold test' (Graham 1949) to provide constraints on the age of magnetisation in relation to the age of formation of the rocks. However, a key observation is that the direction of characteristic magnetisation of the hostrocks is quite distinct from that of the fault rocks. This rules out the possibility that the magnetisation of all rocks in the area has been reset by a later static geological event and helps validate the use of the faultrock magnetisation vectors as age indicators.

The oldest interval of geological time for which palaeomagnetic data are available for this region is the period 1900-900Ma. The data for this interval have been taken from the compilation of Piper (1988). The corresponding apw curve is shown in Fig 5-14, together with the Äspö palaeomagnetic pole positions defined from the present study.

Unfortunately, there are few published palaeomagnetic data for Baltica for the interval 900 to 600Ma. Relevant palaeomagnetic data for the interval 600 to 250Ma have been reviewed recently by Torsvik et al (1992). These data indicate that Baltica had docked with Laurentia (including North America and Greenland) and Eastern Avalonia (including southern England) by Early Devonian times. These land masses then remained attached together, as part of a single plate, until the opening of the present North Atlantic in the Mesozoic.

By combining palaeomagnetic data from appropriate plates and correcting for known relative motions, Besse and Courtillot (1991) have generated a synthetic apw path for Eurasia for the period since 200Ma. This curve is shown, combined with that of Torsvik et al (1992) for the interval 200 to 500Ma, in Fig 5-15. The combined apw path provides a suitable reference curve for evaluating the new palaeomagnetic data from the Äspö faultrocks.

The palaeomagnetic pole positions for the different components of magnetisation identified in the Äspö rocks are plotted as squares in Figs 5-14 and 5-15. The 95% confidence ellipses for these poles are shown hachured. The age constraints which these pole positions place on the different rock units are discussed for each unit in turn below.

#### (a) Hostrocks (Group C pole)

The Group C pole, derived from the mean hostrock vector, bears no similarity to any part of the Palaeozoic or

Mesozoic apw curve (Fig 5-15). However, this pole does correspond with the Precambrian part of the apw curve, in the interval between 1750 and 1900Ma (Fig 5-14). This palaeomagnetic age for the granitic hostrocks is thus in very good accord with independently-constrained ages for the Småland granitoids of the Äspö area (Table 2-2).

**(b) Epidote veins/breccia and calcite vein (Group A pole)**

The Group A pole, derived from the majority of epidote veins, the calcite vein and the epidote and chlorite breccias intersects both the Precambrian and Phanerozoic apw curves (Figs 5-14 & 5-15). Considering the possible timing of acquisition of magnetisation in these rocks (Section 5.9.2) and the published deformation fracture-filling history at Äspö (Table 2-2), two alternative dating interpretations are possible. The Phanerozoic palaeomagnetic age could date a magnetisation associated with large-scale oxidative fluid flow between about 270 and 190Ma. Alternatively, the Precambrian age would date (primary) vein and breccia formation during hydrothermal circulation associated with emplacement of the anorogenic Göttemar and Uthammar granites, which is independently dated at 1400-1350Ma (Table 2-2). The geological data strongly support the second of these alternative dating interpretations.

**(c) Fault gouge**

As indicated above (Section 5.9.1), the mean fault gouge vector is statistically indistinguishable, at the 95% confidence level, from the Group A vector direction. The mean palaeomagnetic pole for the gouge therefore intersects apw curves for both the Precambrian and Phanerozoic intervals (Figs 5-14 and 5-15). However, it is clear from the field relations and contrasting mineralogical assemblages that the gouge was formed during a much younger episode of faulting than the fracturing responsible for the (Group A) epidote veins and breccia. For this reason, and taking into account the data of Table 2-2, the Phanerozoic date of  $\leq 270-190$ Ma for the acquisition of magnetisation in the gouge is preferred.

**(d) Vein 6 and aplite dyke (Group B pole)**

The Geochemistry Laboratory Vein 6 and the aplite dyke combine to make up the Group B mean vector direction. The corresponding mean palaeomagnetic pole (Table 5-4) intersects the Precambrian and Phanerozoic apw curves at about 1200Ma and 450Ma respectively (Figs 5-14 & 5-15).

The younger palaeomagnetic date falls close to the peak tectonothermal activity in the Scandinavian Caledonides external to Äspö (Section 2.2.3). However, there is no evidence for local igneous intrusion at this time and the published geological history indicates that epidote veining was complete by about 1000Ma (Table 2-2).

For the aplite dyke, the c.1200Ma palaeomagnetic age may also be suspect since: (i) there is no evidence for acid igneous intrusion which postdates the anorogenic Götemar and Uthammar granites of 1400-1350Ma age (Table 2-2) (primary intrusion rather than secondary remagnetisation being indicated by the IRM data); and, (ii) the aplite dyke was seen to be offset by a N-trending epidote vein (Section 3.2.3). It may be noted that the statistical confidence on the mean direction of magnetisation of the aplite dyke is comparatively poor (Table 5-4).

The Geochemistry Laboratory Vein 6 has a complex mineralogy and microstructure (Section 4.3) and it is difficult to be sure what phase or phenomenon is shown in the palaeomagnetic age. It is clear, however, that the palaeomagnetic age is distinctively younger than for the other, similarly oriented epidote veins.

## 5.10 CONCLUSIONS

Measurements of stable remanent magnetisation have been combined with investigations of magnetomineralogy and magnetic fabric and disaggregation experiments to determine palaeomagnetic ages for a variety of host and faultrock samples. The interpreted results are summarized in table form below:

Table 5-5 Summary of palaeomagnetic dating results

Rock Type	Fracture zone	Carrier of stable magnetisation	Preferred mechanism of acquisition of stable magnetisation	Palaeomagnetic age: Preferred age (Alternative age)	
Hostrocks	-	magnetite	primary magmatic	1800Ma	(none)
Fine-grained red granite	NE-3	magnetite & hematite	primary magmatic & hydrothermal?	not resolved	
Protomylonite	EW-3	hematite	deformation & hydrothermal	not resolved	
Epidote veins, carbonate vein, ep & chl breccia	EW-7 & others	hematite	primary crystallization or hydrothermal	1350Ma	(270-190Ma)
Vein 6 & aplite dyke	Geochem. -	hematite magnetite	primary crystallization primary magmatic	1200Ma	(c. 450Ma)
Fault gouge	NE-4	hematite?	cementation diagenesis & hydrothermal	270-190Ma	(1350Ma)

The 'preferred' palaeomagnetic ages are distinguished from the 'alternative' ages in Table 5-5 taking into account the known geological history (Table 2-3) and anticipating the isotopic dating results (Section 6).

The palaeomagnetic age of the hostrocks seems to be well-constrained, it is consistent with independent age data, and it is significantly different than the fault and vein rocks. Attempts to date the mylonitic deformation and the fine-grained red granite in fracture zones EW-3 and NE-3, respectively, were unsuccessful. Magnetite was shown to be the carrier of magnetisation in the fresh granitic hostrocks and magnetite and hematite in the fracture zone granite and mylonite. Magnetic fabric measurements on the protomylonite provide no evidence for deflection of measured remanence directions into the fabric plane.

Most of the conditions for palaeomagnetic dating of faultrocks (Section 5.1) have been satisfied. Some uncertainty remains, however, in the relationship between acquisition of magnetisation and the most recent fault displacement in the sampled veins, breccias and gouge materials.

Epidote, chlorite and calcite-rich veins and cataclasite/breccias from five localities, including Fracture Zone EW-7, are most consistent with a c.1350Ma palaeomagnetic age. These fault and vein systems are mainly NE-trending but also include N-S, NW and E-W trends. The carrier of magnetisation in these faultrocks is hematite. It is surprising that the spherulitic chlorite vein breccia from EW-7 gives a similar palaeomagnetic age to the epidote veins and breccia. It is likely that these veins and faultrocks have experienced minor shearing and extensional veining since acquisition of magnetisation.

The palaeomagnetic ages determined on the aplite dyke from the Information Gallery and the Geochemistry Laboratory fault are difficult to interpret.

Disaggregation and magnetomineralogical experiments have shown that hematite within the finer grainsize component of fault gouge from Fracture Zone NE-4 is the carrier of magnetisation. It seems likely that this magnetisation is related to authigenic mineral growth and, equally, most unlikely that the magnetisation could have survived later fault movements. If this is the case, then the minimum age of the most recent fault movements on the sampled strand of NE-4 is constrained to 270-190Ma (Permian to Lower Jurassic times).

## 6 ISOTOPIC ANALYSES

### 6.1 INTRODUCTION

At its simplest, isotopic direct fault dating involves identifying, physically separating and dating an undisturbed authigenic mineral phase in faultrock. In practice, this procedure is made complicated by several factors. Before considering the results of the present study, therefore, it is appropriate to review some existing isotopic direct dating studies and some of the assumptions and problems involved. For the most part this section is concerned with *K-Ar dating* of authigenic illite in fault gouge.

### 6.2 REVIEW OF EXISTING STUDIES

#### 6.2.1 Radiometric dating of fault gouge

Many accounts of isotopic dating of fabrics in mylonitic rocks exist (eg. Gromet 1991), but far fewer are concerned with direct dating of brittle faultrocks characteristic of upper crustal deformation. Interest in isotopic dating of fault gouge has been stimulated by bedrock stability concerns of the worldwide nuclear industry, and by successful isotopic dating of diagenetic illite in hydrocarbon reservoirs - a reasonable analogue for dating authigenic illite in gouge.

Using the K-Ar technique, Lyons and Snellenburg (1971) dated the  $<2\mu\text{m}$  fraction of gouge from three faults cutting crystalline Palaeozoic rocks in northeastern USA. They obtained early Jurassic ages, consistent with the regional tectonic picture. Although Lyons and Snellenburg considered the 'illite' to be authigenic and fault-related, Murphy et al (1979) appear to have interpreted this to mean that it had formed by mechanical abrasion. Pursuing the idea that cataclasis and frictional heating might reset the K-Ar 'clock' in gouge, Langley (1981) attempted to date the movement of faults cutting Coal Measures strata in England. Using grain size separates down to  $<0.5\mu\text{m}$ , she obtained K-Ar ages corresponding to the diagenetic/detrital age of the wallrocks rather than the demonstrably post-Permian age of faulting.

In an extensive dating study of fault activity along the Median Tectonic Line of Japan, Shibata and co-workers (Shibata and Takagi 1988; Shibata et al 1988; Takagi et al 1989; summarized in English by Takagi and Shibata 1989) found that the  $<2\mu\text{m}$  fraction of eight gouge samples yielded K-Ar ages younger than their wallrocks. (An Rb-Sr pseudo-isochron age for one sample, based on one  $<2\mu\text{m}$  and one 'whole-rock' datapoint, was also in good agreement with the K-Ar age). XRD analyses were used to support the



conclusion that the  $<2\mu\text{m}$  fractions were largely composed of authigenic phases formed during hydrothermal alteration associated with fault movement and cataclasis. Comparable conclusions were drawn by Tanaka et al (1992) in a K-Ar dating study of eleven  $<2\mu\text{m}$  gouge samples from the Akaishi Tectonic Line, also in Japan.

Kralik et al (1987), in a combined K-Ar and Rb-Sr dating study of gouge from faults cutting limestone and schist in the eastern Alps, recognized that it was necessary to isolate and date neo-crystallized phases filling voids in the faultrocks. For each gouge sample, they separated size fractions down to  $<0.5\mu\text{m}$ , characterized the fractions by XRD and SEM, and then dated them. The calculated K-Ar and Rb-Sr ages were mostly in good agreement, significantly younger than the wallrocks, and decreased with decreasing grain size. Rb-Sr model ages were determined from pseudo-isochrons defined by combinations of grain sizes, acid-leachates and their residues. In a further dating study Kralik et al (1992) analyzed the K-Ar and Rb-Sr isotope chemistry of  $<40$ , 5-20 and  $<1\mu\text{m}$  size fractions of granodioritic wallrock, mylonite and gouge from the Grimsel Test Site in Switzerland. Their results suggested that fine-grained new mineral phases grew concurrently in both gouge and mylonite, within an isotopically open system; calculated ages were controlled by the cooling of the granodiorite.

On a different tack, Flinn (1992) notes a Jurassic age for gouge from the Walls Boundary Fault, Scotland determined (by J.A. Miller) using the  $^{39}\text{Ar}/^{40}\text{Ar}$  step-heating technique. (This technique offers the advantages of needing less sample mass and giving an isochron age, although preparation and analysis is more involved).

#### 6.2.2 Stable isotope chemistry of fault gouge

O'Neil (1985) has measured the  $\text{H}_2\text{O}^-$  and  $\text{H}_2\text{O}^+$  contents and their respective oxygen and hydrogen isotopic compositions, in bulk core samples of gouge from the San Andreas Fault. He found that the clay minerals and coexisting pore fluids were not in isotopic equilibrium, indicating that the clays were comparatively old and also that the gouge must have been permeable.

#### 6.2.3 Critical comment

In each of the above studies although the mineralogy of the size fractions was sometimes well-characterized, little effort was made to demonstrate that the material was of authigenic origin. None of the studies include microstructural evidence which demonstrates any genetic or temporal relationship between fault movement and authigenic clay mineral growth.

The importance of comprehensive sample (size fraction) characterization has been emphasized by Shafiqullah et al (1990) in a K-Ar dating study of sub-micron fractions separated from gouge and other faultrocks from a detachment zone in western USA, whilst Lloyd et al (in Maddock 1992) used microstructural analysis of *intact* gouge to assist interpretation of K-Ar dates obtained from sub-micron fractions of gouge from a fault in Wales.

Despite the fact that in most of the above studies it cannot be demonstrated that the dated fractions were composed wholly of authigenic phases, many of the reported K-Ar ages do appear to be geologically realistic. This observation lends some credence to the idea that the isotopic systems in fault gouges may be reset by some combination of heat, fluid activity and deformation as well as neo-crystallization (see Kralik et al, in Maddock 1992).

#### 6.2.4 Note on illite terminology

The terminology used here follows generally accepted conventions in the literature of clay mineralogy. *Illite* is defined by Srodon and Eberl (1984, p.495) as a "non-expanding, dioctahedral, aluminous potassium mica-like mineral which occurs in the clay size (<4 $\mu$ m) fraction". The general chemical formula of illite is  $K_xAl_4(Si_xAl_x)O_{20}(OH)_4$  with  $x < 2$ , whereas the less silicic/more potassic muscovite has an ideal formula of  $K_2Al_4[Si_6Al_2O_{20}](OH)_4$  (eg. Deer et al 1966). In nature, many illites are compositionally close to phengite which has the formula  $K_2Al_{4-x}(Mg, Fe^{2+})_x[Si_{6+x}Al_{2-x}O_{20}](OH)_4$ . *Illitic* (or 'illite') is a more general term used to describe 10 $\text{\AA}$  clay grade materials which may contain a small expanding smectite component (eg. Burley and Flisch 1989). Mixed-layer clays contain interlayered expanding and non-expanding clays. Mixed-layer *illite-smectite* (I/S) contains variable proportions of illite and smectite  $\{(1/2Ca, Na)_{0.7}(Al, Mg, Fe)_4[(SiAl)_8O_{20}](OH)_4 \cdot nH_2O\}$ .

Generalized compositional relationships between illite and related minerals are shown in Fig 6-1.

### 6.3 APPLICATION OF K-AR METHOD TO DIRECT DATING FAULT GOUGE

#### 6.3.1 Systematics

The systematics and general applications of K-Ar dating are described in standard texts (eg. Geyh and Schleicher 1990). In simple terms, radiogenic  $^{40}\text{Ar}$  ( $^{40}\text{Ar}^*$ ) is the daughter product formed by the decay of  $^{40}\text{K}$ . Assuming knowledge of the isotopic abundance of  $^{40}\text{K}$  and the relevant decay constants, the 'age' (see below) of the

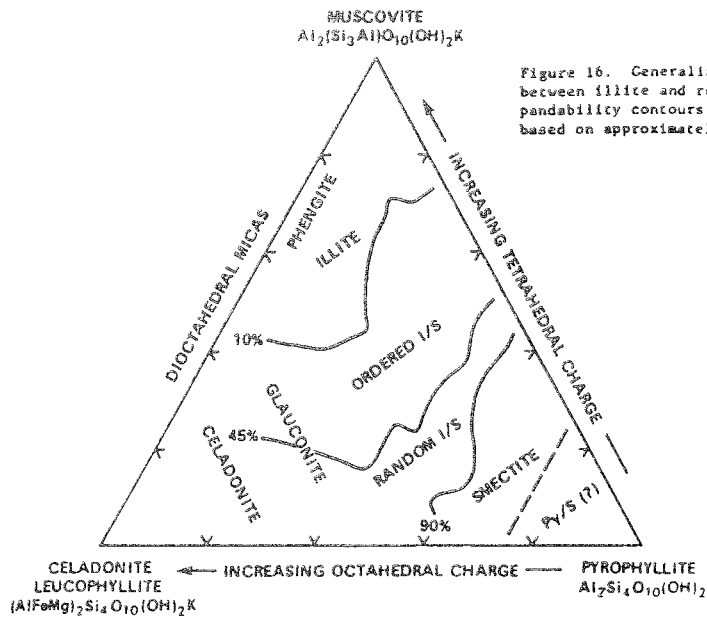


Figure 16. Generalized chemical relationships between illite and related minerals. The expandability contours at 90%, 45%, and 10% are based on approximately 100 analyses of I/S.

Figure 6-1 Physico-chemical classification of illite and related minerals (after Srodon and Eberl 1984).

sample can be determined from measurements of the potassium content and the amount of  $^{40}\text{Ar}^*$ .

The K-Ar method can be applied to mineral separates or whole-rock samples which contain potassium. For a mineral separate, the 'model age' determined may be interpreted as dating the timing of crystallization, cooling, sedimentation or diagenesis as appropriate. Various general assumptions of the K-Ar method, and certain premises specific to dating illitic fault gouge are considered below.

### 6.3.2 General assumptions

The application of the K-Ar dating technique involves several general assumptions, including:

- (i) constant  $^{40}\text{K}/\text{K}$  ratio at present;
- (ii) no structurally-trapped ancient Ar;
- (iii) closed system behaviour;
- (iv) sample preparation has left no impurities.

Hamilton et al (1989) have addressed each of these issues within the context of dating diagenetic illite in hydrocarbon reservoirs.

They found that a 5% variation in  $^{40}\text{K}/\text{K}$  would have an insignificant effect on a 100Ma model age, but that the likelihood and effects of initial Ar trapped during mineral growth are difficult to quantify. Kralik et al (1987) have postulated that kaolinite in fault gouge may have trapped pore-fluid Ar during mineral growth.

Ideally, mineral separation and size fractionation should result in a sample containing single phase authigenic material uncontaminated by non-authigenic phases. Contamination by potassic-mineral grains which are older than the authigenic phase, such as feldspar or mica porphyroclasts in gouge, will contribute an excessively large amount of  $^{40}\text{Ar}^*$  resulting in an erroneously old age. Hamilton et al (1989) have demonstrated that contamination at a level below that detectable by conventional XRD (c. 2%) can significantly affect measured K-Ar ages for 50Ma authigenic illite. The authors recommend transmission electron microscopy (TEM) of dated separates but caution that the comparative grain shapes of authigenic and contaminant phases need to be accounted for in considering the effect of contaminants on apparent ages. Where the contaminant cannot be fully removed, its age and contribution (mass,  $^{40}\text{K}$  and  $^{40}\text{Ar}^*$ ) to the dated fraction should be determined to allow a 'correction factor' to be applied (eg. Burley and Flisch 1989). The effects of contamination as applied to the present study are considered further in later sections.

A basic assumption of any radiometric dating scheme is that the mineral system has remained closed to loss or gain of parent ( $^{40}\text{K}$ ) and daughter ( $^{40}\text{Ar}$ ) isotopes since mineral 'formation' or resetting. Complete resetting of the radiometric 'clock' is effected by open system behaviour with total loss of previously-accumulated  $^{40}\text{Ar}^*$ . Incomplete resetting with partial loss of  $^{40}\text{Ar}^*$  will result in an erroneously young calculated age which is geologically meaningless. For authigenic illite in reservoir rocks, Hamilton et al (1989) suggest that its fine grain size and thermal history make temperature-controlled diffusion the most likely mechanism for Ar-loss. Diffusive Ar loss from illite is probably initiated at about  $150^\circ\text{C}$  (Hunziker 1986). Using a simple model, Hamilton et al (1989) found that for a grain width of  $0.1\mu\text{m}$  and a heating period of 100Ma at a temperature of  $180^\circ\text{C}$ , the calculated age of an illite would be reduced by 15%. For illite in fault gouge the effects of fluid flow and shear stress, as well as grain size and heat, may be significant in controlling Ar diffusion.

### 6.3.3 Dating authigenic illite in fault gouge

In general, isotopic dating of fault gouge to constrain the age of last movement on a fault is only possible if four primary criteria can be satisfied:

- (i) mineral growth is shown on textural grounds to post-date last movement on a fault;
- (ii) the mineral contains a suitable parent radio isotope in its lattice;
- (iii) the mineral has not suffered significant alteration;
- (iv) the mineral can be separated from contaminant phases, or, the effects of contaminants on model ages can be accounted for.

Relevant general assumptions of the K-Ar method have been considered above. There are, in addition, several premises specific to dating authigenic illite in fault gouge which need to be considered.

#### (a) **Timing of authigenesis**

Field and experimental studies (eg. Stel 1981; Rutter and Maddock 1992) indicate that crystal growth in fault rocks follows rapidly after fault movement. This is likely to be the case for authigenic illite in gouge. If, however, there is a significant hiatus between fault slip and illite growth then the ages determined on the clay will underestimate the age of faulting.

The duration of illite growth can affect the calculated age. In an undisturbed system, the K-Ar model age corresponds to an 'average' age of all illitic material

in the dated separate. In most published studies of dating reservoir and fault gouge illites (eg. Lee et al 1989; Kralik et al 1987), measured K-Ar model ages decrease with decreasing grain size. This has been interpreted to indicate that the smallest grain sizes reflect the most recent grain growth. Thus a K-Ar age determined on the finest fractions could again potentially underestimate the age of faulting.

#### **(b) Grain growth**

Paradoxically, it is also possible for the grain size of authigenic illite to increase with decreasing age as a consequence of recrystallization. Such recrystallization, known as 'Ostwald Ripening', is driven in an effort to reduce surface free energy which is maximised where the range of particle sizes is great (Eberl et al 1990). Although this process has been shown to affect the measured isotopic ages of clay minerals (Eberl et al 1990), in the overwhelming number of cases, measured ages decrease with decreasing grain size (as discussed above).

#### **(c) Reactivation and resetting**

Petrographic and microstructural examination of the fault gouges in the present study have demonstrated that they have suffered more than one episode of fault slip and subsequent cementation (ie. authigenic mineral growth). Such reactivation can have various effects on the measured ages.

If reactivation and authigenic mineral growth take place over a geologically short time scale, say a few million years, then for faulting which took place one hundred or more million years ago, the 'averaging' effect on a K-Ar model age may be considered trivial.

If, on the other hand, reactivation and mineral growth occur over a geologically long time scale, say tens to hundreds of million's of years the situation is more complicated. Over these longer time periods it may be anticipated that populations of clay minerals, with distinctive chemistries and morphologies, might be formed during different faulting events. It may also be the case that the isotopic systems of earlier-formed assemblages are wholly or partially reset during later faulting and hydrothermal activity. (Partial resetting is a problem as it will lead to misleading age data). In most situations, illitic material will become progressively coarser-grained with time, and earlier generations may be treated as porphyroclastic contaminants which, ideally, should be isolated and removed during mineral separation.

**(d) Summary statement**

Various assumptions and problems which can complicate dating fault movement by K-Ar geochronology of authigenic clays have been highlighted above. Most of the problems, and certainly those which are likely to have the greatest effect on model ages, are problems of contamination. Separating and analyzing different size fractions of clay-grade fault gouge materials should permit the youngest and finest grained clay population to be dated thereby providing the most reliable minimum age of fault movement.

**6.4 ANALYTICAL METHODS****6.4.1 Mineral separation**

Preliminary mineral separation of the bulk fault gouge samples was designed to: (i) provide quantitative information on the grain size distribution in the gouges (Section 4.8.2); (ii) to isolate grain size fractions suitable for further purification of the quartz component for ESR dating (Section 7); and (iii) to isolate a  $<2\mu\text{m}$  'clay fraction' for isotopic analysis and dating. The separations which involved sieving, gravity-settling and centrifugation were carried out at the Department of Geology, University of Manchester (described in full in Appendix 2). The dated  $<2\mu\text{m}$  fractions were prepared in this way.

Further separation of fractions smaller than  $<2\mu\text{m}$  was performed at the Scottish Universities Research and Reactor Centre (SURRC), East Kilbride following the method outlined by Hamilton et al (1989). Briefly, this involves chemical treatments designed to remove organic matter, carbonates, Fe-oxides and exchangeable cations, de-flocculation and further centrifugation. The target equivalent spherical diameter (ESD) size fractions were  $<2$ ,  $<0.5>0.1$ ,  $<0.1>0.05$  and  $<0.05\mu\text{m}$ . For brevity, these will be referred to as  $<2$ ,  $<0.5$ ,  $<0.1$  and  $<0.05\mu\text{m}$ .

**6.4.2 Mineral characterization****(a) XRD**

XRD analysis of ten dated  $<0.1$  and  $<0.05\mu\text{m}$  separates was carried out using the silicon disc method. This approach has the advantages that only a few mg of sample are required and the discs give minimal background allowing very minor components to be detected. The disadvantage is that the discs cannot withstand heating for further characterization of the clay mineralogy. The analyses were made on a Phillips 1820 automated X-ray diffractometer at the Department of Geology, Imperial

College, London. Using Ni-filtered  $\text{CuK}_\alpha$  radiation, the samples were scanned at a rate of 10s per  $0.02^\circ$  step width using 0.3mm slits from  $2$  to  $40^\circ 2\theta$ . After spraying with glycol the discs were scanned again from  $2$  to  $26^\circ 2\theta$ . The detection limit is estimated at 2%.

#### (b) STEM and SEM

STEM (scanning transmission electron microscopy) analysis was performed on the same separates analyzed by XRD. The analyses were performed to provide complimentary information on the mineralogy, mineral chemistry, grain shape and grain size. For each sample, a flake of the aggregated clay was dispersed in acetone and deposited by pipette onto a carbon-coated formvar covered copper grid; a further C-coat was applied to minimise charging of the clay particles. The grids were examined in a JEOL 120CX STEM fitted with a semi-quantitative energy-dispersive (EDS) X-ray analyzer, at the Department of Metallurgy, Imperial College.

An intact sample of fault gouge was also analyzed by STEM. 3mm diameter Cu foils were glued to an uncovered 'Lakeside' mounted thin-section, cut out and ion-beam thinned using a cold stage to minimise damage to the clays. The foils were C-coated prior to examination.

In a further effort to characterize the mineral chemistry of the dated separates, four grainsize fractions were analyzed by SEM microprobe. The sample material was mixed with a drop of spec-pure methylated spirits, sedimented by pipette onto a polished graphite disc and carbon-coated (after Peters and Hofmann (1984)).

#### 6.4.3 K-Ar analysis

All isotope analyses (K-Ar, Rb-Sr,  $\delta^{18}\text{O}$  and  $\delta\text{D}$ ) were carried out at SURRC.

Potassium was determined by flame photometry (Corning 410C instrument) of acid-digested samples of  $<0.1\text{g}$  mass. Argon was extracted and purified in vacuo from separate samples each weighing  $<0.1\text{g}$ . Single determinations of both K and of Ar were made owing to the limited amounts of sample.  $^{40}\text{Ar}$  was determined by the isotope dilution method using  $^{38}\text{Ar}$  tracer, the analyses being performed on an AEI MS10 mass spectrometer operated in the static mode. Further details of the analytical methods are given in Macintyre and Hamilton (1984) and Miller et al (1991).



#### 6.4.4 Rb-Sr analysis

Analyses and data reduction followed the methods given in Macintyre and Hamilton (1984). Concentrations of Rb and Sr and the  $^{87/86}\text{Sr}$  ratio were determined for a single dissolution of c.50mg of sample. Rb and Sr were separated by ion-exchange chromatography. Concentrations by isotope dilution and isotopic ratios respectively were measured by VG Micromass 30B and VG Isomass 54E. Isochron ages were calculated using an algorithm after D. York.

#### 6.4.5 Stable isotope analysis

Stable isotope analyses followed the methods summarised by Miller et al (1991). Briefly, the samples were vacuum-dried overnight at 200°C to remove adsorbed and interlayer water ( $\text{H}_2\text{O}$ ). Hydrogen was extracted from the dried samples by RF induction furnace at 1200°C, with water vapour converted to  $\text{H}_2$  by reaction with hot uranium. The  $\text{H}_2$  yield was measured manometrically and its isotopic composition measured in a modified VG 602B mass spectrometer previously calibrated against SMOW and SLAP standards. Analytical precision is  $\pm 3\%$  ( $1\sigma$ ). Oxygen was extracted by reaction with  $\text{ClF}_3$  at 680°C overnight. The oxygen was then reduced to  $\text{CO}_2$  by contact with red-hot carbon and analyzed in a VG SIRA 10 mass spectrometer against a reference gas previously calibrated against international standards.

The 'structural' water content ( $\text{H}_2\text{O}^+$ ) of the samples was calculated from the hydrogen yield.

### 6.5 SAMPLE CHARACTERIZATION RESULTS

#### 6.5.1 Sample details

The choice of gouge samples selected for dating was dictated by the amount of material that could be collected. The samples used for isotopic dating are listed in Table 6-1. Details of the fracture and fault zone localities and the petrography of some the bulk samples have been described in Sections 3 and 4 respectively.

Attempts were made to separate grain size fractions down to  $<0.05\mu\text{m}$  from each bulk gouge sample. In practice, variations in the amount of bulk gouge available and the mass-yields of the finest fractions meant that in some cases the smallest fraction which could be analyzed was  $<0.1\mu\text{m}$ . Priority was given to K-Ar and then stable isotope analysis. For sample characterisation priority was given to the finest fractions using XRD and STEM; SEM examination of four separates was made on a trial basis.

Table 6-1 Materials selected for isotopic dating

Fracture Zone or Locality	Sample No	Rock Type	Comment
Information gallery	A91/23	fault gouge	possible vein infill rather than fault? repeat sampling on second (1992 visit)
	A92/7	fault gouge	
	A92/7	feldspar porphyroclasts	
Geochemistry Laboratory	A92/9	cataclasite/vein	
	A92/9	feldspar porphyroclasts	
EW-7	A91/14	chlorite breccia	spherulitic chlorite
NE-4	A91/6	fault gouge	tunnel wall
	A91/32	fault gouge	tunnel floor
	A91/36	cataclasite	tunnel floor
	A91/11	wallrock	whole-rock analysis
NE-3	A91/38	fault gouge	
	A91/39	fault gouge	
	A91/41	wallrock	

A complete listing of analyses performed on the different fractions for each sample is given in Table 6-2.

#### 6.5.2 XRD analysis

The mineralogy of the  $<2\mu\text{m}$  fractions of the majority of the dated gouge samples, as determined by conventional XRD, is shown in Table 4-1. The clay mineralogy of all samples is dominated by mixed-layer I-S, with 5-13% expandable layers and random to ordered structure. Mixed-layer chlorite-smectite, illite and/or kaolinite are also present in some samples, with  $<2\mu\text{m}$  fraction gouges from different localities apparently characterised by different abundances of these phases. In particular, A91/23 from the Information Gallery contains significant amounts of illite and chlorite-smectite whereas these phases are subordinate or absent from fracture zone NE-4 and NE-3 samples. With the exception of sample A91/23, however, the  $<2\mu\text{m}$  fractions also contain significant amount of quartz, feldspar, white mica and/or chlorite, all of which can be assumed to be dominantly porphyroclastic phases (although authigenic K-spar also occurs, see Section 4.5.4).

The mineralogy of ten of the dated finer fractions as determined by silicon disc XRD and by STEM 'point counting' is given in Table 6-3. The XRD traces are shown in Fig 6-2. The XRD analyses show the following:

- (i) The mineralogy of the separates is in all cases dominated by illite or I-S. Discrimination between these two phases by XRD proved problematic because of difficulties in glycolating the separates. In some cases the glycol formed a surface layer rather than mixing properly. Where mixing was achieved,

Table 6-2 Sample fraction characterisation

Sample	K-Ar	$\delta^{18}\text{O}$ & $\delta\text{D}$	XRD	STEM	SEM
A91/23 <2 $\mu\text{m}$	✓	-	✓	-	-
<0.5 $\mu\text{m}$	✓	✓	-	-	-
<0.1 $\mu\text{m}$	✓	✓	*✓	✓	-
<0.05 $\mu\text{m}$	✓	✓	*✓	✓	✓
A92/7 <2 $\mu\text{m}$	✓	✓	-	-	-
<0.1 $\mu\text{m}$	✓	✓	-	-	✓
<0.05 $\mu\text{m}$	✓	✓	✓	✓	-
A92/9 <2 $\mu\text{m}$	✓	✓	-	-	-
<0.1 $\mu\text{m}$	✓	✓	-	-	✓
<0.05 $\mu\text{m}$	✓	-	-	-	✓
A91/6 <2 $\mu\text{m}$	✓	-	✓	-	-
<0.5 $\mu\text{m}$	✓	✓	-	-	-
<0.1 $\mu\text{m}$	✓	✓	*✓	✓	-
A91/32 <2 $\mu\text{m}$	✓	-	✓	-	-
<0.5 $\mu\text{m}$	✓	✓	-	-	-
<0.1 $\mu\text{m}$	✓	✓	*✓	✓	-
<0.05 $\mu\text{m}$	✓	✓	*✓	✓	-
A91/36 <2 $\mu\text{m}$	✓	-	✓	-	-
<0.5 $\mu\text{m}$	✓	✓	-	-	-
<0.1 $\mu\text{m}$	✓	-	*✓	✓	-
A91/38 <2 $\mu\text{m}$	✓	-	✓	-	-
<0.5 $\mu\text{m}$	✓	-	-	-	-
<0.1 $\mu\text{m}$	✓	✓	*✓	✓	-
A91/39 <2 $\mu\text{m}$	✓	-	✓	-	-
<0.5 $\mu\text{m}$	✓	✓	-	-	-
<0.1 $\mu\text{m}$	✓	✓	*✓	✓	-
<0.05 $\mu\text{m}$	✓	✓	*✓	✓	-

Note: \* denotes XRD analysis by silicon disc technique (otherwise conventional 'clay fraction' analysis)

however, there is little difference between air-dried and glycolated traces. Comparison of these analyses with the more comprehensive XRD analyses performed on the <2 $\mu\text{m}$  fractions of the same samples would tend to favour I-S with a small component of expanding phases rather than illite, except perhaps A91/23.

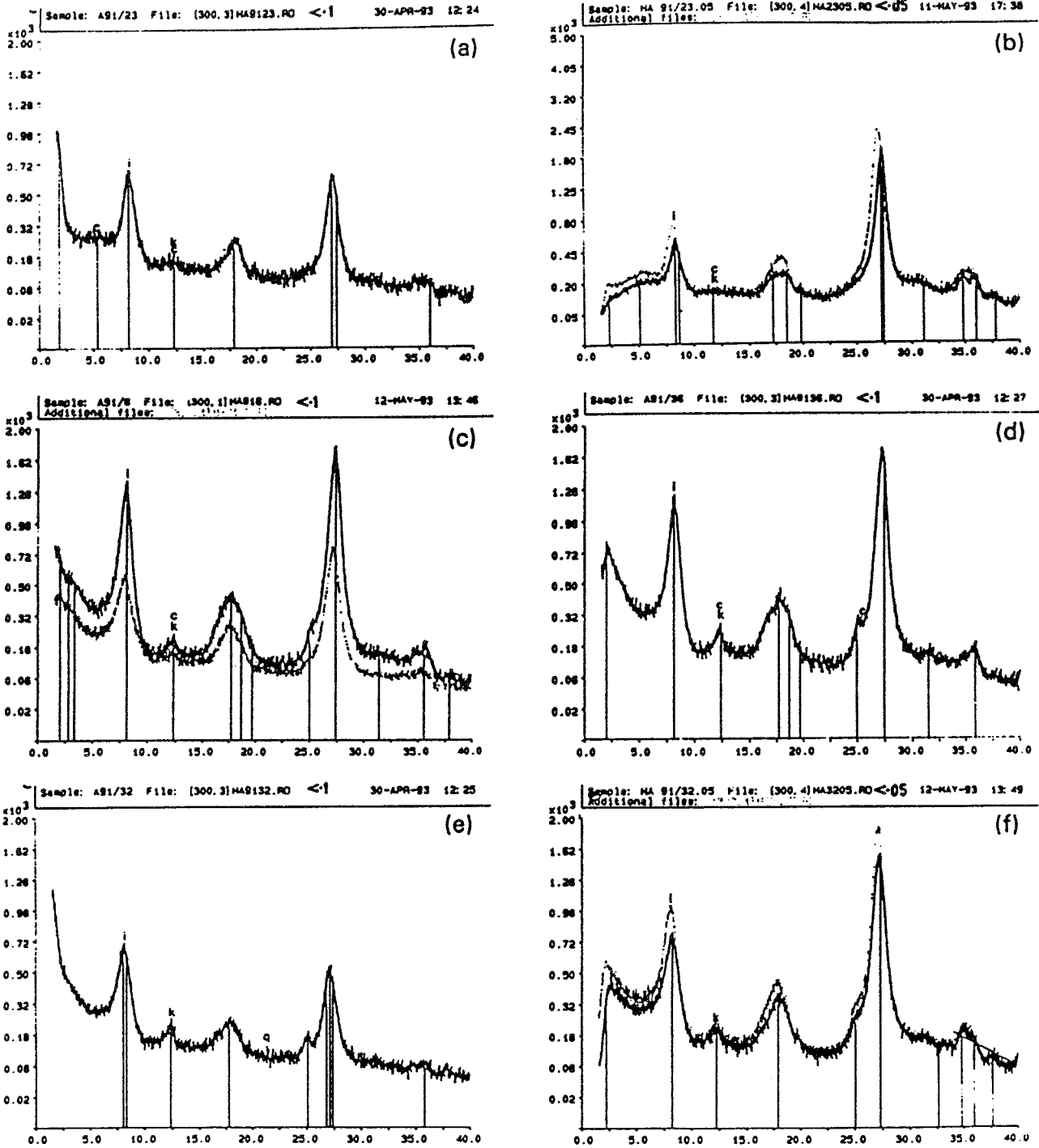


Figure 6-2 XRD traces of selected dated gouge size fractions. (a) A91/23 [ $<0.1\mu\text{m}$ ]; (b) A91/23 [ $<0.05\mu\text{m}$ ]; (c) A91/6 [ $<0.1\mu\text{m}$ ]; (d) A91/36 [ $<0.1\mu\text{m}$ ]; (e) A91/32 [ $<0.1\mu\text{m}$ ]; (f) A91/32 [ $<0.05\mu\text{m}$ ].

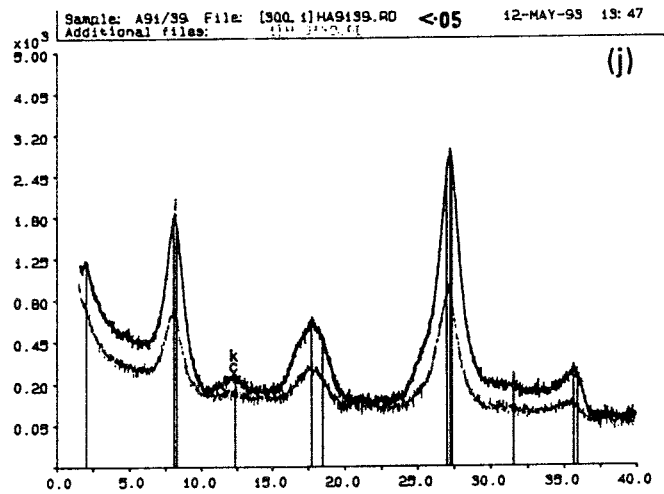
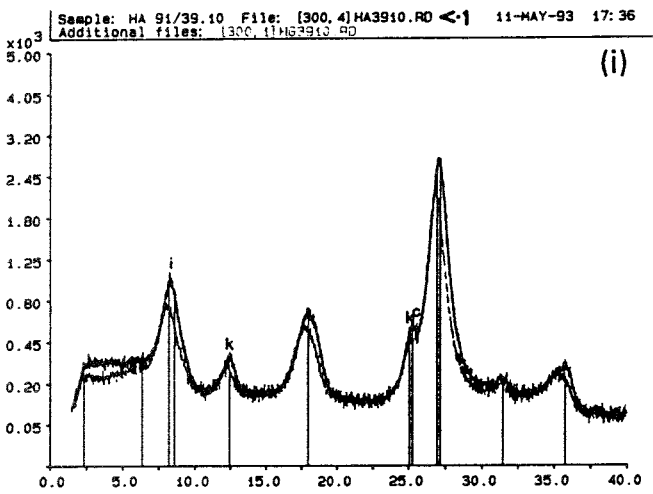
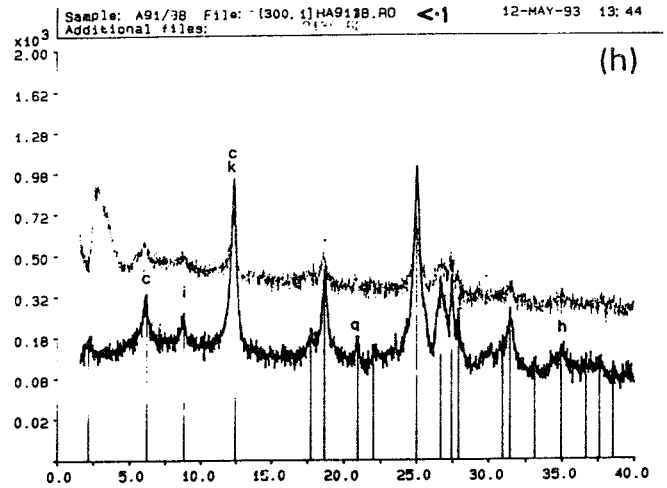
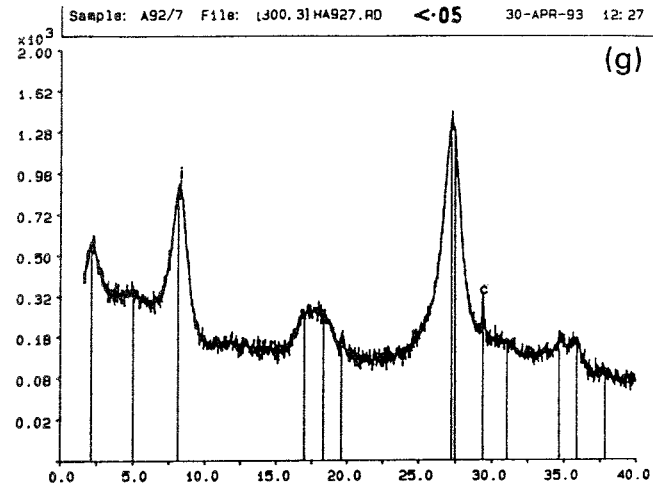


Figure 6-2 (cont) XRD traces of selected dated gouge size fractions. (g) A92/7 [ $<0.05\mu\text{m}$ ]; (h) A91/38 [ $<0.1\mu\text{m}$ ]; (i) A91/39 [ $<0.1\mu\text{m}$ ]; (j) A91/39 [ $<0.05\mu\text{m}$ ].

- (ii) Minor or trace amounts of kaolinite and/or chlorite were detected in more than half of the separates and are present in each of the fracture zones sampled. Quartz was detected in two separates, and calcite in one.
- (iii) The purest separates of illitic material indicated by XRD are both size fractions of A91/23, and A91/39 [ $<0.05\mu\text{m}$ ].
- (iv) The least pure separate is A91/38 [ $<0.1\mu\text{m}$ ] which is contaminated by several mineral phases including K-spar and albite. Trace amounts of K-spar were also detected in A92/7 [ $<0.1\mu\text{m}$ ].

Table 6-3 Summary XRD mineralogy, STEM 'area modal' analyses and grain sizes for dated gouge fractions

SAMPLE SIZE FRACTION	A91/23 $<0.1\mu\text{m}$		A91/23 $<0.05\mu\text{m}$		A92/7 $<0.05\mu\text{m}$		A91/6 $<0.1\mu\text{m}$		A91/32 $<0.1\mu\text{m}$	
	STEM	XRD	STEM	XRD	STEM	XRD	STEM	XRD	STEM	XRD
illite/I-S	100	D	97	D	87	D	98	D	95	D
kaolinite	-	T	-	T	-	-	-	M	-	M
chlorite	-	T	-	T	-	-	-	T	1	-
quartz	-	-	1	*	13	-	2	-	4	T
K-feldspar	-	-	-	-	-	-	-	-	-	-
albite	-	-	-	-	-	-	-	-	-	-
calcite	-	-	-	-	-	M	-	-	-	-
CaSO <sub>4</sub>	-	-	2	-	-	-	-	-	-	-
pyrite	-	-	T	-	-	-	-	-	-	-
hematite	-	-	-	-	-	-	-	-	-	-
Measured size ( $\mu\text{m}$ )	99% $<0.4$ 58% $<0.1$		92% $<0.2$ 25% $<0.05$		98% $<0.2$ 42% $<0.05$		95% $<0.4$ 58% $<0.1$		99% $<0.4$ 52% $<0.1$	

SAMPLE SIZE FRACTION	A91/32 $<0.05\mu\text{m}$		A91/36 $<0.1\mu\text{m}$		A91/38 $<0.1\mu\text{m}$		A91/39 $<0.1\mu\text{m}$		A91/39 $<0.05\mu\text{m}$	
	STEM	XRD	STEM	XRD	STEM	XRD	STEM	XRD	STEM	XRD
illite/I-S	98	D	92	D	91	D	99	D	100	D
kaolinite	-	M	-	M	-	-	-	M	-	M
chlorite	-	?	-	M	1	M	-	M	-	-
quartz	1	-	8	-	6	M	1	-	-	-
K-feldspar	-	-	-	-	2	M	-	-	-	-
albite	-	-	-	-	-	M	-	-	-	-
calcite	1	-	-	-	-	-	-	-	-	-
CaSO <sub>4</sub>	-	-	-	-	-	-	-	-	-	-
pyrite	-	-	-	-	-	-	-	-	-	-
hematite	-	-	-	-	-	T	-	-	-	-
Measured size ( $\mu\text{m}$ )	98% $<0.2$ 53% $<0.05$		98% $<0.4$ 58% $<0.1$		98% $<0.4$ 38% $<0.1$		100% $<0.4$ 51% $<0.1$		96% $<0.2$ 52% $<0.05$	

Note: 1) D = dominant phase; M = minor phase; T = trace; ? = possible presence  
2) measured size = grain lengths for c. 100 grains

6.5.3 STEM analysis

For each grain size separate prepared for STEM analysis, the maximum and minimum dimensions of about 100 grains were measured directly from the screen image at known magnification. Lath- and euhedral to subhedral platy grains were assumed to be illite, a few grains of illite were semi-quantitatively analyzed from each sample; other grains were also analyzed to determine their composition. The results of these analyses are presented as TEM micrographs (Fig 6-3) and cross-plots of grain length against width (Fig 6-4), together with 'area modal analyses' and summary grainsize statistics (Table 6-3). The mineral analyses are considered in the next section.

The STEM measurements and observations indicate:

- (i) The STEM data compliment the XRD results in confirming that the separates are dominated by illitic material, typically >90% of the area mode. With the exception of A92/7 [ $<0.05\mu\text{m}$ ], the degree of contamination by non-illitic phases is small.
- (ii) The measured grainsize distributions confirm that the separations were effective. In most cases, significantly more than 50% of the measured grains have a length less than twice the nominal equivalent spherical diameter (ESD); maximum grain lengths are usually about four times the nominal ESD.
- (iii) The most widespread and abundant non-illitic phase detected by STEM is quartz. The quartz particles vary in size but tend to be concentrated in the coarser tails. In the  $<0.1\mu\text{m}$  fraction of sample A91/38 (FZ NE-3) coarse grains of quartz have an anhedral habit suggesting that, like the feldspar in this separate, they are porphyroclastic in origin (Fig 6-3j). In contrast, the euhedral form of a quartz grain in the  $<0.1\mu\text{m}$  fraction of sample A91/6 indicates that it is authigenic.
- (iv) A specific search was made for K-spar, potentially the most serious contaminant contributing potassium and radiogenic argon to the system. STEM analysis confirmed the XRD-indicated presence of K-spar in the  $<0.1\mu\text{m}$  fraction of A91/38, but not that suspected in the  $<0.1\mu\text{m}$  fraction of A92/7. The K-spar in A91/38 [ $<0.1\mu\text{m}$ ] is coarse-grained (0.3-0.4 $\mu\text{m}$  length) and subhedral to anhedral in form (Fig 6-3j). In this sample from NE-3, the K-spar is almost certainly porphyroclastic rather than authigenic in origin.
- (v) The grain shapes of the illitic materials vary from one separate to another, and to a lesser extent within individual separates.

Strongly-euhedral pseudo-hexagonal plates and laths are particularly prominent in A91/23 [ $<0.05\mu\text{m}$ ], A91/32 [ $<0.05\mu\text{m}$ ], A91/38 [ $<0.1\mu\text{m}$ ] and A91/39 [ $<0.1\mu\text{m}$ ] (Fig 6-3b, h & k). Most notably, the euhedral laths and plates seen in A91/32 [ $<0.05\mu\text{m}$ ] are closely similar in form to the demonstrably authigenic euhedral illitic material seen by SEM examination of fracture surfaces of the intact gouge material (cf. Fig 4-11).

Less-strongly euhedral pseudo-hexagonal plates and laths were apparent in A91/23 [ $<0.1\mu\text{m}$ ], A91/6 [ $<0.1\mu\text{m}$ ], A91/36 [ $<0.1\mu\text{m}$ ], A91/32 [ $0.1\mu\text{m}$ ], A92/7 [ $<0.05\mu\text{m}$ ] and A91/39 [ $<0.05\mu\text{m}$ ] (Fig 6-3).

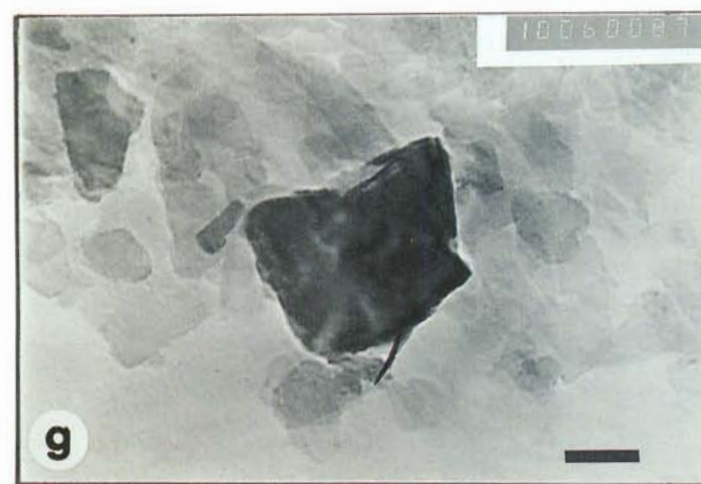
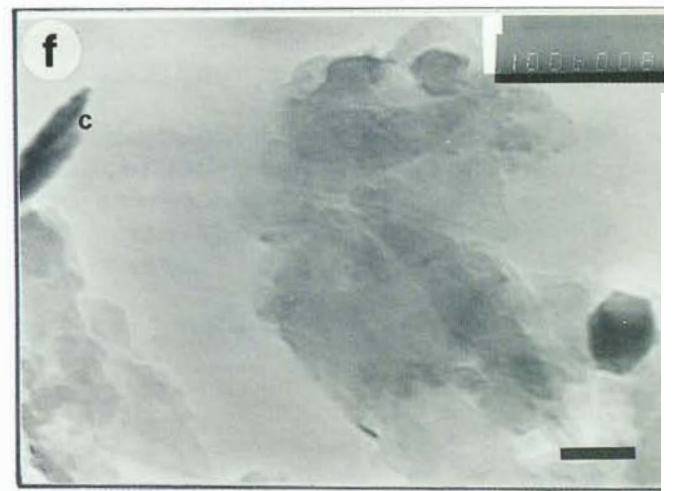
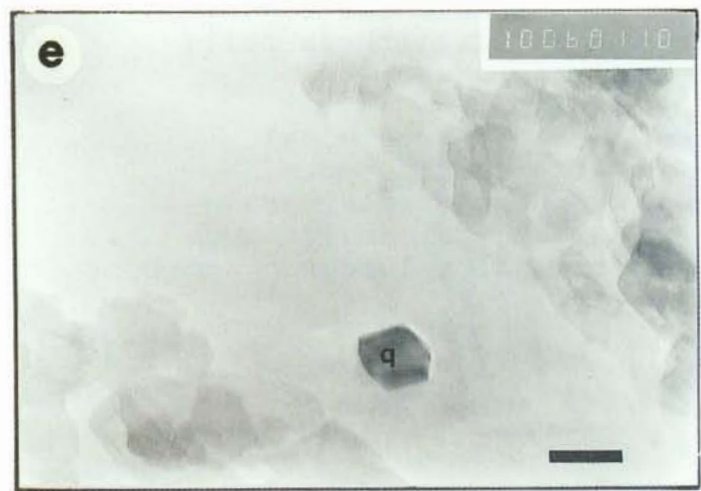
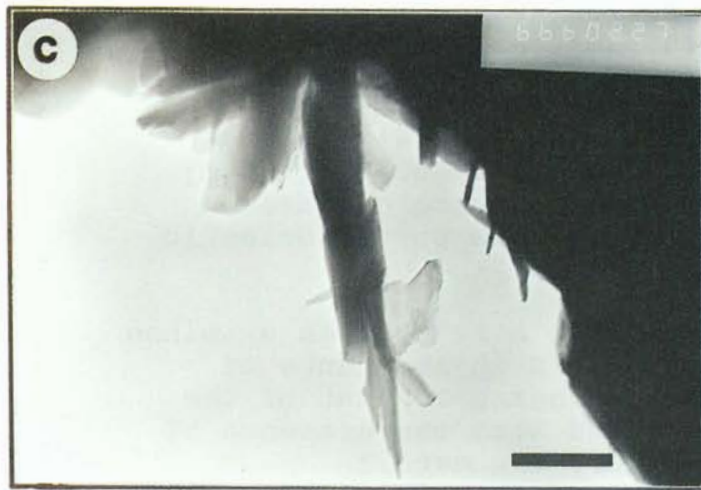
Larger and thicker, equant but anhedral illitic grains occur in A91/32 [ $<0.1\mu\text{m}$ ] and A92/7 [ $<0.05\mu\text{m}$ ]. In both cases the size and appearance of these grains might suggest that they are porphyroclastic rather than authigenic.

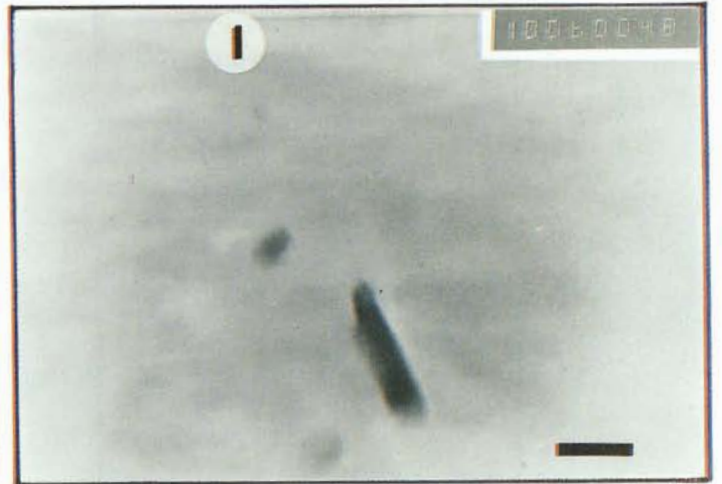
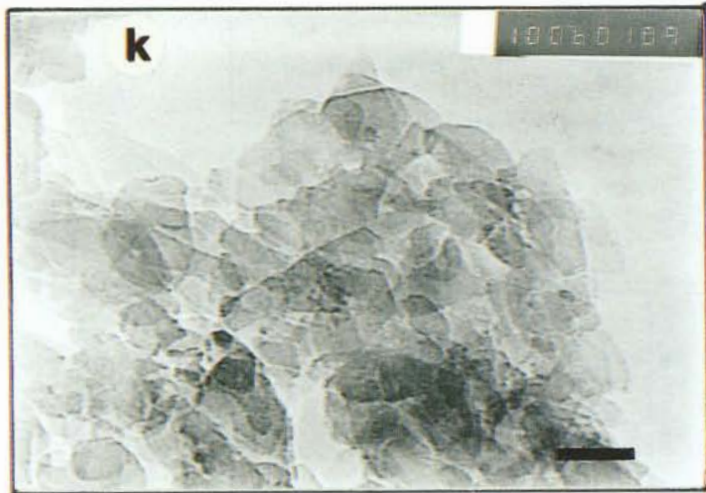
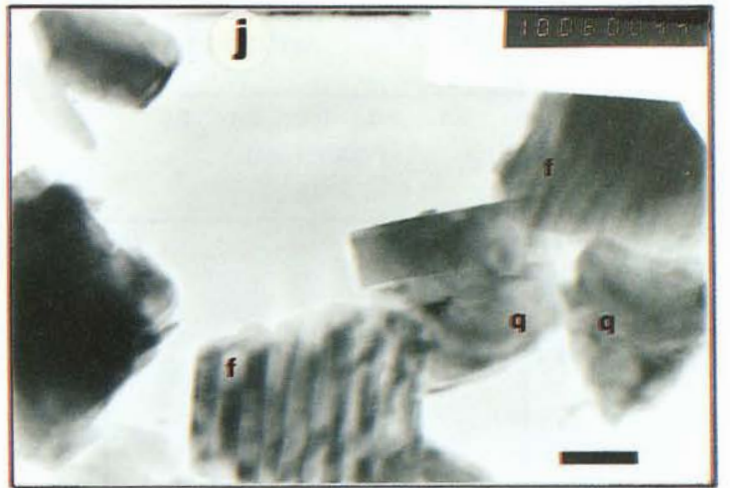
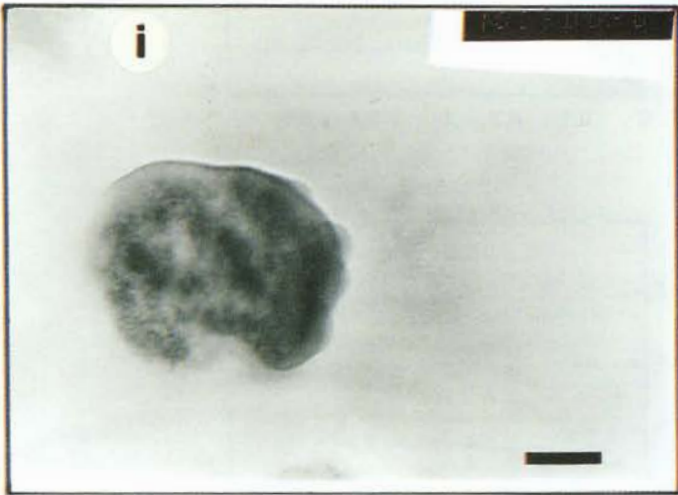
- (vi) Intact gouge from NE-4 (sample A91/30B) was examined by STEM. The analysis confirmed an abundance of illitic laths of similar grain size to that of the separates (Fig 4-4c & d), and also the presence of fine-grained quartz. However, the detail characteristics of the grain shapes and microstructures could not be assessed due to problems in ion-thinning the samples (three foils were thinned).

Using the size and mineralogical data, 'area modal analyses' were estimated. It is important to note, however, that because of the very inequant clay grain shapes (ie. they are thin), the area modal analyses do not correspond directly to conventional volumetric modal analyses.

**Figure 6-3** [overleaf] TEM micrographs of dated grain size separates and intact gouge. (a) A91/23 [ $<0.1\mu\text{m}$ ] showing equant and lath-shaped illites; (b) A91/23 [ $<0.05\mu\text{m}$ ] showing aggregates of lath illite; (c), (d) A91/36 intact gouge showing fine-grained illite; (e) A91/6 [ $<0.1\mu\text{m}$ ] showing pseudo-hexagonal illite and euhedral quartz grain (q); (f) A91/36 [ $<0.1\mu\text{m}$ ] showing mainly euhedral illite and chlorite lath (c); (g) A91/32 [ $<0.1\mu\text{m}$ ] showing equant, lath and large irregular illite; (h) A91/32 [ $<0.05\mu\text{m}$ ] showing pure separate of euhedral lath and platy illite grains; (i) A92/7 [ $<0.05\mu\text{m}$ ] showing ; (j) A91/38 [ $<0.1\mu\text{m}$ ] showing large quartz (q) and feldspar (f) grains as well as illite; (k) A91/39 [ $<0.1\mu\text{m}$ ] showing pure separate of euhedral lath and platy illite; (l) A91/39 [ $<0.05\mu\text{m}$ ] showing single illite lath.







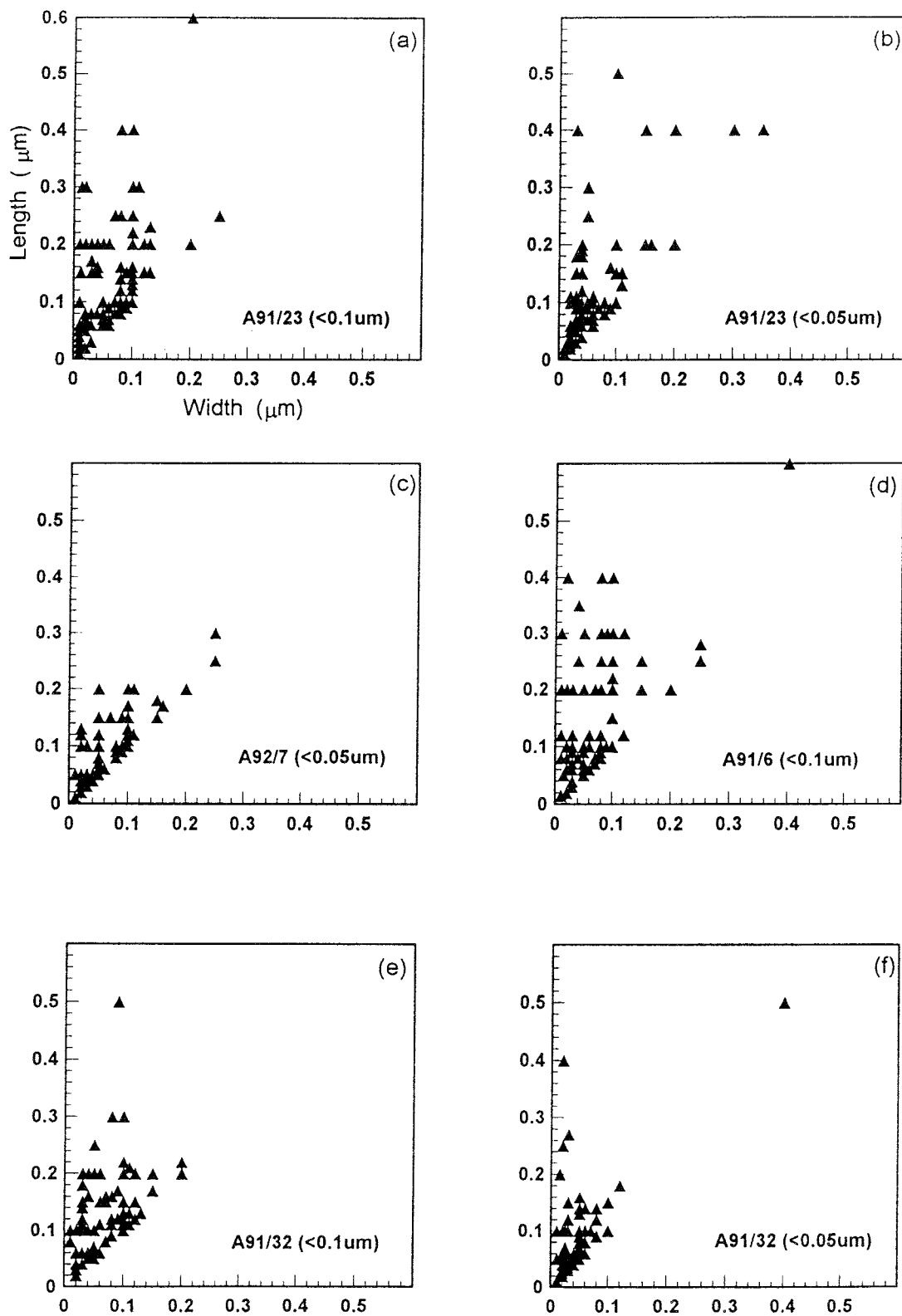


Figure 6-4 Scatter plots showing TEM measured length vs. width dimensions for selected dated separates. About 100 grains were measured for each sample. See text for discussion.

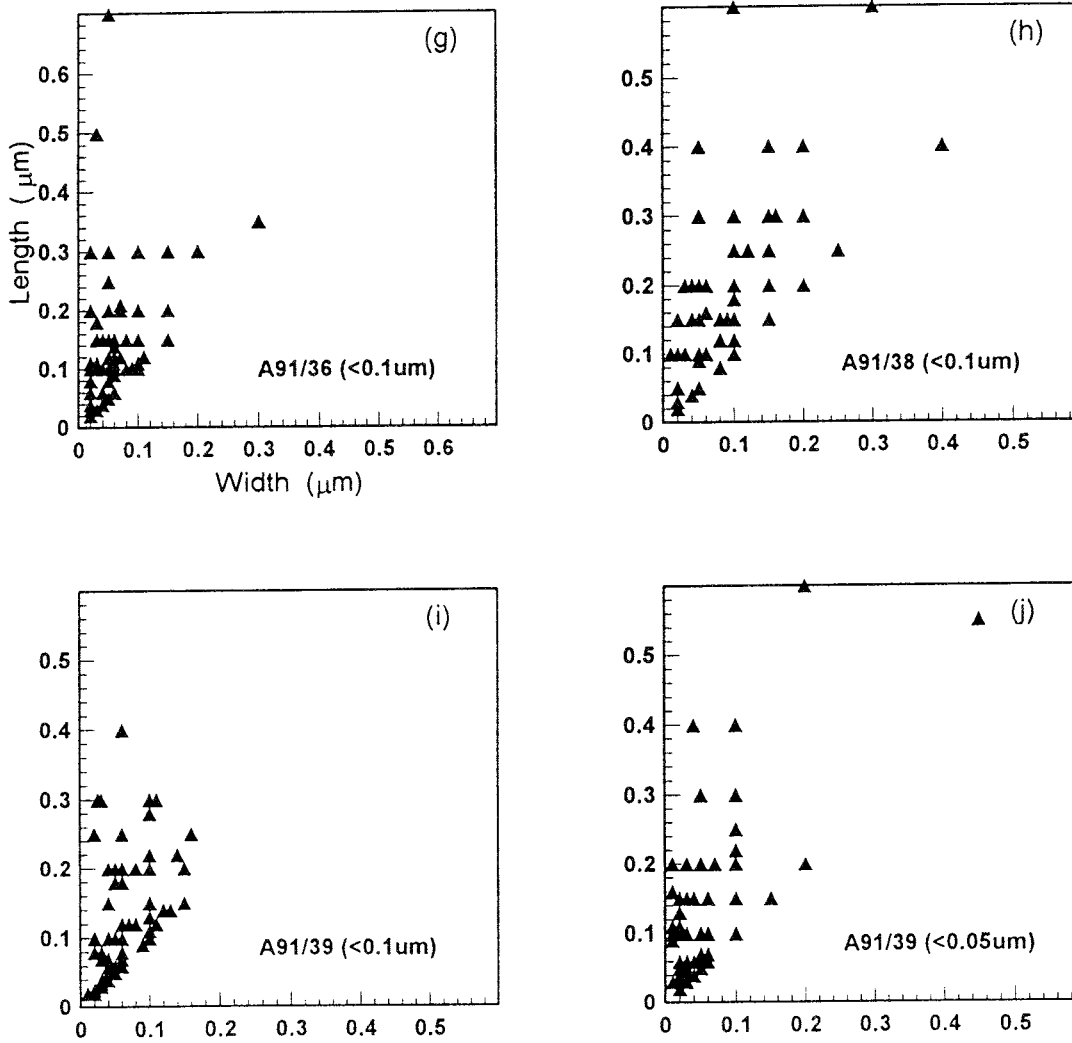


Figure 6-4 (cont)

#### 6.5.4 Mineral chemistry of illitic gouge

Quantitative SEM microprobe analyses of illitic materials from selected intact gouge samples and dated separates are shown in Table 6-4, and semi-quantitative STEM analyses of selected dated separates are given in Table 6-5. Although these constitute an incomplete suite of analyses they do permit some further interpretation.

Difficulty was encountered in de-flocculating separates for SEM microprobe analysis which may have affected the analyses due to beam-specimen geometry effects. The most reproducible and highest-total analyses were obtained by enlarging the beam to 10 $\mu$ m diameter and reducing the count time to 30s live time. Such analyses would, of course, tend to average any mixtures of mineral phases.

##### (a) SEM analyses

- (i) Authigenic illitic material filling late fractures in sample A91/30B from Fracture Zone NE-4 (Fig 4-9) has a composition, with water-content assumed from the analysis totals, consistent with I-S (Table 6-4, column 1). However, the potassium-content and assumed water-content are slightly lower and higher respectively than those measured in ten dated separates from three gouge samples from NE-4 (Tables 6-7 and 6-9).
- (ii) Authigenic phases, between the porphyroclasts in sample AS14.10 (see Figs 4-10 and 4-11) have an illitic composition (Table 6-4, columns 2 and 3).
- (iii) Sericite after feldspar, is a potential K- and Ar-bearing contaminant, but it is compositionally very different from the illitic gouge materials. Specifically, it contains more titania, alumina and potash but less magnesia and volatiles than all the analyzed gouge illitic materials (Table 6-4, column 4).
- (iv) The composition of intact illitic material and <0.1 and <0.05 $\mu$ m separates from sample A92/9 is fairly similar (Table 6-4, columns 5, 6 and 7). However, the SEM analyses and the K-determinations made for dating (Table 6-7) suggest that the separates are more potassic than the intact illitic material. The SEM analyses are consistent with I-S with a small percentage of expanding layers. No very significant difference in composition is apparent between the two grain size fractions (The high Na-content of the <0.05 $\mu$ m fraction of A92/9 is due to salt contamination confirmed by a chlorine peak).

Table 6-4 SEM microprobe analyses of illitic materials

	1	2	3	4	5	6	7	8	9
SiO <sub>2</sub>	51.83 (2.40)	56.34	44.20	46.63 (1.12)	51.27 (1.79)	52.42 (3.06)	50.82 (2.32)	51.49 (2.32)	51.53 (2.40)
TiO <sub>2</sub>	0.00 (0.00)	0.00	3.00	0.45 (0.39)	0.00 (0.00)	0.00 (0.00)	0.00 (0.00)	0.00 (0.00)	0.00 (0.00)
Al <sub>2</sub> O <sub>3</sub>	21.86 (0.98)	17.66	18.55	29.95 (1.35)	21.75 (0.51)	21.09 (1.12)	19.94 (0.54)	21.04 (1.10)	20.99 (1.02)
FeO	1.13 (0.30)	3.10	2.98	5.14 (0.97)	5.57 (2.18)	3.18 (0.36)	3.22 (0.18)	5.96 (0.15)	5.98 (0.28)
MnO	0.00 (0.00)	0.00	0.00	0.00 (0.00)	0.00 (0.00)	0.00 (0.00)	0.00 (0.00)	0.00 (0.00)	0.00 (0.00)
MgO	3.13 (0.24)	2.49	2.56	1.87 (1.06)	4.36 (1.52)	3.86 (0.30)	3.59 (0.32)	3.51 (0.30)	3.73 (0.36)
CaO	0.74 (0.17)	0.62	0.00	0.00 (0.00)	0.71 (0.10)	0.68 (0.03)	0.37 (0.53)	0.74 (0.15)	0.05 (0.11)
Na <sub>2</sub> O	0.00 (0.00)	0.23	0.81	0.11 (0.19)	0.10 (0.17)	0.12 (0.16)	3.25 (0.43)	0.00 (0.00)	0.77 (0.14)
K <sub>2</sub> O	4.95 (0.54)	6.79	6.38	8.60 (0.34)	5.71 (0.32)	6.85 (0.48)	6.46 (0.25)	7.06 (0.26)	6.97 (0.26)
Total	83.64	87.23	78.48	92.76	89.48	88.20	87.65	89.80	90.00
Oxygen	22.00 (0.00)	22.00	22.00	22.00 (0.00)	22.00 (0.00)	22.00 (0.00)	22.00 (0.00)	22.00 (0.00)	22.00 (0.00)
Si	7.51 (0.07)	7.98	7.10	6.43 (0.04)	7.20 (0.20)	7.40 (0.02)	7.33 (0.04)	7.28 (0.02)	7.27 (0.04)
Al	3.73 (0.07)	2.95	3.51	4.87 (0.24)	3.60 (0.12)	3.51 (0.05)	3.39 (0.06)	3.50 (0.02)	3.49 (0.03)
Fe2	0.14 (0.03)	0.37	0.40	0.59 (0.12)	0.65 (0.25)	0.38 (0.02)	0.39 (0.03)	0.71 (0.03)	0.71 (0.05)
Mg	0.67 (0.03)	0.53	0.61	0.38 (0.22)	0.91 (0.31)	0.81 (0.02)	0.77 (0.04)	0.74 (0.03)	0.78 (0.05)
Ca	0.12 (0.03)	0.09	0.14	0.00 (0.00)	0.11 (0.02)	0.10 (0.01)	0.06 (0.08)	0.11 (0.02)	0.01 (0.02)
Na	0.00 (0.00)	0.06	0.00	0.03 (0.05)	0.03 (0.05)	0.03 (0.04)	0.91 (0.09)	0.00 (0.00)	0.21 (0.04)
K	0.92 (0.10)	1.23	1.31	1.51 (0.04)	1.02 (0.08)	1.23 (0.05)	1.19 (0.09)	1.27 (0.04)	1.25 (0.02)
Ti	0.00 (0.00)	0.00	0.36	0.04 (0.04)	0.00 (0.00)	0.00 (0.00)	0.00 (0.00)	0.00 (0.00)	0.00 (0.00)
Mn	0.00 (0.00)	0.00	0.00	0.00 (0.00)	0.00 (0.00)	0.00 (0.00)	0.00 (0.00)	0.00 (0.00)	0.00 (0.00)
Total Cat	13.08 (0.10)	13.20	13.44	13.86 (0.00)	13.52 (0.25)	13.47 (0.01)	14.03 (0.06)	13.61 (0.04)	13.72 (0.04)

- 1 mean and standard deviation (bracketed) of 10 analyses of illitic material in late fractures, sample A91/30B, Fracture Zone NE-4
- 2,3 fault gouge matrix interstitial to porphyroclasts, sample AS14.10, Fracture Zone NE-4
- 4 mean and standard deviation of 3 analyses of sericite after feldspar and biotite, core sample KAS5/FR/1-2, Fracture Zone EW-5
- 5 mean and standard deviation of 3 analyses of illitic material enclosing prehnite but predating calcite, sample A92/9
- 6 mean and standard deviation of 5 analyses of <0.1 $\mu$ m fraction of sample A92/9 (sedimented sample)
- 7 mean and standard deviation of 4 analyses of <0.05 $\mu$ m fraction of sample A92/9 (sedimented sample)
- 8 mean and standard deviation of 4 analyses of <0.1 $\mu$ m fraction of sample A92/7 (sedimented sample)
- 9 mean and standard deviation of 6 analyses of <0.05 $\mu$ m fraction of sample A91/23 (sedimented sample)

Table 6-5 Example STEM semi-quantitative analyses of illitic materials in selected gouge size fractions

	A92/7 <0.1 $\mu$ m	A91/23 <0.1 $\mu$ m	A91/23 <0.05 $\mu$ m	A91/6 <0.1 $\mu$ m	A91/32 <0.1 $\mu$ m	A91/32 <0.05 $\mu$ m	A91/36 <0.1 $\mu$ m	A91/38 <0.1 $\mu$ m	A91/39 <0.1 $\mu$ m	A91/39 <0.05 $\mu$ m
SiO <sub>2</sub>	61.50	62.50	59.40	58.20	59.70	59.90	62.50	61.60	60.40	59.60
TiO <sub>2</sub>	-	-	-	-	-	-	-	-	-	-
Al <sub>2</sub> O <sub>3</sub>	23.10	20.60	22.70	22.60	19.40	23.00	23.80	19.60	24.60	21.70
FeO	4.60	5.20	2.70	5.70	4.90	2.50	3.50	8.00	1.70	7.20
MnO	0.10	0.10	0.00	0.70	0.10	0.10	0.10	0.30	0.30	0.10
MgO	0.10	1.10	3.30	1.80	3.50	2.20	0.10	0.20	2.50	0.10
CaO	1.20	0.90	3.00	1.80	3.20	2.80	1.00	0.70	1.40	2.00
Na <sub>2</sub> O	0.30	0.30	0.20	0.20	0.00	0.80	0.30	0.30	0.60	0.20
K <sub>2</sub> O	9.00	9.20	8.60	8.90	9.20	8.80	8.70	9.20	8.40	9.00
Total	99.90	99.90	99.90	99.90	100.00	100.10	100.00	99.90	99.90	99.90
Oxygen	22.00	22.00	22.00	22.00	22.00	22.00	22.00	22.00	22.00	22.00
Si	7.72	7.87	7.47	7.44	7.62	7.52	7.76	7.88	7.50	7.63
Al	3.42	3.06	3.36	3.40	2.92	3.40	3.48	2.96	3.60	3.27
Fe2	0.48	0.55	0.28	0.61	0.52	0.26	0.36	0.86	0.18	0.77
Mg	0.02	0.21	0.62	0.34	0.67	0.41	0.02	0.04	0.46	0.02
Ca	0.16	0.12	0.40	0.25	0.44	0.38	0.13	0.10	0.19	0.27
Na	0.07	0.07	0.05	0.05	0.00	0.20	0.07	0.07	0.14	0.05
K	1.44	1.48	1.38	1.45	1.50	1.41	1.38	1.50	1.33	1.47
Ti	-	-	-	-	-	-	-	-	-	-
Mn	0.01	0.01	0.00	0.08	0.01	0.01	0.01	0.03	0.03	0.01
Total Cat	13.33	13.37	13.56	13.61	13.67	13.58	13.22	13.43	13.44	13.49

Note: 1) all analyses are semi-quantitative  
2) - = not analyzed

- (v) The  $<0.1$  and  $<0.05\mu\text{m}$  separates from the Information Gallery gouge zone are nearly indistinguishable in composition but are notably more Fe- and K-rich than the (duplicate) A92/9 separates (Table 6-4, columns 8 and 9). The potassium-contents determined by microprobe are closely similar to those measured during K-Ar analysis (Table 6-7). On average, the potassium-content of the dated fractions from the Information gallery are about 0.5wt% K higher than the dated fractions from the other three fracture zones. This observation, together with the XRD results of the  $<2\mu\text{m}$  fraction of A91/23 (Table 4-1), suggests a greater content of illite relative to I-S in these samples.
- (vi) The microprobe oxide totals provide a semi-quantitative estimate of the water-content of the illitic materials. The mineral separates were plasma-dried at  $<100^\circ\text{C}$  prior to SEM analysis which may have resulted in some loss of  $\text{H}_2\text{O}$ . The analysis totals however are consistent with an illite composition or I-S with only a few percent expanding layers. Similarly, the  $\text{H}_2\text{O}^+$  contents of those separates whose stable isotope compositions were determined (Table 6-9) provide confirmation of the small number of expanding layers.

### (c) STEM analyses

Semi-quantitative analyses of illitic materials in the gouge fractions examined by STEM are given in Table 6-5. These analyses confirm the illitic composition of the material but are insufficiently quantitative to allow further comment.

## 6.6 K-Ar RESULTS

### 6.6.1 Countryrocks

Although the broad geological history of Äspö is well-understood, radiometric ages for the rocks are scarce (Section 2). For this reason a small number of K-Ar analyses of countryrocks were performed to provide a framework for the interpretation of the model ages for the gouge materials. Various countryrock components in the four fracture and gouge zones were analyzed (Table 6-1). The results are listed in Table 6-6.

Wallrock K-feldspar from Fracture Zone NE-3 and low-potassium, alkali-feldspar porphyroclasts ( $250\text{-}2000\mu\text{m}$  fraction) yielded K-Ar model ages in the range c. 1100-1300Ma. In contrast, similar low-potassium alkali feldspar porphyroclasts of the same grain size from the Geochemistry Laboratory fault yielded a model age of



755Ma. The 1100-1300Ma ages are consistent with isotopic closure following intrusion of the anorogenic granites (Table 2-1). The 755Ma model age substantially postdates the youngest intrusions and suggests that fault-related activity either suppressed the closure age or caused Ar-loss from the porphyroclastic feldspar.

Spherulitic vein chlorite associated with quartz from Fracture Zone EW-7 (see Figs 3-4 and 4-5) yielded a model age of 718Ma. A wholerock sample of countryrock from the related NE-4 Fracture Zone yielded the youngest measured age of any countryrock sample of 437Ma.

The K-Ar model ages for the various analyzed hostrock and porphyroclast components extend over a range of 843 million years. This undoubtedly reflects real differences in the ages of these components and variation in their closure temperatures, but may also result from isotopic disturbance related to fault movements and fluid flow. Much more isotopic data (including different systems) is required to fully elucidate the origin and thermal history of the country rocks at Äspö. However, the present analyses do provide adequate data for modelling the effects of contamination of authigenic gouge materials by wallrock-derived porphyroclastic phases (Section 6.6.4).

#### 6.6.2 Gouge materials

The K-Ar analyses of the gouge separates are presented in full in Table 6-7 and the frequency distribution of model ages is shown as a function of grain size in Fig 6-5. Several features of the data are immediately apparent:

- (i) The model ages range from  $706 \pm 14.2$  to  $301.5 \pm 6.4$ Ma, with the  $1\sigma$  error generally proportional to the age and of the order of  $\pm 2.5\%$ .
- (ii) The gouge model ages are younger, irrespective of the size fraction, than all wallrock and porphyroclast model ages except for the NE-4 wholerock sample.
- (iii) Although the youngest model age corresponds to a  $<0.05\mu\text{m}$  fraction and the oldest model ages generally correspond to  $<2\mu\text{m}$  fractions (Fig 6-5), the relationship between model age and grain size is not straightforward. In only three of the eight samples does the model age systematically decrease with decreasing grain size. For five of the eight samples, however, the smallest fraction yielded the youngest age; in a sixth sample (A91/23), the age of the smallest fraction is within error of the youngest age obtained; a seventh sample (A91/38) is contaminated by porphyroclastic feldspar.

Table 6-6 K-Ar isotope analyses of wallrock and porphyroclast phases

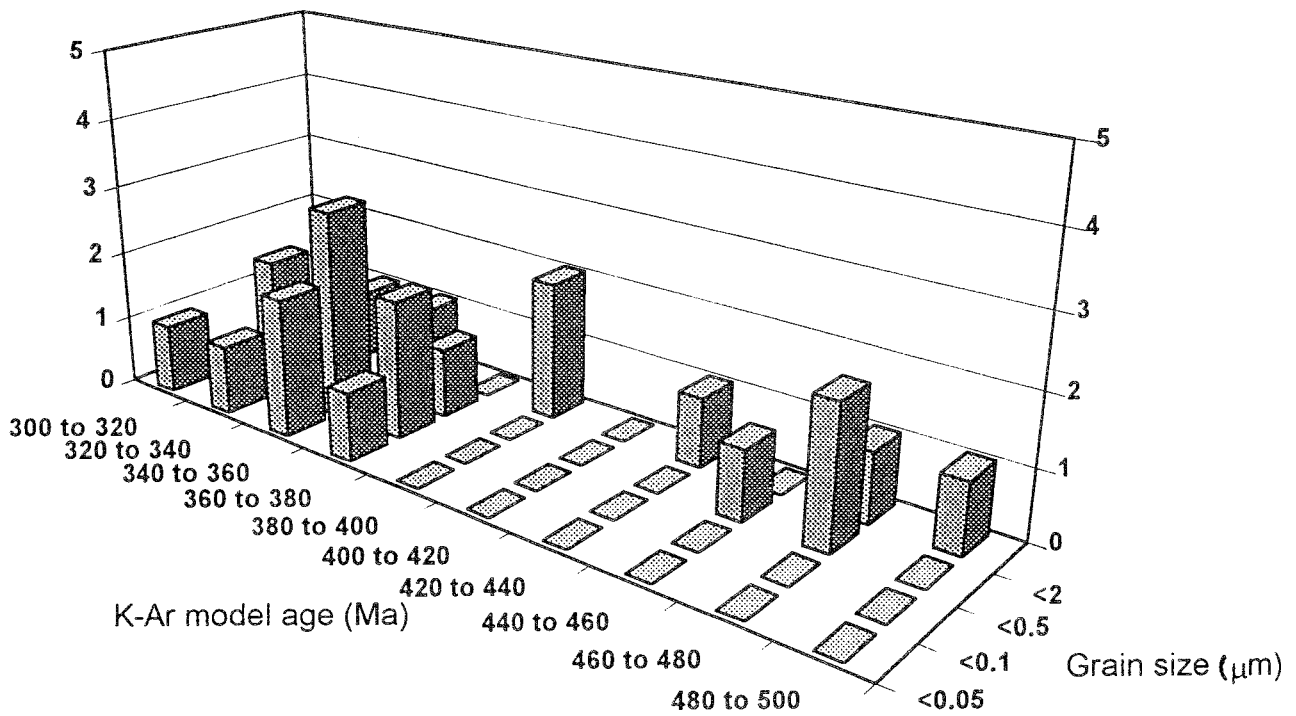
Sample	K (wt.%)	<sup>40</sup> K (x10 <sup>-8</sup> mol/g)	<sup>40</sup> Ar* (x10 <sup>-10</sup> mol/g)	<sup>36</sup> Ar (x10 <sup>-12</sup> mol/g)	% <sup>40</sup> Ar*	<sup>40</sup> Ar/ <sup>36</sup> Ar	<sup>40</sup> K/ <sup>36</sup> Ar	K-Ar Model Age (Ma, ± 1σ)	Comments
A92/7 Alkali-feldspar duplicate	0.90 0.90	2.68 2.68	29.10 27.57	64.15 29.32	15.07 26.97	300 348	417.8 914.2	1280 ± 104 1231 ± 57	Information gallery, clasts in gouge
A92/9 Alkali-feldspar duplicate	1.46 1.46	4.36 4.36	23.78 23.67	37.52 15.09	19.97 38.09	319 412	1162.1 2889.5	756 ± 46 753 ± 26	Geochemistry laboratory, clasts in gouge
A91/11 whole-rock	4.09	12.21	37.16	0.46	94.36	8104	266294	437 ± 9	NE-4 wallrock
A91/14 chlorite	0.25	0.75	3.83	0.74	63.55	823	10209.1	718 ± 17	EW-7 vein phase
A91/41 K-feldspar	9.63	28.74	252.10	2.82	96.83	9215	101761	1097 ± 22	NE-3 wallrock

Note: <sup>40</sup>Ar\* = radiogenic argon

Table 6-7 K-Ar isotope analyses of gouge clay mineral separates

Sample	K (wt.%)	<sup>40</sup> K (x10 <sup>-8</sup> mol/g)	<sup>40</sup> Ar* (x10 <sup>-10</sup> mol/g)	<sup>36</sup> Ar (x10 <sup>-12</sup> mol/g)	% <sup>40</sup> Ar*	<sup>40</sup> Ar/ <sup>36</sup> Ar	<sup>40</sup> K/ <sup>36</sup> Ar	K-Ar Model Age (Ma, ±1σ)	Comments
A91/23 <2μm	6.12	18.27	39.19	1.05	92.13	5831	173971	335.8 ± 6.8	Information gallery
<0.5μm	6.17	18.41	43.75	1.94	88.03	2567	95129	368.5 ± 7.6	"
<0.1μm	6.10	18.21	40.01	1.22	91.03	3591	148773	343.3 ± 7.0	"
<0.05μm	5.92	17.67	39.08	2.04	86.53	2215.11	86689.29	345.3 ± 7.2	"
A92/7 <2μm	6.09	18.18	41.88	2.28	86.20	2135.00	79887.9	358.4 ± 7.5	"
<0.1μm	6.47	19.31	40.18	1.68	88.65	2691.67	114712.9	326.6 ± 6.8	"
<0.05μm	5.43	16.21	36.02	1.57	88.15	2609.01	103493.6	346.9 ± 7.2	"
A92/9 <2μm	5.61	16.74	41.88	1.89	88.01	2522.12	88765.49	386.0 ± 8.0	Geochemistry Laboratory
<0.1μm	6.23	18.59	40.39	2.36	85.31	2003.62	78709.53	339.6 ± 7.1	"
<0.05μm	5.08	15.16	31.87	2.91	79.08	1386.40	52169.07	329.7 ± 7.2	"
A91/6 <2μm	5.09	15.19	41.81	1.52	89.35	3085	100168	420.5 ± 8.7	Fracture Zone NE-4
<0.5μm	5.57	16.62	50.97	2.09	89.04	2733.49	79404.91	462.8 ± 9.6	"
<0.1μm	5.31	15.85	36.32	1.99	85.95	2126.51	79724.57	356.7 ± 7.5	"
A91/32 <2μm	5.86	17.49	55.13	0.90	94.03	4529	194521	474.2 ± 9.6	"
<0.5μm	5.38	16.06	48.89	1.47	91.40	3633	109092	459.9 ± 9.4	"
<0.1μm	5.49	16.39	39.69	1.60	88.76	2792	102332	374.9 ± 7.8	"
<0.05μm	5.24	15.64	36.77	2.54	83.42	1737.10	61645.28	365.0 ± 7.7	"
A91/36 <2μm	5.62	16.77	54.41	1.09	93.80	5331	154179	486.3 ± 9.9	"
<0.5μm	6.04	18.03	54.33	1.98	90.15	3041.20	90975.96	455.9 ± 9.4	"
<0.1μm	5.47	16.33	39.39	1.56	88.95	2820.45	103995.6	373.7 ± 7.7	"
A91/38 <2μm	5.19	15.49	77.73	0.98	95.84	8260	157650	706.1 ± 14.2	Fracture Zone NE-3
<0.5μm	4.68	13.97	47.37	4.06	80.79	1442.67	34375.73	505.6 ± 10.9	"
<0.1μm	4.77	14.24	63.26	1.57	92.82	4344.49	90769.62	637.5 ± 13.0	"
A91/39 <2μm	5.83	17.40	44.82	1.30	91.54	3757	133544	396.3 ± 8.1	"
<0.5μm	5.23	15.61	31.98	4.22	73.21	1034.52	36977.08	322.0 ± 7.2	"
<0.1μm	5.77	17.22	37.35	2.62	83.04	1715.66	65701.65	339.2 ± 7.2	"
<0.05μm	5.49	16.39	31.25	2.03	83.69	1842.73	80883.82	301.5 ± 6.4	"

Note: <sup>40</sup>Ar\* = radiogenic argon



**Figure 6-5** Frequency distribution of K-Ar model ages as a function of grain size of gouge separates. The <2, <0.5 and <0.1 $\mu\text{m}$  size fractions of A91/38 which gave model ages of 638, 506 and 706Ma respectively, are omitted from the diagram.

- (iv) Apparently significant differences are evident between samples from the different faults and fracture zones.
- (v) The seven Information Gallery gouge separates, which have higher K-contents (mean 6.05wt%) than the other samples, yielded a continuously-overlapping range (ie. overlapping error bars) of model ages from 327-369Ma with no clear grain size dependence. Model ages for four of the separates fall within error of each other, with a mean age of 342.8Ma. The youngest model age was determined on a  $<0.1\mu\text{m}$  fraction with a high proportion of quartz detected by STEM.
- (vi) The Geochemistry Laboratory separates, with a slightly lower K-content, show a systematic decrease in age with smaller grain size. The youngest model ages from the Geochemistry Laboratory and Information Gallery are within analytical error (mean = 328.5Ma).
- (vii) Two of the three NE-4 gouge samples show a systematic decrease in model age with decreasing grain size, spanning in excess of 100Ma. The youngest model age is given by the single  $<0.05\mu\text{m}$  separate, The four smallest separates, which have closely similar K-contents, occupy a continuously-overlapping range of 357-374Ma.
- (viii) Dramatic differences are apparent between the two samples from fracture Zone NE-3. The three separates of A91/38 all have low K-contents (mean 4.88 wt.%) and model ages  $>500\text{Ma}$ . The four separates of A91/39 have higher K-contents (mean 5.58 wt.%) and show a systematic decrease in age with decreasing grain size. The  $<0.05\mu\text{m}$  fraction model age of  $301.5\pm 6.4\text{Ma}$  is the youngest age measured in any sample.

### 6.6.3 Isotopic disturbance and mixing

Evidence of isotopic disturbance (ie. excess initial  $^{40}\text{Ar}$  or post-closure loss/gain of Ar) and of contamination by mixing of two or more independent mineral systems can be detected by cross-plotting K vs.  $^{40}\text{Ar}^*$ ,  $^{(40/36)}\text{Ar}$  vs.  $^{40}\text{K}$  and  $^{(40/36)}\text{Ar}$  vs.  $1/^{36}\text{Ar}$  (eg Harper 1970; Burley and Flisch 1989). In the K vs.  $^{40}\text{Ar}^*$ , an undisturbed and uncontaminated single genetically-related mineral population would plot on a straight line which intercepts the axes at the origin. In the same way on the  $^{(40/36)}\text{Ar}$  vs.  $^{40}\text{K}/^{36}\text{Ar}$  diagram an undisturbed and uncontaminated sample suite would plot on a straight line which intersects the  $^{(40/36)}\text{Ar}$  axis at the (constant) atmospheric ratio of 295.5. If the system is undisturbed and uncontaminated, then the straight lines in both plots define an isochron whose slope is proportional to the age of the sample

suite. A straight line can, however, also result from a variable mixture of two components with differing original potassium concentrations, resulting in a mixing line which has no real age significance (although this may be addressed by modelling). Mixtures of this type are identifiable on the  $(40/36)\text{Ar}$  vs.  $1/36\text{Ar}$  diagram where they plot as a linear array intersecting the  $(40/36)\text{Ar}$  at the atmospheric ratio.

Plots of K vs.  $^{40}\text{Ar}^*$ ,  $(40/36)\text{Ar}$  vs.  $^{40}\text{K}$  and  $(40/36)\text{Ar}$  vs.  $1/^{36}\text{Ar}$  for gouge separates from each of the four localities are shown in Figs 6-6 to 6-9 respectively.

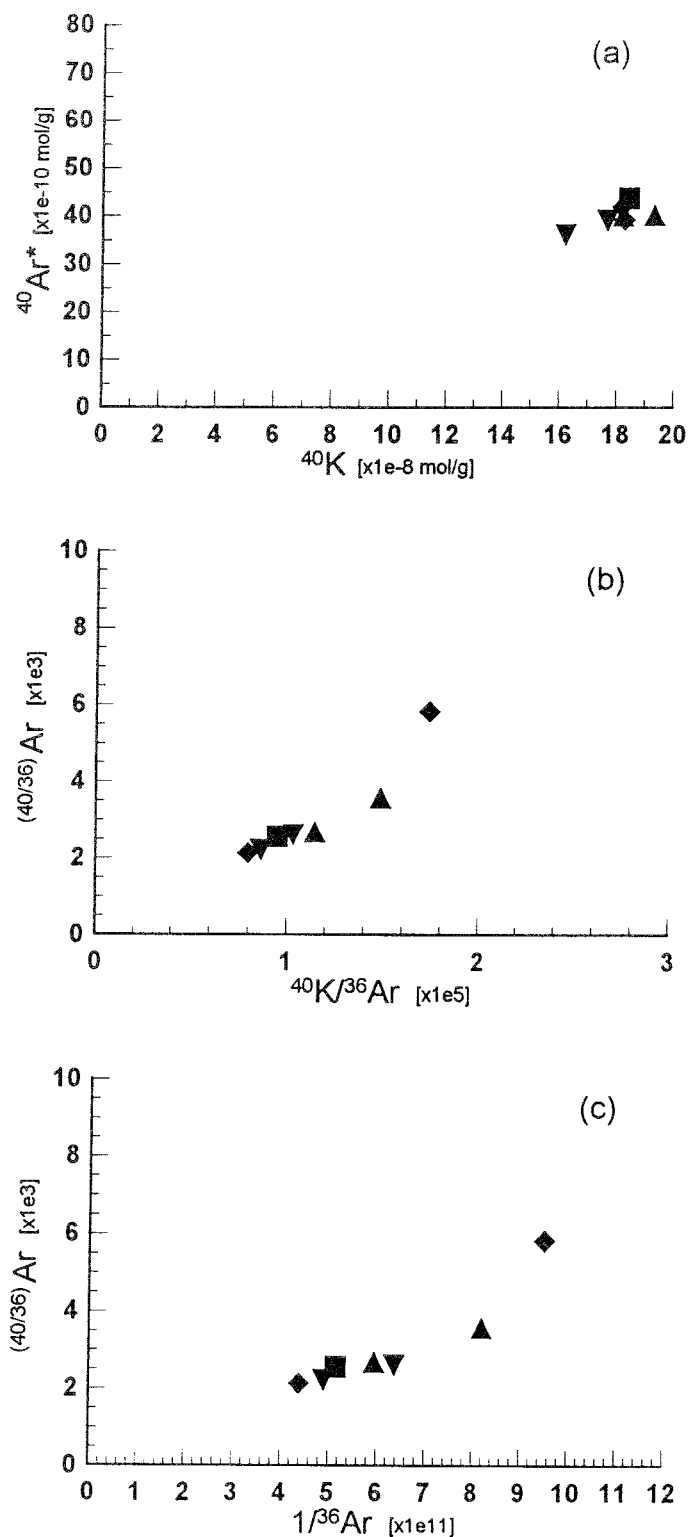
Figures 6-6 to 6-9 indicate isotopic disturbance and/or mixing of argon sources in each suite of samples. Comparable plots, but in terms of grain size rather than locality, confirm that mixing is pronounced especially in the  $<2$  and  $<0.5\mu\text{m}$  gouge fractions.

It is difficult to assess the degree of isotopic disturbance, if any, but mixing of two component systems, at least, can be simply modelled in respect of porphyroclast contamination.

#### 6.6.4 Porphyroclast contamination modelling

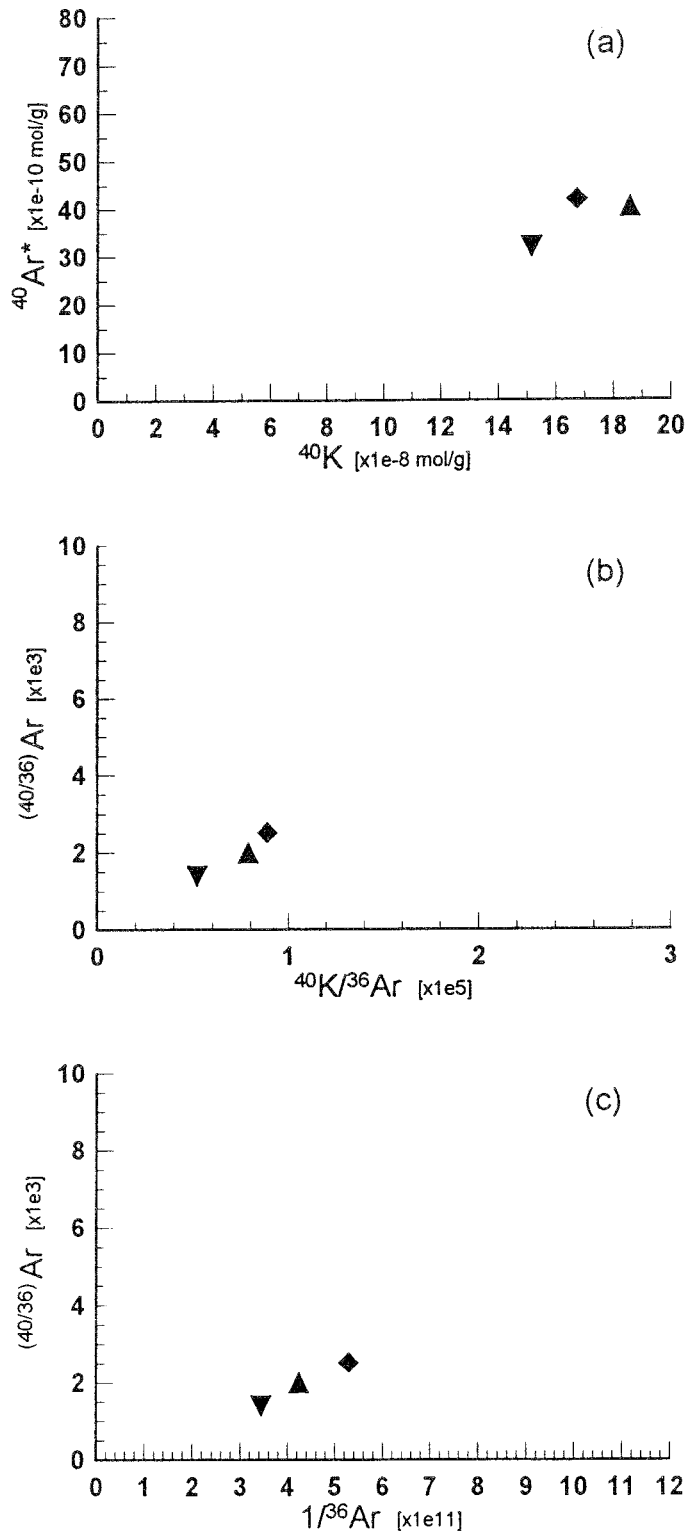
The petrographic, XRD and TEM observations together with the K-Ar isotopic data, all point to contamination of at least the larger size fractions analyzed by (older) K- and Ar-bearing porphyroclastic phases. The effects of such contamination on the measured ages can be simply modelled. This is illustrated below for samples from Fracture Zone NE-3.

Choosing the gouge sample which gave the youngest K-Ar model age of 302Ma (A91/39 [ $<0.05\mu\text{m}$ ], Table 6-7), and its corresponding wallrock which gave a K-feldspar model age of 1097Ma (A91/41, Table 6-6), the effects of contamination are shown in Fig 6-10. Assuming the sample to be uncontaminated by porphyroclastic feldspar (as suggested for this sample by XRD and TEM), the increase in apparent age due to *addition* of 1097Ma K-feldspar is shown by the upper line (of positive slope) in Fig 6-10. With the exception of sample A91/38, the entire range of measured gouge model ages (302-486Ma) is encompassed by the span of apparent ages modelled by the addition of up to 12wt% 1097Ma age K-feldspar contaminant. Furthermore, the concentrations of  $^{40}\text{K}$  and  $^{40}\text{Ar}^*$  'corrected' for contamination are compatible with the measured ranges of concentrations although there is no simple correlation between K-content and measured age.



### INFORMATION GALLERY

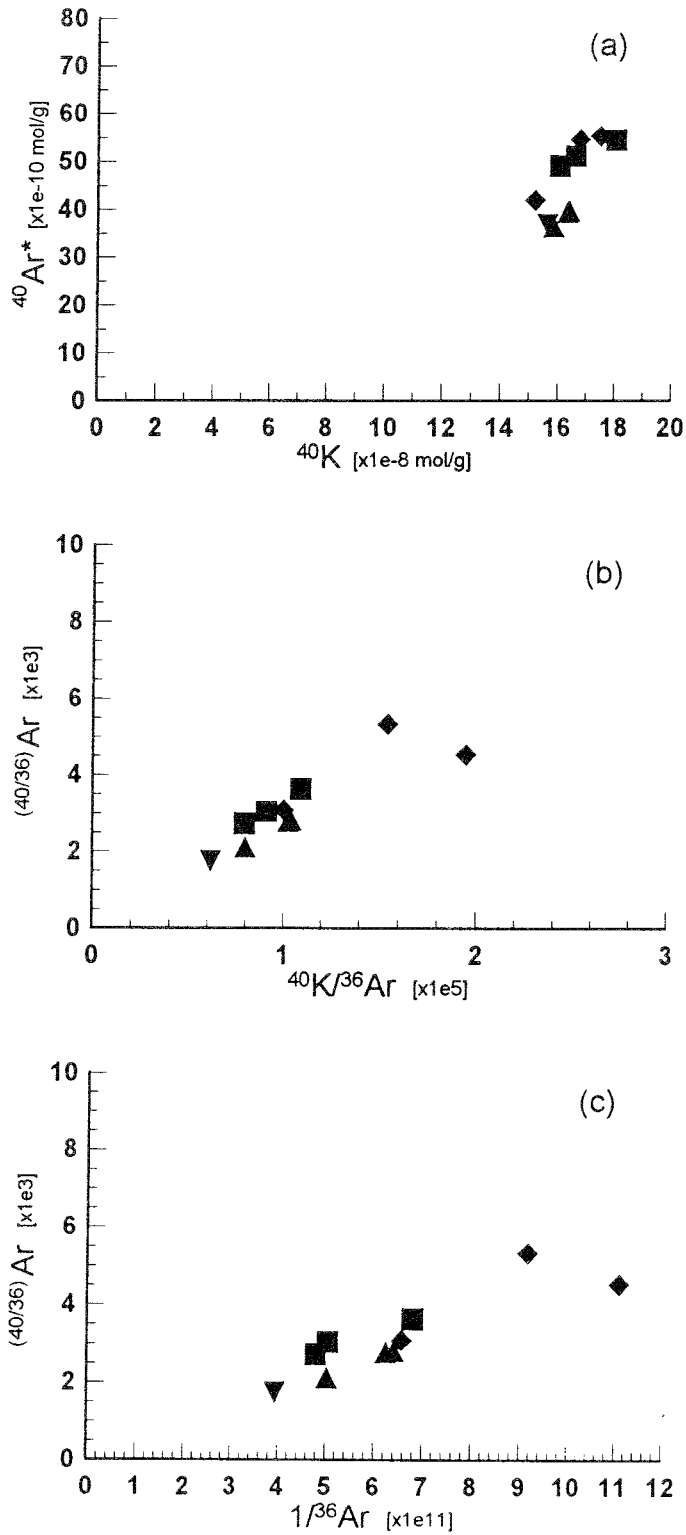
**Figure 6-6** K-Ar isotopic data for Information Gallery gouge separates. Diamonds =  $<2\mu\text{m}$ , squares =  $<0.5\mu\text{m}$ , inverted triangles =  $<0.1\mu\text{m}$  and triangles =  $<0.05\mu\text{m}$  fraction.



GEOCHEMISTRY LABORATORY

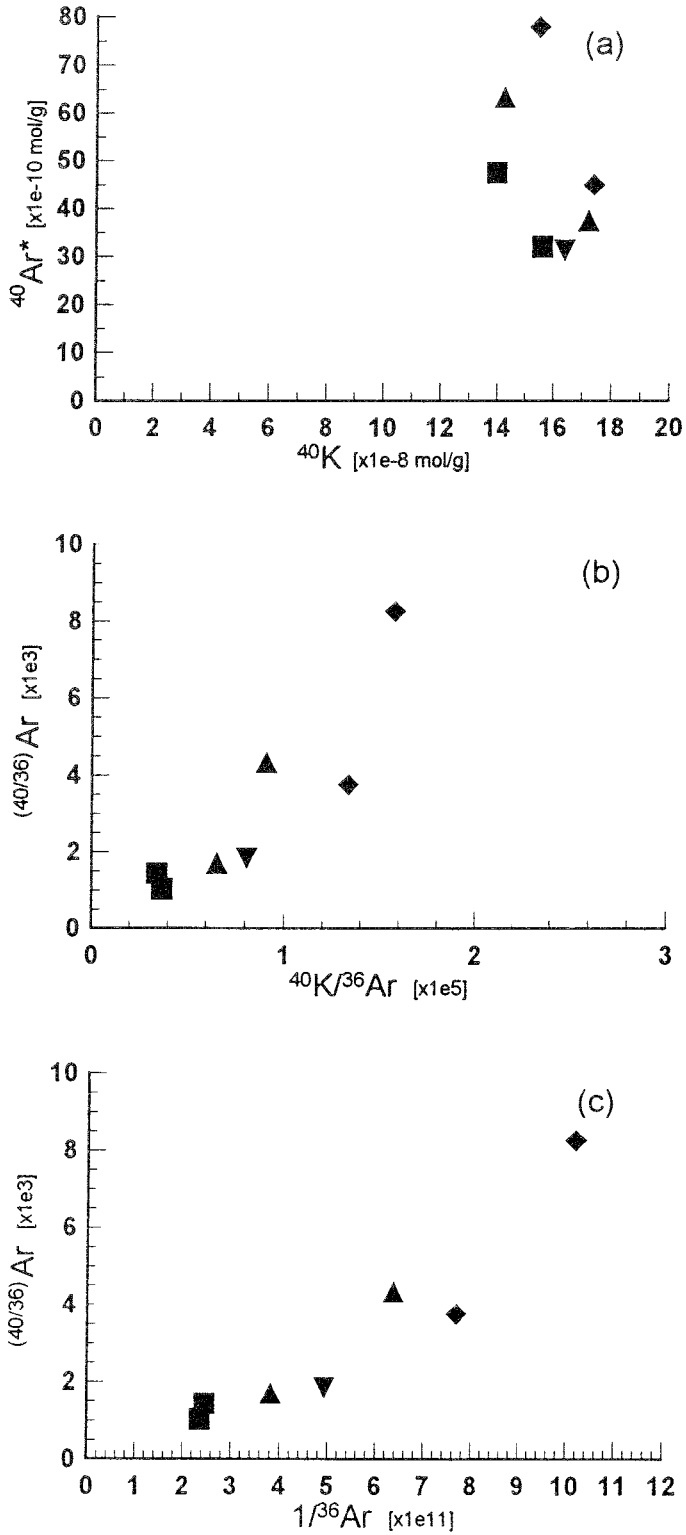
Figure 6-7 K-Ar isotopic data for Geochemistry Laboratory gouge separates. Symbols as Fig 6-6.





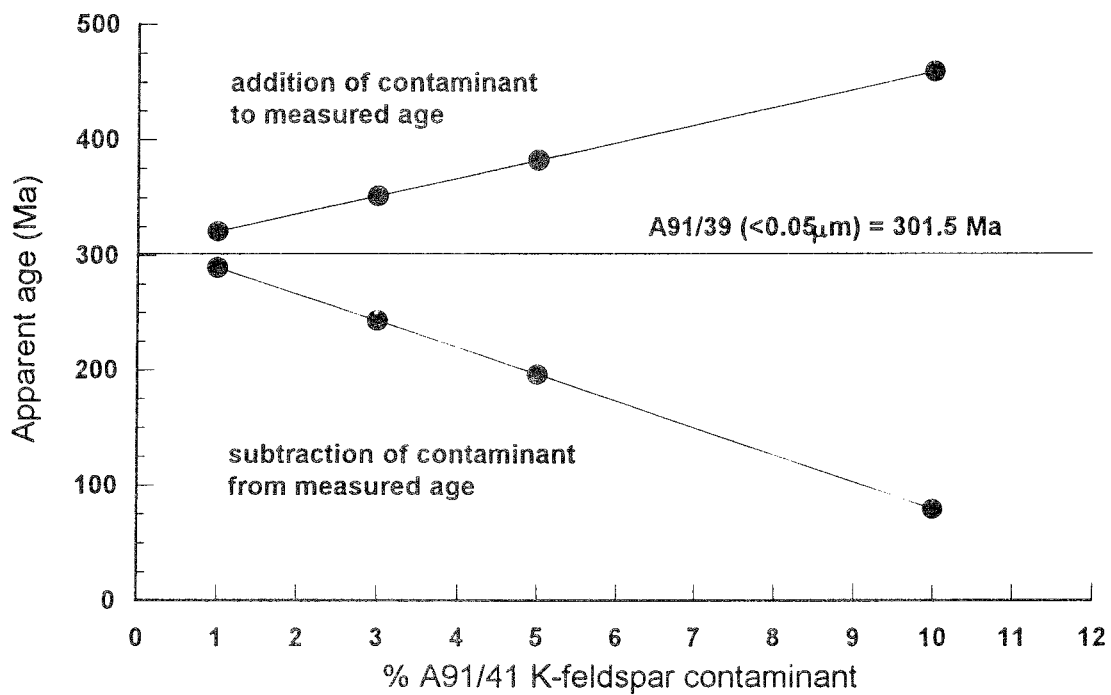
**FRACTURE ZONE NE-4**

**Figure 6-8** K-Ar isotopic data for Fracture Zone NE-4 gouge separates. Symbols as Fig 6-6.



**FRACTURE ZONE NE-3**

**Figure 6-9** K-Ar isotopic data for Fracture Zone NE-3 gouge separates. Symbols as Fig 6-6.



**Figure 6-10** Effect of feldspar contamination on apparent K-Ar age of gouge. The model uses the measured K-Ar ages of 301.5Ma and 1097Ma for gouge A91/39 [ $<0.05\mu\text{m}$ ] and K-spar separated from the wallrock A91/41 of Fracture Zone NE-3, respectively. (see text for details).

This modelling clearly does not prove that the range of gouge K-Ar model ages is attributable to K-feldspar contamination; this is, however, a plausible explanation. In support of this it is reasonable that contamination at the 1-2% level in the  $<0.1$  and  $<0.05\mu\text{m}$  fractions may not have been detected by XRD and TEM examination, and also that some of the  $<2\mu\text{m}$  gouge fractions may contain  $\geq 10\%$  feldspar.

Making the alternative assumption (which is not supported by observation) that sample A91/39 [ $<0.05\mu\text{m}$ ] is contaminated, the decrease in apparent age due to *subtraction* of the same K-feldspar contaminant is shown by the lower line in Fig 6-10. Because of the simple proportionality this line has a steeper (negative) slope than the 'addition' line leading to a dramatic decrease in apparent age.

Comparable modelling of the other analyzed wallrock/porphyroclast phases as contaminants demonstrates that these would have far less effect on the measured ages because of their low potassium contents. For example, *subtraction* of 10wt% A92/7 alkali feldspar with a 1280Ma model age (Table 6-6) from A91/39 [ $<0.05\mu\text{m}$ ] would cause a reduction in the apparent age of less than 30Ma.

The available XRD, TEM, SEM and microprobe analyses point towards the finest fractions of each gouge being very largely made-up of a single population. Nevertheless, neither the effects of contamination by older, non-authigenic illitic material nor of isotopic disturbance through illitization of I-S or smectite formation from illite can be wholly discounted. The available observations and analyses together with the modelling data suggest that such contamination or disturbance would be likely to perturb the K-Ar ages by a few tens of millions of years at most.

## 6.7 Rb-Sr RESULTS

The Rb-Sr dating attempt was made on a one-off basis in an attempt to assess the suitability of the technique and for comparison with the K-Ar dating results. The Rb-Sr isotopic compositions of four coarse-grained fractions of gouge and cataclasite all from Fracture Zone NE-4 were measured in an attempt to define an isochron. The results of the analyses are given in Table 6-8.

The analyses give an 'isochron' age of  $497 \pm 68\text{Ma}$  ( $2\sigma$ ) with an initial  $^{87/86}\text{Sr}$  ratio of 0.71041. Although it is difficult to interpret this errorchron because of the large scatter, it is noteworthy that the Rb-Sr errorchron age is not significantly different from the oldest K-Ar model ages determined on the same samples (Table 6-7). This observation may indicate that both the Rb-Sr and K-

Ar systems of the mixed mineral assemblages of these coarse fractions of gouge were reset during Caledonian times.

Table 6-8 Rb-Sr isotopic data

Sample	$^{87}\text{Rb}/^{86}\text{Sr}$	$^{87/86}\text{Sr}$	$2\sigma$	Rb (ppm)	Sr (ppm)
A91/6 <2 $\mu\text{m}$	6.291963	0.752196	40	443.72	204.93
A91/32 <2 $\mu\text{m}$	1.304851	0.719293	33	376.44	835.65
A91/32 >2<8 $\mu\text{m}$	0.615669	0.714817	37	162.51	764.27
A91/36 <2 $\mu\text{m}$	2.807281	0.731965	30	388.40	401.25

Note:  $2\sigma$  errors are for the last two decimal places of the  $^{87/86}\text{Sr}$  ratios.

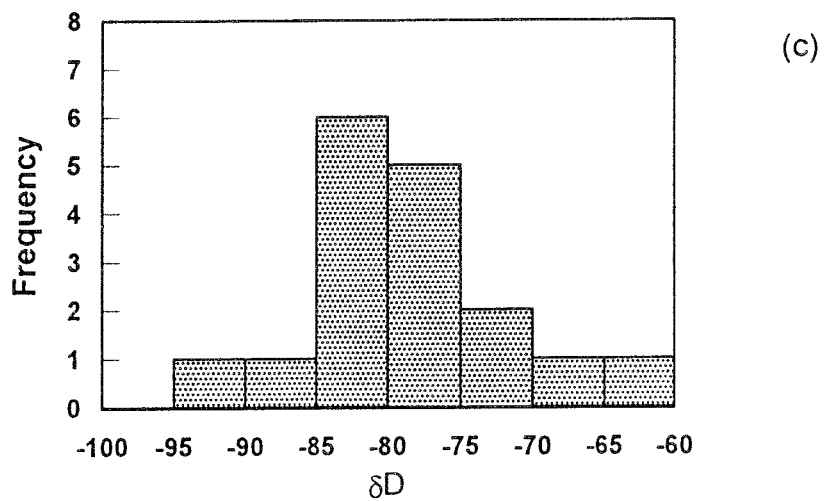
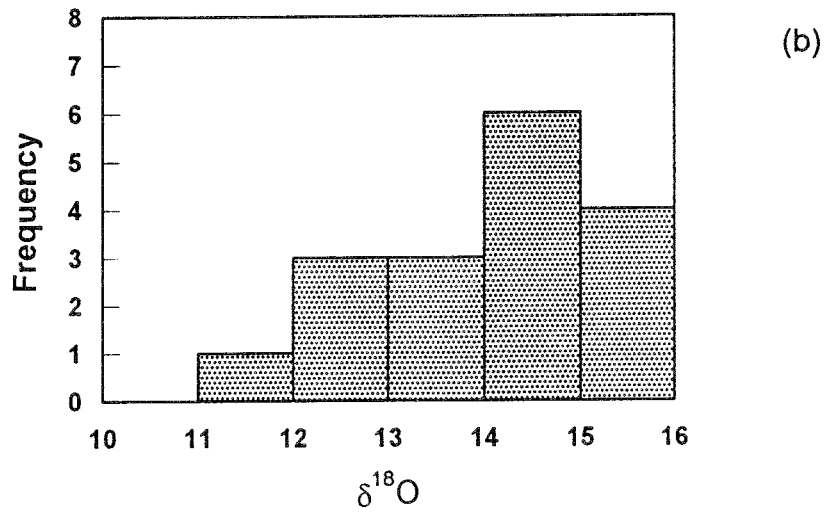
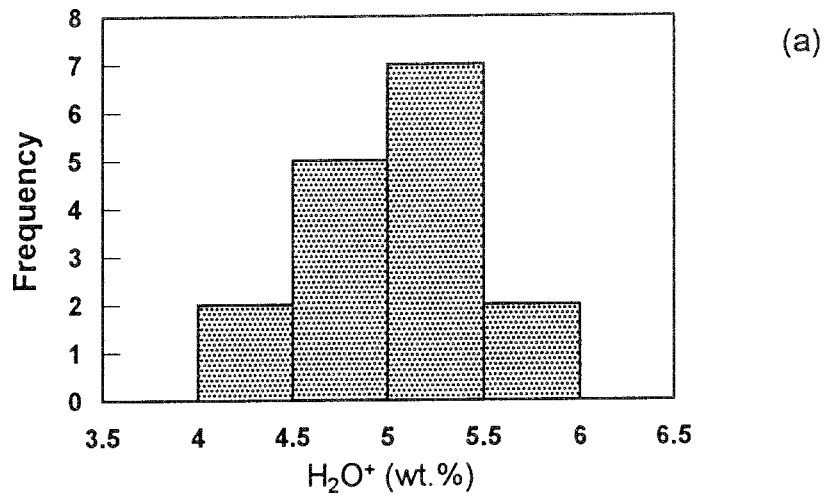
## 6.8 STABLE ISOTOPE ANALYSES

Oxygen and hydrogen stable isotope analyses were performed on all the <0.1 and <0.05 $\mu\text{m}$  fractions from samples where sufficient material remained after K-Ar analysis. The  $\delta^{18}\text{O}$  and  $\delta\text{D}$  values of selected <2 and <0.5 $\mu\text{m}$  fractions were also measured.

### 6.8.1 Results

The measured  $\delta^{18}\text{O}$  and  $\delta\text{D}$  values, together with  $\text{H}_2\text{O}^+$  contents, are listed in Table 6-9 and plotted in histogram form in Fig 6-11. In this figure, and in the statistics discussed below, A91/38 [<0.1 $\mu\text{m}$ ] is excluded as the  $\text{H}_2\text{O}^+$  and  $\delta^{18}\text{O}$  analyses for this separate are considered suspect. A number of comments can be made on the results:

- (i) The  $\delta^{18}\text{O}$  values for the clay separates range between +11.5 and +15.6‰. The  $\delta^{18}\text{O}$  histogram has a strong mode at about 14‰ (Fig 6-11b); the mean value of  $\delta^{18}\text{O}$  is  $14.0 \pm 1.6$ ‰ ( $1\sigma$ ,  $n=17$ ).
- (ii) The  $\delta\text{D}$  values range between -94 and -62‰. The  $\delta\text{D}$  histogram has a strong mode around -8‰ (Fig 6-11c); the mean value of  $\delta\text{D}$  is  $-79 \pm 7.3$ ‰ ( $1\sigma$ ,  $n=17$ ).
- (iii) There are no systematic relationships apparent between grain size and the measured  $\delta^{18}\text{O}$  or  $\delta\text{D}$  values.
- (iv) The within-sample differences in measured  $\delta^{18}\text{O}$  and  $\delta\text{D}$  are nearly as great and greater, respectively, than the between-sample differences. The greatest difference in  $\delta\text{D}$  (-32‰) between the <0.5 and <0.1 $\mu\text{m}$  fractions of A91/6 is nearly twice as great the largest between-sample difference with A91/6 excluded.



**Figure 6-11** Histograms showing (a) the H<sub>2</sub>O<sup>+</sup> content, (b)  $\delta^{18}\text{O}$  values, and (c)  $\delta\text{D}$  values of selected dated gouge separates (see Table 6-9).

Table 6-9 Stable isotope analyses of gouge clay mineral separates

Sample	$\delta D_{SMOW}(\text{‰})$	$\delta^{18}O_{SMOW}(\text{‰})$	H <sub>2</sub> O <sup>+</sup> (wt%)	Comments
A91/23 <0.5 $\mu$ m	-82	+13.0	5.4	Information Gallery
<0.1 $\mu$ m	-86	+11.5	5.6	"
<0.05 $\mu$ m	-80	+15.4	4.7	"
A92/7 <2 $\mu$ m	-83	+14.5	5.0	"
<0.1 $\mu$ m	-83	+13.9	5.0	"
<0.05 $\mu$ m	-82	+13.7	5.1	"
A92/9 <2 $\mu$ m	-77	+15.2	4.9	Geochemistry Laboratory
<0.1 $\mu$ m	-76	+14.6	4.9	"
A91/6 <0.5 $\mu$ m	-62	+12.8	4.3	Fracture Zone NE-4
<0.1 $\mu$ m	-94	+14.4	4.9	"
A91/32 <0.5 $\mu$ m	-77	+15.6	5.9	"
<0.1 $\mu$ m	-81	+14.5	5.4	"
<0.05 $\mu$ m	-73	+14.4	4.4	"
A91/36 <0.5 $\mu$ m	-68	+12.0	5.2	"
A91/38 <0.1 $\mu$ m	-70	+8.49	>3.6	Fracture Zone NE-3
A91/39 <0.5 $\mu$ m	-71	+12.2	5.1	"
<0.1 $\mu$ m	-78	+15.6	4.8	"
<0.05 $\mu$ m	-81	+14.4	4.6	"

- (v) The  $\delta D$  values for six separates (3 size fractions) from the Information Gallery gouge samples (A91/23 and A92/7) all lie within the analytical error range. Their average value is slightly more negative ( $-4\text{‰}$ ) than the overall mean. The  $\delta^{18}O$  values for the same six separates are more variable and, on average, slightly lower (by  $0.3\text{‰}$ ) than the overall mean.
- (vi) There is no correlation of  $\delta^{18}O$  with either  $\delta D$  ( $r = -0.23$ ) or H<sub>2</sub>O<sup>+</sup> ( $r = -0.17$ ; mean H<sub>2</sub>O<sup>+</sup> =  $5.0 \pm 0.4$  wt.%,  $1\sigma$ ,  $n=17$ ), nor of  $\delta D$  with H<sub>2</sub>O<sup>+</sup> ( $r = -0.32$ ).
- (vii) There is no correlation between the  $\delta D$  values and the measured K-Ar model ages ( $r = 0.54$ ).

### 6.8.2 Discussion

In spite of the relatively small number of stable isotope analyses, a first-pass interpretation of the data may be made, taking into account the mineralogy and K-Ar model ages of the separates together with information on the isotopic composition of the Äspö groundwaters.

In the modelling discussed below, mean values of  $\delta^{18}\text{O}$  and  $\delta\text{D}$  for 17 separates (excluding A91/38 [ $<0.1\mu\text{m}$ ]) are used. This is justified by the fact that the mean values lie close to the modal values, and also the observation that the mean values are insensitive to exclusion of selected coarser fractions ( $<2$ ,  $<0.5\mu\text{m}$ ) which might be considered appropriate on the grounds of possible contamination by porphyroclastic hydrogen- and oxygen-bearing phases.

#### (a) Illite- $\delta^{18}\text{O}$ -temperature

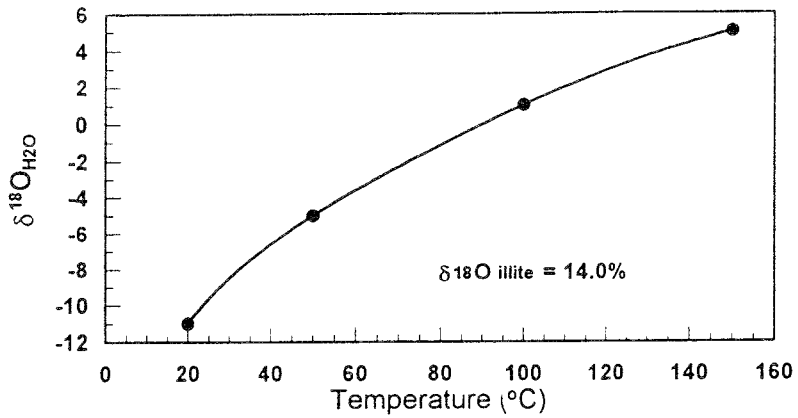
The temperature-dependent oxygen isotope composition of water in equilibrium with illite having  $\delta^{18}\text{O} = 14.0\text{‰}$  is plotted in Fig 6-12. The curve was generated using an approximation derived from the isotope fractionation equation recommended by Savin and Lee (1988). The curve indicates that for formation of illite at a temperature  $\leq 90^\circ\text{C}$  and with  $\delta^{18}\text{O}$  equal to the mean measured value of the gouge separates, surface-derived fluids (ie.  $\delta^{18}\text{O} \leq 0\text{‰}$ ) must have been involved.

#### (b) $\delta\text{D}$ values

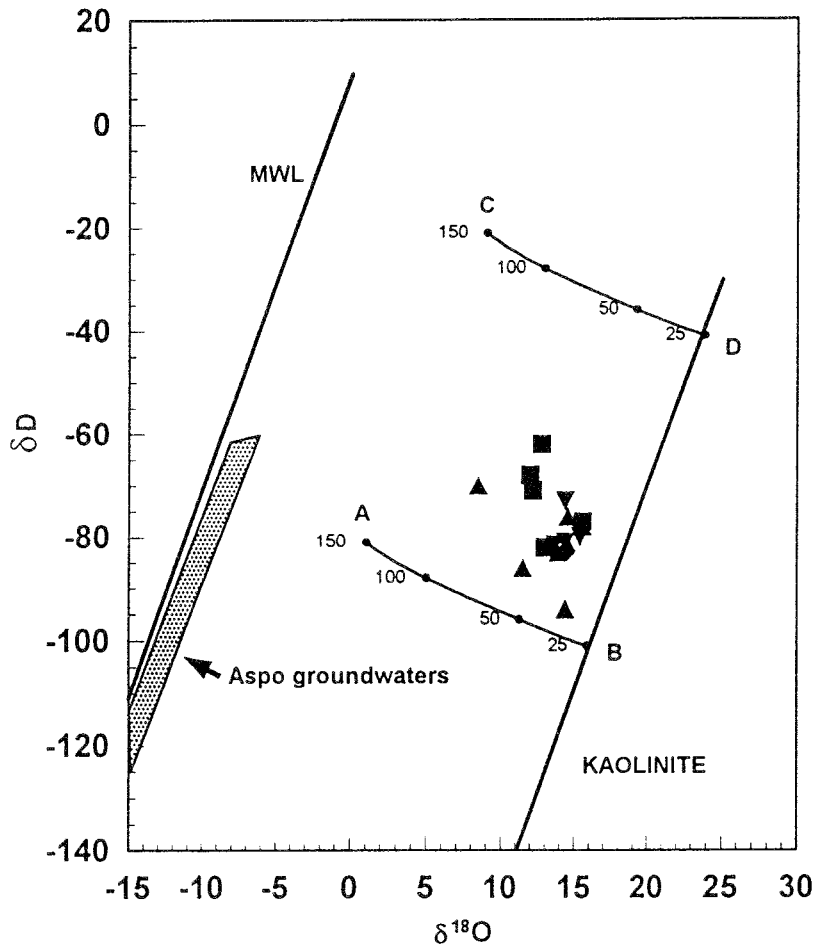
The isotopic composition of hydrogen in clay minerals is very sensitive to exchange with fluids (eg. Longstaffe and Ayalon 1990; Fallick et al 1993), such that measured  $\delta\text{D}$  values can reflect equilibrium with the most recent 'pore' fluid. The fault gouge illitic material must have been precipitated from fluid(s) of distinctive isotopic composition, but may later have come into contact with other, isotopically-distinct groundwater(s). On a large scale the interaction between groundwater and fault gouge will have been controlled by the post-c.300Ma (ie. age of the illite) tectonic and glacial history at Äspö.

The spread of measured  $\delta\text{D}$  values for the gouge fractions is comparatively small, particularly if A91/6 is omitted (range=18‰, n=16), suggesting a reasonably close approach to equilibrium. Porphyroclastic contaminants such as chlorite, and authigenic kaolinite may broaden the range in measured  $\delta\text{D}$  values. The uniformity of  $\delta\text{D}$  values for all size fractions of the Information Gallery gouge samples (A91/23 & A92/7, Table 6-9) is striking. Qualitatively, this conforms with the mineral purity and tight spread of K-Ar model ages for these samples, and suggests that  $\delta\text{D}$  is very close to equilibrium.





6-12



6-13

**Figure 6-12** Plot showing the oxygen isotopic composition of water in equilibrium with illite of  $\delta^{18}\text{O} = 14.0\%$  as a function of temperature.

**Figure 6-13**  $\delta\text{D}$  vs.  $\delta^{18}\text{O}$  crossplot for gouge clay mineral separates. Symbols as Fig 6-6. See text for details.

The poor correlation between  $\delta D$  and K-Ar model ages suggests that hydrogen isotope exchange between fluid and gouge clay has had minimal effect on the K-Ar isotope systematics of the clay. This is an important observation which increases confidence in the interpretation and meaningfulness of the measured K-Ar model ages.

### (c) $\delta^{18}O$ - $\delta D$ crossplot

The measured  $\delta^{18}O$  and  $\delta D$  values of the gouge clay separates are cross-plotted in Fig 6-13. The present-day global meteoric water line (MWL,  $\delta D = 8 * \delta^{18}O + 10$ ; Craig 1961) and a line defined by weathering-product kaolinite at the earth's surface (KAOLINITE; Faure 1986) are included in the diagram for reference. The stable isotopic compositions of the Äspö gouge separates fall to the higher-temperature, lefthand side of the kaolinite line. This is characteristic of nearly all measured isotopic compositions of clay minerals

The  $\delta^{18}O$ - $\delta D$  composition of groundwaters from 'subsurface' to >500m depth sampled from boreholes at Äspö plot within an elongate field parallel to MWL (Tullborg et al 1991; Fig 6-13). The Äspö groundwaters thus show more negative  $\delta D$  values than would be expected from the corresponding  $\delta^{18}O$  values; this fractionation has been attributed to various possible hydrogeological processes (Tullborg et al 1991). The shallow subsurface waters at Äspö can be approximated by an isotopic composition of  $\delta^{18}O = -8\text{‰}$  and  $\delta D = -60\text{‰}$  (see Tullborg et al 1991, Fig 8). Using this water composition, the equilibrium isotopic composition of 'illite' as a function of temperature has been approximated using the fractionation equations recommended by Savin and Lee (1988), and is plotted as Line A-B in Fig 6-13. For hydrogen, the relevant equation describes fractionation between 'illite-smectite' and water, rather than illite as in the case of oxygen, and requires several vital assumptions - see Savin and Lee (1988) .

In Fig 6-13 the Äspö gouge separates plot well above the 'illite' equilibrium line (A-B) suggesting that the clays equilibrated with a fluid with a less-negative  $\delta D$  composition, that is no longer uniquely represented or has not been sampled at Äspö.

One possibility is that the fluid associated with growth of the gouge illite was a brine with a heavier isotopic composition than the present-day groundwaters. A scenario could be envisaged in which illite growth in the faults took place at, say, 100°C under a cover of 2-3km of Palaeozoic sediments (see Section 2). To examine this possibility the isotopic composition of illite in equilibrium with 'brine' having a composition of  $\delta^{18}O = +1\text{‰}$  and  $\delta D = 0\text{‰}$  is plotted as Line C-D in Fig 6-13. In

this case, the difference between the locus of equilibrium values along Line C-D and the plotted sample  $\delta^{18}\text{O}$ - $\delta\text{D}$  values could be accounted for by incomplete equilibration with the present-day Äspö groundwaters, perhaps limited by kinetic factors.

## 6.9 SYNTHESIS OF RESULTS

K-Ar model ages for various wallrock and porphyroclast phases from the Information Gallery, Geochemistry Laboratory, EW-7, NE-4 and NE-3 faults and fracture zones range from 1280 to 437Ma. The older ages (1280-1097Ma) determined on wallrock and porphyroclastic feldspar separates may be related to isotopic closure in the feldspars following the thermal pulse associated with intrusion of the 1350Ma Göttemar and Uthammar granites.

The 437±9Ma model age for a wholerock sample of wallrock granite from Fracture Zone NE-4, together with an Rb-Sr 'errorchron' age of 497±68 for faultrocks from the same fracture zone, suggests some thermal and/or deformation activity of broadly Caledonian age.

A K-Ar model age of 718Ma for spherulitic chlorite from Fracture Zone EW-7 is substantially younger than the existing interpretation of a pre-1100Ma age for this phase (Table 2-3). This K-Ar age may approximate the true age of the chlorite or be a closure effect.

Clearly, these few K-Ar ages for the countryrock and early fault/vein phases do not permit a more sophisticated interpretation. To properly understand the origin and thermal history of the countryrocks, further isotopic analyses (including other systems) are required. The existing analyses have, however, allowed simple modelling of the effects of wallrock porphyroclast contamination of the gouge separates to be undertaken.

Fine grainsize separates (<2, <0.5, <0.1 & <0.05 $\mu\text{m}$ ) of illitic material from eight gouge samples from four fault and fracture zones gave K-Ar model ages in the range 706 to 302Ma. In general, the model ages decrease with grainsize although the relationship is not simple. XRD, electron microscope and microprobe analysis was used to characterize the separates. This confirmed that the coarser grainsize separates are contaminated by K-bearing porphyroclasts, such as K-spar, but that the finer separates consist largely of authigenic 'illite'.

The gouge separates from the Information Gallery fault gave K-Ar model ages in the range 369-327Ma, and showed the least variation with grainsize of any suite of samples. Gouge fractions separated from the Geochemistry Laboratory fault gave model ages of 386-330Ma.

Gouge separates from Fracture Zone NE-4 gave model ages in the range 486-357Ma although the four finest fractions occupy a continuously overlapping range of 357-374Ma.

Gouge separates from two individual faults within Fracture Zone NE-3 gave radically different age ranges. Three separates from the older fault (as shown by field relations) gave model ages in the range 706-506Ma, whereas four separates from the younger fault gave ages in the range 396-302Ma. The 302Ma model age was the youngest age measured for any sample.

The effects of feldspar contamination on the measured ages has been modelled and provides a plausible explanation for much of the observed variation in age, particularly with varying grain size of the separates. The question remains however as to whether there are real differences in the ages of authigenic 'illite' (which shows some variation in habit and composition) between the different faults and fracture zones. The youngest measured ages are as follows: Information Gallery, 327Ma; Geochemistry Laboratory, 330Ma; Fracture Zone NE-4, 357Ma; and, Fracture Zone NE-3 302Ma. The Information Gallery and Geochemistry Laboratory youngest ages are within analytical error, but 30 million years older and younger than fracture zones NE-3 and NE-4 respectively. Taking into account the many potential sources of error (discussed earlier) it is most likely that the authigenic 'illite' in each of the faults grew at least 250 million years ago and, more probably, at around 300Ma. Since the authigenic 'illite' grew after fault movement this constrains the age of the most recent fault movements to this timeframe.

The oxygen and hydrogen isotopic compositions of selected dated gouge separates, of various grain sizes, from the four fracture zones are similar. This observation combined with the XRD and TEM mineralogical data suggests that the effects of contamination by porphyroclastic phases on the stable isotope composition are small. The measured  $\delta^{18}\text{O}$  and  $\delta\text{D}$  values in the gouge separates are not in equilibrium with the present-day Äspö groundwaters. Two end-member models of the equilibrium oxygen and hydrogen isotopic composition in illite-water pairs have been considered. A possible scenario is that the gouge 'illite' was precipitated from an isotopically-heavier brine and has partially equilibrated with the present-day groundwaters at Äspö.

A poor correlation between  $\delta\text{D}$  and K-Ar model ages suggests that hydrogen isotope exchange between fluid and fault gouge 'illite' has had a minimal effect on the K-Ar systematics of gouge 'illite'. This observation increases confidence in the interpretation of the measured K-Ar model ages.

## 7 ESR ANALYSES

### 7.1 INTRODUCTION

#### 7.1.1 Background

Electron spin resonance (ESR) dating is a radiometric technique which, like luminescence dating, relies on the measurement of the degree of accumulated natural radiation damage within crystalline materials to assess sample age (reviewed by Grün 1989; Geyh and Schleicher 1990). The 'event' being dated may represent formation of the material (eg. tooth enamel, coral or travertine), heating (eg. volcanic rocks and archaeological burnt flint), exposure to sunlight (eg. prior to the deposition of sediments) or exposure to high stress (eg. during faulting).

In silicate minerals, irradiation excites electrons which are subsequently trapped within the crystal lattice, and are manifest as paramagnetic centres with characteristic ESR signals (Fig 7-1a & b). These signals are measured in a spectrometer which subjects the sample to microwave radiation within a controlled magnetic field. The intensity of the ESR signal, which is proportional to the number of trapped electrons, is dependent upon: (i) the environmental dose rate; (ii) the number and affinity of traps; and (iii) the duration of irradiation (ie. age). Thus the sample acts as a dosimeter which measures the doses from all radioactive sources ( $\alpha$ ,  $\beta$  and  $\gamma$ ) in its immediate environment (c. 30cm diameter) plus a portion of cosmic radiation. An ESR age is determined from the following relationship (eg. Grün 1992):

$$AD = \int_0^t D(t) dt$$

The dose rate,  $D$ , is determined by *in-situ* gamma-ray spectroscopy and chemical analysis for U,  $^{40}\text{K}$  and Th, of the sample and its immediate surroundings. The (natural) accumulated dose,  $AD$ , is determined by stepwise artificial irradiation of sample aliquots which causes an increase in the ESR signal intensity. Extrapolation back to zero ESR intensity allows determination of  $AD$  (Fig 7-1c).

The maximum age that may be dated by ESR is limited by: (i) saturation, where all the electron traps are filled; and, (ii) thermal stability, which describes the mean life of a trapped electron at the defect site. The lower age limit is constrained by the sensitivity of the mineral to radiation, the environmental dose rate and the sensitivity of the ESR spectrometer.

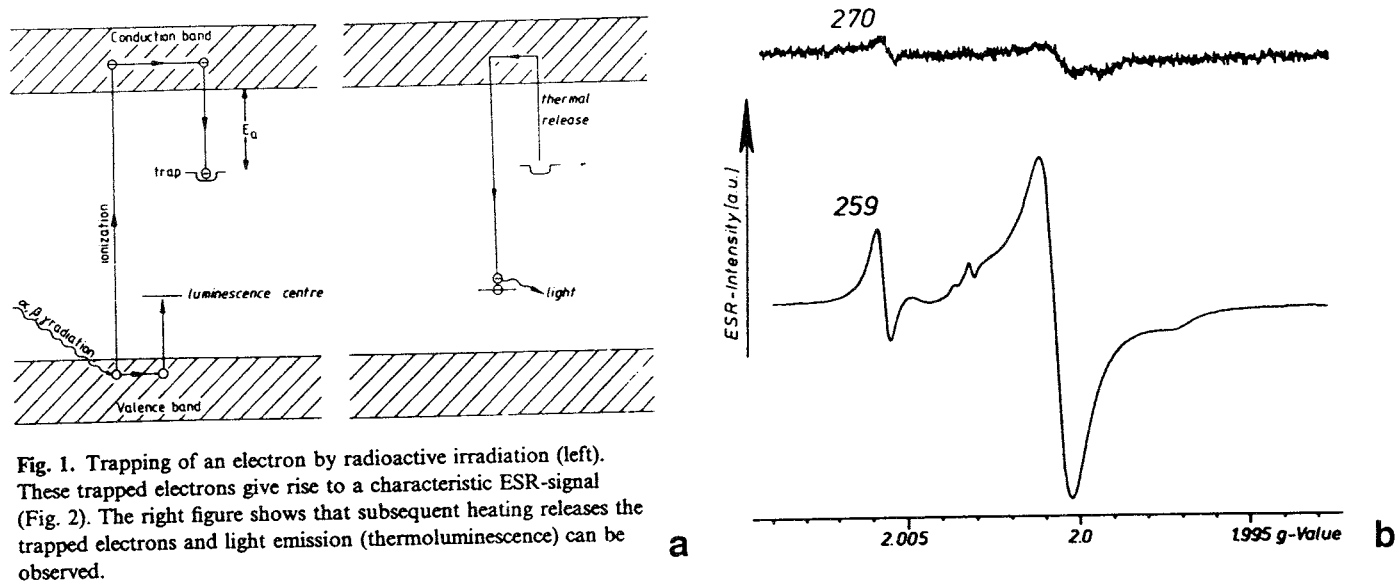


Fig. 1. Trapping of an electron by radioactive irradiation (left). These trapped electrons give rise to a characteristic ESR-signal (Fig. 2). The right figure shows that subsequent heating releases the trapped electrons and light emission (thermoluminescence) can be observed.

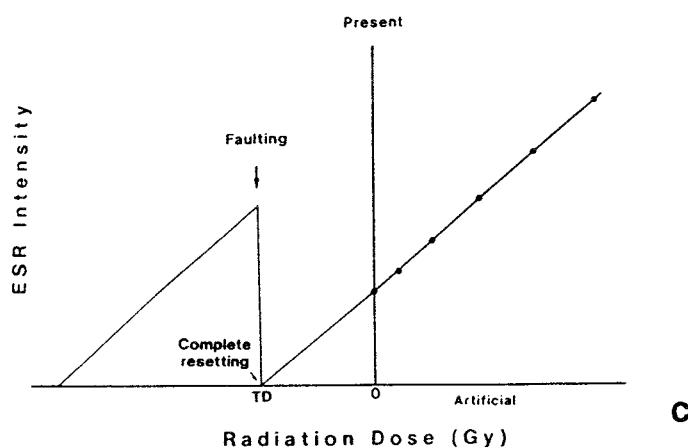


Figure 7-1 (a) Irradiation causing trapping of an electron which gives rise to a characteristic ESR signal (left). Subsequent heating releases trapped electrons causing thermoluminescence (right). (b) ESR spectrum of a very young (upper) and a very old (lower) speleothem. The large signal of the old speleothem is due to the long irradiation time (= age). The g-value is proportional to the ratio of microwave frequency over the magnetic field strength. The g-value is characteristic for a specific paramagnetic centre and independent of equipment configurations. The relative ESR intensity is in non-calibrated arbitrary units (a.u.). (c) Principle of ESR dating of fault movements. TD corresponds to the accumulated dose - see text. (figures from Fukuchi (1992) and Grün (1992))

### 7.1.2 ESR dating of quartz from fault gouge

The potential for direct fault dating by ESR was first appreciated by Ikeya and co-workers (Miki and Ikeya 1982; Ikeya et al 1982). They found that artificial irradiation increased the ESR signals in quartz grains separated from fault gouge, and that hydrostatic pressure and heat suppressed the signals. Thus it was proposed that the ESR signals in quartz gouge may be reset (to time,  $t=0$ ) by faulting, owing to the actions of stress and/or heat.

Subsequent observations on natural quartz gouge together with experimental studies and theoretical considerations, have indicated that zeroing of the ESR 'clock' (resetting) during fault movement may be related to several factors, including: temperature, hydrostatic pressure, normal stress, shear stress, displacement and displacement rate, grain size, exposure to light and, perhaps, hydrothermal activity (Grün 1992 and references therein). Although the physical mechanisms of resetting during faulting (eg. plastic or brittle deformation) remain poorly understood, on balance it seems that stress rather than heat (cf. Fukuchi 1992) is the most effective resetting agent in gouge bearing faults.

The ESR spectrum of quartz is complex, and normally exhibits five different paramagnetic centres (see Section 7.4). Each paramagnetic centre responds differently to applied stress, thus allowing some internal check on whether full resetting was achieved. Grains of different size also respond differently to applied stress, and measurements from a range of grain sizes may also provide evidence of full resetting at the time of fault movement.

In practice, the major problem for ESR fault dating is in determining whether or not a sample was completely reset during the last faulting event (Grün 1992). Sampling and analytical criteria are emerging which optimise the collection of completely reset material and demonstrating that is the case. Under ideal circumstances, the following criteria should be adopted:

- (i) Quartz should be extracted from narrow (<2cm) gouge seams flanked by wallrock (Ito and Sawada 1985); such samples will have experienced maximum shear stress and shear strain during a single slip event;
- (ii) Samples should be collected from minimum depths, corresponding to depths at the time of fault slip, of >20m for reverse faults, >70m for strike slip faults and >100m for normal faults (Ito and Sawada 1985); these criteria reflect a minimum level of normal or shear stress during faulting (although no account is made of pore fluid pressure);

- (iii) Minimum displacement during the most recent fault movement (dating target) should be >50cm (Ariyama 1985); this criterion is suggested by experimental studies;
- (iv) The ESR signals characteristic of several paramagnetic centres for more than one grain size should be measured, for the reasons indicated above (Fukuchi 1988; Buhay et al 1988; Grün 1992).

The effects of multiple slip events involving repeated cataclasis within single gouge seams, on resetting has barely yet been addressed. Clearly, proper petrographic characterisation of quartz gouge materials to be dated by ESR is important. For example, mixed populations of porphyroclastic and authigenic quartz, relating to fault slip and subsequent fluid activity respectively, would be expected to yield a 'mixed' ESR age. A correlation between the surface textures of fault gouge quartz grains and their ESR ages has been observed by Kanaori et al (1985). Although the viability of 'texture dating' as a stand-alone technique, remains highly questionable (cf. Kanaori et al 1985) further investigation by, for example, cathodoluminescence would seem worthwhile.

For quartz separated from fault gouge, ESR dating applies to the 1000 to 1-2 million year range, which approximates to the Quaternary Era (Grün 1992). Accuracy is in the range  $\pm 10-20\%$  for one standard deviation. Both the age range and accuracy depend on the sample characteristics and environmental dose rate. Since radiation is attenuated by water, it is necessary to assess the in-situ water content. Uncertainty in former water content leads to some slight increase in overall uncertainty in the age estimate, though for ESR dating in general this is not usually a significant contribution to the overall uncertainty.

In summary, ESR direct dating of fault movements is at a relatively early stage of development and, at the present time, it is difficult to assess the reliability of the technique. The principal uncertainties have been highlighted above. A considerable number of ESR ages considered to date the most recent movement on faults have now been published but none are constrained by accurate independently-determined ages (Grün 1992).

## 7.2 SAMPLE COLLECTION AND FIELD MEASUREMENTS

A series of fault gouge and wall rock samples from Fracture Zones NE-4, NE-3 and the clay seam at chainage 118m was collected for ESR dating. (These are the same bulk gouge samples for which isotopic dating was applied on the clay fractions (Section 6). Various attributes of



the gouge samples, pertinent to their suitability for ESR dating (Section 7.1.2), are shown in Table 7-1.

Table 7-1 Characteristics of gouges sampled for ESR dating

Sample	Fracture Zone	Gouge seam width (cm)	Gouge seam depth (m)	Displacement across gouge seam	Comment
A91/23	-	2-5	16	unknown; cm's?	discrete fault(?) gouge seam
A91/6	NE-4	1	117	unknown; 0.1-10m range?	discrete fault gouge seam; possible single slip event
A91/8	NE-4	1	117	unknown; 0.1-10m range?	discrete fault gouge seam; possible single slip event
A91/32	NE-4	2-5	117	unknown; 1-10 + m range?	bulk sample; multiple faulting events
A91/38	NE-3	2-5	130	unknown; 0.1-10m range?	discrete fault gouge seam; possible single slip event
A91/39	NE-3	1	130	unknown; 0.1-10m range?	discrete fault gouge seam; possible single slip event

It is clear from Table 7-1 that all of the gouge samples except A91/23 meet the minimum depth criterion, all but one (A91/32) was sampled from a discrete gouge seam flanked by wallrock but the unknown parameter for all samples is the magnitude of displacement during last movement. The ranges of displacement suggested are 'guesstimates' based on observations of gouge faults elsewhere.

The environmental radiation dose received by the samples as determined by in-situ gamma-ray spectrometry is shown in Table 7-3 (the raw data are presented in Appendix 4). The bulk gouge samples were collected and stored in doubled-up, airtight polythene bags to retain moisture.

### 7.3 MINERAL SEPARATION PROCEDURES

The extraction of quartz from sediments, pottery and volcanic rocks has been undertaken for thermoluminescence (TL) dating of these materials for several decades, and more recently the extraction of quartz from granite for ESR measurement has been performed by the present author (EJR). Using such techniques together with those described by Buhay et al (1988) and Grün and Fenton (1990), quartz was extracted from the fault gouge samples A91/6, 8, 23, 32, 38, 39.

Initial sample preparation was undertaken concurrently with the clay fraction separations (Appendix 2) made for isotopic dating analysis. Microscopic examination of several grain size fractions for each of the six samples indicated that the larger fractions contained a considerable fraction of polymineralic (lithic) fragments. The grain size of any quartz separated from these degraded lithic fragments would clearly not be represented by the clast grain size. For this reason material from coarse grain size fractions was not used; clay-poor grain size fractions from 75-250 $\mu\text{m}$  were prepared for ESR analysis. Unfortunately, this meant that any variation in ESR signal intensity with grain size could not be assessed. All preparation was performed in normal laboratory lighting conditions.

Further sample preparation first involved treatment with concentrated hydrochloric acid (HCl) to remove any carbonate present, and also small quantities of fluorite which were visible under the polarizing microscope. All samples reacted strongly on contact with the HCl, suggesting that considerable concentrations of carbonate were indeed present. Following treatment in HCl for around five minutes when all signs of reaction had subsided, the samples were washed copiously with distilled water.

The samples were then treated with concentrated (40%) hydrofluoric acid (HF) for approximately 60 minutes at room temperature. This treatment is used widely in the TL preparation of quartz grains, and fulfils two roles. First, the acid slowly dissolves the outer portion of the quartz grains, etching to a depth of approximately 20 $\mu\text{m}$  during the course of the treatment. This removes most of the zone which has been exposed to alpha irradiation from outside the grain, and allows calculation of the average beta and gamma dose to the grain.

Secondly, the acid dissolves clay minerals (which were not present in this case), feldspars and micas, usually leaving only quartz and heavy minerals. However, the degree of etching of these phases depends on their grain size and composition as well as other variables such as temperature.

In all of the gouge samples, considerable quantities of feldspar remained after the HF acid treatment. Following the HF treatment, samples were washed with distilled water, HCl to remove fluorides formed during the HF treatment, and more distilled water. In order to remove the feldspar still remaining, the samples were immersed in concentrated (38%) fluorosilicic acid ( $\text{H}_2\text{SiF}_6$ ) for several weeks at room temperature. (This treatment has been found to be effective in removing feldspars without dissolving the quartz when separating quartz from crushed granites).

Even after an extended period in  $H_2SiF_6$ , feldspar was still present in all the samples. It is not clear whether the particular feldspars present are intrinsically more resistant, or whether the fact that the samples came from within a fault gouge is important.

Following the  $H_2SiF_6$  treatment the samples were washed with distilled water. Heavy minerals were removed with the use of a solution of sodium polytungstate density  $2.67gcm^{-3}$ . The fraction less dense than  $2.62gcm^{-3}$  (primarily alkali feldspar) was also removed from each sample. The polytungstate solution was washed off with copious quantities of distilled water.

While most of the remaining feldspar was removed by the density separation, some samples still had some plagioclase remaining. These samples were given a further  $H_2SiF_6$  treatment of around one week. Optical microscopy indicated good separation of quartz was achieved for five samples.

The mineral separation procedure is summarized in Table 7-2, and the gradual purification of sample A91/23 is illustrated in Fig 7-2.

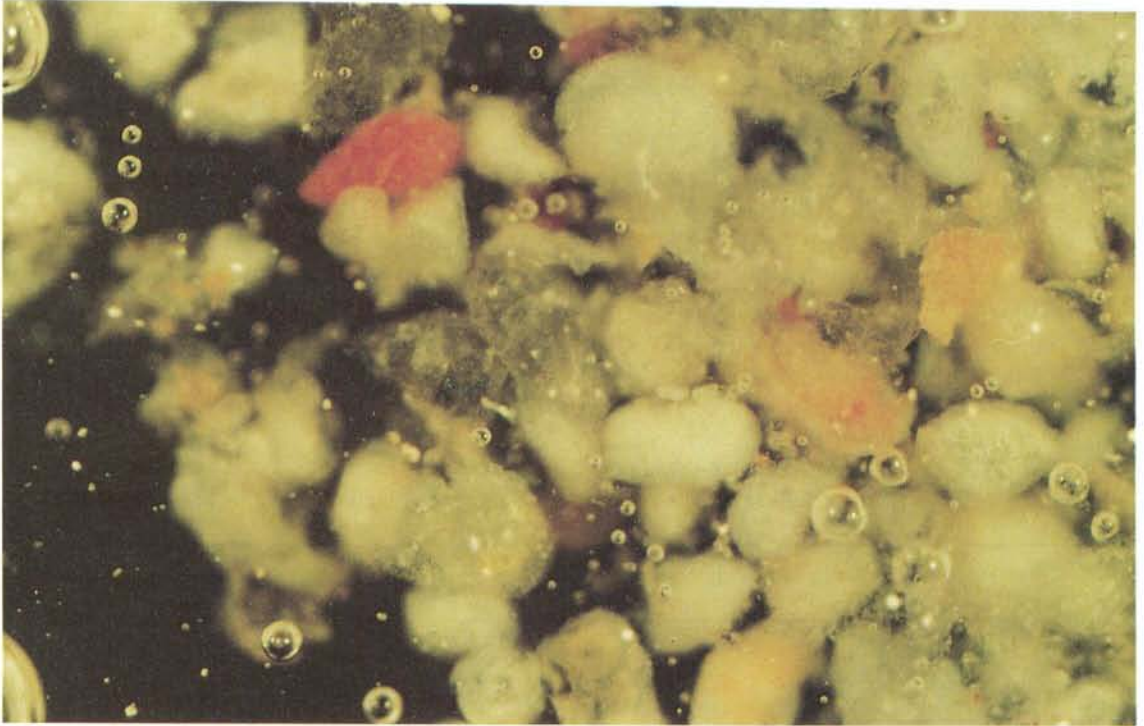
Table 7-2 Summary of mineral separation procedures

Step	Treatment	Effect
1	5min conc HCl	remove $CaCO_3$
2	60min conc HF	etch quartz grains
3	1min dil HCl	remove fluorite
4	6weeks $H_2SiF_6$	dissolve feldspars
5	fraction $>2.67 g.cm^{-3}$ removed by heavy liquid separation	remove heavy minerals
6	fraction $<2.62 g.cm^{-3}$ removed by heavy liquid separation	remove remaining alkali feldspars
7	1week $H_2SiF_6$	fully dissolve remaining plagioclase

**Figure 7-2** [overleaf] Reflected light photomicrographs showing the progressive purification of quartz from gouge sample A91/23. **(a)** Unmounted grains of the untreated sample (after clay extraction) showing mainly cloudy or red feldspars and clear quartz grains, with a grain size of about  $200\mu m$ ; [FOTO ESR/1]; **(b)** gelatin mount of grains following HCl and HF treatment; many feldspar grains remain although clearer quartz grains are also visible; 2X magnification of (a), [FOTO ESR/3]; **(c)** unmounted quartz grains after completion of mineral separation; some frostiness of the dry grains is due to acid treatments; same magnification as (a), [FOTO ESR/5].



**a**



**b**



**c**

Using the separated quartz grains, ten aliquots of 100.0 ± 0.1 mg were weighed out for each sample into small glass (durham) tubes. For each sample, the individual aliquots were exposed to different gamma doses using an <sup>60</sup>Co irradiation facility housed in the Department of Chemical Engineering, Imperial College, University of London. The gamma doses were as follows: 0, 2, 4, 8, 16, 32, 64, 128, 256 and 512Gy. Each aliquot of a single sample was irradiated in the same position, and the different doses were administered simply by changing the irradiation exposure time. Following the first set of ESR measurements, the samples were irradiated again using the same facility, resulting in cumulative gamma doses of: 0, 15, 30, 59, 118, 235, 470, 940, 1,880 and 3,760Gy.

## 7.4 MEASUREMENT AND RESULTS

### 7.4.1 Environmental radiation dosimetry

The environmental radiation dosimetry determined by *in-situ* gamma-ray spectrometry is presented in Table 7-3. Laboratory determinations of the U, Th and K concentrations in the bulk (wallrock and gouge) samples were made by neutron activation analysis undertaken by XRAL of Ontario, Canada. These results together with determinations of the water content of selected bulk samples are shown in Table 7-4.

Table 7-3 Environmental dosimetry determined from portable gamma-ray spectrometry measurements

Probe reading No	Related sample	Comment	Gamma dose rate (Gy/ka)
1	A91/8	5cm from gouge seam 3	1.70
2	A91/7	10cm from gouge seam 2	1.74
3	A91/6	20cm from gouge seam 1	1.82
4	A91/6,7,8	2m from gouge seam 1	2.21
5	A91/3	25cm from gouge seam 3	1.94
6	A91/6,7,8	5m from gouge seam 3	2.70
7&10	A91/6	in gouge seam 1	1.07
8&11	A91/7	in gouge seam 2	1.70
9&12	A91/8	in gouge seam 3	1.85
1-14		side tunnel at 670m	5.21
10-17	A91/23	in gouge seam	1.80
18-22	A91/32,36	in gouge seam	1.35
23-27	A91/32,36	50cm N of gouge samples	1.40

Note: probe reading nos. refer to raw data given in Appendix 4

Table 7-4 Results of neutron activation analyses and water content determinations on bulk gouge and wallrock samples

Sample	Fracture Zone	Rock type	U (ppm)	Th (ppm)	K (%)	Water (wt.%)
A91/23	Info. Gall.	gouge	2.42 ± 0.12	4.43 ± 0.11	7.57 ± 0.37	16.3
A91/25	Info. Gall.	granite wallrock	2.00 ± 0.10	4.70 ± 0.24	2.80 ± 0.14	nd
A91/6	NE-4	gouge	3.18 ± 0.16	2.64 ± 0.07	1.30 ± 0.06	11.1
A91/7	NE-4	gouge	1.96 ± 0.10	3.81 ± 0.09	1.80 ± 0.09	7.7
A91/8	NE-4	gouge	1.60 ± 0.08	5.76 ± 0.13	3.20 ± 0.16	11.1
A91/9	NE-4	gouge float	2.80 ± 0.14	20.00 ± 1.00	3.10 ± 0.16	nd
A91/10	NE-4	granite wallrock	3.80 ± 0.19	7.00 ± 0.35	2.00 ± 0.10	nd
A91/11	NE-4	granite wallrock	2.40 ± 0.12	17.00 ± 0.85	4.10 ± 0.21	nd
A91/12	NE-4	gouge	2.57 ± 0.13	2.13 ± 0.07	1.40 ± 0.06	10.4
A91/32	NE-4	gouge	6.87 ± 0.34	12.66 ± 0.22	4.63 ± 0.23	11.8
A91/36	NE-4	cataclasite	5.93 ± 0.30	10.20 ± 0.19	4.14 ± 0.20	7.7
A91/17	EW-7	fault breccia	6.50 ± 0.33	74.00 ± 3.70	5.10 ± 0.26	nd
A91/18	EW-7	granite wallrock	3.50 ± 0.18	14.00 ± 0.70	3.10 ± 0.16	nd
A91/19	EW-7	granite wallrock	6.60 ± 0.33	50.00 ± 2.50	4.70 ± 0.24	nd
A91/38	NE-3	gouge	5.49 ± 0.27	24.27 ± 0.40	7.76 ± 0.38	8.1
A91/39	NE-3	gouge	6.55 ± 0.33	24.15 ± 0.40	8.90 ± 0.40	13.1
A91/40	NE-3	granite wallrock	4.30 ± 0.22	35.00 ± 1.75	4.80 ± 0.24	nd
A91/41	NE-3	granite wallrock	5.00 ± 0.25	26.00 ± 1.30	4.10 ± 0.21	nd

Note: all NAA measurements were made by XRAL, Ontario, Canada. The errors quoted represent 5% uncertainty.

A number of observations may be made from these analyses:

- (i) The U, K and Th contents of the bulk gouge samples from Fracture Zones EW-7, NE-3 and NE-4 are broadly comparable with those determined by Landstrom and Tullborg (1993) for various size fractions of gouge in tunnel and core samples from Fracture Zone NE-1.
- (ii) The U contents for all samples are <10ppm but the Th contents show substantial variation from 2 to 74ppm. This may reflect variability in the modal content of Th-rich accessory minerals. The high Th contents in samples A91/17 and A91/19 correlate well with the high gamma dose rate associated with these samples
- (iii) The 'loosely-bound' water contents (H<sub>2</sub>O<sup>-</sup> determined by drying) measured for five bulk gouge samples from NE-4 are very similar. A particularly high water content (16.3 wt.%) was measured in sample A91/23.

- (iv) The potassium contents of the bulk gouge samples vary by a factor of two or more but are, in general, significantly higher than the corresponding wallrocks. The potassium contents of the bulk gouge samples do not correspond simply with the potassium concentrations measured in clay separates from the same samples (Table 6-6). This probably relates to variation in the quantities of K-spar in the bulk samples.

#### 7.4.2 ESR spectrometry

The ESR signals of the aliquots from six samples were measured using a JEOL RE1X spectrometer housed in the Godwin Laboratory, Subdepartment of Quaternary Research, University of Cambridge. Measurements were performed at room temperature (cavity temperature 14°C) to observe the E', Ge and OHC centres, at -170°C with gas flow cooling to observe the Al centre and at liquid nitrogen temperature (-196°C) with a finger dewar in order to observe the Al and Ti centres.

The initial room temperature spectra showed the three commonly observed quartz room temperature signals associated with the E' ( $g=2.001$ ), Ge ( $g=1.997$ ) and OHC ( $g=c.2.006$ ) centres respectively (Figs 7-3 and 7-4). In all six samples the OHC and E' signals were large and easily measured, whilst the Ge was significantly smaller.

A certain amount of confusion in the literature exists concerning the OHC centre due to different authors referring to different ESR signals by this name. Following Rink and Odom (1991), the signal referred to here as the OHC is the broad signal centred at around  $g=2.006$  which partially overlaps the E' signal, rather than the narrower signal at  $g=2.011$  (eg. Grün 1992) which was not observed in these samples. This broad signal comprising several components (OHC) is usually observed to be independent of applied gamma dose, and cannot thus be used to derive accumulated dose (AD) (see Rink and Odom 1991). Normal behaviour was observed for the OHC centre in all samples, with no dependence on applied gamma dose.

The Ge signal was observed in all samples, though small in comparison to the E' signal. In four of the samples the Ge signal showed no appreciable variation with applied gamma dose, characteristic of saturated behaviour. This condition is reached at long time intervals (typically >200-300ka) after resetting events. Two samples (A91/23 and A91/38), however, displayed unusual behaviour of the Ge centre, decreasing in signal size with increasing applied gamma dose (Figs 7-4a and 7-4b respectively). This behaviour has been described only rarely in the literature for luminescence or ESR growth characteristics. This negative form of growth is usually

associated with total applied doses significantly greater than the range of accumulated dose (AD) within which the sample is datable.

Several authors have observed dependence of the Ge signal to light exposure in some samples, although the degree of light sensitivity appears sample dependent. These samples were prepared under normal laboratory lighting conditions and subject to light exposure following irradiation and during measurement. However, it is not felt that light sensitivity of this signal could be responsible for the above observations.

The behaviour of the E' centre was found to vary between the different samples. Sample A91/39 showed no change in signal size with applied gamma dose (Fig 7-4c), ie. saturated behaviour. The E' signals of samples A91/23 and A91/38 decreased with dose, as did their Ge signals (Figs 7-4a and 7-4b). The E' signals from these three samples cannot be used to derive a value of AD, presumably due to their antiquity.

The E' signals from the remaining samples did, however, show some growth as a function of applied gamma dose. In all cases the amount of growth was small, characteristic of a condition close to saturation. A consequence of this is that any extrapolation to determine the AD is associated with a large uncertainty. Sample A91/32 had an interesting form of growth, apparently reaching saturation, with further growth commencing at higher doses. Though this behaviour has been recorded for the ESR signal in mollusca (Katzenberger and Willems 1988) and the luminescence of quartz (Ervanne et al 1992), it has not been previously seen in the ESR signal of quartz.

The E' signal is known to be composed of several different components (Weil 1984), and the growth behaviour has previously been described as complex. It is felt that this centre is not simple to interpret in the absence of a simple exponential growth curve. However, in the case of the three samples which do display some growth of the E' centre, only slight growth is observed as the samples are close to saturation. As mentioned above, this effectively renders the samples undatable (with any degree of accuracy) due to the large uncertainty associated with the extrapolation of the growth curve over such a large range. However, it is possible to estimate roughly the minimum AD for these samples (around 400Gy) and using the environmental dose rate data to derive a minimum age (see below).

While the Al signal was measured for four samples at liquid nitrogen (LN<sub>2</sub>) temperature (-196°C), for samples A91/6 and A91/8 measurements were made at -170°C using a JEOL VT100 variable temperature unit operating with cold nitrogen gas blown across the sample (Fig 7-6a). This



unit, which is fitted to the ESR spectrometer, is able to hold the sample temperature stable to  $\pm 0.1^\circ\text{C}$ . As it is not possible to measure the Ti centre at this temperature, the samples were also measured at  $\text{LN}_2$  temperature using a vacuum finger dewar.

A common problem associated with the measurement of ESR signals at  $\text{LN}_2$  temperatures using a finger dewar is the 'noise' created by the nitrogen liquid boiling. As bubbles form in the nitrogen within the cavity they can change the geometry of the medium through which the microwaves travel, effectively removing the tuned cavity from the resonance condition. To a certain extent these problems may be overcome by very long integration times and repeat measurement. In the case of these samples it was found that they contained exceedingly strong Al signals. Occasional disruption of the measurement was caused by bubbling, but repeat measurements adequately defined the signal. Very good reproducibility was observed between subsequent scans of the same signal.

No measurable Ti signal was observed in any of the samples, presumably due to low natural concentrations of Ti within the quartz. Sample A91/6 appeared to have a very weak signal of approximately the expected shape at the relevant g-values (Fig 7-5a). This signal was, however, of the same order of magnitude as the noise and it was not possible to make statistically significant quantitative measurements.

For each of the samples the Al signal at the highest and lowest dose point were measured (Figs 7-6) for the first applied gamma dose range (max. 512Gy). In all samples, whether measured at  $-170^\circ\text{C}$  or at  $-196^\circ\text{C}$ , the Al signal increased very slightly with dose, but in no case was this increase greater than 17% of the natural signal. Table 7-5 summarizes the signal growth for all of the centres and shows the percentage increase of the Al signal from the natural to the 512Gy dose point. It is interesting to note that the largest increases for the Al signal are observed for those samples which show a decrease in the Ge and E' signals with applied gamma dose. This may suggest that these decreases are due to charge transfer from the Ge and E' centres to the Al centre.

Because the increase of the Al signal with dose over the first applied dose range (max. 512Gy) was small, the same sample aliquots were subject to a further set of gamma doses, ranging from 0 to 3,760Gy (see above). As before the natural (0Gy dose point) and maximum (3,760Gy) aliquots of each sample were measured. All measurements were performed at liquid nitrogen temperature ( $-196^\circ\text{C}$ ). Samples A91/32 and 38 were measured using identical measurement conditions to the previous liquid nitrogen measurements. However, it was found that using a

microwave power of 20mW rather than 100mW reduced the noise, and the remaining four samples were measured at this power.

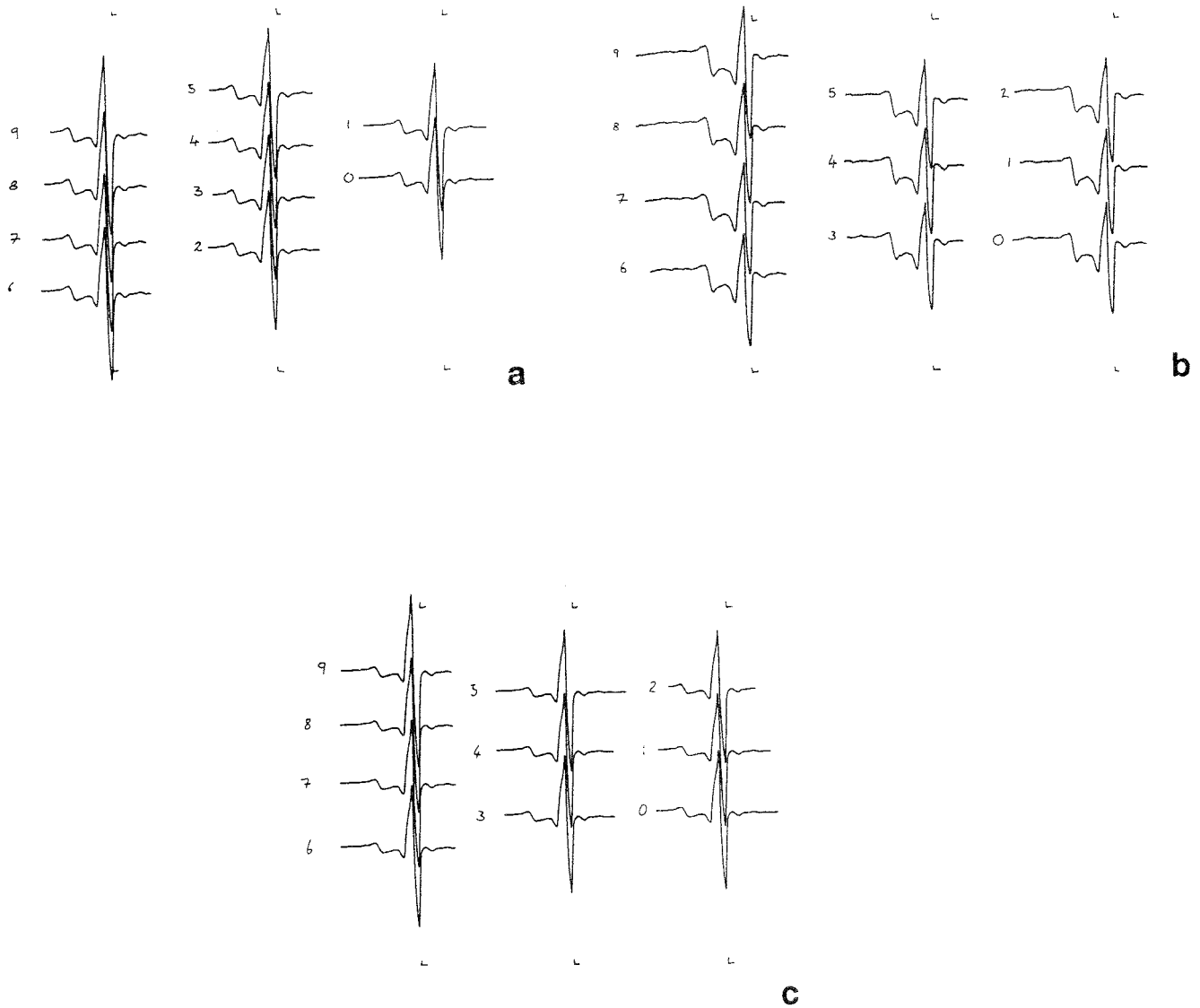
Despite the very high maximum applied dose (3,760Gy) for the second suite of ESR measurements, for five of the samples only slight (<10%) Al signal growth was observed (see Fig 7-7 and Table 7-5). Signal growth of 23% was observed for sample A91/6, the sample which displayed the least growth in the first set of measurements after exposure to 512Gy. However, considering the huge gamma dose to which these samples were exposed, it is felt that these observations confirm the previous conclusion that the samples were all effectively at or close to saturation.

These observations suggest that Al signal measurements may be somewhat scattered, possibly as a result of position irreproducibility within the cavity due to bubbling of liquid nitrogen. If all the difference between pairs of measurements of the same sample is due to scatter, this suggests a scatter of around 8%. This is not particularly likely as for all but one pair of observations (A91/38 second measurement) the signal increases with applied gamma dose. However, the effects of scatter do not affect the basic observation that very little signal growth is observed even after the application of a huge gamma dose.

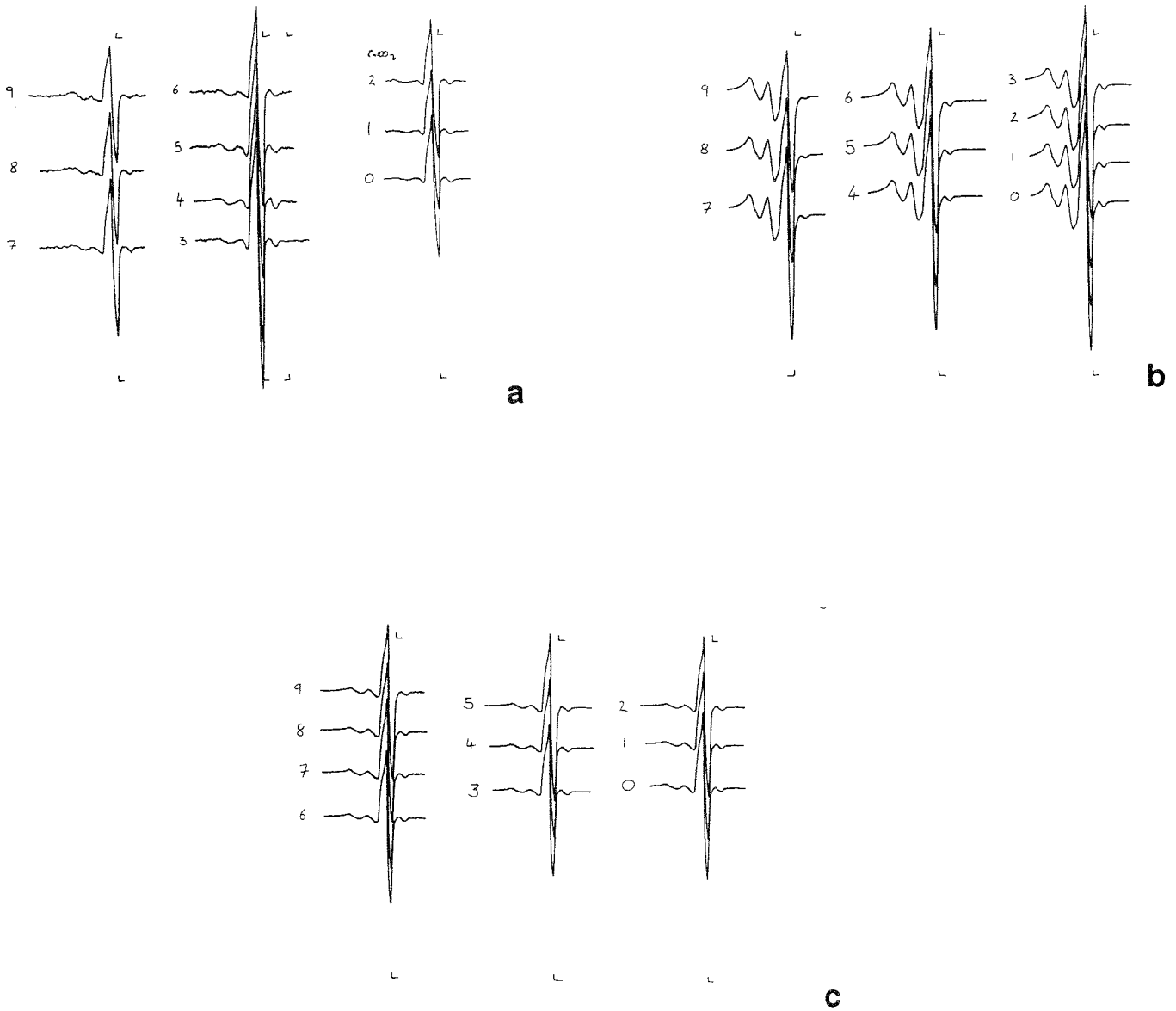
Table 7-5 Summary of signal growth

Sample	Signal					
	E'	OHC	Ge	Ti	Al-1st	Al-2nd
A91/6	G	U	S	-	+3.3%	+23.4%
A91/8	G	U	S	-	+8.5%	+1.8%
A91/23	D	U	D	-	+16.4%	+9.5%
A91/32	G	U	S	-	+3.8%	+4.3%
A91/38	D	U	D	-	+13.6%	-8.0%
A91/39	S	U	S	-	+10.6%	+8.5%

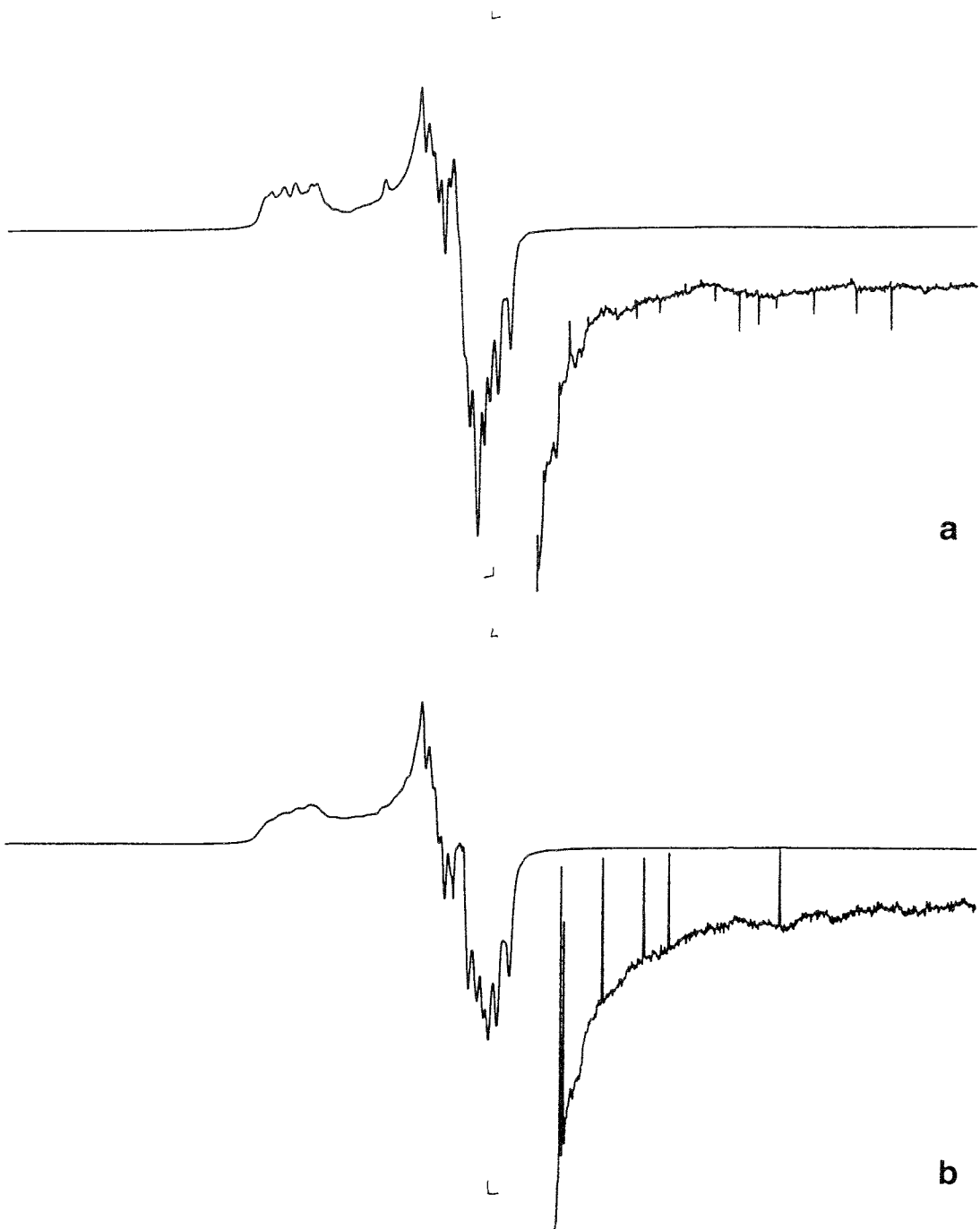
Note: G = some growth of signal as a function of applied gamma dose (see text); U = unaffected by gamma dose; D = some decrease of signal as a function of applied gamma dose; S = no change in signal size due to saturation; - = no signal observed; values for the Al signal are the percentage change from the natural to the highest dose point. Values for the Al signal are the percentage change from the natural to the maximum dose point for the first (max dose 512Gy) and second (max dose 3,760Gy) measurements respectively.



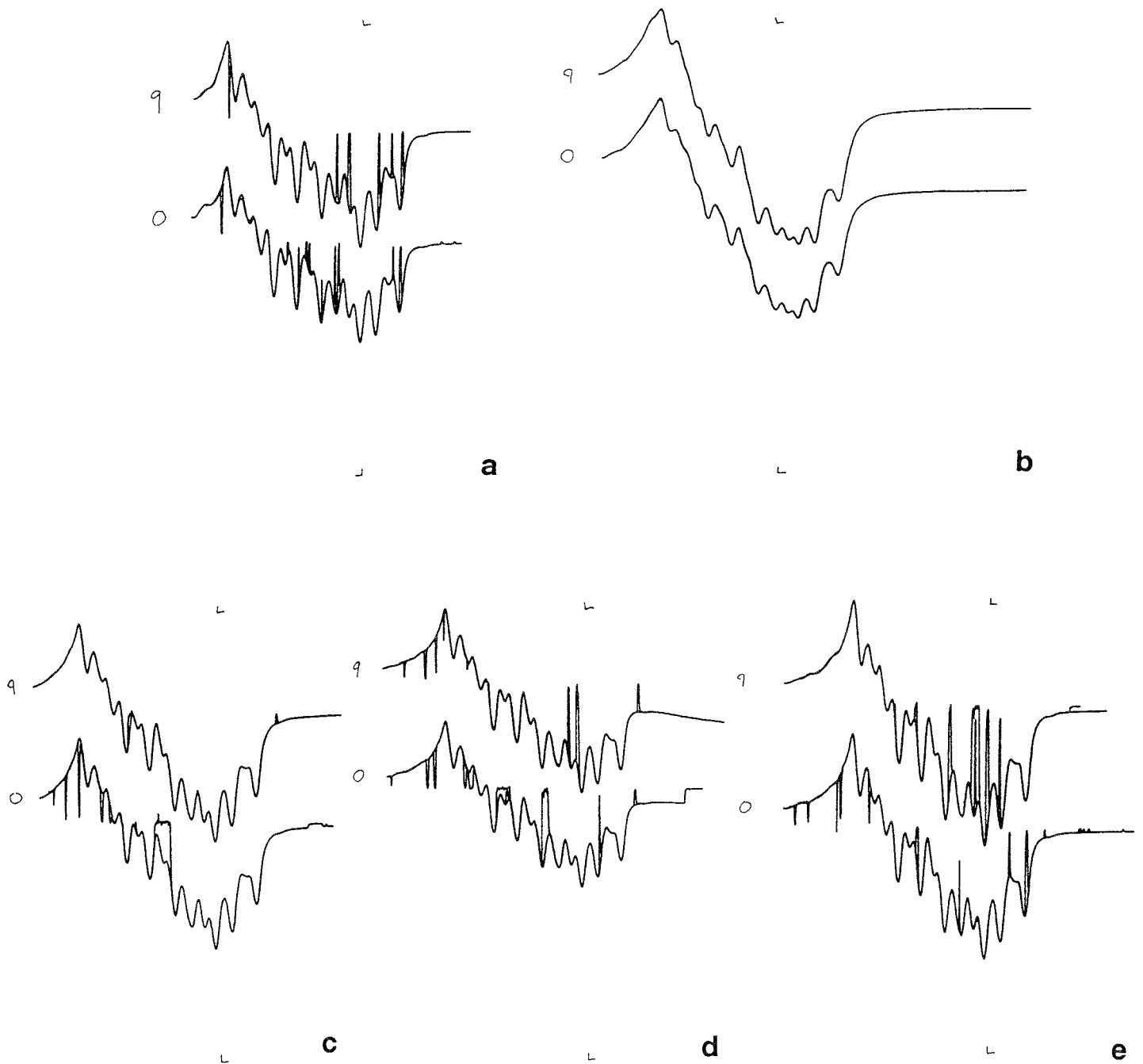
**Figure 7-3** (a) The 1st harmonic ESR signals from 10 aliquots of sample A91/6 measured at room temperature. The different aliquots (for all samples) received different gamma doses: aliquot 0, 0Gy; aliquot 1, 2Gy; 2, 4Gy; 3, 8Gy; 4, 16Gy; 5, 32Gy; 6, 64Gy; 7, 128Gy; 8, 256Gy; 9, 512Gy. Measurement conditions are recorded in the top right corner. The large signal in the centre is that of the E' centre, the small signal to the right the Ge, and the double signal to the left of the E' is the OHC centre. Slight increase with applied gamma dose is observed. (b) Sample A91/8, otherwise as for otherwise as for (a). (c) Sample A91/32, otherwise as for (a).



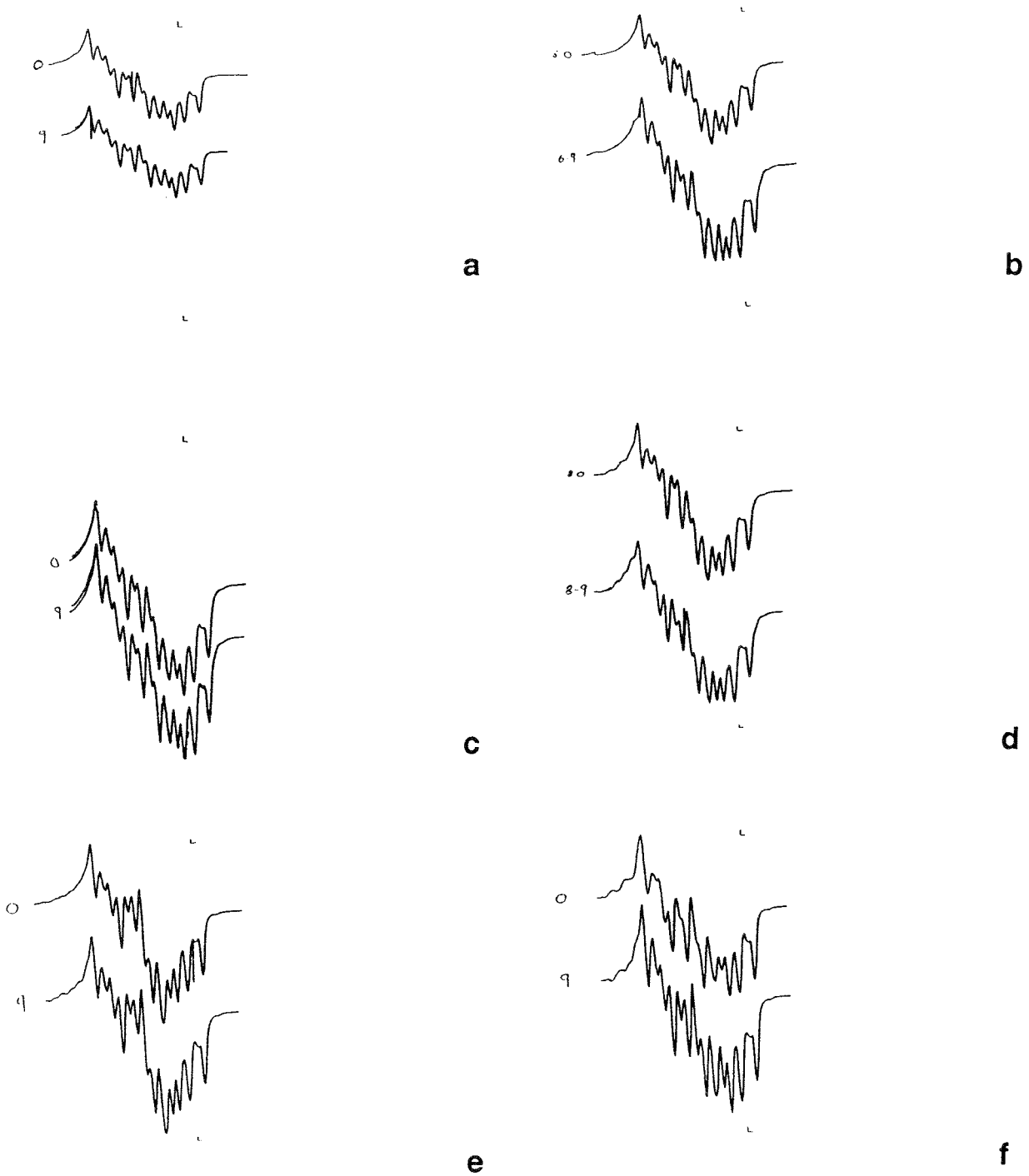
**Figure 7-4** (a) Sample A91/23, otherwise as for 7-3a. (b) Sample A91/38, otherwise as for Fig 7-3a. (c) Sample A91/39, otherwise as for Fig 7-3a.



**Figure 7-5** (a) Liquid nitrogen temperature spectra for sample A91/6. In the upper spectrum the Al centre is clearly observed with its characteristic splitting. No Ti centre is observed. The lower spectrum shows part of the field measured at higher gain (100 times as great) in the region of the Ti signal. Small signals of the order of the noise are observed which may represent a very weak Ti signal. (b) Conditions similar to (a) for sample A91/8. No Ti signal is observed in the lower spectrum.



**Figure 7-6** (a) The highest (9) and lowest (0) dose aliquots from sample A91/8 measured at  $-170^{\circ}\text{C}$ . In both aliquots a large Al signal is measured. The size of the signal does not change significantly with gamma dose demonstrating saturation. (b) The Al signal from sample A91/23 measured at liquid nitrogen temperature. The highest (9) and lowest (0) dose points are shown. The occasional very sharp, short duration signals are noise caused by bubbling of the liquid nitrogen. (c) Sample A91/32, otherwise as for (b). (d) Sample A91/38, otherwise as for (b). (e) Sample A91/39, otherwise as for (b).



**Figure 7-7** (a) Al signals measured at liquid nitrogen temperature. The highest (3,760Gy) and lowest (0Gy) dose points are shown for the second set of ESR measurements. Sample A91/38, microwave power 100mW. (b) Sample A91/6, microwave power 20mW. (c) Sample A91/32, microwave power 100mW. (d) Sample A91/8, microwave power 20mW. (e) Sample A91/39, microwave power 20mW. (f) Sample A91/23, microwave power 20mW.

## 7.5 INTERPRETATION AND DATING

The ESR results can be summarized briefly as follows. Three paramagnetic centres which are useful in the ESR dating of quartz were observed in the samples (E', Ge and Al centres). In all cases, even after the application of a 3,760Gy additive gamma dose, there was not sufficient growth over the applied gamma dose range to allow the extrapolation of the growth curve to determine a value of AD (accumulated dose), a behaviour which is consistent with signal saturation. The E' and Ge signals of two samples showed a decrease with applied gamma dose, further suggesting saturation had already been achieved. Thus the ESR data suggests that the quartz gouge samples have not been reset by fault movement in the recent geological past.

It is difficult to put a figure on the minimum time since last resetting of the ESR signals as this depends on the saturation behaviour of the individual samples. When the signals are close to saturation it is not possible to observe this behaviour, which may vary between samples. If typical saturation characteristics are assumed, then the data from the E' centres which were seen to increase (samples A91/6, A91/8 and A91/32, from Fracture Zone NE-4) would suggest minimum AD values of the order of 400Gy. Using the measured radioactivity data, this corresponds to a minimum age of around 225,000 years before present. It should be re-emphasized that this minimum value relies on the assumption of typical growth characteristics of the E' centre which cannot be observed owing to the saturated nature of the signals.

This minimum age estimate would in general seem low when the data from the Al centres is reviewed. In general, the Al centre reaches saturation at greater dose values than the E' or Ge centres, and so when saturation has been reached for these centres, the Al centre continues to grow. For all the samples, the Al centre showed virtually no growth due to saturation, even up to a maximum dose of 3,760Gy suggesting no indication of resetting of this signal within the region of the last million years.

## 7.6 CONCLUSIONS

Quartz has been separated for ESR dating from a total of six fault gouge samples collected from Fracture Zones NE-4 and NE-3, and from chainage 118m. The samples were chosen to optimize, as far as was possible, the likelihood of resetting of the ESR signals during any recent faulting event.

The primary conclusion from the ESR measurements is that there is no indication of resetting of the signals by fault movement along Fracture zones NE-3 and NE-4 within



the past several hundred thousand to one million years. The estimation of minimum age of resetting relies, however, on the assumption of typical growth characteristics. In the absence of a substantial part of the growth curve being observable, this assumption is unavoidable.

## 8 CONCLUSIONS AND RECOMMENDATIONS

### 8.1 SUMMARY OF RESULTS

The direct fault dating trials at the Äspö Hard Rock Laboratory have successfully tightened the constraints on various phases of fault movement and vein mineralization in the significant Fracture Zones EW-7, NE-4 and NE-3, together with a number of minor faults.

Comprehensive conclusions for each dating method have been presented at the ends of the relevant sections. Only the principal conclusions of the study are summarized here:

- 1) Fracture zones EW-7, NE-4, NE-3 and various minor faults contain faultrocks whose mineralogy and microstructures are testament to a prolonged and polyphase history of movement. Early fault displacement was accommodated by ductile, semi-plastic, mylonitic deformation. This occurred before 1350Ma at temperatures in excess of 350°C, perhaps corresponding to depths up to 10km.
- 2) The most recent fault movements seen in fracture zones NE-4, NE-3 and minor faults, involved the formation of poorly-lithified fault gouge cemented by authigenic 'illite'. Deformation in the gouge was largely accommodated by cataclasis and diffusive mass transfer mechanisms. Fault gouge formation can occur at any depth from several kilometres to near the surface.
- 3) Whereas the mylonites almost certainly formed during aseismic shear, the brittle cataclasites and gouge formed at higher strain-rates, probably during palaeoseismic earthquakes. The amounts of strain and displacement associated with the various faultrocks is difficult to quantify but is considered to be measurable in metres to tens of metres rather than hundreds and thousands of metres.
- 4) Planar tectonic and magnetic susceptibility fabrics measured in two samples are consistent with normal dip-slip (down to the southeast) displacement during gouge formation in Fracture Zone NE-4. (The mylonites also contain kinematic indicators but these were not considered during the present study.)
- 5) Quartz grains were separated from seven gouge samples, from NE-4, NE-3 and a minor fault, for ESR dating. ESR spectra were measured for various paramagnetic centres (E', OHC, Ge and Al) in the quartz. The measurements indicated that saturation had been achieved prior to artificial irradiation, and therefore resetting of the ESR signals by fault movement had not occurred in the

recent geological past. Assuming normal signal growth characteristics, the minimum age of resetting - which is inherently limited by the technique - is of the order of several hundred thousand years to one million years.

6) Palaeomagnetic dating involves comparison with a pre-established chronology. Palaeomagnetic ages were therefore determined for countryrock, cataclasite and vein samples, as well as, the younger gouges. The country rock samples yielded a Proterozoic palaeomagnetic age (c.1800Ma), consistent with independent age data. Stable components of magnetisation in epidote-rich cataclasites and veins overlapped late Proterozoic and Palaeozoic parts of the polar wander. Geological data support the late-Proterozoic age for acquisition of magnetisation. A stable component of magnetisation in gouge from Fracture Zone NE-4 is not significantly different in orientation from the epidote veins. However, a Permo-Triassic (c.270-190Ma) age of magnetisation is preferred on geological grounds and from comparison with the isotopic dating results. The magnetisation may correspond to a diagenetic event following fault movement. Disaggregation and rock magnetic measurements indicate that about two-thirds of the total magnetisation of gouge specimens is carried by the fine-grained matrix. The magnetisation of the gouge is therefore likely to date from the time of fault movement, or to post-date it. The principal carrier of magnetisation in the faultrocks is hematite rather than magnetite as in the country rocks. This suggests that magnetisation of the faultrocks may be associated with oxidative fluid flow, related to or post-dating fault movement.

8) Isotopic dating employed the K-Ar technique. K-Ar analyses of five 'wallrock' samples gave model ages in the range 1280-437Ma. Fine grainsize fractions ( $<2\mu\text{m}$  to  $<0.05\mu\text{m}$ ) were separated from eight gouge samples from fracture zones NE-4, NE-3 and two minor faults, to try to isolate the authigenic 'illite'. The separates were examined by scanning and transmission electron microscopy and XRD. K-Ar model ages measured on the separates ranged from 706 to 302Ma (Precambrian to Upper Carboniferous). The finest grainsize fractions generally gave younger model ages than the coarser fractions due to contamination potassium-bearing porphyroclasts. Taking into account such contamination, it is likely that the authigenic 'illite' was formed at least 250 million years ago, after the most recent significant fault movements. Trial Rb-Sr dating of gouge separates from NE-4 was also undertaken.

9) The oxygen and hydrogen isotopic compositions of the dated clay fractions are not in equilibrium with present-day groundwaters at Äspö. It is possible that the clays were precipitated from an isotopically-heavier brine and have partially equilibrated with present-day waters.

10) The ages given by the various dating methods reflect both inherent differences in the techniques and differences in the phase or phenomenon being dated. Nevertheless, the results of the palaeomagnetic and K-Ar analyses of gouges strongly suggest that authigenic mineral growth in fracture zones NE-4, NE-3 and two other minor faults took place at least 250 million years ago. The most recent fault movements are interpreted to precede this mineral growth. It is possible that the fault movements and mineral growth took place at elevated temperature due to burial under a cover of Palaeozoic sediments.

10) Finally, the above observations suggest that any activity in the Äspö area during the Quaternary and Holocene had little effect on the examined fault/fracture zones.

## 8.2 RECOMMENDATIONS

This preliminary multi-disciplinary trial of fault dating techniques has met the objectives of the study and demonstrated the potential for direct fault dating to become a standard component of investigations on the long-term stability of bedrock.

The state-of-the-art of the dating and microstructural characterization techniques used in this study is improving rapidly (eg. Pevear 1992). Any future studies should take advantage of such improvements. For the illitic gouge materials consideration might be given to  $^{40}\text{Ar}/^{39}\text{Ar}$  dating including laser probe techniques assuming that Ar-recoil could be controlled. Rb-Sr leachate techniques also offer the possibility of providing further dating information. Further mineral characterization using fully-quantitative XRD and analytical TEM methods should also be considered.

Finally, the present study has indicated a need for additional isotopic dating information on the countryrocks at Äspö.

9 REFERENCES

- Ahlin, S. 1982. NNE-SSW striking Precambrian faults of southwestern Sweden. *Geol. Forens. Forh.* 104, 182-185.
- Ahlin, S. 1987. Phanerozoic faults in the Vastergotland Basin area, SW Sweden. *Geol. Forens. Forh.* 104, 182-185.
- Ariyama, T. 1985. Conditions for resetting the ESR clock during faulting. *ESR Dating and Dosimetry, Ionics, Tokyo*, 249-255.
- Basset 1985. Silurian. In, Gee, D.G. & Sturt, B.A. (eds), *The Caledonide Orogen - Scandinavia and Related Areas*. Wiley, New York.
- BEQE, 1992. A review of the seismotectonics of Sweden. BEQE Rept. 43-01-R-001. Prepared for SKB.
- Bergstrom, & Gee, 1985. Cambrian. In, Gee, D.G. & Sturt, B.A. (eds), *The Caledonide Orogen - Scandinavia and Related Areas*. Wiley, New York.
- Bruton, D.L., Lindstrom, M. & Owen, A.W. 1985. The Ordovician of Scandinavia. In, Gee, D.G. & Sturt, B.A. (eds), *The Caledonide Orogen - Scandinavia and Related Areas*. Wiley, New York, pp273-282.
- Besse, J. & Courtillot, V. 1991. Revised and synthetic apparent polar wander paths for the African, Eurasian, North American and Indian plates, and true polar wander since 200Ma. *J. Geophys. Res.* 96, 4029-4050.
- Borradaile, G.J., Keeler, W., Alford, C. & Sarvas, P. 1987. Anisotropy of magnetic susceptibility of some metamorphic minerals. *Phys. Earth Plan. Int.* 48, 161-166.
- Buhay, W.M., Schwarcz, H.P. and Grün, R. 1988. ESR dating of fault gouge: the effect of grain size. *Quaternary Science Reviews*, 7, 515-522.
- Burley, S.D. & Flisch, M. 1989. K-Ar geochronology and the timing of detrital I/S clay illitization and authigenic illite precipitation in the Piper and Tartan fields, Outer Moray Firth, UK North Sea. *Clay Minerals* 24, 285-315.
- Cande, S.C. & Kent, D.V. 1992. A new geomagnetic polarity time scale for the Late Cretaceous and Cenozoic. *J. Geophys. Res.* 97, 13917-13951.
- Craig, H. 1961. Isotopic variations in meteoric waters. *Science* 133, 1702-1703.
- Deer, W.A., Howie, R.A. & Zussman, J. 1966. An introduction to the rock-forming minerals. Longman, London. 528pp.
- Eberl, D.D., Srodon, J., Kralik, M., Taylor, B.E. & Peterman, Z.E. 1990. Ostwald ripening of clays and metamorphic minerals. *Science* 248, 474-477.
- Eliasson, T. 1993. Mineralogy, geochemistry and petrophysics of red coloured granite adjacent to fractures. SKB TR 93-06
- Ervanne, H., Jungner, H. and Räsänen M. 1992. Dating of fluvial sediments from the Amazon lowland in Peru. *Quaternary Science Reviews*, 11, 71-73.

- Fallick, A.E., Haszeldine, R.S. & Pearson, M.J. 1993. Overview of clay mineral stable isotope ( $\delta^{18}\text{O}$ ,  $\delta\text{D}$ ) systematics in the northern North Sea. Abstract, Mineralogical Society (Clay Minerals Group) Meeting on Diagenesis, Overpressure and Reservoir Quality. 25-26 March, Cambridge, UK.
- Faure, G. 1986. Principles of isotope geology. 2nd edition. Wiley, New York, 589pp.
- Flinn, D. 1992. The history of the Walls Boundary fault, Shetland: the northward continuation of the Great Glen fault from Scotland. *J. Geol. Soc. Lond.* 149, 721-726.
- Floden, T. 1980. Seismic stratigraphy and bedrock geology of the central Baltic. *Stockholm Contrib. Geol.* 35, 1-240.
- Fry, N. 1984. The field description of metamorphic rocks. Geological Society of London, Handbook Series.
- Fukuchi, T. 1988. Applicability of ESR dating using multiple centres to fault movement - The case of the Itoigawa-Shizuoka Tectonic Line, a major fault in Japan. *Quaternary Science Reviews* 7, 509-514.
- Fukuchi, T. 1992. ESR studies for absolute dating of fault movements. *J. Geol. Soc. Lond.* 149, 265-272.
- Geyh, M.A. & Schleicher, H. 1990. Absolute age determination. Springer-Verlag, Berlin 503pp.
- Gorbatshev, R. 1980. The Precambrian development of southern Sweden. *Geol. Forens. Forh.* 102, 129-136.
- Gorbatshev, R. 1985. Precambrian basement of the Scandinavian Caledonides. In, Gee, D.G. & Sturt, B.A. (eds), *The Caledonide Orogen - Scandinavia and Related Areas*. Wiley, New York.
- Gorbatshev, R., Lindh, A., Solyom, Z., Laitakari, I., Aro, K., Lobach-Zhuchenko, S.B., Markov, M.S., Ivliev, A.I. & Bryhni, I. 1987. Mafic dyke swarms of the Baltic Shield. In, Halls, H.C. & Fahrig, W.F., (eds), *Mafic Dyke Swarms*, *Geol. Soc. Canada Spec. Pap.* 34, pp361-372.
- Graham, J.W. 1949. The stability and significance of magnetism in sedimentary rocks. *J. Geophys Res.* 54, 131-167.
- Gromet, L.P. 1991. Direct dating of deformational fabrics. In, Heaman, J.N. & Ludden, J.N., (eds), *Applications of Radiogenic Isotope Systems to Problems in Geology*. Mineralogical Society of Canada Short Course Handbook, Vol. 19, 165-189.
- Grün, R. 1989. Electron spin resonance (ESR) dating. *Quaternary International* 1, 65-109.
- Grün, R. 1992. Some remarks on ESR dating of fault movements. *J. Geol. Soc. Lond.* 149, 261-264.
- Grün, R. and Fenton, C. 1990. Internal dose rates of quartz grains separated from fault gouge. *Ancient TL*, 8, 26-28.
- Gutmanis, J.C., Hailwood, E.A., Maddock, R.H. & Vita-Finzi, C. 1991. The use of dating techniques to constrain the age of fault activity: a case history from north Somerset, United Kingdom. *Quart. J. Eng. Geol.* 24, 363-374.
- Hailwood, E.A. 1989. *Magnetostratigraphy*. *Geol. Soc. Lond. Spec. Rept. No 19*, 84pp.
- Hailwood, E.A., Maddock, R.H., Fung, T. & Rutter, E.H. 1992. Palaeomagnetic analysis of fault gouge and dating fault movement, Anglesey, North Wales. *J. Geol. Soc. Lond.* 149, 273-284.

- Hamilton, P.J., Kelley, S. and Fallick, A.E. 1989. K-Ar dating of illite in hydrocarbon reservoirs. *Clay Minerals* 24, 215-231.
- Harper, C.T. 1970. Graphical solutions to the problems of radiogenic Ar loss from metamorphic minerals. *Eclogae Geologicae Helvetica* 63, 119-140.
- Hunziker, J.C. 1986. The evolution of illite to muscovite: an example of the behaviour of isotopes in low grade metamorphic terrains. *Chem. Geol.* 57, 31-40.
- Ikeya, M., Miki, T. & Tanaka, K. 1982. Dating of a fault by electron spin resonance on intrafault materials. *Science* 215, 1392-1393.
- Ito, T. & Sawada, S. 1985. Reliable criteria for selection of sampling points for ESR fault dating. *ESR Dating & Dosimetry, Ionics, Tokyo*, 229-237.
- Kanaori, Y., Tanaka, K. & Miyakoshi, K. 1985. Further studies on the use of quartz grains from fault gouges to establish the age of faulting. *Engineering Geology* 21, 175-194.
- Katzenberger, O. and Willems, N. 1988. Interferences encountered in the determination of AD of mollusc samples. *Quaternary Science Reviews*, 7, 485-489.
- Klingspor, I. 1973. A preliminary report on the dating by the K/Ar method of a basaltic neck at Gobnehall, southern Sweden. *Geol. Foren. Forh.* 95, 287-289.
- Kornfalt, K-A & Wikman, H. 1987. Description to the map of solid rocks around Simpevarp. SKB PR 25-87-02.
- Kralik, M., Clauer, N. Holnsteiner, R. Heumer, H. and Kappel, F. 1992. Recurrent fault activity in the Grimsel Test site (GTS, Switzerland): revealed by Rb-Sr, K-Ar and tritium isotope techniques. *J. Geol. Soc. Lond.* 149, 293-301.
- Landstrom, O. & Tullborg, E-L. 1993. Results of a geochemical study of Zone NE-1, based on samples from the Aspo tunnel and drillcore KAS 16 (395 to 451m). SKB PR 25-93-01.
- Langley, K.M. 1981. Dating the time of movement of faults in the Coal Measures of the East Midlands. *Mercian Geologist* 8, 133-142.
- Lee, M.J, Aronson, J.L. & Savin, S.M. 1989. Timing and conditions of Permian Rotliegende sandstone diagenesis, southern North Sea: K/Ar and oxygen isotopic data. *Bull. Amer. Assoc. Petrol. Geol.* 73, 195-215.
- Liboriussen, J., Ashton, P. and Tygesen, T. 1987. The tectonic evolution of the Fennoscandian border zone, Denmark. *Tectonophys.* 137, 21-29.
- Longstaffe, F.J. & Ayalon, A. 1990. Hydrogen-isotope geochemistry of diagenetic clay minerals from Cretaceous sandstones, Alberta, Canada: evidence for exchange. *Appl. Geochem.* 5, 657-668.
- Lundqvist, J. 1979. Precambrian of Sweden. *Sveriges Geol. Undersok. Ser. C* 768.
- Lyons, J.B & Snellenburg, J. 1971. Dating faults. *Bull. Geol. Soc. Amer.* 82, 1749-1752.
- Macintyre, R.M. and Hamilton, P.J. 1984. Isotopic geochemistry of lavas from sites 553 and 555. Initial Repts. Deep Sea Drilling Project LXXXI, 775-781.

- Maddock, R.H., 1992, Absolute dating of fault movements. *J. Geol. Soc. Lond.* 149, 249-250.
- Martinsson, A. 1968. Cambrian palaeontology of Fennoscandian basement fissures. *Lethaia* 1, 137-155.
- McClay, K.R., Norton, M.G., Coney, P. & Davis, G.H. 1986. Collapse of the Caledonian Orogen and the Old Red Sandstone. *Nature* 323, 147-149.
- Miki, T. & Ikeya, M. 1982. Physical basis of fault dating with ESR. *Naturwissenschaften* 69390-391.
- Miller, W.M., Fallick, A.E., Leake, B.E., Macintyre, R.M. and Jenkin, G.R.T. 1991. Fluid disturbed hornblende ages from the Dalradian rocks of Connemara, western Ireland. *J. Geol. Soc. Lond.* 148, 985-992.
- Morner, N-A. 1989. Postglacial faults and fractures on Äspö. SKB PR 25-89-24.
- Munier, R. 1989. Brittle tectonics on Äspö, SE Sweden. SKB PR 25-89-15.
- Munier, R. 1992. Update of structural models for the Äspö area; emphasis on brittle deformation. SKB PR 25-92-07.
- Munier, R. 1993. Four-dimensional analysis of fracture arrays at the Äspö Hard Rock Laboratory, SE Sweden. *Eng. Geol.* 33, 159-175.
- Murphy, P.J., Briedis, J. & Peck, J.H. 1979. Dating techniques for fault investigations. *Geol. Soc. Amer. Revs. Eng. Geol.* 4, 153-168.
- Norling, E. and Bergstrom, J. 1987. Mesozoic and Cenozoic evolution of Scania, southern Sweden, *Tectonophysics* 137, 7-19.
- O'Neil, J.R. 1985. Water-rock interaction in fault gouge. *Pure & Appl. Geophys.* 122, 440-446.
- Perroud, H., Rombardet, M. & Bruton, D.L. 1992. Palaeomagnetic constraints upon the palaeogeographic position of the Baltic Shield in the Ordovician. *Tectonophysics.* 201, 97-120.
- Pevear, D.R. 1992. Illite age analysis, a new tool for basin thermal history analysis. In, Kharaka, Y.K. & Maest, A.S. (eds), *Proc. 7th Int. Symp. Water-Rock Interaction* pp.1251-1254.
- Piper, J.D.A., 1988. Palaeomagnetic Database. Redwood Burn Ltd.
- Printzlau, I. and Larsen, O. 1972. K/Ar determinations on alkaline olivine basalts from Skane, southern Sweden. *Geol. Forens. Forh.* 94, 259-269.
- Ramberg, I.B. and Speldjnaes, N. 1978. The tectonic history of the Oslo region. In, Ramberg, I.B. and Neumann, E.R., eds, *Tectonics and geophysics of continental rifts*, Reidel, Dordrecht.
- Richter, C., van der Pluum, B.A. & Housen, B.A. 1993. The quantification of crystallographic preferred orientation using magnetic anisotropy. *J. Struct. Geol.* 15, 113-116.
- Rink, J. and Odom, L. 1991. Natural alpha recoil particle radiation and ionizing radiation sensitivities in quartz detected with ESR: Implications for geochronometry. *Nuclear Tracks* 18, 163-173.



- Roberts, & Gee, D. G. 1985. Timing of deformation in the Caledonide Orogen. In, Gee, D.G. & Sturt, B.A. (eds), The Caledonide Orogen - Scandinavia and Related Areas. Wiley, New York.
- Rutter, E.H., Maddock, R.H., Hall, S.H. & White, S.H. 1986. Comparative microstructures of natural and experimentally produced clay-bearing fault gouges. *Pure & Appl. Geophys.* 124, 3-30.
- Rutter, E.H. & Maddock, R.H. 1992. On the mechanical properties of synthetic kaolinite/quartz fault gouge. *Terra Nova* 4, 489-500.
- Samuelsson, L. 1975. Palaeozoic fissure fillings and tectonism of the Goteborg area, southwestern Sweden. *Sveriges Geol. Undersok. Ser. C* 69, 43pp.
- Savin, S.M. & Lee, E. 1988. Isotopic studies of phyllosilicates. In, Bailey, S.W. (ed), *Hydrous Phyllosilicates*. *Min. Soc. Amer. Revs. Mineral.* 19, pp189-223.
- Shafiqullah, M. & Damon, P.E. 1974. Evaluation of K-Ar isochron methods. *Geochim. Cosmochim. Acta.* 38, 1341-1358.
- Shafiqullah, M., Damon, P.E., Davis, G.H. & Glasmann, J.R. 1990. Timing of structural movements through K-Ar dating of fault products - submicron clay gouge, cataclasite and breccia. 86th Ann. Mtg. Geol. Soc. Amer. Abstracts with Programs 22, 82.
- Shibata, K., Sugiyama, Y., Takagi, H. & Uchiumi, S. 1988. Isotopic ages of rocks along the Median Tectonic Line in the Yoshino area, Nara Prefecture. *Bull. Geol. Surv. Japan* 39, 759-781.
- Shibata, K. & Takagi, H. 1988. Isotopic ages of rocks and intrafault materials along the Median Tectonic Line - an example in the Bungui-toge area, Nagano Prefecture. *J. Geol. Soc. Japan* 94, 35-50.
- Sibson, R.H. 1977. Fault rocks and fault mechanisms. *J. Geol. Soc. Lond.* 133, 191-213.
- Sivhed, U. 1991. A pre-Quaternary, post-Palaeozoic erosional channel deformed by strike-slip faulting, Scania, southern Sweden. *Geols. Foren. Forh.* 113, 139-143.
- Srodon, J. & Eberl, D.D. 1984. Illite. In, Ribbe, P.H. (ed), *Micas*. *Min. Soc. Amer. Rev. Mineral.* 13.
- Stel, H. 1981. Crystal growth in cataclasites: diagnostic microstructures and implications. *Tectonophys.* 78, 585-600.
- Tagaki, H., Shibata, K., Sugiyama, Y., Uchiumi, S. and Matsumoto, A. 1989. Isotopic ages of rocks along the Median Tectonic Line in the Kayumi area, Mie Prefecture. *J. Mineral. Petrol. Econ. Geol.* 84, 75-88. (in Japanese with english abstract)
- Talbot, C.J. 1990. Some clarification of the tectonics of Äspö and its surroundings. SKB PR 25-90-15.
- Talbot, C.J. 1991. Preliminary structural geology underground in the Äspö hard rock laboratory. SKB PR 25-92-03.

- Talbot, C.J. 1991. Simplified palaeostresses from large populations of faults or semi-ductile shears. Abstract of Presentation to Geological Society, London, Tectonic Studies Group Annual Meeting, Edinburgh.
- Talbot, C.J. & Munier, R. 1989. Faults and fracture zones in Äspö. SKB PR 25-89-11.
- Talbot, C.J., Riad, L. & Munier, R. 1988. The geological structures and tectonic history of Äspö SE Sweden. SKB PR 25-88-05.
- Tanaka, H., Saka, Y., Abe, T., Kohama, S. & Itaya, T. 1992. Fault gouges and their K-Ar ages from the Akaisha Tectonic Line, central Japan. J. Geol. Soc. Japan 98, 39-48.
- Torsvik, T.H., Smethurst, M.A., Van der Voo, R. Trench, A., Abrahamsen, N. & Halvorsen, E. 1992. Baltica: A synopsis of Vendian-Permian palaeomagnetic data and their palaeotectonic implications. Earth Sci. Revs. 33, 133-152.
- Tullborg, E-L, Larson, S.A. Bjorklund, L., Samuelsson, L. & Stigh, J. 1994. A fore deep basin to the Caledonides - evidences of molasse sedimentation. 21st Nordic Geological Winter Meeting Abstract pp.215.
- Tullborg, E-L. Wallin, B. & Landstrom, O. 1990. Hydro-geochemical studies of fracture minerals from water conducting fractures and deep groundwaters at Äspö. SKB PR 25-90-01.
- Ulmishek, G. 1991. Geologic evolution and petroleum resources of the Baltic basin. Amer. Assoc. Petrol. Geol. Memoir 51, 603-632.
- Vidal, G. 1984. Lake Vattern. Geol. Forens. Forh. 106, 397.
- Weil, J.A. 1984. A review of electron spin spectroscopy and its applications to the study of paramagnetic defects in crystalline quartz. Phys. Chem. Miner., 10, 149-165.
- Wikberg, P., Gustafson, G., Rhen, I. and Stanfors, R. 1991. Äspö Hard Rock Laboratory. Evaluation and conceptual modelling based on the pre-investigations. SKB TR 91-22.

## A1.1

**APPENDIX 1      LIST OF SEM MICROPROBE AND STEM ANALYSES**

Note:      1) see Table 3-1 (main text) for location of samples.  
              2) the analyses were recalculated using MACSUITE.  
              2) the analyses follow this tabulation.

Sample	Analysis No	SEM Micro-graph No	Phase	Comment
A91/2	AN1	18	K-spar	vein cutting cataclasite containing epidote clasts
	AN2	18	calcite	within vein of AN1
	AN3	18	epidote	clast within cataclasite
	AN4	18	K-spar	clast within cataclasite
	AN5	20	K-spar	vein cutting cataclasite
	AN6	20	chlorite	cataclasite matrix
	AN7	20	epidote	clast within cataclasite
	AN8	20	epidote	within 'intact' wallrock
A91/4	AN1	63	epidote	centre yellow euhedral grain cut by cataclasite
	AN2	63	epidote	rim yellow euhedral grain cut by cataclasite
	AN3	64	epidote	grain within slickenside zone
	AN4	64	epidote	grain within slickenside zone
	AN5	65	chlorite	?clast within slickenside zone
	AN6	65	epidote	?clast within slickenside zone
	AN7	65	albite	slickenside zone
	AN8	67	prehnite	fractured vein healed by K-spar, cutting slickenside
	AN9	67	prehnite	repeat of AN8
	AN10	68	epidote	porphyroclast in late cataclasite
	AN11	68	prehnite	matrix of late cataclasite
	AN12	68	K-spar	matrix of late cataclasite
A91/14	AN1	48	chlorite	vein
	AN2	48	epidote	porphyroclast
A91/15	AN1	-	K-spar	porphyroclast in chlorite vein breccia
	AN2	-	epidote	porphyroclast in chlorite vein breccia
	AN3	-	chlorite	vein breccia matrix
	AN4	-	chlorite	vein breccia matrix
	AN5	-	epidote	within (polymineralic) mylonite porphyroclast
A91/21	AN1	-	K-spar	host
	AN2	40	epidote	host
	AN3	40	epidote	cataclasite matrix
	AN4	41	calcite	vein cutting cataclasite, mangoan
	AN5	41	K-spar	associated with calcite in vein cutting cataclasite
A91/29	AN1	-	K-spar	within mylonite
	AN2	-	epidote	within mylonite
	AN3	-	albite	within mylonite
	AN5	-	sphene	associated with epidote
	AN6	-	K-spar	porphyroclast in cataclasite cutting mylonite
	AN7	-	epidote	porphyroclast in cataclasite cutting mylonite
	AN8	-	albite	porphyroclast in cataclasite cutting mylonite
	AN9	-	chlorite	vein cutting mylonite and cataclasite
	AN10	-	Fe-oxide	exsolved/altered from chlorite vein

## A1.2

Sample	Analysis No	SEM Micro-graph No	Phase	Comment	
A91/30B	AN1	43-45	K-spar	euhedral habit, infilling fracture	
	AN1a	43-45	K-spar	euhedral habit, infilling fracture	
	AN2	43-45	illite	wispy habit, infilling fracture	
	AN3	43-45	illite	wispy habit, infilling fracture	
	AN10	-	illite	wispy habit	
	AN11	-	illite	wispy habit	
	AN12	-	K-spar	euhedral habit	
	AN13	-	K-spar	euhedral habit	
	AN14	-	illite	wispy habit	
	AN15a	-	illite	wispy habit	
	AN15b	-	illite	wispy habit	
	AN16	-	illite	wispy habit	
	AN17	-	K-spar	euhedral habit	
	AN18	-	illite	wispy habit	
	AN19	80,81	K-spar	euhedral habit	
	AN20	80,81	K-spar	?corroded porphyroclast or damaged during preparation	
	AN21	80,81	illite	wispy habit	
	AN22	80,81	illite	wispy habit	
	A91/36	AN1		K-spar	porphyroclast in calcite vein
		AN2		epidote	porphyroclast in calcite vein
		AN3		calcite	vein matrix, Fe- & Mn-rich
		AN4		calcite	?porphyroclast, pure CaCO <sub>3</sub>
AN5			calcite	vein, pure CaCO <sub>3</sub>	
AS14.10	AN1	-	epidote	within lithic porphyroclast	
	AN2	-	chlorite	within lithic porphyroclast	
	AN3	-	K-spar	within lithic porphyroclast	
	AN4	-	epidote	within lithic porphyroclast	
	AN5	-	K-spar	within lithic porphyroclast	
	AN7	-	K-spar	porphyroclast cut by quartz vein	
	AN8	-	epidote	within lithic porphyroclast	
	AN9	-	chlorite	porphyroclast	
	AN10	24	K-spar	porphyroclast in grey-green gouge	
	AN11	24	gouge	grey-green gouge?	
	AN12	27	gouge	grey-green gouge?	
	AN13	29	gouge	calcite-rich mixture/phase	
	AN14	29	gouge	iron-rich mixture/phase	
	A92/1	AN1	51	calcite	vein margin
AN2		-	calcite	vein centre	
AN3		-	calcite	vein centre	
AN4		-	calcite	vein margin	
A92/2	AN1	53	calcite	vein	
	AN2	53	calcite	vein	
	AN3	54	calcite	centre of fluorite vein	
	AN4	54	calcite	centre of fluorite vein	
	AN5	57	calcite	bright zoned, matrix of cataclasite	
	AN6	57	calcite	dark zoned, matrix of cataclasite	
	AN7	58,59	calcite	dark zoned, within (a)	
	AN8	58,59	calcite	bright zoned, within (a)	
	AN9	58,59	fluorite	luminescent, adjacent (b)	
	AN10	58,59	fluorite	luminescent, within (b)	
	AN11	58,59	calcite	within (c)	
	AN12	58,59	calcite	centre of fluorite vein (d)	
	AN13	58,59	calcite	dark zoned, within (e)	
	AN14	58,59	calcite	bright zoned, within (e)	
	AN15	58,59	epidote	porphyroclast in (e)	
	AN16	58,59	calcite	centre of fluorite vein (f)	
	AN17	58,59	calcite	centre of fluorite vein (f)	
	AN18	-	epidote	within main cataclasite	
	AN19	61	K-spar	vein cutting main cataclasite	

## A1.3

Sample	Analysis No	SEM Micro-graph No	Phase	Comment
A92/4	AN1	69	calcite	vein cutting mylonite
	AN2	70	K-spar	within calcite vein
	AN3	-	epidote	mylonite matrix
	AN4	-	epidote	mylonite matrix
	AN5	71	calcite	vein cutting mylonite
A92/9	AN1	83	calcite	late, main vein
	AN2	83	illite	wispy, enclosing prehnite
	AN3	83	prehnite	drusy
	AN4	83	prehnite	drusy
	AN5	83	prehnite	drusy
	AN6	83	illite	wispy, enclosing prehnite
	AN7	83	illite	wispy, enclosing prehnite
KAS5/FR/ 1-2	AN1	2	K-spar	euhedral
	AN2	2	albite	anhedral
	AN3	2	epidote	anhedral
	AN4	2	chlorite	anhedral
	AN5	5	K-spar	with exsolved blebs of albite
	AN6	5	albite	exsolution lamellae in AN5
	AN7	5	chlorite	associated with sphene
	AN8	5	sphene	associated with chlorite
	AN9	5	epidote	centre of grain
	AN10	5	epidote	rim of grain
	AN11	4	epidote	small irregular grain
	AN12	4	K-spar	veinlet cutting epidote
	AN13	4	K-spar	repeat of AN12
	AN14	4	K-spar	exsolved Ba-rich phase within AN12, also contains Fe-ox
	AN15	4	apatite	cut by K-spar veinlet of AN12
	AN16	4	albite	large grain
	AN17	4	'sericite'	alteration on albite of AN16
	AN18	9	'biotite'	porphyroclast
	AN19	9	K-spar	porphyroclast
	AN20	10	epidote	porphyroclast
	AN21	10	'sericite'	porphyroclast
	AN22	10	albite	porphyroclast
	AN23	10	K-spar	porphyroclast
KAS8/FR/ 3	AN1	14	K-spar	small grain in cataclasite
	AN2	14	K-spar	large porphyroclast
	AN3	14	biotite	small grain associated with K-spar of AN2
	AN4	15	epidote	porphyroclast within cataclasite
	AN5	15	K-spar	porphyroclast within cataclasite
	AN6	15	feldspar	cataclasite matrix?
	AN7	16	K-spar	porphyroclast
	AN8	16	epidote	porphyroclast
	AN9	16	chlorite	porphyroclast
	AN10	17	chlorite	within quartz vein cutting wallrock
SEM-MICROPROBE ANALYSES OF DATED MINERAL SEPARATES				
A92/9 <0.1 $\mu$ m separate	AN1	87	illite	1 $\mu$ m probe, 100s live time
	AN2	87	illite	1 $\mu$ m probe, 100s live time
	AN3	87	illite	1 $\mu$ m probe, 100s live time
	AN4	87	illite	1 $\mu$ m probe, 100s live time
	AN5	87	illite	10 $\mu$ m probe, 100s live time
	AN6	87	illite	10 $\mu$ m probe, 30s live time

## A1.4

Sample	Analysis No	SEM Micro-graph No	Phase	Comment
A92/9 <0.05 $\mu$ m separate	AN1 AN2 AN3 AN4 AN5 AN6 AN7		illite illite illite illite illite illite illite	10 $\mu$ m probe, 30s live time 10 $\mu$ m probe, 30s live time, same cluster as AN1 10 $\mu$ m probe, 30s live time 10 $\mu$ m probe, 30s live time 10 $\mu$ m probe, 30s live time 10 $\mu$ m probe, 30s live time 10 $\mu$ m probe, 30s live time
A92/7 <0.1 $\mu$ m separate	AN1 AN2 AN3 AN4	-	illite illite illite illite	10 $\mu$ m probe, 30s live time 10 $\mu$ m probe, 30s live time 10 $\mu$ m probe, 30s live time 10 $\mu$ m probe, 30s live time
A91/23 <0.05 $\mu$ m separate	AN1 AN2 AN3 AN4 AN5 AN6 AN7	-	illite illite illite illite illite illite illite	10 $\mu$ m probe, 30s live time 10 $\mu$ m probe, 30s live time 10 $\mu$ m probe, 30s live time 10 $\mu$ m probe, 30s live time 10 $\mu$ m probe, 30s live time 10 $\mu$ m probe, 30s live time 10 $\mu$ m probe, 30s live time
STEM SEMI-QUANTITATIVE ANALYSES OF DATED MINERAL SEPARATES				
A91/23 <0.1 $\mu$ m			illite	
A91/23 <0.05 $\mu$ m			illite	
A92/7 <0.1			illite	
A91/6 <0.1 $\mu$ m			illite	
A91/32 <0.1 $\mu$ m			illite	
A91/32 <0.05 $\mu$ m			illite	
A91/36 <0.1 $\mu$ m			illite	
A91/38 <0.1 $\mu$ m			illite	
A91/39 <0.1 $\mu$ m			illite	
A91/39 <0.05 $\mu$ m			illite	

Sample Analysis No	A91/2								A91/4						
	AN1	AN2	AN3	AN4	AN5	AN6	AN7	AN8	AN1	AN2	AN3	AN4	AN5	AN6	AN7
SiO2	65.06	0.37	37.70	63.58	64.60	36.68	36.79	36.98	38.13	37.60	38.07	38.10	27.72	38.01	69.79
TiO2	0.00	0.00	0.00	0.00	0.00	0.00	0.00	0.00	0.00	0.00	0.00	0.00	0.00	0.00	0.00
Al2O3	17.84	0.00	21.87	17.80	17.84	16.55	21.17	19.88	22.18	22.21	22.75	24.17	20.07	23.26	19.76
Cr2O3	0.00	0.00	0.00	0.00	0.00	0.00	0.00	0.00	0.00	0.00	0.00	0.00	0.00	0.00	0.00
FeO	0.00	0.00	12.29	0.33	0.00	18.28	12.64	15.08	13.28	13.25	12.29	10.41	20.94	11.93	0.31
MnO	0.00	0.60	0.00	0.00	0.00	0.31	0.33	0.00	0.00	0.00	0.27	0.31	0.61	0.33	0.00
MgO	0.00	0.00	0.25	0.00	0.00	11.14	0.00	0.00	0.00	0.00	0.00	0.00	17.87	0.00	0.00
NiO	0.00	0.00	0.00	0.00	0.00	0.00	0.00	0.00	0.00	0.00	0.00	0.00	0.00	0.00	0.00
CaO	0.23	55.15	22.18	0.28	0.21	4.64	22.07	22.94	23.04	22.72	22.69	22.72	0.14	22.64	0.00
Na2O	0.00	0.00	0.00	0.00	0.00	0.00	0.00	0.00	0.00	0.00	0.00	0.00	0.00	0.00	10.97
K2O	15.51	0.28	0.36	15.98	15.13	1.02	0.00	0.00	0.00	0.00	0.00	0.00	0.11	0.00	0.00
P2O5	0.00	0.00	0.00	0.00	0.00	0.00	0.00	0.00	0.00	0.00	0.00	0.00	0.00	0.00	0.00
Cl	0.00	0.00	0.00	0.00	0.00	0.00	0.00	0.00	-	-	-	-	-	-	-
S	0.00	0.00	0.00	0.00	0.00	0.12	0.00	0.00	-	-	-	-	-	-	-
Total	98.64	56.40	94.65	97.97	97.78	88.62	93.00	94.88	96.63	95.78	96.07	95.71	87.46	96.17	100.83
Oxygen	8.00	6.00	25.00	8.00	8.00	28.00	25.00	25.00	25.00	25.00	25.00	25.00	28.00	25.00	8.00
Si	3.03	0.04	6.34	3.00	3.03	7.32	6.32	6.32	6.30	6.27	6.30	6.26	5.72	6.27	3.01
Al	0.98	0.00	4.33	0.99	0.99	3.89	4.29	4.00	4.32	4.37	4.43	4.68	4.88	4.52	1.01
Fe2	0.00	0.00	1.73	0.01	0.00	3.05	1.82	2.16	1.84	1.85	1.70	1.43	3.61	1.65	0.01
Mg	0.00	0.00	0.06	0.00	0.00	3.31	0.00	0.00	0.00	0.00	0.00	0.00	5.49	0.00	0.00
Ca	0.01	5.86	4.00	0.01	0.01	0.99	4.06	4.20	4.08	4.06	4.02	4.00	0.03	4.00	0.00
Na	0.00	0.00	0.00	0.00	0.00	0.00	0.00	0.00	0.00	0.00	0.00	0.00	0.00	0.00	0.92
K	0.92	0.04	0.08	0.96	0.91	0.26	0.00	0.00	0.00	0.00	0.00	0.00	0.03	0.00	0.00
Ti	0.00	0.00	0.00	0.00	0.00	0.00	0.00	0.00	0.00	0.00	0.00	0.00	0.00	0.00	0.00
P	0.00	0.00	0.00	0.00	0.00	0.00	0.00	0.00	0.00	0.00	0.00	0.00	0.00	0.00	0.00
Mn	0.00	0.05	0.00	0.00	0.00	0.05	0.05	0.00	0.00	0.00	0.04	0.04	0.11	0.05	0.00
Cr	0.00	0.00	0.00	0.00	0.00	0.00	0.00	0.00	0.00	0.00	0.00	0.00	0.00	0.00	0.00
Total Cat	4.94	5.98	16.53	4.98	4.93	18.87	16.54	16.68	16.54	16.55	16.49	16.41	19.86	16.48	4.95
Ab	0			0	0										
An	1			1	1										100
Or	99			99	99										0
															0

Sample Analysis No	A91/4					A91/14		A91/15					A91/21		
	AN8	AN9	AN10	AN11	AN12	AN1	AN2	AN1	AN2	AN3	AN4	AN5	AN1	AN2	AN3
SiO2	44.01	43.77	37.75	45.01	66.56	27.43	39.10	65.11	38.32	27.41	27.82	37.78	65.34	38.55	38.31
TiO2	0.00	0.00	0.00	0.00	0.00	0.00	0.00	0.00	0.00	0.00	0.00	0.00	0.00	0.00	0.00
Al2O3	21.47	23.10	22.71	24.10	17.95	18.13	22.84	18.03	23.14	18.38	18.15	22.65	18.27	20.80	21.99
Cr2O3	0.00	0.00	0.00	0.00	0.00	0.00	0.00	0.00	0.00	0.00	0.00	0.00	0.00	0.00	0.00
FeO	3.38	1.17	12.35	0.75	0.00	26.73	13.18	1.55	12.36	25.14	25.44	11.71	0.00	15.06	13.19
MnO	0.00	0.00	0.00	0.00	0.00	0.25	0.00	0.00	0.30	0.28	0.38	0.33	0.00	0.00	0.00
MgO	0.00	0.00	0.00	0.00	0.00	15.37	0.00	0.50	0.00	16.49	16.18	0.00	0.00	0.23	0.00
NiO	0.00	0.00	0.00	0.00	0.00	0.00	0.00	0.00	0.00	0.00	0.00	0.00	0.00	0.00	0.00
CaO	26.78	26.91	22.59	27.09	0.00	0.00	23.69	0.00	22.90	0.00	0.12	22.54	0.00	23.43	23.59
Na2O	0.00	0.00	0.00	0.00	0.00	0.35	0.00	0.00	0.00	0.00	0.00	0.00	0.00	0.00	0.00
K2O	0.00	0.00	0.00	0.00	15.66	0.00	0.10	14.66	0.00	0.00	0.00	0.00	16.14	0.00	0.00
P2O5	0.00	0.00	0.00	0.00	0.00	-	-	-	-	-	-	-	-	-	-
Cl	-	-	-	-	-	-	-	-	-	-	-	-	-	-	-
S	-	-	-	-	-	-	-	-	-	-	-	-	-	-	-
Total	95.64	94.95	95.40	96.95	100.17	88.26	98.91	99.85	97.02	87.70	88.09	95.01	99.75	98.07	97.08
Oxygen	25.00	25.00	25.00	25.00	8.00	28.00	25.00	8.00	25.00	28.00	28.00	25.00	8.00	25.00	25.00
Si	6.99	6.92	6.28	6.93	3.05	5.79	6.31	3.00	6.28	5.76	5.83	6.30	3.02	6.34	6.31
Al	4.02	4.30	4.46	4.38	0.97	4.51	4.34	0.98	4.47	4.56	4.48	4.45	0.99	4.03	4.27
Fe2	0.45	0.16	1.72	0.10	0.00	4.72	1.78	0.06	1.69	4.42	4.46	1.63	0.00	2.07	1.82
Mg	0.00	0.00	0.00	0.00	0.00	4.83	0.00	0.03	0.00	5.17	5.06	0.00	0.00	0.06	0.00
Ca	4.56	4.56	4.03	4.47	0.00	0.00	4.09	0.00	4.02	0.00	0.03	4.03	0.00	4.13	4.16
Na	0.00	0.00	0.00	0.00	0.00	0.14	0.00	0.00	0.00	0.00	0.00	0.00	0.00	0.00	0.00
K	0.00	0.00	0.00	0.00	0.91	0.00	0.02	0.86	0.00	0.00	0.00	0.00	0.95	0.00	0.00
Ti	0.00	0.00	0.00	0.00	0.00	0.00	0.00	0.00	0.00	0.00	0.00	0.00	0.00	0.00	0.00
P	0.00	0.00	0.00	0.00	0.00	0.00	0.00	0.00	0.00	0.00	0.00	0.00	0.00	0.00	0.00
Mn	0.00	0.00	0.00	0.00	0.00	0.05	0.00	0.00	0.04	0.05	0.07	0.05	0.00	0.00	0.00
Cr	0.00	0.00	0.00	0.00	0.00	0.00	0.00	0.00	0.00	0.00	0.00	0.00	0.00	0.00	0.00
Total Cat	16.01	15.93	16.49	15.88	4.93	20.03	16.54	4.94	16.49	19.96	19.93	16.47	4.96	16.64	16.56
Ab					0			0					0		
An					0			0					0		
Or					100			100					100		



Sample No Analysis No	A91/21		A91/21								A91/30B				
	AN4	AN5	AN1	AN2	AN3	AN5	AN6	AN7	AN8	AN9	AN10	AN1	AN1a	AN2	AN3
SiO2	0.00	66.91	65.88	38.37	69.93	30.39	65.66	38.44	69.61	28.51	13.29	67.99	69.64	55.50	50.75
TiO2	0.00	0.00	0.20	0.00	0.00	35.19	0.27	0.00	0.00	0.00	0.33	0.20	0.44	0.00	0.00
Al2O3	0.00	18.38	18.24	22.79	19.18	2.25	17.93	24.59	19.70	18.85	10.19	19.29	19.11	23.37	21.75
Cr2O3	0.00	0.00	0.00	0.00	0.00	0.00	0.00	0.00	0.00	0.00	0.00	0.00	0.00	0.00	0.00
FeO	0.00	0.00	0.00	11.94	0.00	1.85	0.00	9.22	0.00	21.98	59.87	0.00	0.00	0.88	0.94
MnO	1.06	0.00	0.00	0.00	0.00	0.00	0.00	0.24	0.00	0.36	0.00	0.00	0.00	0.00	0.00
MgO	0.16	0.00	0.00	0.00	0.00	0.00	0.00	0.00	0.00	16.86	9.42	0.00	0.00	3.31	2.94
NiO	0.00	0.00	0.00	0.00	0.00	0.00	0.00	0.00	0.00	0.00	0.00	0.00	0.00	0.00	0.00
CaO	51.38	0.39	0.00	22.94	0.28	27.93	0.00	22.97	0.23	0.14	0.00	0.17	0.00	0.65	0.60
Na2O	0.00	0.31	0.00	0.00	9.87	0.00	0.00	0.00	10.45	0.00	0.00	0.00	0.27	0.00	0.00
K2O	0.00	14.13	15.10	0.12	0.09	0.00	15.28	0.00	0.13	0.00	0.00	12.74	11.62	4.44	4.10
P2O5	-	-	-	-	-	-	-	-	-	-	-	-	-	-	-
Cl	-	-	-	-	-	-	-	-	-	-	-	-	-	-	-
S	-	-	-	-	-	-	-	-	-	-	-	-	-	-	-
Total	52.60	100.12	99.42	96.16	99.35	97.61	99.14	95.46	100.12	86.70	93.10	100.39	101.08	88.15	81.08
Oxygen	6.00	8.00	8.00	25.00	8.00	20.00	8.00	25.00	8.00	28.00	10.00	8.00	8.00	22.00	22.00
Si	0.00	3.04	3.03	6.33	3.05	4.08	3.03	6.29	3.02	5.94	1.22	3.04	3.07	7.56	7.53
Al	0.00	0.98	0.99	4.43	0.98	0.36	0.98	4.74	1.01	4.63	1.10	1.02	0.99	3.75	3.80
Fe2	0.00	0.00	0.00	1.65	0.00	0.21	0.00	1.26	0.00	3.83	4.59	0.00	0.00	0.10	0.12
Mg	0.03	0.00	0.00	0.00	0.00	0.00	0.00	0.00	0.00	5.24	1.29	0.00	0.00	0.67	0.65
Ca	5.88	0.02	0.00	4.05	0.01	4.01	0.00	4.03	0.01	0.03	0.00	0.01	0.00	0.10	0.10
Na	0.00	0.03	0.00	0.00	0.83	0.00	0.00	0.00	0.88	0.00	0.00	0.00	0.02	0.00	0.00
K	0.00	0.82	0.89	0.03	0.01	0.00	0.90	0.00	0.01	0.00	0.00	0.73	0.65	0.77	0.78
Ti	0.00	0.00	0.01	0.00	0.00	3.55	0.01	0.00	0.00	0.00	0.02	0.01	0.02	0.00	0.00
P	0.00	0.00	0.00	0.00	0.00	0.00	0.00	0.00	0.00	0.00	0.00	0.00	0.00	0.00	0.00
Mn	0.10	0.00	0.00	0.00	0.00	0.00	0.00	0.03	0.00	0.06	0.00	0.00	0.00	0.00	0.00
Cr	0.00	0.00	0.00	0.00	0.00	0.00	0.00	0.00	0.00	0.00	0.00	0.00	0.00	0.00	0.00
Total Cat	6.00	4.89	4.91	16.47	4.88	12.20	4.92	16.34	4.92	19.74	8.21	4.80	4.76	12.95	12.96
Ab		3	0		98		0		98			0	3		
An		2	0		2		0		1			1	0		
Or		95	100		1		100		1			99	97		

Sample No Analysis No	AN10	AN11	AN12	AN13	AN14	A91/30B		AN16	AN17	AN18	AN19	AN20	AN21	AN22	A91/36
						AN15a	AN15b								AN1
SiO2	50.82	51.58	65.92	65.35	52.23	50.89	48.74	48.63	67.72	45.89	66.74	68.12	54.25	54.91	64.79
TiO2	0.00	0.00	0.19	0.48	0.00	0.00	0.00	0.00	0.27	0.00	0.26	0.18	0.00	0.00	0.20
Al2O3	21.55	20.86	18.66	18.55	23.04	21.60	20.88	20.57	18.53	18.62	18.90	19.25	22.96	22.06	18.01
Cr2O3	0.00	0.00	0.00	0.00	0.00	0.00	0.00	0.00	0.00	0.00	0.00	0.00	0.00	0.00	0.00
FeO	1.27	0.92	0.00	0.00	1.08	0.84	1.07	1.01	0.00	1.26	0.00	0.00	0.00	1.56	1.71
MnO	0.00	0.00	0.00	0.00	0.00	0.00	0.00	0.00	0.00	0.00	0.00	0.00	0.00	0.00	0.00
MgO	3.08	2.88	0.00	0.00	3.31	3.12	2.94	2.80	0.00	2.65	0.00	0.00	3.43	3.46	0.00
NiO	0.00	0.00	0.00	0.00	0.00	0.00	0.00	0.00	0.00	0.00	0.00	0.00	0.00	0.00	0.00
CaO	0.82	0.45	0.00	0.00	0.92	0.78	0.71	1.00	0.00	0.61	0.00	0.00	0.00	0.00	0.00
Na2O	0.00	0.00	0.30	0.00	0.00	0.00	0.00	0.00	0.00	0.00	0.00	0.00	0.00	0.00	0.28
K2O	5.52	4.36	13.96	14.43	5.40	5.64	4.67	5.06	13.52	4.23	14.10	15.31	5.41	4.87	15.24
P2O5	0.00	0.00	0.00	0.00	0.00	0.00	0.00	0.00	0.00	0.00	0.00	0.00	0.00	0.00	0.00
Cl	-	-	-	-	-	-	-	-	-	-	-	-	-	-	-
S	-	-	-	-	-	-	-	-	-	-	-	-	-	-	-
Total	83.06	81.05	99.03	98.81	85.98	82.87	79.01	79.07	100.04	73.26	100.00	102.86	88.47	87.63	99.44
Oxygen	22.00	22.00	8.00	8.00	22.00	22.00	22.00	22.00	8.00	22.00	8.00	8.00	22.00	22.00	8.00
Si	7.46	7.65	3.03	3.02	7.39	7.48	7.48	7.48	3.06	7.59	3.03	3.02	7.47	7.59	3.00
Al	3.73	3.65	1.01	1.01	3.84	3.74	3.78	3.73	0.99	3.63	1.01	1.01	3.72	3.59	0.98
Fe2	0.16	0.11	0.00	0.00	0.13	0.10	0.14	0.13	0.00	0.17	0.00	0.00	0.18	0.20	0.01
Mg	0.67	0.64	0.00	0.00	0.70	0.68	0.67	0.64	0.00	0.65	0.00	0.00	0.70	0.71	0.00
Ca	0.13	0.07	0.00	0.00	0.14	0.12	0.12	0.17	0.00	0.11	0.00	0.00	0.13	0.09	0.03
Na	0.00	0.00	0.03	0.00	0.00	0.00	0.00	0.00	0.00	0.00	0.00	0.00	0.00	0.00	0.03
K	1.03	0.83	0.82	0.85	0.98	1.06	0.91	0.99	0.78	0.89	0.82	0.87	0.95	0.86	0.90
Ti	0.00	0.00	0.01	0.02	0.00	0.00	0.00	0.00	0.01	0.00	0.01	0.01	0.00	0.00	0.01
P	0.00	0.00	0.00	0.00	0.00	0.00	0.00	0.00	0.00	0.00	0.00	0.00	0.00	0.00	0.00
Mn	0.00	0.00	0.00	0.00	0.00	0.00	0.00	0.00	0.00	0.00	0.00	0.00	0.00	0.00	0.00
Cr	0.00	0.00	0.00	0.00	0.00	0.00	0.00	0.00	0.00	0.00	0.00	0.00	0.00	0.00	0.00
Total Cat	13.19	12.94	4.89	4.89	13.18	13.18	13.09	13.15	4.83	13.04	4.87	4.90	13.15	13.04	4.96
Ab			3												3
An															3
Or			97	100					100		100	100			94

Sample No Analysis No	A91/36				AS14.10											
	AN2	AN3	AN4	AN5	AN1	AN2	AN3	AN4	AN5	AN7	AN8	AN9	AN10	AN11	AN12	
SiO2	38.05	0.25	0.19	0.00	38.42	29.24	65.41	38.67	66.30	65.28	38.98	26.82	66.83	56.34	44.20	
TiO2	0.00	0.00	0.00	0.00	0.00	0.20	0.20	0.00	0.00	0.00	0.00	0.00	0.00	0.00	3.00	
Al2O3	22.57	0.00	0.00	0.00	23.36	17.97	18.15	22.63	18.47	17.82	23.69	13.83	17.79	17.66	18.55	
Cr2O3	0.00	0.00	0.00	0.00	0.00	0.00	0.00	0.00	0.00	0.00	0.00	0.00	0.00	0.00	0.00	
FeO	12.29	2.42	0.00	0.00	10.80	17.51	0.21	11.52	0.00	0.00	10.76	39.36	0.00	3.10	2.98	
MnO	0.00	3.83	0.00	0.00	0.00	0.33	0.00	0.00	0.00	0.00	0.00	0.00	0.00	0.00	0.00	
MgO	0.00	0.20	0.00	0.00	0.00	20.98	0.00	0.00	0.00	0.00	0.00	5.35	0.00	2.49	2.56	
NiO	0.00	0.00	0.00	0.00	0.00	0.00	0.00	0.00	0.00	0.00	0.00	0.00	0.00	0.00	0.00	
CaO	23.17	50.64	54.33	54.32	22.99	0.49	0.24	22.57	0.00	0.15	23.11	0.26	0.00	0.62	0.81	
Na2O	0.00	0.00	0.00	0.00	0.00	0.00	0.00	0.29	0.37	0.00	0.00	0.00	0.00	0.23	0.00	
K2O	0.00	0.00	0.00	0.00	0.00	0.00	15.30	0.25	14.67	16.19	0.11	0.00	14.25	6.79	6.38	
P2O5	-	-	-	-	-	-	-	-	-	-	-	-	-	-	-	
Cl	-	-	-	-	-	-	-	-	-	-	-	-	-	-	-	
S	-	-	-	-	-	-	-	-	-	-	-	-	-	-	-	
Total	96.08	57.34	54.52	54.32	95.57	86.72	99.51	95.93	99.81	99.44	96.65	85.62	98.87	87.23	78.48	
Oxygen	25.00	6.00	6.00	6.00	25.00	28.00	8.00	25.00	8.00	8.00	25.00	28.00	8.00	22.00	22.00	
Si	6.30	0.03	0.02	0.00	6.33	5.96	3.02	6.38	3.03	3.03	6.34	6.30	3.07	7.98	7.10	
Al	4.40	0.00	0.00	0.00	4.53	4.32	0.99	4.40	1.00	0.97	4.54	3.83	0.96	2.95	3.51	
Fe2	1.70	0.20	0.00	0.00	1.49	2.99	0.01	1.59	0.00	0.00	1.46	7.73	0.00	0.37	0.40	
Mg	0.00	0.03	0.00	0.00	0.00	6.38	0.00	0.00	0.00	0.00	0.00	1.87	0.00	0.53	0.61	
Ca	4.11	5.40	5.96	6.00	4.06	0.11	0.01	3.99	0.00	0.01	4.03	0.07	0.00	0.09	0.14	
Na	0.00	0.00	0.00	0.00	0.00	0.00	0.00	0.09	0.03	0.00	0.00	0.00	0.00	0.06	0.00	
K	0.00	0.00	0.00	0.00	0.00	0.00	0.90	0.05	0.86	0.96	0.02	0.00	0.84	1.23	1.31	
Ti	0.00	0.00	0.00	0.00	0.00	0.03	0.01	0.00	0.00	0.00	0.00	0.00	0.00	0.00	0.36	
P	0.00	0.00	0.00	0.00	0.00	0.00	0.00	0.00	0.00	0.00	0.00	0.00	0.00	0.00	0.00	
Mn	0.00	0.32	0.00	0.00	0.00	0.06	0.00	0.00	0.00	0.00	0.00	0.00	0.00	0.00	0.00	
Cr	0.00	0.00	0.00	0.00	0.00	0.00	0.00	0.00	0.00	0.00	0.00	0.00	0.00	0.00	0.00	
Total Cat	16.50	5.98	5.98	6.00	16.41	19.85	4.93	16.50	4.92	4.97	16.40	19.79	4.87	13.20	13.44	
Ab							0		4	0			0			
An							1		0	1			0			
Or							99		96	99			100			

A1.9

Sample No	AS14.10		A92/1				A92/2								
Analysis No	AN13	AN14	AN1	AN2	AN3	AN4	AN1	AN2	AN3	AN4	AN5	AN6	AN7	AN8	AN9
SiO2	18.17	7.76	0.00	0.00	0.00	0.00	0.16	0.00	0.00	0.13	0.26	0.00	0.00	0.24	6.49
TiO2	0.00	1.28	0.00	0.00	0.00	0.00	0.00	0.00	0.00	0.00	0.00	0.00	0.00	0.00	0.00
Al2O3	1.80	3.05	0.00	0.00	0.00	0.00	0.00	0.00	0.00	0.00	0.00	0.00	0.00	0.00	2.97
Cr2O3	0.00	0.00	0.00	0.00	0.00	0.00	0.00	0.00	0.00	0.00	0.00	0.00	0.00	0.00	0.00
FeO	0.64	71.62	0.25	0.00	0.00	0.00	0.00	0.00	0.00	0.00	0.00	0.00	0.00	0.00	0.00
MnO	0.00	0.00	0.00	0.00	0.00	0.00	0.00	0.00	0.65	0.81	1.39	0.00	0.63	1.88	0.00
MgO	0.55	0.59	0.00	0.00	0.00	0.00	0.42	0.00	0.00	0.00	0.00	0.00	0.00	0.00	0.00
NiO	0.00	0.00	0.00	0.00	0.00	0.00	0.00	0.00	0.00	0.00	0.00	0.00	0.00	0.00	0.00
CaO	42.31	0.30	55.82	55.55	55.71	56.01	54.74	55.34	55.02	56.24	54.74	55.80	54.89	54.27	67.98
Na2O	0.00	0.48	0.00	0.00	0.00	0.00	0.00	0.00	0.00	0.00	0.00	0.00	0.00	0.00	0.24
K2O	0.74	1.26	0.00	0.00	0.00	0.00	0.00	0.00	0.00	0.00	0.12	0.09	0.00	0.00	2.44
P2O5	-	-	0.00	0.00	0.00	0.00	0.00	0.17	0.00	0.00	0.00	0.00	0.00	0.00	0.00
Cl	-	-	-	-	-	-	-	-	-	-	-	-	-	-	-
S	-	-	-	-	-	-	-	-	-	-	-	-	-	-	-
Total	64.21	86.34	56.07	55.55	55.71	56.01	55.32	55.51	55.67	57.18	56.51	55.89	55.52	56.39	80.12
Oxygen	22.00	22.00	6.00	6.00	6.00	6.00	6.00	6.00	6.00	6.00	6.00	6.00	6.00	6.00	10.00
Si	4.61	2.00	0.00	0.00	0.00	0.00	0.02	0.00	0.00	0.01	0.03	0.00	0.00	0.02	0.70
Al	0.54	0.93	0.00	0.00	0.00	0.00	0.00	0.00	0.00	0.00	0.00	0.00	0.00	0.00	0.38
Fe2	0.14	15.47	0.02	0.00	0.00	0.00	0.00	0.00	0.00	0.00	0.00	0.00	0.00	0.00	0.00
Mg	0.21	0.23	0.00	0.00	0.00	0.00	0.06	0.00	0.00	0.00	0.00	0.00	0.00	0.00	0.00
Ca	11.51	0.08	5.98	6.00	6.00	6.00	5.91	5.96	5.94	5.91	5.82	5.99	5.95	5.79	7.84
Na	0.00	0.24	0.00	0.00	0.00	0.00	0.00	0.00	0.00	0.00	0.00	0.00	0.00	0.00	0.05
K	0.24	0.42	0.00	0.00	0.00	0.00	0.00	0.00	0.00	0.00	0.02	0.01	0.00	0.00	0.34
Ti	0.00	0.25	0.00	0.00	0.00	0.00	0.00	0.00	0.00	0.00	0.00	0.00	0.00	0.00	0.00
P	0.00	0.00	0.00	0.00	0.00	0.00	0.00	0.01	0.00	0.00	0.00	0.00	0.00	0.00	0.00
Mn	0.00	0.00	0.00	0.00	0.00	0.00	0.00	0.00	0.06	0.07	0.12	0.00	0.05	0.16	0.00
Cr	0.00	0.00	0.00	0.00	0.00	0.00	0.00	0.00	0.00	0.00	0.00	0.00	0.00	0.00	0.00
Total Cat	17.24	19.61	6.00	6.00	6.00	6.00	5.98	5.96	6.00	5.99	5.98	6.01	6.00	5.98	9.31
Ab															
An															
Or															

A1.10

Sample No Analysis No	A92/2		AN12	AN13	AN14	AN15	AN16	AN17	AN18	A92/2	A92/4				
	AN10	AN11								AN19	AN1	AN2	AN3	AN4	AN5
SiO2	1.29	0.14	0.00	0.15	0.14	38.11	0.00	0.00	38.24	66.19	0.59	63.98	38.00	37.83	0.20
TiO2	0.00	0.00	0.00	0.00	0.00	0.00	0.00	0.00	0.00	0.00	0.00	0.00	0.00	0.00	0.00
Al2O3	0.00	0.00	0.00	0.00	0.00	22.71	0.00	0.00	22.46	18.34	0.26	17.75	22.51	22.99	0.00
Cr2O3	0.00	0.00	0.00	0.00	0.00	0.00	0.00	0.00	0.00	0.00	0.00	0.00	0.00	0.00	0.00
FeO	0.00	0.00	0.00	0.00	0.00	12.04	0.00	0.00	12.98	0.38	0.00	2.22	12.97	11.93	0.00
MnO	0.00	1.14	1.06	0.55	1.87	0.00	0.56	2.12	0.00	0.00	1.24	0.00	0.00	0.00	0.79
MgO	0.00	0.00	0.00	0.00	0.00	0.00	0.00	0.00	0.00	0.26	0.27	0.35	0.00	0.00	0.00
NiO	0.00	0.00	0.00	0.00	0.00	0.00	0.00	0.00	0.00	0.00	0.00	0.00	0.00	0.00	0.00
CaO	76.81	55.41	54.87	55.49	54.58	22.88	51.25	54.84	22.73	0.31	52.79	0.22	22.89	22.62	55.57
Na2O	0.29	0.00	0.00	0.00	0.00	0.00	0.00	0.00	0.00	0.25	0.00	0.00	0.00	0.00	0.00
K2O	0.36	0.00	0.00	0.00	0.10	0.00	0.00	0.00	0.00	14.78	0.00	15.48	0.00	0.00	0.19
P2O5	0.28	0.00	0.00	0.00	0.00	0.00	0.00	0.00	0.00	0.00	0.00	0.00	0.00	0.00	0.00
Cl	-	-	-	-	-	-	-	-	-	-	-	-	-	-	-
S	-	-	-	-	-	-	-	-	-	-	-	-	-	-	-
Total	79.03	56.69	55.93	56.19	56.69	95.74	51.81	56.96	96.41	100.51	55.15	100.00	96.37	95.37	56.75
Oxygen	10.00	6.00	6.00	6.00	6.00	25.00	6.00	6.00	25.00	8.00	6.00	8.00	25.00	25.00	6.00
Si	0.15	0.01	0.00	0.02	0.01	6.31	0.00	0.00	6.32	3.02	0.06	2.98	6.28	6.28	0.02
Al	0.00	0.00	0.00	0.00	0.00	4.43	0.00	0.00	4.37	0.99	0.03	0.97	4.39	4.50	0.00
Fe2	0.00	0.00	0.00	0.00	0.00	1.67	0.00	0.00	1.79	0.01	0.00	0.09	1.79	1.66	0.00
Mg	0.00	0.00	0.00	0.00	0.00	0.00	0.00	0.00	0.00	0.02	0.04	0.02	0.00	0.00	0.00
Ca	9.57	5.88	5.91	5.92	5.81	4.06	5.95	5.82	4.02	0.02	5.69	0.01	4.06	4.03	5.88
Na	0.07	0.00	0.00	0.00	0.00	0.00	0.00	0.00	0.00	0.02	0.00	0.00	0.00	0.00	0.00
K	0.05	0.00	0.00	0.00	0.01	0.00	0.00	0.00	0.00	0.86	0.00	0.92	0.00	0.00	0.02
Ti	0.00	0.00	0.00	0.00	0.00	0.00	0.00	0.00	0.00	0.00	0.00	0.00	0.00	0.00	0.00
P	0.03	0.00	0.00	0.00	0.00	0.00	0.00	0.00	0.00	0.00	0.00	0.00	0.00	0.00	0.00
Mn	0.00	0.10	0.09	0.05	0.16	0.00	0.05	0.18	0.00	0.00	0.11	0.00	0.00	0.00	0.07
Cr	0.00	0.00	0.00	0.00	0.00	0.00	0.00	0.00	0.00	0.00	0.00	0.00	0.00	0.00	0.00
Total Cat	9.84	5.99	6.00	5.99	5.99	16.47	6.00	6.00	16.50	4.93	5.93	4.99	16.52	16.47	5.99
Ab										2		0			
An										2		1			
Or										96		99			

A1.11

Sample No Analysis No	A92/9							KAS5/FR/1-2							
	AN1	AN2	AN3	AN4	AN5	AN6	AN7	AN1	AN2	AN3	AN4	AN5	AN6	AN7	AN8
SiO2	0.31	49.61	42.58	43.82	43.31	53.17	51.03	65.12	70.35	38.21	28.20	63.49	69.71	28.95	31.11
TiO2	0.00	0.00	0.21	0.28	0.00	0.00	0.00	0.54	0.00	0.00	0.00	0.70	0.00	0.00	31.91
Al2O3	0.00	21.17	21.61	22.18	22.76	22.06	22.03	18.60	19.43	22.89	17.76	18.27	19.65	17.42	5.27
Cr2O3	0.00	0.00	0.00	0.00	0.20	0.00	0.00	0.00	0.00	0.00	0.00	0.00	0.00	0.00	0.00
FeO	0.00	7.37	3.11	2.43	1.45	6.19	3.15	0.36	0.42	12.01	22.66	0.22	0.00	21.53	2.03
MnO	0.00	0.00	0.00	0.00	0.00	0.00	0.00	0.00	0.00	0.29	0.40	0.00	0.00	0.46	0.00
MgO	0.00	5.97	0.00	0.00	0.00	4.17	2.94	0.00	0.00	0.00	17.75	0.00	0.00	18.43	0.88
NiO	0.00	0.00	0.00	0.00	0.00	0.00	0.00	0.00	0.00	0.00	0.00	0.00	0.00	0.00	0.00
CaO	55.97	0.76	26.16	26.47	26.34	0.59	0.78	0.17	0.16	22.67	0.12	0.00	0.15	0.00	0.00
Na2O	0.00	0.30	0.00	0.00	0.00	0.00	0.00	0.44	9.31	0.00	0.00	0.26	9.06	0.00	27.73
K2O	0.00	5.58	0.00	0.00	0.00	5.48	6.08	14.38	0.00	0.00	0.00	14.09	0.14	0.00	0.00
P2O5	0.00	0.00	0.00	0.00	0.00	0.00	0.00	0.00	0.30	0.00	0.00	0.00	0.00	0.00	0.00
Cl	-	-	-	-	-	-	-	-	-	-	0.00	0.00	0.00	0.00	0.00
S	-	-	-	-	-	-	-	0.00	0.00	0.00	0.00	0.00	0.00	0.00	0.00
Total	56.28	90.76	93.67	95.18	94.06	91.66	86.01	99.61	99.97	96.07	86.89	97.03	98.71	86.79	98.93
Oxygen	6.00	22.00	22.00	22.00	22.00	22.00	22.00	8.00	8.00	25.00	28.00	8.00	8.00	28.00	20.00
Si	0.03	6.98	6.07	6.11	6.09	7.27	7.35	2.99	3.04	6.31	5.91	2.99	3.04	6.02	4.09
Al	0.00	3.51	3.63	3.65	3.77	3.56	3.74	1.01	0.99	4.45	4.38	1.02	1.01	4.27	0.82
Fe2	0.00	0.87	0.37	0.28	0.17	0.71	0.38	0.01	0.02	1.66	3.97	0.01	0.00	3.75	0.22
Mg	0.00	1.25	0.00	0.00	0.00	0.85	0.63	0.00	0.00	0.00	5.54	0.00	0.00	5.72	0.17
Ca	5.94	0.12	4.00	3.96	3.97	0.09	0.12	0.01	0.01	4.01	0.03	0.00	0.01	0.00	3.90
Na	0.00	0.08	0.00	0.00	0.00	0.00	0.00	0.04	0.78	0.00	0.00	0.02	0.77	0.00	0.00
K	0.00	1.00	0.00	0.00	0.00	0.96	1.12	0.84	0.00	0.00	0.00	0.85	0.01	0.00	0.00
Ti	0.00	0.00	0.02	0.03	0.00	0.00	0.00	0.02	0.00	0.00	0.00	0.03	0.00	0.00	3.15
P	0.00	0.00	0.00	0.00	0.00	0.00	0.00	0.00	0.01	0.00	0.00	0.00	0.00	0.00	0.00
Mn	0.00	0.00	0.00	0.00	0.02	0.00	0.00	0.00	0.00	0.04	0.07	0.00	0.00	0.08	0.00
Cr	0.00	0.00	0.00	0.00	0.00	0.00	0.00	0.00	0.00	0.00	0.00	0.00	0.00	0.00	0.00
Total Cat	5.97	13.81	14.09	14.03	14.02	13.43	13.34	4.93	4.83	16.47	19.90	4.91	4.84	19.84	12.35
Ab								4	99			3	98		
An								1	1			0	1		
Or								95	0			97	1		

Sample No	KAS5/FR/1-2														
Analysis No	AN9	AN10	AN11	AN12	AN13	AN14	AN15	AN16	AN17	AN18	AN19	AN20	AN21	AN22	AN23
SiO2	37.86	37.69	37.87	64.61	65.88	61.71	0.30	69.01	45.79	47.91	65.40	38.37	46.20	69.68	65.41
TiO2	0.00	0.00	0.21	0.00	0.00	2.16	0.00	0.00	0.00	0.73	0.00	0.00	0.61	0.00	0.21
Al2O3	23.87	22.89	23.39	17.94	18.08	18.97	0.00	20.00	30.98	30.46	18.28	23.06	28.42	19.61	18.37
Cr2O3	0.00	0.00	0.00	0.00	0.00	0.00	0.00	0.00	0.00	0.00	0.00	0.00	0.00	0.00	0.00
FeO	10.91	11.77	10.92	0.00	0.00	0.00	0.00	0.00	4.90	4.31	0.28	12.27	6.20	0.00	0.45
MnO	0.00	0.00	0.00	0.00	0.00	0.00	0.00	0.00	0.00	0.00	0.00	0.00	0.00	0.00	0.00
MgO	0.00	0.00	0.00	0.00	0.00	0.21	0.00	0.22	0.91	1.70	0.00	0.00	3.01	0.00	0.00
NiO	0.00	0.00	0.00	0.00	0.00	0.00	0.00	0.00	0.00	0.00	0.00	0.00	0.00	0.00	0.00
CaO	22.97	22.54	22.69	0.00	0.19	0.00	57.62	0.51	0.00	0.00	0.00	22.76	0.00	0.14	0.00
Na2O	0.00	0.00	0.00	0.27	0.00	0.46	0.00	9.83	0.00	0.00	0.00	0.00	0.33	10.12	0.24
K2O	0.00	0.00	0.00	15.09	14.78	13.21	0.14	0.00	8.49	8.99	14.76	0.00	8.33	0.00	15.29
P2O5	0.00	0.00	0.00	0.00	0.00	0.00	0.00	0.00	0.00	0.00	0.00	0.00	0.00	0.00	0.00
Cl	0.00	0.00	0.00	0.00	0.00	0.00	0.00	0.00	0.00	0.00	0.00	0.00	0.00	0.00	0.00
S	0.00	0.00	0.00	0.00	0.00	0.00	0.00	0.00	0.00	0.00	0.00	0.00	0.00	0.00	0.00
Total	95.61	94.89	95.08	97.91	98.93	96.72	103.64	99.57	91.07	94.10	98.72	96.46	93.10	99.55	99.97
Oxygen	25.00	25.00	25.00	8.00	8.00	8.00	10.00	8.00	22.00	22.00	8.00	25.00	22.00	8.00	8.00
Si	6.24	6.29	6.28	3.03	3.04	2.91	0.02	3.00	6.41	6.48	3.03	6.30	6.40	3.03	3.01
Al	4.64	4.50	4.57	0.99	0.98	1.06	0.00	1.03	5.11	4.86	1.00	4.47	4.64	1.01	1.00
Fe2	1.50	1.64	1.51	0.00	0.00	0.00	0.00	0.00	0.57	0.49	0.01	1.69	0.72	0.00	0.02
Mg	0.00	0.00	0.00	0.00	0.00	0.02	0.00	0.01	0.19	0.34	0.00	0.00	0.62	0.00	0.00
Ca	4.06	4.03	4.03	0.00	0.01	0.00	3.89	0.02	0.00	0.00	0.00	4.01	0.00	0.01	0.00
Na	0.00	0.00	0.00	0.03	0.00	0.04	0.00	0.83	0.00	0.00	0.00	0.00	0.09	0.85	0.02
K	0.00	0.00	0.00	0.90	0.87	0.80	0.01	0.00	1.52	1.55	0.87	0.00	1.47	0.00	0.90
Ti	0.00	0.00	0.03	0.00	0.00	0.08	0.00	0.00	0.00	0.07	0.00	0.00	0.06	0.00	0.01
P	0.00	0.00	0.00	0.00	0.00	0.00	2.43	0.00	0.00	0.00	0.00	0.00	0.00	0.00	0.00
Mn	0.00	0.00	0.00	0.00	0.00	0.00	0.00	0.00	0.00	0.00	0.00	0.00	0.00	0.00	0.00
Cr	0.00	0.00	0.00	0.00	0.00	0.00	0.00	0.00	0.00	0.00	0.00	0.00	0.00	0.00	0.00
Total Cat	16.44	16.46	16.41	4.94	4.90	4.90	3.92	4.90	13.80	13.79	4.91	16.46	14.00	4.89	4.95
Ab				3	0	5		97		100	0			99	2
An				0	1	0		3			0			1	0
Or				97	99	95		0			100			0	98

A1.13

Sample No	KAS8/FR/3									
Analysis No	AN1	AN2	AN3	AN4	AN5	AN6	AN7	AN8	AN9	AN10
SiO2	64.03	65.51	33.87	38.02	66.62	67.42	63.93	37.47	29.35	26.77
TiO2	0.35	0.00	0.00	0.00	0.00	0.00	0.24	0.00	0.00	0.00
Al2O3	17.31	18.42	18.88	22.57	17.72	20.06	17.77	22.75	18.57	11.68
Cr2O3	0.00	0.00	0.00	0.00	0.00	0.00	0.00	0.20	0.00	0.00
FeO	1.05	0.00	19.40	11.83	0.00	0.00	0.00	11.29	18.43	38.84
MnO	0.00	0.00	0.24	0.00	0.00	0.00	0.00	0.00	0.34	0.00
MgO	0.77	0.00	15.08	0.00	0.00	0.00	0.00	0.00	17.09	5.69
NiO	0.00	0.00	0.00	0.00	0.00	0.00	0.00	0.00	0.00	0.00
CaO	0.53	0.15	0.25	22.91	0.00	1.01	0.00	22.66	0.20	0.59
Na2O	1.13	0.34	0.66	0.00	0.00	10.09	0.00	0.00	0.00	0.00
K2O	12.10	15.34	1.41	0.00	14.51	0.00	15.45	0.00	0.00	0.00
P2O5	0.00	0.00	0.00	0.00	0.00	0.00	0.00	0.00	0.00	0.00
Cl	0.00	0.00	0.00	0.00	0.00	0.00	0.00	0.00	0.00	0.00
S	0.00	0.00	0.00	0.00	0.00	0.00	0.00	0.00	0.00	0.00
Total	97.27	99.76	89.79	95.33	98.85	98.58	97.39	94.37	83.98	83.57
Oxygen	8.00	8.00	22.00	25.00	8.00	8.00	8.00	25.00	28.00	28.00
Si	3.00	3.01	5.25	6.32	3.07	2.98	3.02	6.28	6.18	6.47
Al	0.96	1.00	3.45	4.42	0.96	1.04	0.99	4.50	4.61	3.33
Fe2	0.04	0.00	2.52	1.65	0.00	0.00	0.00	1.58	3.25	7.86
Mg	0.05	0.00	3.49	0.00	0.00	0.00	0.00	0.00	5.37	2.05
Ca	0.03	0.01	0.04	4.08	0.00	0.05	0.00	4.07	0.05	0.15
Na	0.10	0.03	0.20	0.00	0.00	0.86	0.00	0.00	0.00	0.00
K	0.72	0.90	0.28	0.00	0.85	0.00	0.93	0.00	0.00	0.00
Ti	0.01	0.00	0.00	0.00	0.00	0.00	0.01	0.00	0.00	0.00
P	0.00	0.00	0.00	0.00	0.00	0.00	0.00	0.00	0.00	0.00
Mn	0.00	0.00	0.03	0.00	0.00	0.00	0.00	0.00	0.06	0.00
Cr	0.00	0.00	0.00	0.00	0.00	0.00	0.00	0.03	0.00	0.00
Total Cat	4.92	4.95	15.26	16.47	4.88	4.93	4.95	16.46	19.51	19.86
Ab	12	3			0	95	0			
An	3	1			0	5	0			
Or	85	96			100	0	100			



Sample Analysis No	A92/9 <0.1um						A92/9 <0.05um						
	AN1	AN2	AN3	AN4	AN5	AN6	AN1	AN2	AN3	AN4	AN5	AN6	AN7
SiO2	53.75	25.26	51.61	53.78	55.45	47.52	45.29	51.72	40.24	42.69	53.46	48.03	50.07
TiO2	0.00	0.00	0.00	0.00	0.00	0.00	0.00	0.00	0.00	0.00	0.00	0.00	0.00
Al2O3	21.82	10.14	20.54	21.14	22.41	19.52	17.80	20.04	15.40	16.48	20.57	19.27	19.87
Cr2O3	0.00	0.00	0.00	0.00	0.00	0.00	0.00	0.00	0.00	0.00	0.00	0.00	0.00
FeO	2.83	3.00	3.46	3.56	3.27	2.77	3.13	3.10	3.16	3.33	3.18	3.12	3.49
MnO	0.00	0.00	0.00	0.00	0.00	0.00	0.00	0.00	0.00	0.00	0.00	0.00	0.00
MgO	4.14	1.52	3.69	3.92	4.13	3.43	2.96	3.49	2.85	3.07	4.00	3.24	3.64
NiO	0.00	0.00	0.00	0.00	0.00	0.00	0.00	0.00	0.00	0.00	0.00	0.00	0.00
CaO	0.64	0.55	0.68	0.71	0.70	0.66	0.30	1.13	0.00	0.00	0.00	0.00	0.35
Na2O	0.31	0.00	0.29	0.00	0.00	0.00	3.07	3.70	2.82	3.03	3.50	2.74	3.06
K2O	6.82	5.23	6.38	7.36	7.33	6.38	5.83	6.22	6.03	6.57	6.28	6.57	6.76
P2O5	0.00	0.00	0.00	0.00	0.00	0.00	0.00	0.00	0.00	0.39	0.00	0.00	0.00
Cl	-	-	-	-	-	-	-	-	-	-	-	-	-
S	-	-	-	-	-	-	-	-	-	-	-	-	-
Total	90.31	45.70	86.65	90.47	93.29	80.28	78.38	89.40	70.50	75.56	90.99	82.97	87.24
Oxygen	22.00	22.00	22.00	22.00	22.00	22.00	22.00	22.00	22.00	22.00	22.00	22.00	22.00
Si	7.39	7.20	7.42	7.43	7.40	7.38	7.32	7.32	7.31	7.23	7.38	7.32	7.28
Al	3.54	3.41	3.48	3.44	3.53	3.57	3.39	3.34	3.30	3.29	3.35	3.46	3.41
Fe2	0.33	0.72	0.42	0.41	0.37	0.36	0.42	0.37	0.48	0.47	0.37	0.40	0.42
Mg	0.85	0.65	0.79	0.81	0.82	0.79	0.71	0.74	0.77	0.78	0.82	0.74	0.79
Ca	0.09	0.17	0.11	0.11	0.10	0.11	0.05	0.17	0.00	0.00	0.00	0.00	0.06
Na	0.08	0.00	0.08	0.00	0.00	0.00	0.96	1.02	0.99	1.00	0.94	0.81	0.86
K	1.20	1.90	1.17	1.30	1.25	1.26	1.20	1.12	1.40	1.42	1.11	1.28	1.25
Ti	0.00	0.00	0.00	0.00	0.00	0.00	0.00	0.00	0.00	0.00	0.00	0.00	0.00
P	0.00	0.00	0.00	0.00	0.00	0.00	0.00	0.00	0.00	0.00	0.00	0.00	0.00
Mn	0.00	0.00	0.00	0.00	0.00	0.00	0.00	0.00	0.00	0.00	0.00	0.00	0.00
Cr	0.00	0.00	0.00	0.00	0.00	0.00	0.00	0.00	0.00	0.00	0.00	0.00	0.00
Total Cat	13.48	14.04	13.46	13.50	13.46	13.47	14.06	14.08	14.24	14.19	13.96	14.00	14.07

Sample Analysis No	A92/7 <0.1um				A92/23 <0.05um						
	AN1	AN2	AN3	AN4	AN1	AN2	AN3	AN4	AN5	AN6	AN7
SiO2	51.67	54.07	48.44	51.80	49.43	55.03	49.20	52.12	44.99	49.94	53.46
TiO2	0.00	0.00	0.00	0.00	0.00	0.00	0.00	0.00	0.00	0.00	0.00
Al2O3	21.05	22.23	19.58	21.32	20.01	22.65	20.43	20.84	17.57	20.22	21.76
Cr2O3	0.00	0.00	0.00	0.00	0.00	0.00	0.00	0.00	0.00	0.00	0.00
FeO	5.92	6.16	5.97	5.79	6.05	5.63	5.92	5.72	5.51	6.20	6.36
MnO	0.00	0.00	0.00	0.00	0.00	0.00	0.00	0.00	0.00	0.00	0.00
MgO	3.56	3.73	3.08	3.68	3.38	4.37	3.77	3.80	2.80	3.44	3.60
NiO	0.00	0.00	0.00	0.00	0.00	0.00	0.00	0.00	0.00	0.00	0.00
CaO	0.51	0.85	0.80	0.79	0.00	0.00	0.00	0.28	0.00	0.00	0.00
Na2O	0.00	0.00	0.00	0.00	0.71	0.98	0.90	0.70	0.42	0.59	0.72
K2O	6.79	7.40	6.94	7.09	6.88	7.25	6.71	7.00	6.78	6.68	7.27
P2O5	0.00	0.00	0.00	0.00	0.00	0.00	0.00	0.00	0.00	0.00	0.00
Cl	-	-	-	-	-	-	-	-	-	-	-
S	-	-	-	-	-	-	-	-	-	-	-
Total	89.50	94.44	84.81	90.47	86.46	95.91	86.93	90.46	78.07	87.07	93.17
Oxygen	22.00	22.00	22.00	22.00	22.00	22.00	22.00	22.00	22.00	22.00	22.00
Si	7.30	7.26	7.28	7.26	7.28	7.25	7.20	7.31	7.36	7.29	7.29
Al	3.51	3.52	3.47	3.52	3.47	3.52	3.53	3.44	3.39	3.48	3.50
Fe2	0.70	0.69	0.75	0.68	0.75	0.62	0.73	0.67	0.75	0.76	0.73
Mg	0.75	0.75	0.69	0.77	0.74	0.86	0.82	0.79	0.68	0.75	0.73
Ca	0.08	0.12	0.13	0.12	0.00	0.00	0.00	0.04	0.00	0.00	0.00
Na	0.00	0.00	0.00	0.00	0.20	0.25	0.26	0.19	0.13	0.17	0.19
K	1.22	1.27	1.33	1.27	1.29	1.22	1.25	1.25	1.41	1.24	1.26
Ti	0.00	0.00	0.00	0.00	0.00	0.00	0.00	0.00	0.00	0.00	0.00
P	0.00	0.00	0.00	0.00	0.00	0.00	0.00	0.00	0.00	0.00	0.00
Mn	0.00	0.00	0.00	0.00	0.00	0.00	0.00	0.00	0.00	0.00	0.00
Cr	0.00	0.00	0.00	0.00	0.00	0.00	0.00	0.00	0.00	0.00	0.00
Total Cat	13.56	13.61	13.65	13.61	13.73	13.72	13.79	13.70	13.72	13.68	13.69

Sample No Analysis No	A91/6 <0.1um	A91/23 <0.1um	A91/23 <0.05um	A91/32 <0.1um	A91/32 <0.05um	A91/36 <0.1um	A91/38 <0.1um	A91/39 <0.1um	A91/39 <0.05um	A92/7 <0.1um
SiO2	58.20	62.50	59.40	59.70	59.90	62.50	61.60	60.40	59.60	61.50
TiO2	--	--	--	--	--	--	--	--	--	--
Al2O3	22.60	20.60	22.70	19.40	23.00	23.80	19.60	24.60	21.70	23.10
Cr2O3	--	--	--	--	--	--	--	--	--	--
FeO	5.70	5.20	2.70	4.90	2.50	3.50	8.00	1.70	7.20	4.60
MnO	0.70	0.10	0.00	0.10	0.10	0.10	0.30	0.30	0.10	0.10
MgO	1.80	1.10	3.30	3.50	2.20	0.10	0.20	2.50	0.10	0.10
NiO	--	--	--	--	--	--	--	--	--	--
CaO	1.80	0.90	3.00	3.20	2.80	1.00	0.70	1.40	2.00	1.20
Na2O	0.20	0.30	0.20	0.00	0.80	0.30	0.30	0.60	0.20	0.30
K2O	8.90	9.20	8.60	9.20	8.80	8.70	9.20	8.40	9.00	9.00
P2O5	--	--	--	--	--	--	--	--	--	--
Cl	--	--	--	--	--	--	--	--	--	--
S	--	--	--	--	--	--	--	--	--	--
Total	99.90	99.90	99.90	100.00	100.10	100.00	99.90	99.90	99.90	99.90
Oxygen	22.00	22.00	22.00	22.00	22.00	22.00	22.00	22.00	22.00	22.00
Si	7.44	7.87	7.47	7.62	7.52	7.76	7.88	7.50	7.63	7.72
Al	3.40	3.06	3.36	2.92	3.40	3.48	2.96	3.60	3.27	3.42
Fe2	0.61	0.55	0.28	0.52	0.26	0.36	0.86	0.18	0.77	0.48
Mg	0.34	0.21	0.62	0.67	0.41	0.02	0.04	0.46	0.02	0.02
Ca	0.25	0.12	0.40	0.44	0.38	0.13	0.10	0.19	0.27	0.16
Na	0.05	0.07	0.05	0.00	0.20	0.07	0.07	0.14	0.05	0.07
K	1.45	1.48	1.38	1.50	1.41	1.38	1.50	1.33	1.47	1.44
Ti	0.00	0.00	0.00	0.00	0.00	0.00	0.00	0.00	0.00	0.00
P	0.08	0.01	0.00	0.01	0.01	0.01	0.03	0.03	0.01	0.01
Mn	0.00	0.00	0.00	0.00	0.00	0.00	0.00	0.00	0.00	0.00
Cr	0.00	0.00	0.00	0.00	0.00	0.00	0.00	0.00	0.00	0.00
Total Cat	13.61	13.37	13.56	13.67	13.58	13.22	13.43	13.44	13.49	13.33

**APPENDIX 2      SAMPLE PREPARATION**

The samples were separated using procedures described in detail in the CMSU Quality Management Procedures Manual. The system has been audited in accord with BS 5750 by external quality consultants to satisfy Nirex UK Ltd QA requirements. The following is a brief summary of methodology used.

**A2.1 SAMPLE TREATMENT**

Samples were washed and disaggregated by hand under DIW. The suspensions generated were then left to stand for a few minutes to allow the  $>75\mu\text{m}$  components to drop out. The remaining suspensions were then carefully decanted for gravity and centrifuge separation. The coarser sediment fractions were then size sorted by sieving.

**Coarse Sediment Separation**

The coarse separates were fractionated using a stack of BSI standard sieves with 2mm, 1mm,  $500\mu\text{m}$ ,  $250\mu\text{m}$  and  $75\mu\text{m}$  meshes. Fractions were wet sieved and dried in a low temperature oven at approximately  $40^{\circ}\text{C}$  for up to 3 days. These fractions were then weighed and doubly bagged. All surplus suspensions collected in the receiver below the  $75\mu\text{m}$  mesh sieve were poured into the clay suspension fractions for further separation.

**Clay Fraction Separation**

The  $<75\mu\text{m}$  fractions for each sample were separated into 4 further fractions assuming equivalent spherical diameters and an assumed mineral density of  $1.65\text{ g.cm}^{-3}$  using Stoke's Law. The fractions were:  $>20<75\mu\text{m}$ ,  $>8<20\mu\text{m}$ ,  $>2<8\mu\text{m}$  and  $<2\mu\text{m}$ . No material  $>75\mu\text{m}$  was detected in the earlier decanted suspensions. The  $>8\mu\text{m}$  fractions were separated in gravity settling tubes. The  $<8\mu\text{m}$  fractions were separated by centrifuge. In each successive fraction repeated washes ensured minimal contamination from the finer components. All  $<75\mu\text{m}$  fractions were dried and homogenised using a freeze drier and their weights recorded.

The distribution of size fractions is shown in Table A2.1.

## A2.2

### A2.2 OBSERVATIONS OF WET CLAY COLOURS DURING SEPARATION PROCEDURES

#### A91/39

Sample exhibited a dark green colour in all size fractions.

#### A91/38

Sample exhibited a dark brown colour in all size fractions.

#### A91/36

Sample exhibited a light brown colour in all size fractions.

#### A91/32

The  $<2\mu\text{m}$  fraction from this sample showed 3 colours: light brown (coarsest), dark brown and an unusual blue component (finest).

#### A91/23

Two distinct coloured components were noted in this sample: dark green and light brown. Separation of these two coloured components was observed in each clay fraction, the unmixing being most apparent in the finer fractions due probably to the use of a centrifuge. In the gravity settling tubes the green and brown components separated within minutes at room temperature. The green component settled after the brown in all the size fractions. In the  $<2\mu\text{m}$  the brown fraction separated into a heavier brown and a light brown component, with the light brown dominating by volume.

#### A91/8A

Sample showed a light brown colour in all size fractions.

#### A91/7A

Sample showed a medium brown colour in all size fractions.

#### A91/6

Sample was white to very pale brown colour in all size fractions.

## A2.3

Table A2.1 Dry weights for all separated size fractions in grams and by percentage

Sample No	Size Fraction	Fraction wt (g)	wt.% of total
A91/39	>2mm	113.74	40.9
	>1<2mm	50.65	18.2
	>0.5<1mm	31.39	11.3
	>250<500 $\mu$ m	26.21	9.4
	>75<250 $\mu$ m	25.84	9.3
	>20<75 $\mu$ m	7.20	2.6
	>8<20 $\mu$ m	6.50	2.3
	>2<8 $\mu$ m	6.93	2.5
	<2 $\mu$ m	9.60	3.5
	Total	278.06	100.0
A91/36	>2mm	250.59	46.7
	>1<2mm	69.61	13.0
	>0.5<1mm	58.57	10.9
	>250<500 $\mu$ m	43.65	8.1
	>75<250 $\mu$ m	47.16	8.8
	>20<75 $\mu$ m	21.85	4.1
	>8<20 $\mu$ m	13.50	2.5
	>2<8 $\mu$ m	23.78	4.4
	<2 $\mu$ m	7.34	1.4
	Total	536.05	99.9
A91/38	>2mm	194.10	23.8
	>1<2mm	107.53	13.2
	>0.5<1mm	94.11	11.5
	>250<500 $\mu$ m	84.56	10.4
	>75<250 $\mu$ m	110.25	13.5
	>20<75 $\mu$ m	89.19	10.9
	>8<20 $\mu$ m	48.61	6.0
	>2<8 $\mu$ m	57.27	7.0
	<2 $\mu$ m	29.55	3.6
	Total	815.17	99.9
A91/32	>2 mm	155.31	25.2
	>1<2mm	75.48	12.3
	>0.5<1mm	68.41	11.1
	>250<500 $\mu$ m	66.49	10.8
	>75<250 $\mu$ m	65.71	10.7
	>20<75 $\mu$ m	58.53	9.5
	>8<20 $\mu$ m	40.97	6.7
	>2<8 $\mu$ m	30.07	4.9
	<2 $\mu$ m	54.42	8.8
	Total	615.39	100.0

## A2.4

Sample No	Size Fraction	Fraction wt (g)	wt. % of total
A91/23	>2mm	46.34	21.4
	>1<2mm	22.40	10.4
	>0.5<1mm	21.00	9.7
	>250<500 $\mu$ m	19.89	9.2
	>75<250 $\mu$ m	24.93	11.5
	>20<75 $\mu$ m	13.42	6.2
	>8<20 $\mu$ m	11.71	5.4
	>2<8 $\mu$ m	19.73	9.1
	<2 $\mu$ m	36.84	17.0
	Total	216.26	99.9
A91/8	>2mm	71.60	30.3
	>1<2mm	39.78	16.8
	>0.5<1mm	28.48	12.0
	>250<500 $\mu$ m	26.36	11.1
	>75<250 $\mu$ m	24.97	10.6
	>20<75 $\mu$ m	7.91	3.3
	>8<20 $\mu$ m	8.53	3.6
	>2<8 $\mu$ m	19.06	8.1
	<2 $\mu$ m	9.68	4.1
	Total	236.37	99.9
A91/7	>2mm	52.74	48.5
	>1<2mm	16.55	15.2
	>0.5<1mm	9.41	8.7
	>250<500 $\mu$ m	9.89	9.1
	>75<250 $\mu$ m	10.48	9.6
	>20<75 $\mu$ m	2.95	2.7
	>8<20 $\mu$ m	3.29	3.0
	>2<8 $\mu$ m	0.38	0.003
	<2 $\mu$ m	3.06	2.8
	Total	108.75	99.603
A91/6	>2mm	69.26	23.4
	>1<2mm	37.84	12.8
	>0.5<1mm	39.34	13.3
	>250<500 $\mu$ m	32.62	11.0
	>75<250 $\mu$ m	35.62	12.0
	>20<75 $\mu$ m	27.30	9.2
	>8<20 $\mu$ m	19.24	6.5
	>2<8 $\mu$ m	25.71	8.7
	<2 $\mu$ m	9.62	3.2
	Total	296.55	100.1

## A3.1

APPENDIX 3 ORIENTATION DATA FOR PALAEOMAGNETIC SAMPLES

Note: 1) see Tables 3-2 and 5-1 for locations of sample sites.  
 2) LBO = loose before orientation.

Site	Core	MAGAZ (deg)	DIP (deg)	Comment
AS1	1	114	71.5 ± 3	
	2	119	72 ± 1.5	
	3	110	74 ± 0.5	
	4	110	76 ± 2.5	
	5	119	76 ± 1.0	
	6	114	70 ± 4.5	
AS2	1	272	75 ± 2	
	2	271	74 ± 1	
	3	274	68 ± 1	
	4	296	64 ± 1	
	5	294	54 ± 1.5	
AS3	-	014	88	bulk sample
AS4	-	016	49	bulk sample
AS5	1		$\theta = 95^\circ$	cube sample
	2		$\theta = 88^\circ$	cube sample
AS6	1	94	72 ± 3	
	2	93	74 ± 2	
	3	95	75 ± 2	
AS7	1	96	72 ± 3	
	2	96	71 ± 3	
	3	96	66 ± 2	
	4	92	66 ± 4	
	5	97	65 ± 1	
AS8	1	022	66 ± 1	
	2	016	68 ± 0.5	
	3	017	69 ± 0.5	
AS9	1	252	116	below horizontal
	2	231	88 ± 2	
	3	248	77 ± 1	
	4	236	78 ± 3	
AS10	1	174	61 ± 1	
	2	162	61.5 ± 1.5	
	3	154	60 ± 2	
	4	181	68 ± 2	
	5	254	61.5 ± 1.5	
	6	215	51.5 ± 1.5	
AS11		229	56 ± 1	
	1	300	44 ± 1	
	2	256	53 ± 2	
	3	268	50 ± 1	
	4	232	43.5 ± 0	
	5	217	64 ± 1	
6	229	56 ± 1		
AS12	-	022	84	bulk sample (overhead)
AS13	-	068	73	bulk sample



A3.2

Site	Core	MAGAZ (deg)	DIP (deg)	Comment
AS14	1	145	50,51	cube sample
	2	169	0,41	cube sample
	3	155	20,61	cube sample
	4	149	0,0	cube sample
	5	144	0,0	cube sample poor orientation
	6	128	20,0	cube sample
	7	155	40,41	cube sample
	8	167	20,0	cube sample
	9	119	20,0	cube sample
	10	162	0,3r	cube sample
ASV1				bulk sample
AS20	1	185	21	15cm from E wall
	2	179	46 ± 1.0	26cm
	3	351	23 ± 1.0	30cm
	4	200	34.5 ± 1.5	39cm
	5	196	54.5 ± 1.5	74cm
	6	205	38 ± 1.0	81cm
AS21	1	244	14 ± 1.0	LBO
	2	187	17	
	3	231	15 ± 1.0	
	4	252	19	LBO
	5	298	12.5	
	6	241	16 ± 1.0	LBO
AS22	1	348	9	
	2	323	23.5 ± 1.5	
	3	015	21	LBO
	4	016	15	LBO
	5	160	12 ± 2	LBO
	6	205	13	LBO
AS23	1	314	16 ± 1.0	
	2	272	19	
	3	177	26 ± 1	
	4	173	20 ± 1.0	
	5	168	27 ± 2.0	LBO
AS24	-	202	79	strike & dip
AS25	-	020	95	strike & dip
AS26	-	202	88	strike & dip
	-	202	87	strike & dip
	-	202	85	strike & dip
AS27	-	317	75	mean strike & dip
	-			
AS28	1	250	80 ± 1.0	
	2	237	87 ± 1.0	
	3	234	82 ± 1.0	LBO
	4	250	72	
	5	329	73	
	6	327	79 ± 3.0	LBO
AS29	-	193	103	strike & dip; overturned
	-			strike & dip
	-	195	90	strike & dip
	-	192	88	

## A4.1

## APPENDIX 4

IN-SITU GAMMA-RAY SPECTROMETRY

Table A4-1 In-situ gamma-ray spectrometer measurements at chainage 120m

Count Sequence No	Background counts in 10s	Monazite standard counts in 10s	Sample time to 1K counts
1	160		
2	145		
3	146		
4	167		
5	123		
6		10377	
7		10231	
8		10234	
9		10028	
10			71
11			79
12			77
13			71
14			99
15			81
16			83
17			87

Table A4-2 In-situ gamma-ray spectrometer measurements at fracture zone EW-7, side tunnel, chainage 670m

Count Sequence No	Background counts in 10s	Monazite standard counts in 10s	Sample time to 1K counts
1	203		
2	189		
3	162		
4	176		
5	210		
6		9704	
7		9682	
8		9489	
9		10185	
10		10318	
11		10313	
12		10370	
13		10370	
14			25
15			25
16			25
17			25
18			31
19			33
20			30
21			31

A4.2

Table A4-3 In-situ gamma-ray spectrometer measurements at fracture zone NE-4, tunnel wall, chainage 850m

Count Sequence No	Background counts in 10s	Monazite standard counts in 10s	Sample time to 1K counts
1	170		
2	162		
3	169		
4	159		
5	147		
6	160		
7	138		
8	135		
9	155		
10	175		
11		11576	
12		11451	
13		11357	
14		11649	
15		11263	
16		13976	
17		10368	
18		10087	
19		10270	
20		10120	
21		10153	
22		10237	
23			86
24			84
25			80
26			66
27			75
28			54
29			138
30			88
31			82
32			133
33			84
34			75
35		10367	
36		10518	
37		10340	

# List of SKB reports

## Annual Reports

1977-78

TR 121

### **KBS Technical Reports 1 – 120**

Summaries

Stockholm, May 1979

1979

TR 79-28

### **The KBS Annual Report 1979**

KBS Technical Reports 79-01 – 79-27

Summaries

Stockholm, March 1980

1980

TR 80-26

### **The KBS Annual Report 1980**

KBS Technical Reports 80-01 – 80-25

Summaries

Stockholm, March 1981

1981

TR 81-17

### **The KBS Annual Report 1981**

KBS Technical Reports 81-01 – 81-16

Summaries

Stockholm, April 1982

1982

TR 82-28

### **The KBS Annual Report 1982**

KBS Technical Reports 82-01 – 82-27

Summaries

Stockholm, July 1983

1983

TR 83-77

### **The KBS Annual Report 1983**

KBS Technical Reports 83-01 – 83-76

Summaries

Stockholm, June 1984

1984

TR 85-01

### **Annual Research and Development Report 1984**

Including Summaries of Technical Reports Issued during 1984. (Technical Reports 84-01 – 84-19)

Stockholm, June 1985

1985

TR 85-20

### **Annual Research and Development Report 1985**

Including Summaries of Technical Reports Issued during 1985. (Technical Reports 85-01 – 85-19)

Stockholm, May 1986

1986

TR 86-31

### **SKB Annual Report 1986**

Including Summaries of Technical Reports Issued during 1986

Stockholm, May 1987

1987

TR 87-33

### **SKB Annual Report 1987**

Including Summaries of Technical Reports Issued during 1987

Stockholm, May 1988

1988

TR 88-32

### **SKB Annual Report 1988**

Including Summaries of Technical Reports Issued during 1988

Stockholm, May 1989

1989

TR 89-40

### **SKB Annual Report 1989**

Including Summaries of Technical Reports Issued during 1989

Stockholm, May 1990

1990

TR 90-46

### **SKB Annual Report 1990**

Including Summaries of Technical Reports Issued during 1990

Stockholm, May 1991

1991

TR 91-64

### **SKB Annual Report 1991**

Including Summaries of Technical Reports Issued during 1991

Stockholm, April 1992

1992

TR 92-46

### **SKB Annual Report 1992**

Including Summaries of Technical Reports Issued during 1992

Stockholm, May 1993

## Technical Reports

### List of SKB Technical Reports 1993

TR 93-01

#### **Stress redistribution and void growth in butt-welded canisters for spent nuclear fuel**

B L Josefson<sup>1</sup>, L Karlsson<sup>2</sup>, H-Å Häggblad<sup>2</sup>

<sup>1</sup> Division of Solid Mechanics, Chalmers University of Technology, Göteborg, Sweden

<sup>2</sup> Division of Computer Aided Design, Luleå University of Technology, Luleå, Sweden

February 1993

TR 93-02

#### **Hydrothermal field test with French candidate clay embedding steel heater in the Stripa mine**

R Pusch<sup>1</sup>, O Karnland<sup>1</sup>, A Lajudie<sup>2</sup>, J Lechelle<sup>2</sup>, A Bouchet<sup>3</sup>

<sup>1</sup> Clay Technology AB, Sweden

<sup>2</sup> CEA, France

<sup>3</sup> Etude Recherche Materiaux (ERM), France  
December 1992

TR 93-03

#### **MX 80 clay exposed to high temperatures and gamma radiation**

R Pusch<sup>1</sup>, O Karnland<sup>1</sup>, A Lajudie<sup>2</sup>, A Decarreau<sup>3</sup>,

<sup>1</sup> Clay Technology AB, Sweden

<sup>2</sup> CEA, France

<sup>3</sup> Univ. de Poitiers, France

December 1992

TR 93-04

#### **Project on Alternative Systems Study (PASS).**

##### **Final report**

October 1992

TR 93-05

#### **Studies of natural analogues and geological systems.**

##### **Their importance to performance assessment**

Fredrik Brandberg<sup>1</sup>, Bertil Grundfelt<sup>1</sup>,

Lars Olof Höglund<sup>1</sup>, Fred Karlsson<sup>2</sup>,

Kristina Skagius<sup>1</sup>, John Smellie<sup>3</sup>

<sup>1</sup> KEMAKTA Konsult AB

<sup>2</sup> SKB

<sup>3</sup> Conterra AB

April 1993

TR 93-06

#### **Mineralogy, geochemistry and petrophysics of red coloured granite adjacent to fractures**

Thomas Eliasson

Chalmers University of Technology and University of Göteborg, Department of Geology, Göteborg, Sweden

March 1993

TR 93-07

#### **Modelling the redox front movement in a KBS-3 nuclear waste repository**

L Romero, L Moreno, I Neretnieks

Department of Chemical Engineering,

Royal Institute of Technology, Stockholm, Sweden

May 1993

TR 93-08

#### **Äspö Hard Rock Laboratory Annual Report 1992**

SKB

April 1993

TR 93-09

#### **Verification of the geostatistical inference code INFERENS, Version 1.1, and demonstration using data from Finnsjön**

Joel Geier

Golder Geosystem AB, Uppsala

June 1993

TR 93-10

#### **Mechanisms and consequences of creep in the nearfield rock of a KBS-3 repository**

Roland Pusch, Harald Hökmark

Clay Technology AB, Lund, Sweden

December 1992

TR 93-11

#### **Post-glacial faulting in the Lansjärv area, Northern Sweden.**

##### **Comments from the expert group on a field visit at the Molberget post-glacial fault area, 1991**

Roy Stanfors (ed.)<sup>1</sup>, Lars O Ericsson (ed.)<sup>2</sup>

<sup>1</sup> R S Consulting AB

<sup>2</sup> SKB

May 1993

TR 93-12

#### **Possible strategies for geoscientific classification for high-level waste repository site selection**

Lars Rosén, Gunnar Gustafson

Department of Geology, Chalmers University of Technology and University of Göteborg

June 1993

TR 93-13

#### **A review of the seismotectonics of Sweden**

Robert Muir Wood

EQE International Ltd, Warrington, Cheshire, England

April 1993

TR 93-14

**Simulation of the European ice sheet through the last glacial cycle and prediction of future glaciation**

G S Boulton, A Payne

Department of Geology and Geophysics,  
Edinburgh University, Grant Institute, Edinburgh,  
United Kingdom  
December 1992

TR 93-15

**Analysis of the regional groundwater flow in the Finnsjön area**

Anders Boghammar, Bertil Grundfelt, Hans Widén  
Kemakta Konsult AB  
June 1993

TR 93-16

**Kinetic modelling of bentonite - canister interaction. Implications for Cu, Fe, and Pb corrosion in a repository for spent nuclear fuel**

Paul Wersin, Jordi Bruno, Kastriot Spahiu  
MBT Tecnologia Ambiental, Cerdanyola, Spain  
June 1993

TR 93-17

**Oxidation of uraninite**

Janusz Janeczek, Rodney C Ewing  
Department of Earth & Planetary Science, University  
of New Mexico, Albuquerque, NM, USA  
June 1993

TR 93-18

**Solubility of the redox-sensitive radionuclides <sup>99</sup>Tc and <sup>237</sup>Np under reducing conditions in neutral to alkaline solutions. Effect of carbonate**

Trygve E Eriksen<sup>1</sup>, Pierre Ndalamba<sup>1</sup>, Daqing Cui<sup>1</sup>,  
Jordi Bruno<sup>2</sup>, Marco Caceci<sup>2</sup>, Kastriot Spahiu<sup>2</sup>

<sup>1</sup> Dept. of Nuclear Chemistry, Royal Institute of  
Technology, Stockholm, Sweden

<sup>2</sup> MBT Tecnologia Ambiental, Cerdanyola, Spain  
September 1993

TR 93-19

**Mechanical properties of fracture zones**

Bengt Leijon  
Conterra AB  
May 1993

TR 93-20

**The Fracture Zone Project - Final report**

Peter Andersson (ed.)  
Geosigma AB, Uppsala, Sweden  
September 1993

TR 93-21

**Development of "CHEMFRONTS", a coupled transport and geochemical program to handle reaction fronts**

Catharina Bäverman

Department of Chemical Engineering, Royal Institute  
of Technology, Stockholm, Sweden  
October 1993

TR 93-22

**Carbon transformations in deep granitic groundwater by attached bacterial populations characterized with 16S-rRNA gene sequencing technique and scanning electron microscopy**

Susanne Ekendahl, Johanna Arlinger, Fredrik Ståhl,  
Karsten Pedersen

Department of General and Marine Microbiology,  
University of Göteborg, Göteborg, Sweden  
October 1993

TR 93-23

**Accelerator transmutation of wastes (ATW)**

**– Prospects and safety**

Waclaw Gudowski, Kjell Pettersson,

Torbjörn Thedéen

Royal Institute of Technology, Stockholm, Sweden  
November 1993